

SOURCE PARAMETERS AND SOURCE MECHANISM OF SEISMIC EVENTS OCCURRING  
IN SEQUENCES AT A POLISH COPPER MINE AND SOUTH AFRICAN GOLD MINE:  
SEARCH FOR POSSIBLE TIME VARIATIONS

S. J. Gibowicz, B. Domanski, P. Wiejacz

Institute of Geophysics  
Polish Academy of Sciences  
ul. Ks. Janusza 64  
01-452 Warsaw, Poland

**DISTRIBUTION STATEMENT A**

Approved for public release;  
Distribution Unlimited

Final Report for the U. S. Department of the Air Force  
European Office of Aerospace Research and Development

Special Contract SPC-94-4073

24 September 1994 - 24 September 1995

**DTIC QUALITY INSPECTED 3**

15 November 1995

19980311 154

**REPORT DOCUMENTATION PAGE**

Form Approved OMB No. 0704-0188

Public reporting burden for this collection of information is estimated to average 1 hour per response, including the time for reviewing instructions, searching existing data sources, gathering and maintaining the data needed, and completing and reviewing the collection of information. Send comments regarding this burden estimate or any other aspect of this collection of information, including suggestions for reducing this burden to Washington Headquarters Services, Directorate for Information Operations and Reports, 1215 Jefferson Davis Highway, Suite 1204, Arlington, VA 22202-4302, and to the Office of Management and Budget, Paperwork Reduction Project (0704-0188), Washington, DC 20503.

1. AGENCY USE ONLY (Leave blank)		2. REPORT DATE  15 November 1995		3. REPORT TYPE AND DATES COVERED  Final Report	
4. TITLE AND SUBTITLE  Source Parameters and Source Mechanism of Seismic Events Occurring in Sequences at a Polish Copper Mine and South African Gold Mine: Search for Possible Time Variations				5. FUNDING NUMBERS  F6170894W0760	
6. AUTHOR(S)  Prof Slavomir J. Gibowicz					
7. PERFORMING ORGANIZATION NAME(S) AND ADDRESS(ES)  Polish Academy of Sciences ul. Ks. Janusza 64 Warszawa 01-452 Poland				8. PERFORMING ORGANIZATION REPORT NUMBER  N/A	
9. SPONSORING/MONITORING AGENCY NAME(S) AND ADDRESS(ES)  EOARD PSC 802 BOX 14 FPO 09499-0200				10. SPONSORING/MONITORING AGENCY REPORT NUMBER  SPC 94-4073	
11. SUPPLEMENTARY NOTES					
12a. DISTRIBUTION/AVAILABILITY STATEMENT  Approved for public release; distribution is unlimited.				12b. DISTRIBUTION CODE  A	
13. ABSTRACT (Maximum 200 words)  This report results from a contract tasking Polish Academy of Sciences as follows: Investigate the swarm-like behavior of seismic events from Polish and South African mines.					
14. SUBJECT TERMS  Nil				15. NUMBER OF PAGES  170	
				16. PRICE CODE N/A	
17. SECURITY CLASSIFICATION OF REPORT  UNCLASSIFIED	18. SECURITY CLASSIFICATION OF THIS PAGE  UNCLASSIFIED	19. SECURITY CLASSIFICATION OF ABSTRACT  UNCLASSIFIED		20. LIMITATION OF ABSTRACT  UL	

NSN 7540-01-280-5500

Standard Form 298 (Rev. 2-89)  
Prescribed by ANSI Std. Z39-18  
298-102

## Table of Contents

List of Illustrations.....	iii
List of Tables.....	xiii
ABSTRACT.....	1
 <b>PART I: WESTERN DEEP LEVELS GOLD MINE IN SOUTH AFRICA</b>	
CHAPTER 1: INTRODUCTION.....	3
CHAPTER 2: SEISMIC NETWORK AND DATA.....	6
CHAPTER 3: SEISMIC SEQUENCE OF APRIL 1993.....	9
3.1 Space distribution.....	9
3.2 Time distribution.....	12
3.3 Frequency-magnitude relations and fractal dimension.....	16
CHAPTER 4: SPECTRAL SOURCE PARAMETERS.....	31
4.1 Spectral analysis.....	31
4.2 Relations between various source parameters.....	33
4.3 P-wave energy versus S-wave energy.....	45
4.4 Time distribution of the source parameters.....	49
CHAPTER 5: MOMENT TENSOR INVERSION: SOURCE MECHANISM.....	55
5.1 The method used in the ISS system.....	55
5.2 Source mechanism.....	61
5.3 Space distribution of P, T and B axes.....	64
5.4 Time distribution of P, T and B axes.....	73
CHAPTER 6: SPECTRAL AND MOMENT TENSOR SOURCE PARAMETERS.....	76
CHAPTER 7: CONCLUSIONS.....	83
 <b>PART II: POLKOWICE COPPER MINE IN POLAND</b>	
CHAPTER 1: INTRODUCTION.....	86
CHAPTER 2: GEOLOGICAL STRUCTURE AND TECTONICS.....	88
CHAPTER 3: SEISMIC NETWORK AND DATA.....	90
CHAPTER 4: MINING WORKS, SEISMICITY AND FRACTAL DIMENSION.....	95
4.1 Section G-32.....	95
4.2 Section G-21.....	98

CHAPTER 5: SPECTRAL SOURCE PARAMETERS.....	102
5.1 Spectral analysis.....	102
5.2 Relations between various source parameters.....	107
5.3 Time distribution of the source parameters at section G-32.....	130
5.4 Time distribution of the source parameters at section G-21.....	139
CHAPTER 6: MOMENT TENSOR INVERSION.....	140
6.1 The method.....	140
6.2 Space distribution of the source mechanisms at section G-32.....	143
6.3 Space distribution of the source mechanisms at section G-21.....	152
CHAPTER 7: CONCLUSIONS.....	160
REFERENCES.....	162

## List of Illustrations

### WESTERN DEEP LEVELS GOLD MINE

FIGURE 1. Horizontal distribution of seismic stations (open circles) and selected seismic events (dots) at Western Deep Levels gold mine.....	7
FIGURE 2. Vertical distribution along the N-S direction of seismic stations (open circles) and selected seismic events (dots) at Western Deep Levels gold mine.....	8
FIGURE 3. Horizontal distribution of seismic events forming four sequences, marked by different symbols. The main shocks of each sequence are marked by circled points and are numbered 1, 2, 3, and 4.....	10
FIGURE 4. Vertical distribution along the N-S direction of seismic events forming four sequences, marked by different symbols. The main shocks of each sequence are marked by circled points and are numbered 1, 2, 3, and 4.....	11
FIGURE 5. Cumulative number of seismic events versus time after the occurrence of the first main shock for the four sequences. The main shocks are marked by open circles and are numbered 1, 2, 3, and 4.....	13
FIGURE 6. Logarithm of rate of occurrence versus the consecutive number of time intervals used to calculate the rate of occurrence for the four sequences 1, 2, 3, and 4.....	14
FIGURE 7. Logarithm of rate of occurrence versus logarithm of time after the main shocks for the four sequences. The data are marked by different symbols and for the sake of clarity are separated by one decade. The values of $p$ parameter are also shown for each sequence.....	15
FIGURE 8. Histogram of moment magnitude of all seismic events which occurred during the four sequences.....	17

FIGURE 9. Logarithm of the cumulative number of seismic events versus their moment magnitude for all events from the four sequences. The magnitude interval is $\Delta M=0.2$ and the slope coefficient $b=0.63$ .....	18
FIGURE 10. Frequency-magnitude relations for the four sequences 1, 2, 3, and 4. The observations are marked by different symbols and for the sake of clarity are separated by one decade. The number of observations and the values of parameter $b$ are also indicated.....	19
FIGURE 11. Histogram of distances between the pairs of events from sequence 1, used to estimate the fractal dimension of the sequence.....	21
FIGURE 12. Histogram of distances between the pairs of events from sequence 2, used to estimate the fractal dimension of the sequence.....	22
FIGURE 13. Histogram of distances between the pairs of events from sequence 3, used to estimate the fractal dimension of the sequence.....	23
FIGURE 14. Histogram of distances between the pairs of events from sequence 4, used to estimate the fractal dimension of the sequence.....	24
FIGURE 15. Logarithm of the correlation integral versus logarithm of the distance between the pairs of events from sequence 1 for various distance intervals $dr$ . Circled points are used to estimate the fractal dimension $D$ by the linear regression.....	26
FIGURE 16. Logarithm of the correlation integral versus logarithm of the distance between the pairs of events from sequences 1, 2, 3, and 4. Circled points are used to estimate the fractal dimension $D$ by the linear regression.....	27
FIGURE 17. Parameter $p$ versus parameter $b$ for the four sequences. Utsu's relation $p=4b/3$ is shown by the dashed line.....	29
FIGURE 18. Fractal dimension $D$ versus parameter $b$ for the four sequences. Aki's relation $D=2b$ is adjusted by a term $+0.8$ and is shown by the dashed line.....	30

FIGURE 19. Logarithm of seismic moment estimated from <i>P</i> -wave spectra versus that estimated from <i>S</i> -wave spectra for the four sequences. The straight line corresponds to the same values of both estimates.....	34
FIGURE 20. Logarithm of seismic energy versus logarithm of seismic moment. Linear regression slope coefficient and correlation coefficient $R_c$ are also indicated.....	35
FIGURE 21. Logarithm of <i>P</i> -wave corner frequency versus logarithm of <i>S</i> -wave corner frequency. The slope coefficient of the linear regression is close to one.....	37
FIGURE 22. Logarithm of seismic moment versus logarithm of <i>S</i> -wave corner frequency.....	38
FIGURE 23. Logarithm of Brune stress drop versus logarithm of seismic moment.....	40
FIGURE 24. Logarithm of apparent stress versus logarithm of seismic moment.....	41
FIGURE 25. Logarithm of apparent stress versus logarithm of Brune stress drop. The ratio of Brune stress drop over apparent stress equal to 10 is shown by the dashed line.....	43
FIGURE 26. Logarithm of average displacement versus logarithm of seismic moment.....	44
FIGURE 27. Logarithm of <i>P</i> -wave energy versus logarithm of <i>S</i> -wave energy. The ratio of <i>S</i> -wave energy over <i>P</i> -wave energy equal to 1, 10, and 100 is shown by straight lines.....	46
FIGURE 28. Logarithm of the ratio of <i>S</i> -wave energy over <i>P</i> -wave energy versus logarithm of Brune stress drop.....	47
FIGURE 29. Logarithm of the ratio of <i>S</i> -wave energy over <i>P</i> -wave energy versus logarithm of apparent stress.....	48

FIGURE 30. Source radius versus real time after the occurrence of the first main shock for the four sequences.....	50
FIGURE 31. Source radius versus the number of consecutive seismic events forming the four sequences whose beginnings are clearly marked by the highest values of the source radius.....	51
FIGURE 32. Logarithm of seismic moment $M_0$ (in $N \cdot m$ ), seismic energy $E$ (in $J$ ) and source radius $R_0$ (in $m$ ) versus the number of consecutive seismic events forming the four sequences.....	52
FIGURE 33. Logarithm of Brune stress drop $dS$ (in $MPa$ ), source radius $R_0$ (in $m$ ) and apparent stress $S_a$ (in $MPa$ ) versus the number of consecutive seismic events forming the four sequences. The stress drop is moved up by 3 units for the sake of clarity.....	53
FIGURE 34. An example of the moment tensor solutions for the first seismic event from the selected series. Full description is given in the text.....	59
FIGURE 35. An example of the double-couple moment tensor solution for one of the events from the selected series. Full description is given in the text.....	60
FIGURE 36. The isotropic component versus the double couple component of the general moment tensor solution for 35 seismic events from the four sequences. The correlation coefficient $R_c$ is also indicated.....	62
FIGURE 37. The CLVD component versus the double couple component of the general moment tensor solution for 35 seismic events from the four sequences.....	63
FIGURE 38. Horizontal distribution of normalized eigenvectors (length of 50 $m$ ) describing P (continuous lines), T (dashed lines) and B (dotted lines) axes from double couple moment tensor solutions obtained for 46 seismic events from the four sequences, marked by different symbols. The four main shocks are marked by circled points and numbered 1, 2, 3, 4...	65



FIGURE 39. Horizontal distribution of P axes from 46 seismic events from the four sequences, marked by different symbols. The four main shocks are marked by circled points and numbered 1, 2, 3, and 4.....	66
FIGURE 40. Horizontal distribution of T axes from 46 seismic events from the four sequences, marked by different symbols. The four main shocks are marked by circled points and numbered 1, 2, 3, and 4.....	67
FIGURE 41. Horizontal distribution of B axes from 46 seismic events from the four sequences, marked by different symbols. The four main shocks are marked by circled points and numbered 1, 2, 3, and 4.....	68
FIGURE 42. Vertical distribution along the N-S direction of P (continuous lines), T (dashed lines) and B (dotted lines) axes from 46 seismic events from the four sequences, marked by different symbols. The four main shocks are marked by circled points and numbered 1, 2, 3, and 4....	69
FIGURE 43. Vertical distribution along the N-S direction of P axes from 46 seismic events from the four sequences, marked by different symbols. The four main shocks are marked by circled points and numbered 1, 2, 3, and 4.....	70
FIGURE 44. Vertical distribution along the N-S direction of T axes from 46 seismic events from the four sequences, marked by different symbols. The four main shocks are marked by circled points and numbered 1, 2, 3, and 4.....	71
FIGURE 45. Vertical distribution along the N-S direction of B axes from 46 seismic events from the four sequences, marked by different symbols. The four main shocks are marked by circled points and numbered 1, 2, 3, and 4.....	72
FIGURE 46. Azimuth of B, P and T axes versus the number of consecutive 46 seismic events from the four sequences. The azimuth ranges from 0 to 360 degrees. The P and T axes are separated from the B axis by 360 and 720 degrees, respectively, for the sake of clarity. The beginning of sequences is marked by numbers 1, 2, 3, and 4 on the B axis.....	74

FIGURE 47. Plunge of B, P and T axes versus the number of consecutive 46 seismic events from the four sequences. The plunges ranges from -90 to +90 degrees. The P and T axes are separated from the B axis by 180 and 360 degrees, respectively, for the sake of clarity. The beginning of sequences is marked by numbers 1, 2, 3, and 4 on the B axis..... 75

FIGURE 48. Logarithm of seismic moment estimated from the momet tensor inversion versus that estimated from the spectra for 46 seismic events for which source mechanism is determined. The straigh line corresponds to the same values of both estimates..... 77

FIGURE 49. Logarithm of *P*-wave energy versus logarithm of *S*-wave energy for 46 seismic events for which source mechanism is determined. The ratio of *S*-wave energy over *P*-wave energy equal to 1, 10, and 100 is shown by straight lines..... 78

FIGURE 50. Logarithm of the ratio of *S*-wave over *P*-wave energy versus the double couple component of the general moment tensor solution for 35 seismic events from the four sequences..... 79

FIGURE 51. Logarithm of the ratio of *S*-wave over *P*-wave energy versus the CLVD component of the general moment tensor solution for 35 seismic events from the four sequences..... 80

FIGURE 52. Logarithm of the ratio of *S*-wave over *P*-wave energy versus the isotropic component of the general moment tensor solution for 35 seismic events from the four sequences..... 81

## List of Illustrations

### POLKOWICE COPPER MINE

- FIGURE 1. Horizontal distribution of seismic stations (single-component marked by triangles and three-components by squares) at Polkowice copper mine and selected seismic events (stars) at sections G-32 and G-21..... 91
- FIGURE 2. Histogram of distances between the pairs of seismic events from section G-32 (top) and the correlation integral  $C(r)$  versus the distance (bottom), used to estimate the fractal dimension of the events. 96
- FIGURE 3. Linear approximation of the correlation integral  $C(r)$  as a function of the distance between the pairs of events from section G-32. The fractal dimension  $D$  is also indicated..... 97
- FIGURE 4. Histogram of distances between the pairs of seismic events from section G-21 (top) and the correlation integral  $C(r)$  versus the distance (bottom), used to estimate the fractal dimension of the events. 99
- FIGURE 5. Linear approximation of the correlation integral  $C(r)$  as a function of the distance between the pairs of events from section G-21. The fractal dimension  $D$  is also indicated..... 100
- FIGURE 6. Example of typical seismograms recorded at Polkowice mine from the seismic event of October 6, 1994 with moment magnitude  $M=2.2$ , which occurred at section G-21. The vertical bars show the windows selected for spectral analysis of  $P$  and  $S$  waves, and the time axis is in seconds. 103
- FIGURE 7. Example of a  $P$ -wave displacement spectrum from the seismic event of November 23, 1994 with moment magnitude 1.7, which occurred at section G-32. The spectrum is approximated by two straight lines. The corresponding  $P$ -wave record is shown at the top..... 104
- FIGURE 8. Example of a  $S$ -wave displacement spectrum from the seismic event of September 23, 1994 with moment magnitude 1.8, which occurred at section G-32. The spectrum is approximated by two straight lines. The corresponding  $S$ -wave record is shown at the top..... 105

FIGURE 9. Seismic moment estimated from S-wave spectra versus that estimated from P-wave spectra for seismic events from section G-32. The straight line corresponds to the same value of both estimates.....	108
FIGURE 10. Seismic moment estimated from S-wave spectra versus that estimated from P-wave spectra for seismic events from section G-21. The straight line corresponds to the same value of both estimates.....	109
FIGURE 11. S-wave corner frequency versus P-wave corner frequency for seismic events from section G-32.....	113
FIGURE 12. S-wave corner frequency versus P-wave corner frequency for seismic events from section G-21.....	114
FIGURE 13. Seismic moment versus source radius for seismic events from section G-32. The lines of constant stress drop are also indicated.....	115
FIGURE 14. Seismic moment versus source radius for seismic events from section G-21. The lines of constant stress drop are also indicated.....	116
FIGURE 15. Seismic energy versus seismic moment for events from section G-32. The approximation of data by linear regression is also shown.....	120
FIGURE 16. Seismic energy versus seismic moment for events from section G-21. The approximation of data by linear regression is also shown.....	121
FIGURE 17. Stress drop versus seismic moment for seismic events from section G-32.....	122
FIGURE 18. Stress drop versus seismic moment for seismic events from section G-21.....	123
FIGURE 19. Apparent stress versus seismic energy for seismic events from section G-32.....	124
FIGURE 20. Apparent stress versus seismic energy for seismic events from section G-21.....	125

FIGURE 21. Apparent stress versus stress drop for seismic events from section G-32. The lines of constant ratio of apparent stress over stress drop are also marked.....	126
FIGURE 22. Apparent stress versus stress drop for seismic events from section G-21. The lines of constant ratio of apparent stress over stress drop are also marked.....	127
FIGURE 23. S-wave energy versus P-wave energy for seismic events from section G-32. The ratio of S- over P-wave energy equal to 1, 10, and 100 is shown by straight lines.....	128
FIGURE 24. S-wave energy versus P-wave energy for seismic events from section G-21. The ratio of S- over P-wave energy equal to 1, 10, and 100 is shown by straight lines.....	129
FIGURE 25. Seismic moment, seismic energy and source radius versus time for seismic events from section G-32.....	131
FIGURE 26. Seismic moment, seismic energy and source radius versus the number of consecutive seismic events from section G-32.....	132
FIGURE 27. Seismic moment, stress drop and apparent stress versus the number of consecutive seismic events from section G-32.....	133
FIGURE 28. P-wave energy, S-wave energy and total seismic energy versus the number of consecutive seismic events from section G-32.....	134
FIGURE 29. Seismic moment, seismic energy and source radius versus time for seismic events from section G-21.....	135
FIGURE 30. Seismic moment, seismic energy and source radius versus the number of consecutive seismic events from section G-21.....	136
FIGURE 31. Seismic moment, stress drop and apparent stress versus the number of consecutive seismic events from section G-21.....	137

FIGURE 32. P-wave energy, S-wave energy and total seismic energy versus the number of consecutive seismic events from section G-21.....	138
FIGURE 33. Seismic moment estimated from the moment tensor inversion versus that estimated from the spectra for seismic events from section G-32.....	144
FIGURE 34. Horizontal distribution of full moment tensor solutions for seismic events at section G-32. Equal-area lower-hemisphere projection is used.....	148
FIGURE 35. Horizontal distribution of deviatoric moment tensor solutions for seismic events at section G-32. Equal-area lower-hemisphere projection is used.....	149
FIGURE 36. Horizontal distribution of double couple moment tensor solutions for seismic events at section G-32. Equal-area lower-hemisphere projection is used.....	150
FIGURE 37. Seismic moment estimated from the moment tensor inversion versus that estimated from the spectra for seismic events from section G-32.....	153
FIGURE 38. Horizontal distribution of full moment tensor solutions for seismic events at section G-21. Equal-area lower-hemisphere projection is used.....	157
FIGURE 39. Horizontal distribution of deviatoric moment tensor solutions for seismic events at section G-21. Equal-area lower-hemisphere projection is used.....	158
FIGURE 40. Horizontal distribution of double couple moment tensor solutions for seismic events at section G-21. Equal-area lower-hemisphere projection is used.....	159

**List of Tables**  
**POLKOWICE COPPER MINE**

TABLE 1. Origin time and location of selected seismic events at Polkowice mine section G-32.....	92
Table 2. Origin time and location of selected seismic events at Polkowice mine section G-21.....	93
Table 3. Seismic moment and source radius of seismic events at Polkowice mine section G-32.....	110
Table 4. Seismic moment and source radius of seismic events at Polkowice mine section G-21.....	111
Table 5. Seismic energy and stress release estimate for seismic events at Polkowice mine section G-32.....	117
Table 6. Seismic energy and stress release estimate for seismic events at Polkowice mine section G-21.....	118
Table 7. Full moment tensor solutions for seismic events at section G-32.	145
Table 8. Deviatoric moment tensor solutions for seismic events at section G-32.....	146
Table 9. Double couple moment tensor solutions for seismic events at section G-32.....	147
Table 10. Full moment tensor solutions for seismic events at section G-21.....	154
Table 11. Deviatoric moment tensor solutions for seismic events at section G-21.....	155
Table 12. Double couple moment tensor solutions for seismic events at section G-21.....	156

## ABSTRACT

The investigation conducted under this contract is focused on a search for possible time variations of source parameters and mechanism of seismic events occurring in sequences at Polkowice copper mine in Poland and Western Deep Levels (WDL) gold mine in South Africa. The results of this study are described for WDL in Part I and for Polkowice mine in Part II of this report.

A swarm-like seismic sequence, composed of four main shock-aftershock type sequences, occurred in April 1993 at the WDL mine. Altogether 199 events with moment magnitude from -0.5 to 3.1 were located by the local seismic network. The first sequence lasted 179 hours and the second sequence lasted only 13 hours and was interrupted by the third sequence which lasted 33 hours and was in turn interrupted by the fourth sequence. The parameter  $p$ , describing the rate of occurrence of aftershocks, ranges from 0.7 to 1. The parameter  $b$  from the frequency-magnitude relation has the value of 0.6 for the whole series. The fractal dimension  $D$  has the lowest value of  $D=1.75$  for the first sequence and the highest value of  $D=2.4$  for the second sequence.

Source parameters of all events were determined by spectral analysis of  $P$  and  $S$  waves. The corner frequencies of  $P$  and  $S$  waves are close to each other and they range from 14 to 220 Hz. The corresponding source radius ranges from 6 to 85 m. A display of source parameters as a function of time shows that the four main shocks are most distinctly marked by their source radius. The second and third sequences are characterized by a number of large events in terms of seismic moment and energy, whereas the fourth sequence is of regular pattern, similarly as the first sequence.

For 46 events a moment tensor inversion was performed. For 35 events a general moment tensor solution was obtained and for 11 events only constrained double couple solutions were found. In most cases the double couple component is dominant, ranging from 60 to 90 percent of the solution. A negative correlation between the isotropic and double couple components and between the CLVD and double couple components was found.

An analysis of space distribution of  $P$ ,  $T$  and  $B$  axes from the double couple solutions shows that the distribution of  $B$  axes is the most regular. They tend to act horizontally from the north to the south. The  $P$  axes tend to



act vertically down along the E-W direction and the T axes appear to act vertically up along the same direction. No regular pattern is observed in their distributions with time.

The ratio of S- over P-wave energy ranges from 1 to 30 and for three quarters of the events is less than 10. A positive correlation between the energy ratio and the double couple indicator and inverse correlations between the ratio and the CLVD and isotropic indicators are established. The correlation coefficients are 0.56, -0.41 and -0.47, respectively. They are significant with 99 percent confidence in the first case and with 95 percent confidence in the second and third cases.

In contrast to South African gold mines, seismic sequences are seldom observed in Polish copper mines. The search for regular seismic sequences at Polkowice mine, at sections G-32 and G-21 with the highest level of seismicity, was not successful in a sense used in earthquake seismology. Altogether 34 seismic events from section G-32 and 56 events from section G-21 were selected. The events form close clusters, associated with mining works in the two sections. The two series are characterized by low values of fractal dimension,  $D=2.0$  at section G-32 and  $D=2.2$  at section G-21.

The selected seismic events have moment magnitude ranging from 1.2 to 3.0 and seismic energy between  $1 \cdot 10^4$  and  $1 \cdot 10^8$  J. The corner frequencies of P and S waves range from 2.2 to 13 Hz and the corresponding source radius is in the range from about 75 to 370 m. The stress drop ranges from 0.025 to 0.56 MPa and the apparent stress is about ten times lower than the stress drop. All source parameters show similar distribution in time. There are a few outstanding events with the source parameters of the highest values, while those of the other events are randomly distributed in time.

The deviatoric and double couple moment tensor solutions are similar, whereas the full tensor solutions show occasionally large non-shearing components resulting from the poor geometry of seismic network. In the deviatoric solutions, the contribution of non-shearing components to the mechanism is in most cases less than 20 percent of the solution. Many seismic events at section G-32 show similar source mechanisms, which is the case at section G-21 as well, but their association with mining works is difficult to assess.

## PART I: WESTERN DEEP LEVELS GOLD MINE IN SOUTH AFRICA

### 1. INTRODUCTION

Shallow natural earthquakes seldom occur as isolated events; they usually form well-defined sequences in space and time. Mogi (1963) has divided these sequences into three types: main shock-aftershocks, foreshocks-main shock-aftershocks, and swarm, which he considered as indicating increasing heterogeneity of the source area, although this idea seems to be too general (Scholz, 1990). Foreshock and aftershock sequences are associated with a larger event called the main shock. Earthquake sequences not associated with a dominant event are called swarms.

Foreshocks are smaller events that precede the main shock. They usually occur closely to the main shock hypocenter and are probably a part of the nucleation process (e. g., Scholz, 1990). Their occurrence is rather irregular. Many earthquakes have no foreshocks, and foreshock sequences range from one or two events to small swarms. Jones and Molnar (1979), who made a global survey of forshocks, found that about 60 percent of large earthquakes were preceded by foreshocks.

Aftershocks follow almost all shallow earthquakes and form the most frequently observed earthquake sequences. The globally observed characteristics of aftershocks is the hyperbolical time dependence of their frequency, which is known as the Omori law. The largest aftershock in the sequence is typically at least one magnitude smaller than the main shock (Utsu, 1971). The total seismic moment of aftershocks usually amounts to only about 5 percent of the moment of the main shock (Scholz, 1972). This rule was found to be valid for the 1977 Lubin, Poland, tremor which occurred in a deep copper mine (Gibowicz *et al.*, 1979). Aftershocks begin immediately after the main shock over the entire rupture area and its surroundings, although they are usually concentrated in places where large stress concentrations produced by the main rupture are expected (e. g., Mendoza and Hartzell, 1988).

Earthquake swarms are sequences of earthquakes that often start and end gradually, without a single earthquake dominating in size. They are most often associated with volcanic regions, but this is not a universal rule (Sykes, 1970). There is a tendency for earthquake swarms to occur in and around the focal region long before the large earthquake (Evison, 1977).

Little is known about tremor sequences in mines. There are only a few studies available on this subject, made at a gold mine in South Africa and at a copper mine in Poland. McGarr and Green (1978) have studied foreshock-aftershock sequences of two mine tremors of magnitudes 1.5 and 1.2, which occurred in May 1973 in a region of active mining in the East Rand Propriety Mines near Johannesburg, South Africa. The seismic coverage of the sequences was complete down to magnitudes of -3.5. In the first hour after each event some 140 microaftershocks were recorded with a rate of occurrence decreasing with time in a regular manner. Although the two events occurred within about 50 m of one another and within 12 days, the seismicity before the tremor of magnitude 1.5 was at its normal ambient level of about 4 events per hour, whereas the seismicity before the event of magnitude 1.2 was unusually high, at about 30 events per hour. McGarr and Green (1978) have shown that a main shock-aftershock sequence and sequence similar to a swarm can occur in the same volume of rocks under similar strain conditions.

It seems that in South African gold mines seismic events occurring in sequences are often observed. In contrast, tremor sequences are seldom observed in Polish hard-rock mines. The 1977 tremor of magnitude 4.5, which occurred at the Lubin copper mine, was an exception. It was followed by a regular aftershock sequence with the largest aftershock of magnitude 3.4 (Gibowicz *et al.*, 1979). The frequency-time distribution of aftershocks was typical with a rate of occurrence decaying hyperbolically in time. But the 1987 event of magnitude 4.3, which occurred at the same mine, was followed by a few small aftershocks with the largest two aftershocks of magnitude 2.1, differing considerably from the level of seismicity observed during 3 months preceding the main shock (Gibowicz *et al.*, 1989). The daily release of seismic moment from aftershocks during the first month after the main event was found to be twice smaller than that from the tremors preceding the event. It seems, in general, that aftershocks to seismic events in mines are not as ubiquitous as those in natural seismicity.

Western Deep Levels gold mine, selected for our study, is situated in the Carletonville gold mining district, some 80 km south of Johannesburg. The mine area contains two major conglomerate formations, the Ventersdorp Contact Reef at an average depth of 2 km and the Carbon Leader Reef at a depth of 3 km. The Western Deep Levels lease area extends 10.8 km from east to west and 4 km from north to south. Since its inception, Western Deep Levels has developed into three mines, West, East and South, which operate as separate entities.

On 7 April 1993, an interesting swarm-like sequence of seismic events occurred in the Upper Carbon Leader Back Area at the East mine. These events were associated with several pillars intersected by the Lesser and Greater Green Dykes and the Speckled Dyke. The pillars left along these dykes were not part of the regional stabilising program in use at Western Deep Levels, but were left because of the large amount of waste mining that would have been required had they been removed (A. G. Butler, person. comm., 1993). Very little seismicity has been recorded in the area prior to a moment magnitude 2.7 event which occurred on 7 April as the first event in the sequence. The sequence continued till 19 April and 199 seismic events have been recorded with moment magnitude down to -0.5.

Spectral analysis of seismic waves and moment tensor inversion techniques will be used to study the source parameters and source mechanism of seismic events forming this swarm-like sequence. The spectral analysis will provide the source parameters, such as seismic moment, seismic energy, source dimension, stress drop, apparent stress, to characterize individual events forming the sequence. The moment tensor inversion will provide the source mechanism in the most general form, since moment tensors describe completely the equivalent forces of a seismic point source. A moment tensor will be decomposed into an isotropic part corresponding to a volumetric change, a compensated linear vector dipole describing a sort of uniaxial compression or tension, and a double couple corresponding to a shear failure. The main objective of this study is to investigate possible time variations in terms of the source parameters and source mechanism during the sequence. It should be noted that a few works only have been published so far that are related to the use of moment tensor inversion in studies of seismicity induced by mining (Sato and Fujii, 1989; Fujii and Sato, 1990; Feignier and Young, 1992; McGarr, 1992 a,b; Wiejacz, 1992, 1995).

## 2. SEISMIC NETWORK AND DATA

The Integrated Seismic System (ISS) is in operation at Western Deep Levels from the beginning of 1990s. In 1993 the underground seismic network was composed of 22 three-component stations; several of them in close vicinity to the area where the sequence occurred. Their horizontal distribution against the location of seismic events forming the sequence is shown in Fig. 1, and their vertical distribution along the N-S direction is presented in Fig. 2.

The ISS system has been described in some detail by Mendecki (1993). It is comprised of transducers, remote stations, a communication system, and a central computer. The ISS is digital, intelligent and works in real time. With conversion to a digital format as close as possible to the sensors, maximum dynamic range is ensured. The seismometers allow for a dynamic range greater than 120 dB with a resolution of 12 bits. The standard sampling frequency is 2000 Hz. Digital communication between the remote sites and a central computer permits transmission of waveforms with no amplitude or phase distortion. The remote units are intelligent allowing for immediate processing at the site and effective use of low cost communication lines.

The system performs on-line the quality controlled seismological processing of three-component waveforms, developed to run in an automatic mode. The following functions are executed: *P*-wave picking, rotation of components, *S*-wave picking, source location, calculation of spectral parameters from each *P*, *SH* and *SV* components, moment tensor inversion, and calculation of source parameters.

The sequence of April 1993, selected for this study, is composed of 199 seismic events, recorded, located and processed by the ISS system. Their spectral and source parameters and their moment tensors were estimated in the interactive mode by one of the authors, whereas their location was calculated automatically. Out of 199 events, the general moment tensor inversion was successful for the 35 largest events and for 11 smaller events only restrained double couple solutions were found. The collected data are displayed and discussed in the following sections.

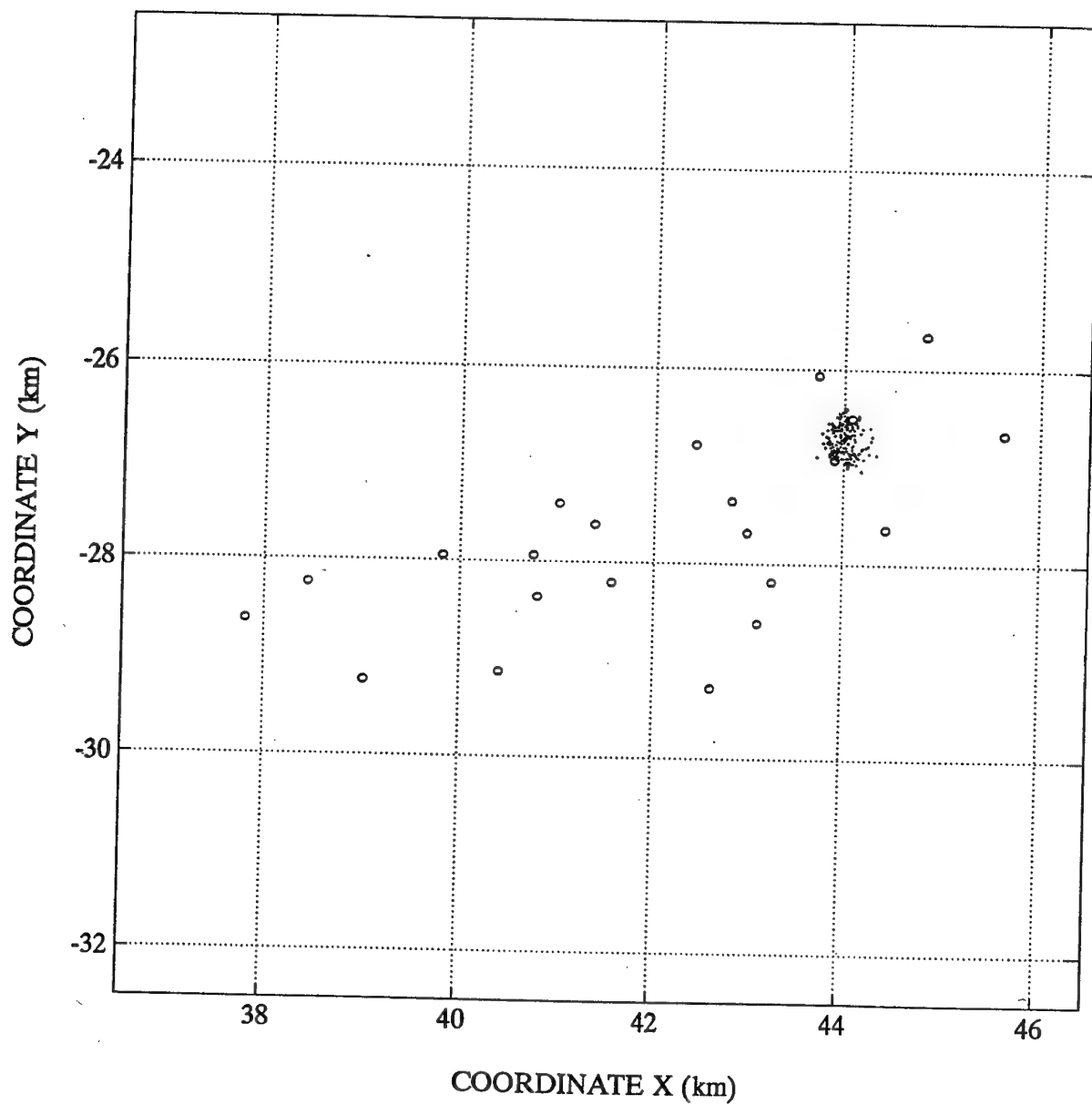


FIGURE 1. Horizontal distribution of seismic stations (open circles) and selected seismic events (dots) at Western Deep Level gold mine.

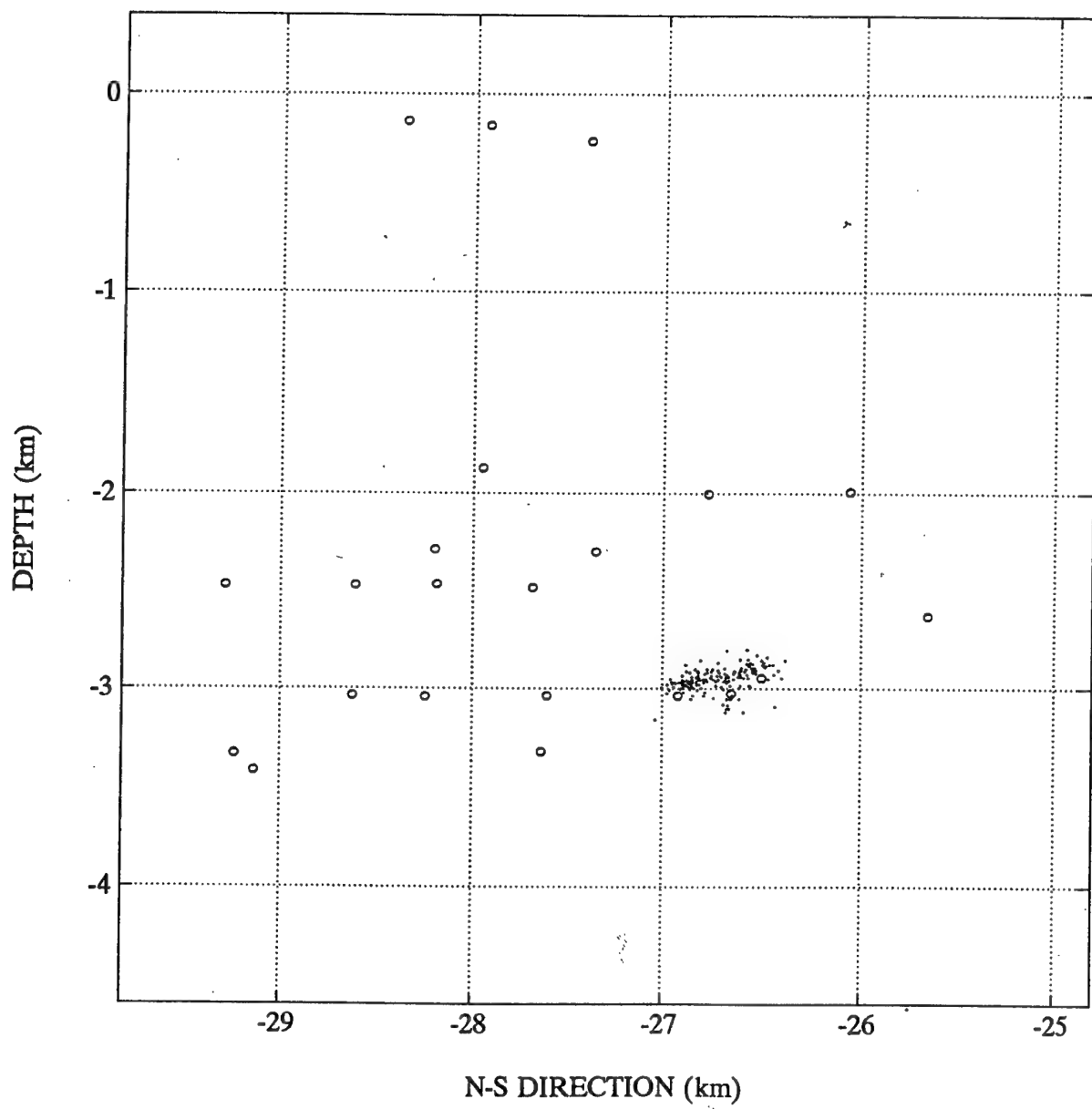


FIGURE 2. Vertical distribution along the N-S direction of seismic stations (open circles) and selected seismic events (dots) at Western Deep Levels gold mine.

### 3. SEISMIC SEQUENCE OF APRIL 1993

The sequence has started on April 7, 1993 at 09h09m local time, when a seismic event with moment magnitude 2.7 has occurred, and ended on April 19 at 05h43m. Very little seismicity has been recorded in the area prior to the magnitude 2.7 event. The sequence was associated with several pillars intersected by the Lesser and Greater Green Dykes and the Speckled Dyke.

Although the sequence as a whole appears to form a swarm-like series, in a sense that no single event is dominant, it is composed in fact of four main shock - aftershock sequences, following closely each other in space and in time. The first main shock of magnitude 2.7 was followed by 38 recorded aftershocks, the second event of the same moment magnitude 2.7 occurred on April 14 at 20h17m and was followed by 63 aftershocks, and third main shock of magnitude 3.1 occurred on April 15 at 09h30m and was followed by 67 aftershocks. The fourth sequence was composed of 25 aftershocks and three main shocks of magnitude 1.5, 2.5 and 2.0, which occurred on April 16 at 18h24m, 18h25m and 18h26m, respectively. These events would correspond to a single main shock of magnitude 2.6. The smallest aftershock out of 199 recorded events was of magnitude -0.5, but the magnitude threshold, above which the set is complete, is -0.3 and the number of recorded events with magnitude above this threshold is 196.

#### 3.1 Space distribution

The accuracy of hypocenter determination ranged between less than 10 m and 40 m; in most cases it was between 10 and 20 m. The events were confined to a volume of rock extending to 630 m in the E-W direction, 670 m in the N-S direction, and 390 m in the vertical direction. The horizontal distribution of seismic events forming the four sequences, marked by different symbols, is shown in Fig. 3, and the vertical crosssection along the N-S direction is presented in Fig. 4. The main shocks in each sequence are marked by circled points and are numbered 1, 2, 3, and 4.



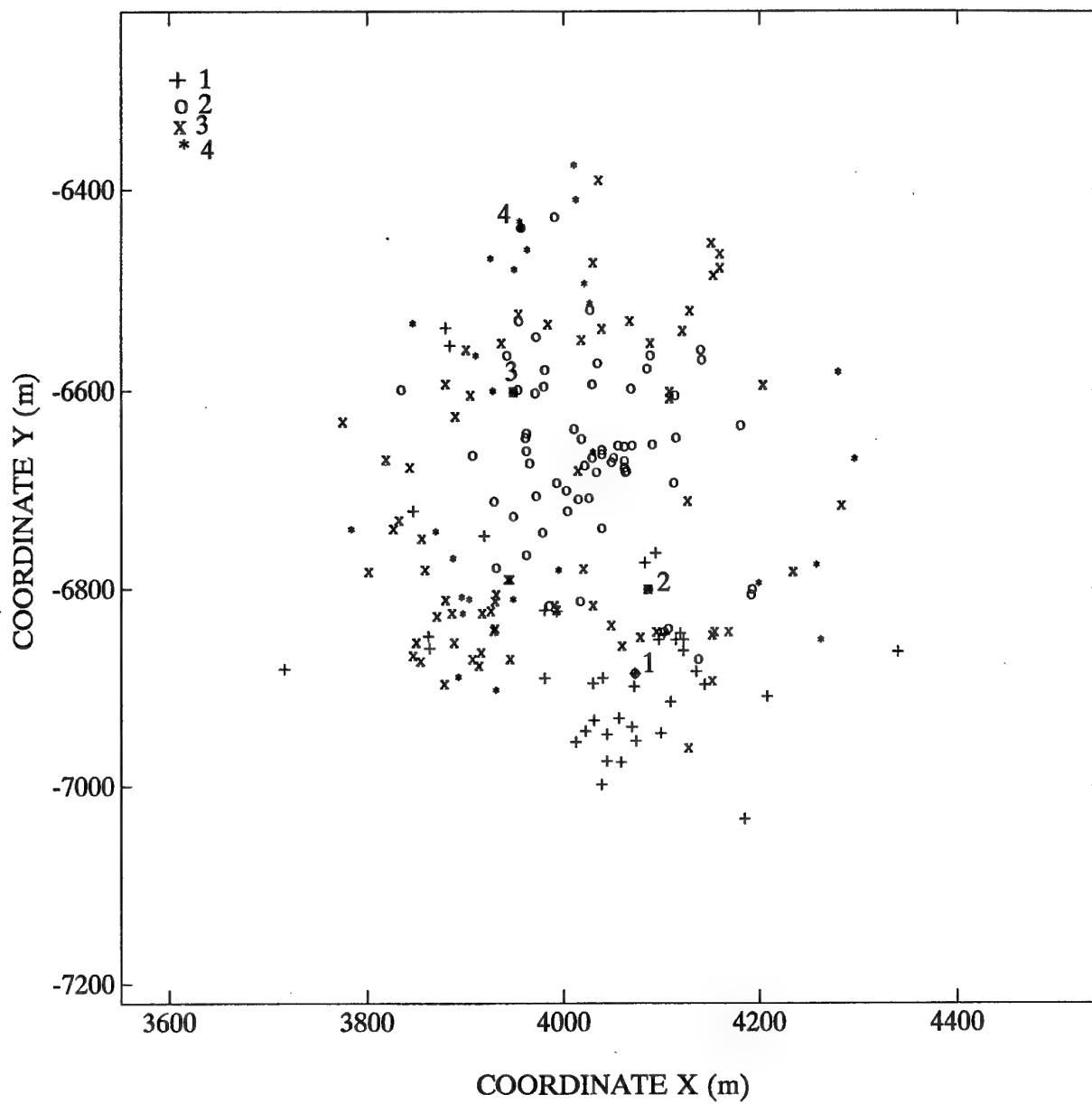


FIGURE 3. Horizontal distribution of seismic events forming four sequences, marked by different symbols. The main shocks of each sequence are marked by circled points and are numbered 1, 2, 3, and 4.

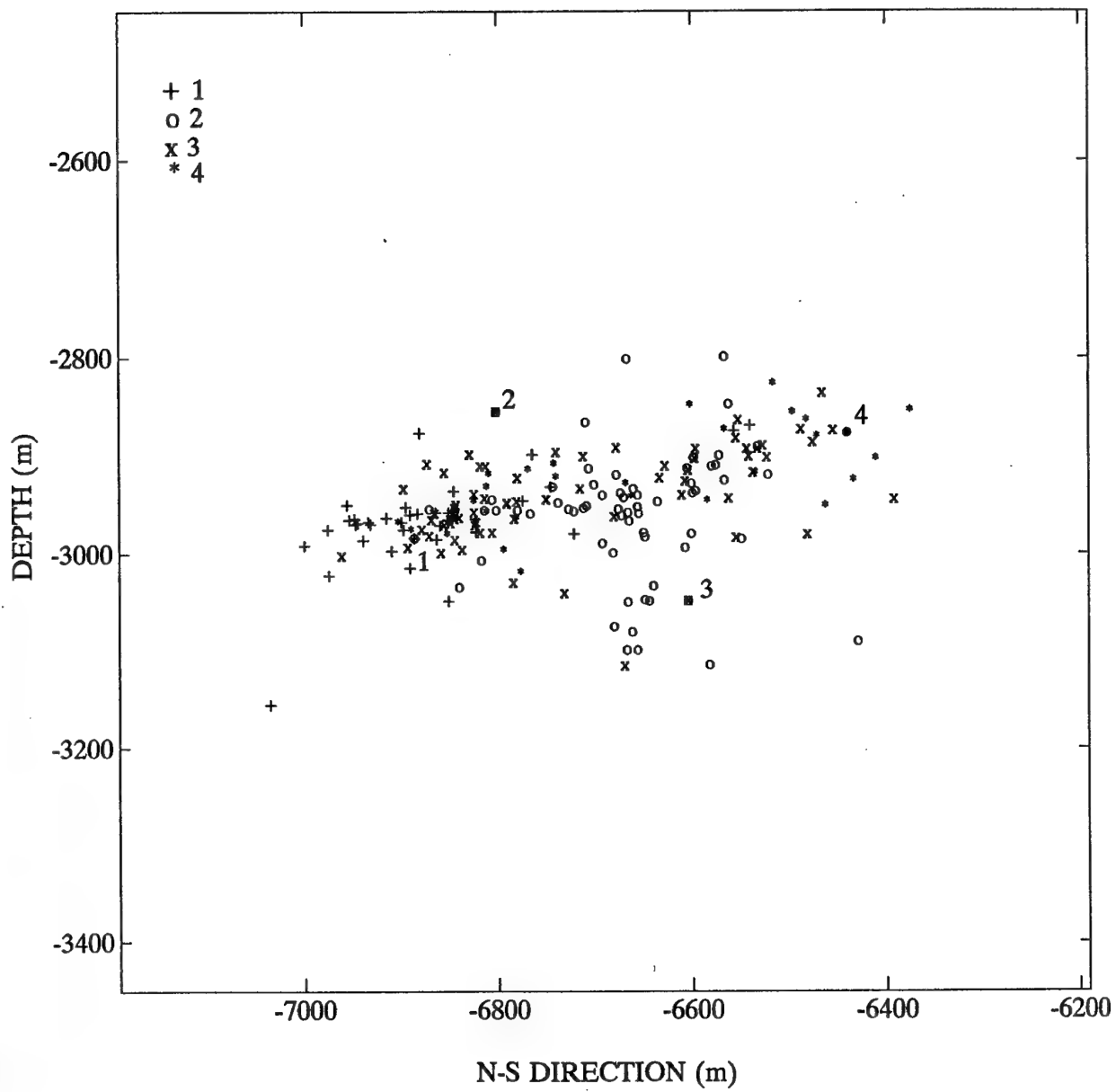


FIGURE 4. Vertical distribution along the N-S direction of seismic events forming four sequences, marked by different symbols. The main shocks of each sequence are marked by circled points and are numbered 1, 2, 3, and 4.

There is some regularity in the space distribution of seismic events forming the four sequences. The first sequence occurred at the southern edge of the rock volume containing the four sequences, the second and third sequences occurred in the middle of the volume, and the main shocks of the fourth sequence occurred at the northern edge of the volume, while their aftershocks moved back to the south (Figs 3 and 4).

### 3.2 Time distribution

Cumulative number of seismic events against the time after the occurrence of the first main shock is shown for the four sequences in Fig. 5. The main shocks are marked by circles and are numbered from 1 to 4. Altogether, the sequences lasted 284 hours. The first sequence lasted 179 hours while the second sequence lasted only 13 hours and had no time for full development as it was followed immediately by the third sequence with the largest main shock of magnitude 3.1, which lasted 33 hours and was in turn interrupted by the fourth sequence lasting 58 hours.

Thus Fig. 5 gives an impression that the last three sequences form in fact one sequence only. Fig. 6 shows that this is not the case. In this figure the rate of occurrence of seismic events after each main shock against the consecutive numbers of the time intervals used to calculate the rate of occurrence is presented. The numbers of time intervals instead of real time are used for the sake of clarity. The rate of occurrence was calculated for a fixed number of seismic events, ranging from 5 to 7, and variable time windows. From Fig. 6 it follows again that the second sequence was suddenly interrupted by the third sequence which possibly was preceded by a few foreshocks.

The parameter  $p$  from the Omori formula  $n(t) = c/t^p$ , where  $c$  is constant, describing the rate of occurrence  $n(t)$  of aftershocks with time  $t$  from the occurrence of the main shock, was also determined. This can be done either by a least-squares method (logarithmic scale) or by the maximum likelihood method (Ogata, 1983); the first method was preferred here. The parameter  $p$  is characteristic to each of aftershock sequence and is independent of the cut-off magnitude of the sequence. It should be noted that the original Omori formula fitted our data better than the modified Omori formula (Utsu, 1961),

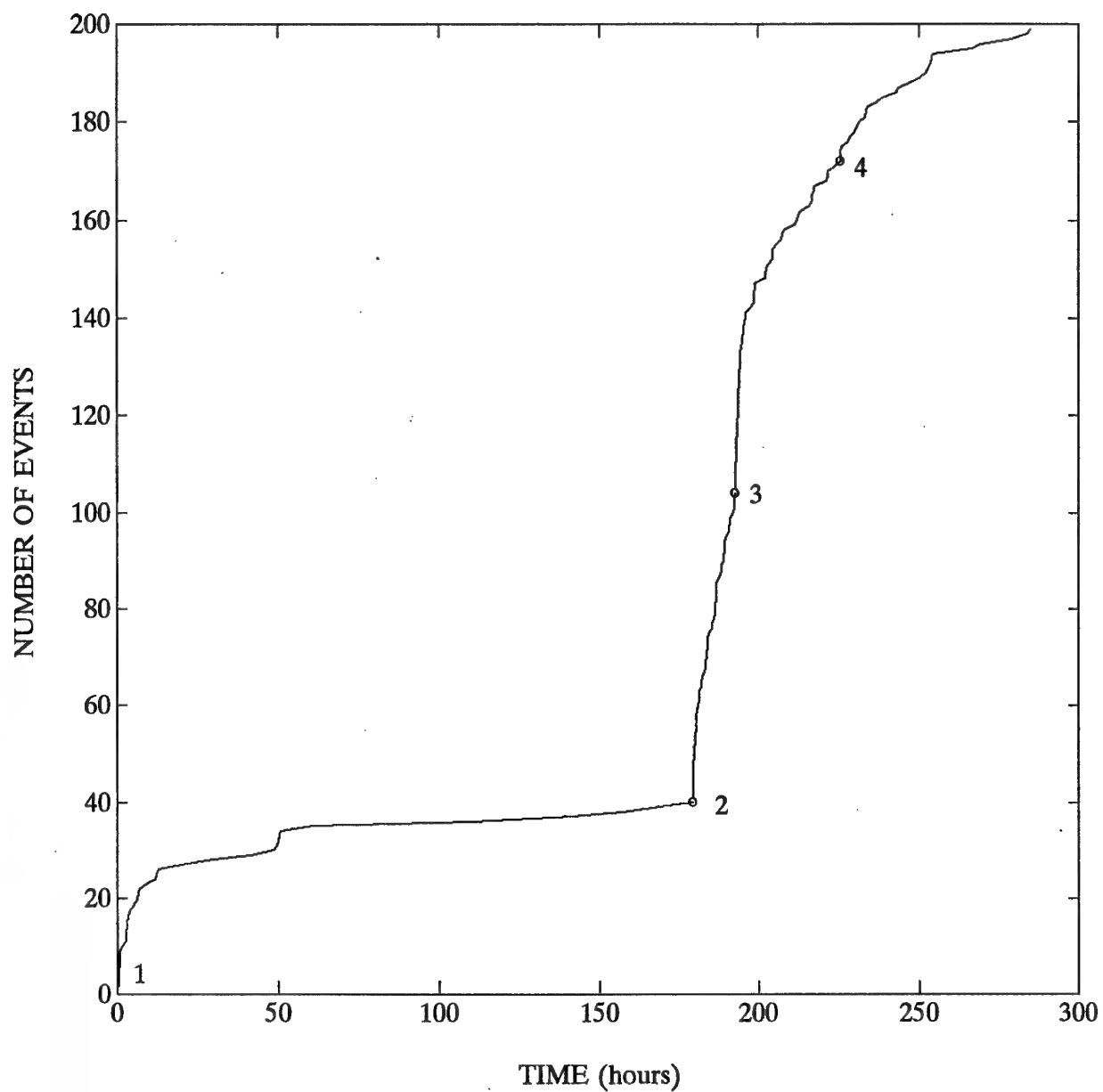


FIGURE 5. Cumulative number of seismic events versus time after the occurrence of the first main shock for the four sequences. The main shocks are marked by open circles and are numbered 1, 2, 3, and 4.

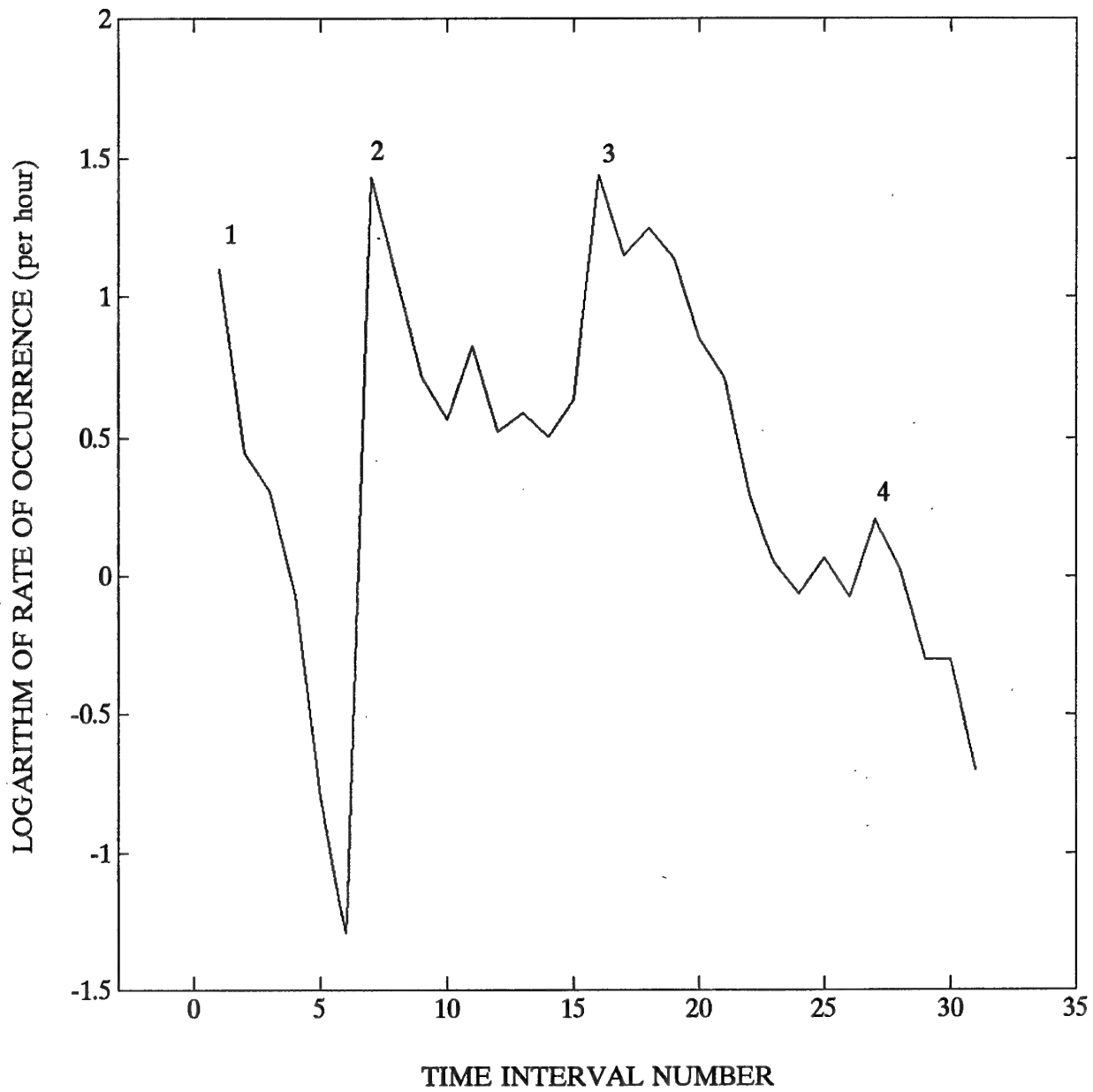


FIGURE 6. Logarithm of rate of occurrence versus the consecutive number of time intervals used to calculate the rate of occurrence for the four sequences 1, 2, 3, and 4.

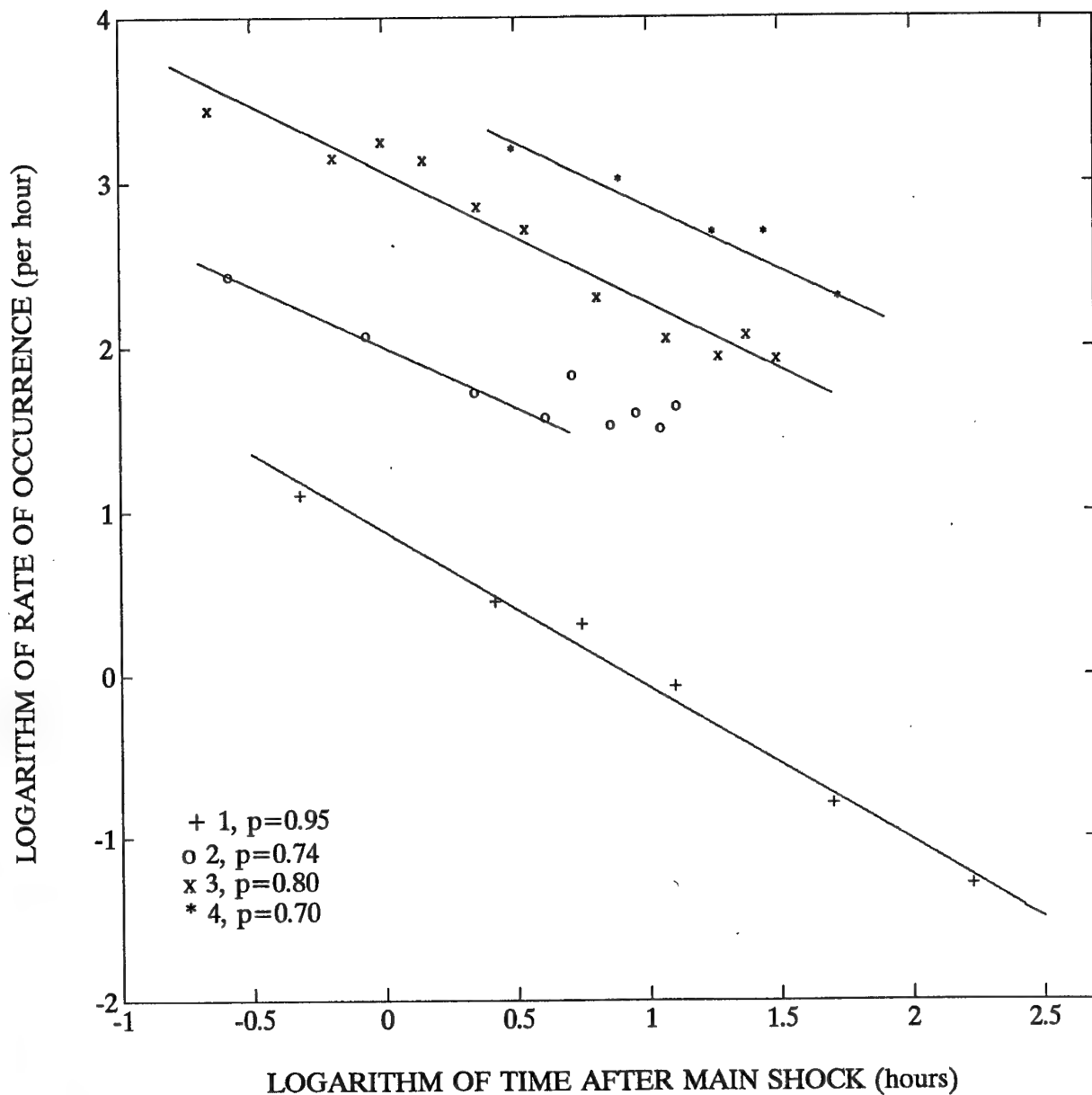


FIGURE 7. Logarithm of rate of occurrence versus logarithm of time after the main shocks for the four sequences. The data are marked by different symbols and for the sake of clarity are separated by one decade. The values of  $p$  parameter are also shown for each sequence.

universally used to describe the rate of occurrence of tectonic aftershocks. This difference could be explained either by different behavior of rock mass in underground mines from that in natural environment or by the fact that our data set is more complete than it is the case in most studies of tectonic earthquakes.

The logarithm of the rate of occurrence as a function of the logarithm of time after each main shock for the four sequences is shown in Fig. 7. The data from each sequence are marked by different symbols and for the sake of clarity they are separated by one decade. The values of  $p$  parameter, ranging from 0.7 to almost 1, are also shown for each sequence. The first sequence, which had time for full development, is characterized by the  $p$  value close to one, most often observed from tectonic aftershocks. The data corresponding to foreshocks preceding the most vigorous third sequence are clearly outstanding between the second and the third sequences; they were not used for the estimate of  $p$  value for the second sequence.

### 3.3 Frequency-magnitude relations and fractal dimension

Moment magnitude  $M$  (Hanks and Kanamori, 1979) of all 199 seismic events was calculated from their seismic moment described in Section 4. Histogram of moment magnitude for all seismic events which occurred during the four sequences is shown in Fig. 8. The analysis of data shows that our data set is complete down to magnitude  $-0.3$  and the number of complete observations is 196. Two events with magnitude smaller than  $-0.3$  were recorded during the first sequence and one event during the third sequence.

The coefficient  $b$  in the Gutenberg-Richter relation  $\log N = a - b M$ , where  $N$  is the number of events with or above magnitude  $M$  and  $a$  and  $b$  are the parameters, describing the frequency-magnitude distribution, is the characteristic parameter of each aftershock sequence and is independent of the cut-off magnitude. The parameter  $b$  can be estimated either by a least squares method or by the maximum likelihood method (Aki, 1965; Utsu, 1965); the first method was preferred here.

The logarithm of the cumulative number of seismic events versus their moment magnitude for all events from the four sequences is shown in Fig. 9.

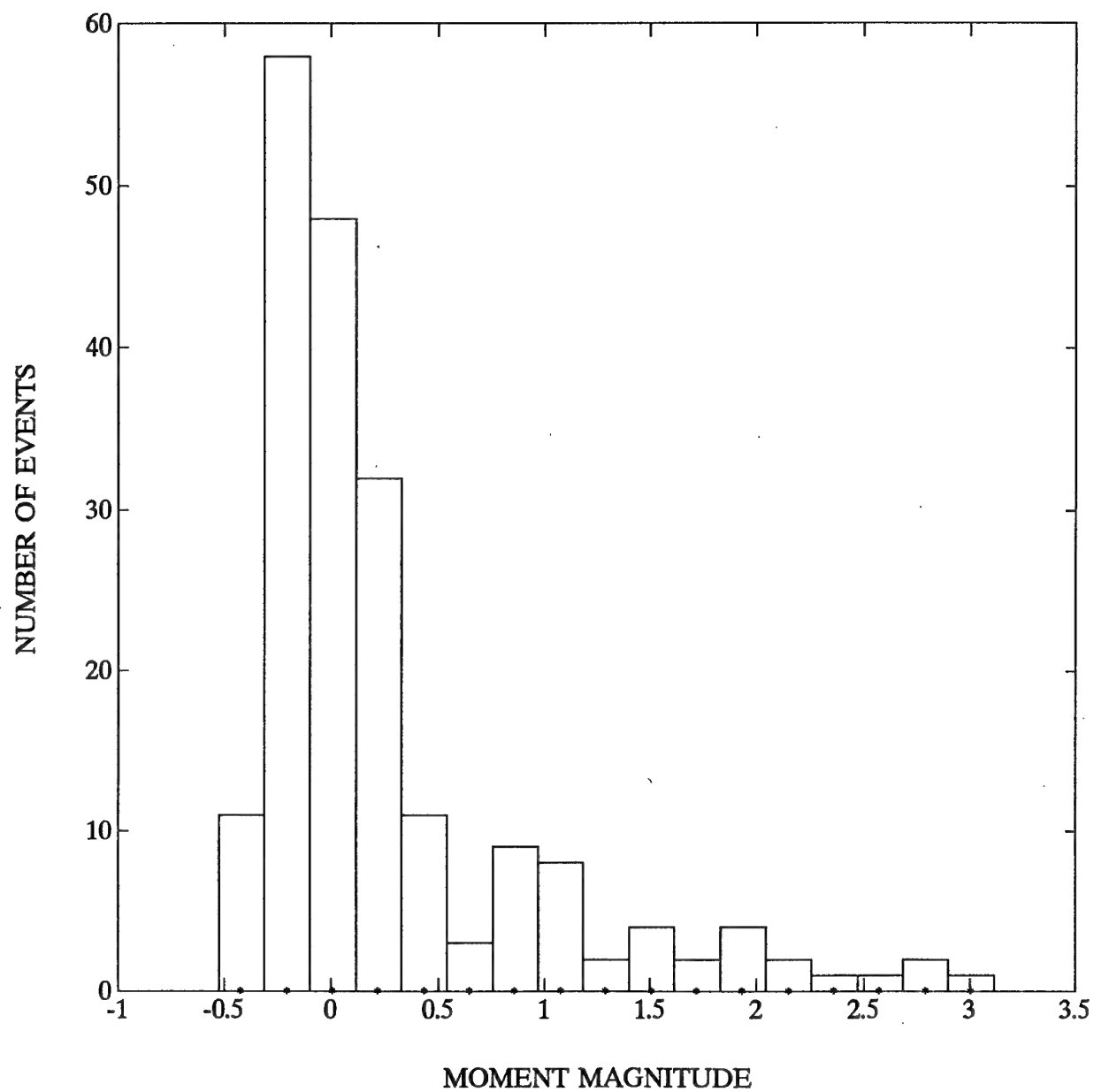


FIGURE 8. Histogram of moment magnitude of all seismic events which occurred during the four sequences.



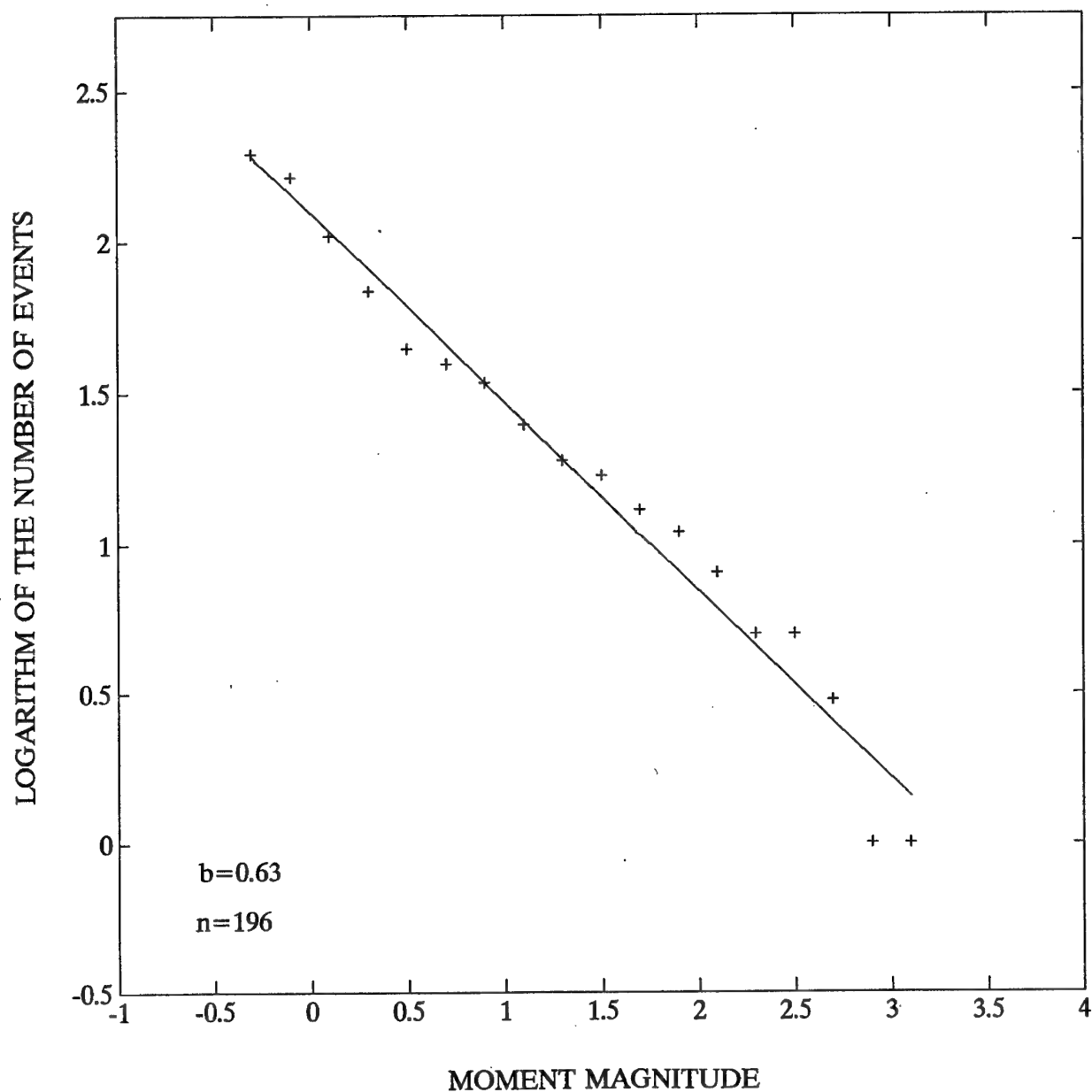


FIGURE 9. Logarithm of the cumulative number of seismic events versus their moment magnitude for all events from the four sequences. The magnitude interval is  $\Delta M=0.2$  and the slope coefficient  $b=0.63$ .

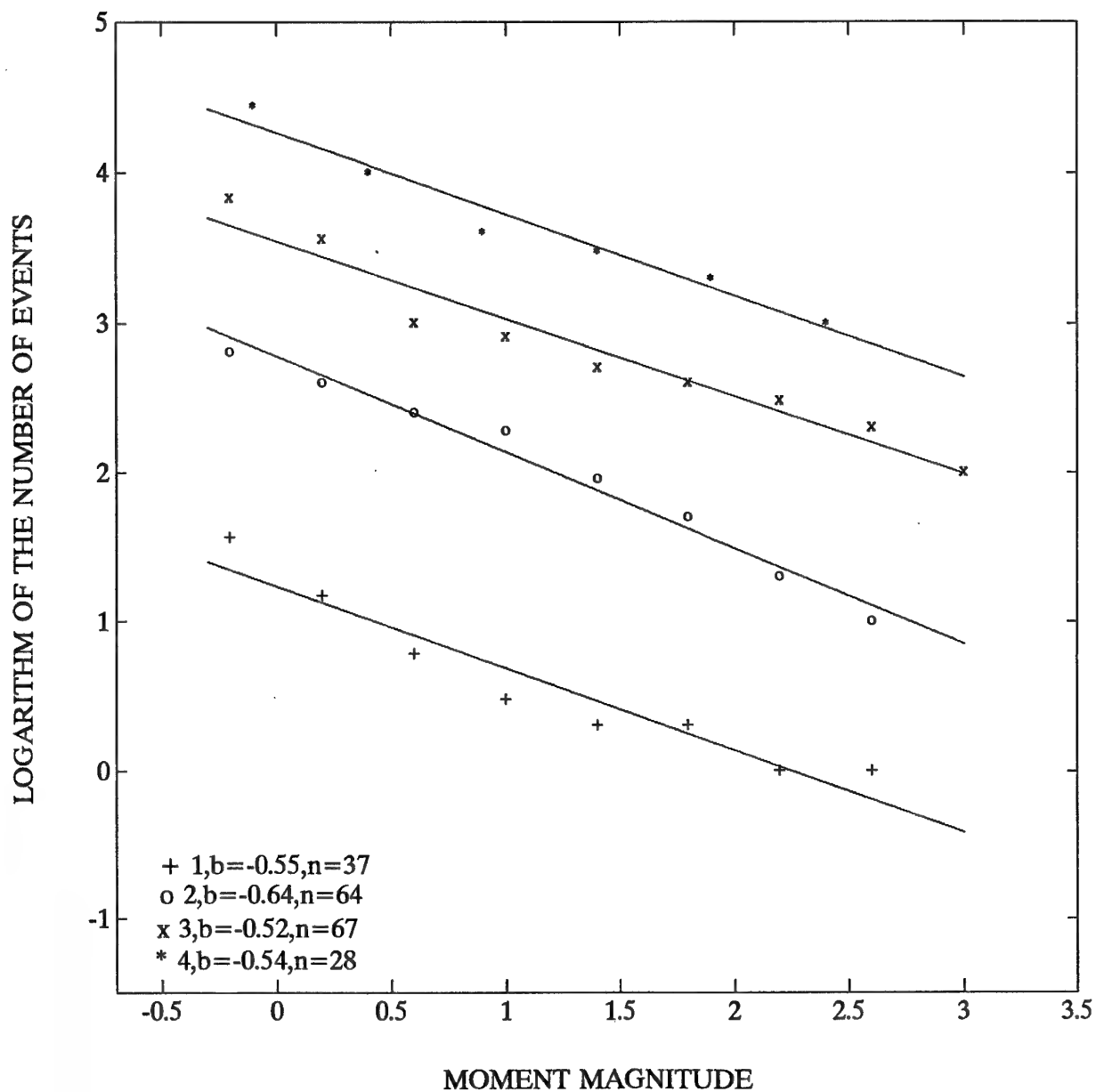


FIGURE 10. Frequency-magnitude relations for the four sequences 1, 2, 3, and 4. The observations are marked by different symbols and for the sake of clarity are separated by one decade. The number of observations and the values of parameter  $b$  are also indicated.

The accepted magnitude interval is  $\Delta M = 0.2$ ; this depends on the accuracy of magnitude estimates and on the number of observations. The calculated value of  $b$  parameter equal to 0.63 is rather low in comparison with  $b$  values found for tectonic aftershock sequences (e. g., Guo and Ogata, 1995). The parameter describes the ratio of large to small events within a given set. The frequency-magnitude relations for the four sequences are shown in Fig. 10. The observations are marked by different symbols and for the sake of clarity are separated by one decade. The number of observations and the values of parameter  $b$  are also indicated. The  $b$  values are low in all cases, ranging from 0.52 to 0.64.

Following the fractal phenomena described by Mandelbrot (1982), the application of the concept in seismology has been reported by many authors. Spatial distribution of epicenters has been shown to be self-similar (e. g., Kagan and Knopoff, 1980; Sadovskiy *et al.*, 1984) and a number of models have been proposed to simulate the seismic process characterized by the Gutenberg-Richter relation and the Omori formula, showing that they correspond to the self-organized critical behavior (e. g., Hirata, 1987; Hirata *et al.*, 1987; Bak and Tang, 1989; Ito and Matsuzaki, 1990). In particular, the parameter  $b$  was considered to be proportional to the fractal dimension (Aki, 1981). Recently, Guo and Ogata (1995) have shown that there are positive correlations between  $p$ - and  $b$ -values and the fractal dimension of hypocenter distribution of aftershocks.

There are various definitions of the fractal dimension: similarity dimension, capacity dimension, information dimension, and correlation dimension (Takayasu, 1990; Hirabayashi *et al.*, 1992). The correlation fractal dimension was determined for our aftershock sequences, similarly as it was done by Guo and Ogata (1995). The correlation integral  $C(r) = 2N(r)/N(N-1)$ , where  $N(r)$  is the number of pairs of hypocenters whose distances are smaller than  $r$  and  $N$  is the total number of selected aftershocks, is considered to determine the fractal dimension of a given set of hypocenters (e. g., Kagan and Knopoff, 1980). If the hypocenter distribution has a fractal structure, then the correlation integral  $C(r)$  should be proportional to  $r^D$ , where  $D$  is the fractal dimension (e. g., Grassberger, 1983).

The distances between the pairs of hypocenters were calculated for each sequence and their histograms are shown in Fig. 11, 12, 13, and 14,

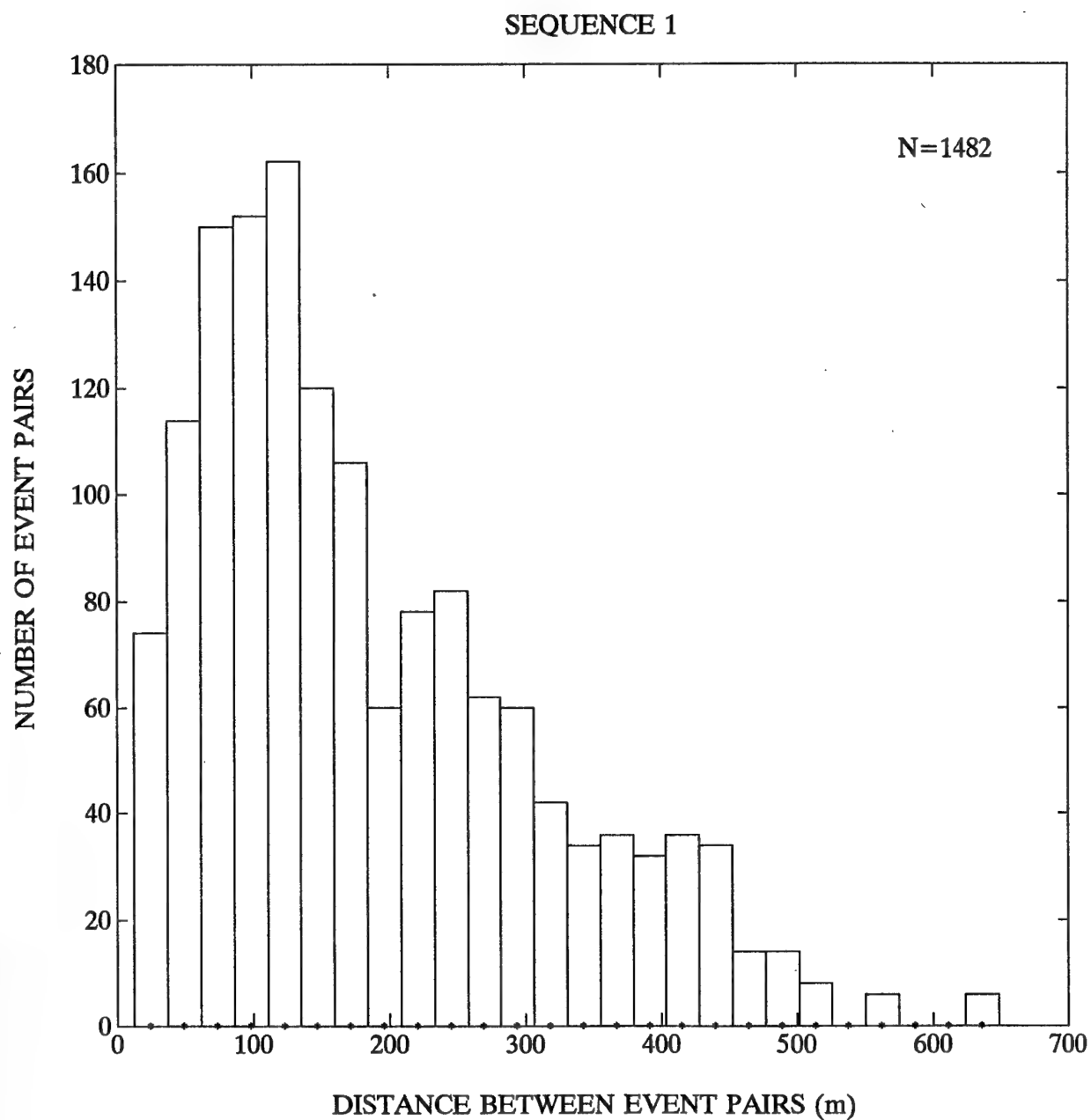


FIGURE 11. Histogram of distances between the pairs of events from sequence 1, used to estimate the fractal dimension of the sequence.

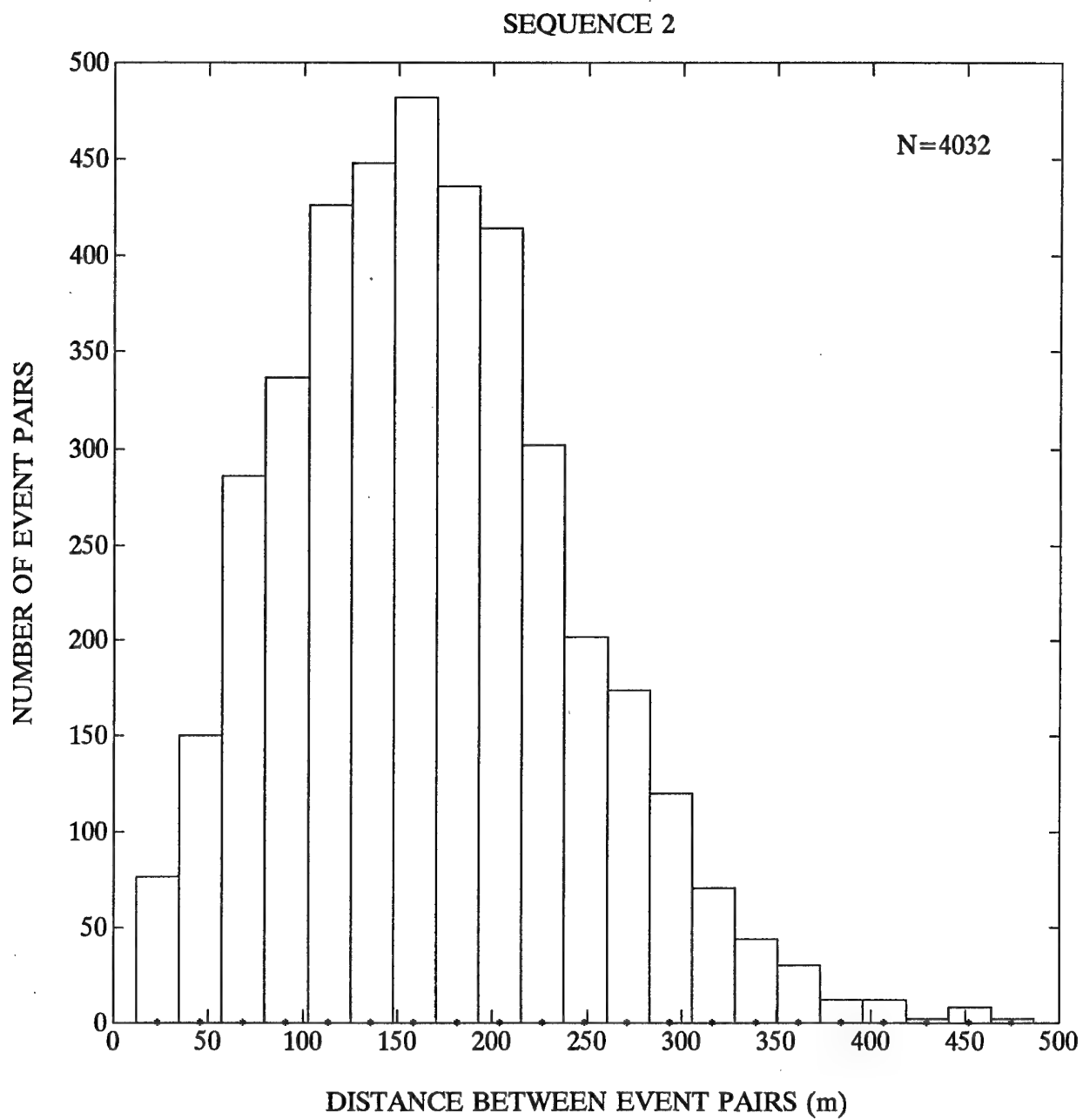


FIGURE 12. Histogram of distances between the pairs of events from sequence 2, used to estimate the fractal dimension of the sequence.

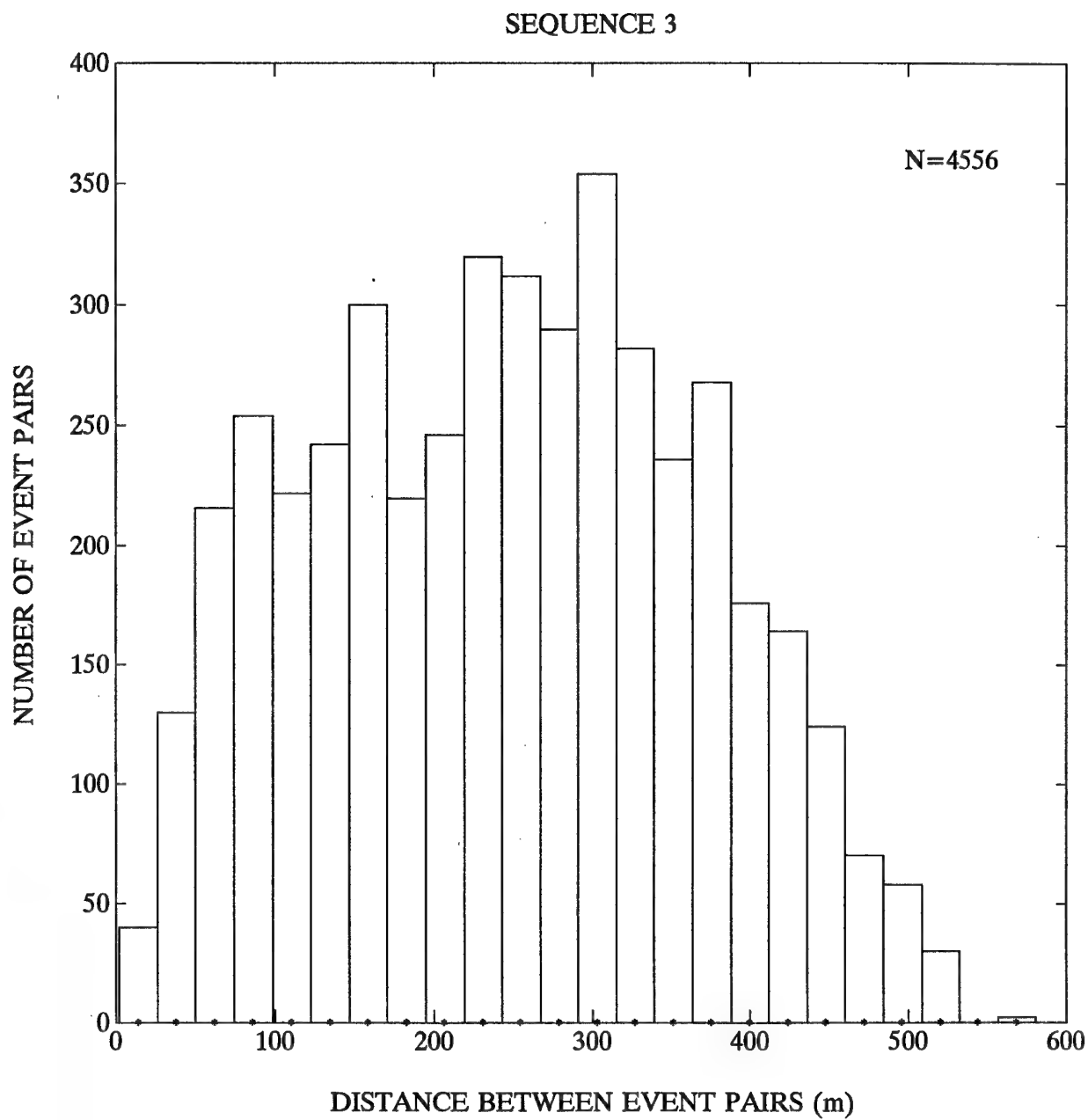


FIGURE 13. Histogram of distances between the pairs of events from sequence 3, used to estimate the fractal dimension of the sequence.

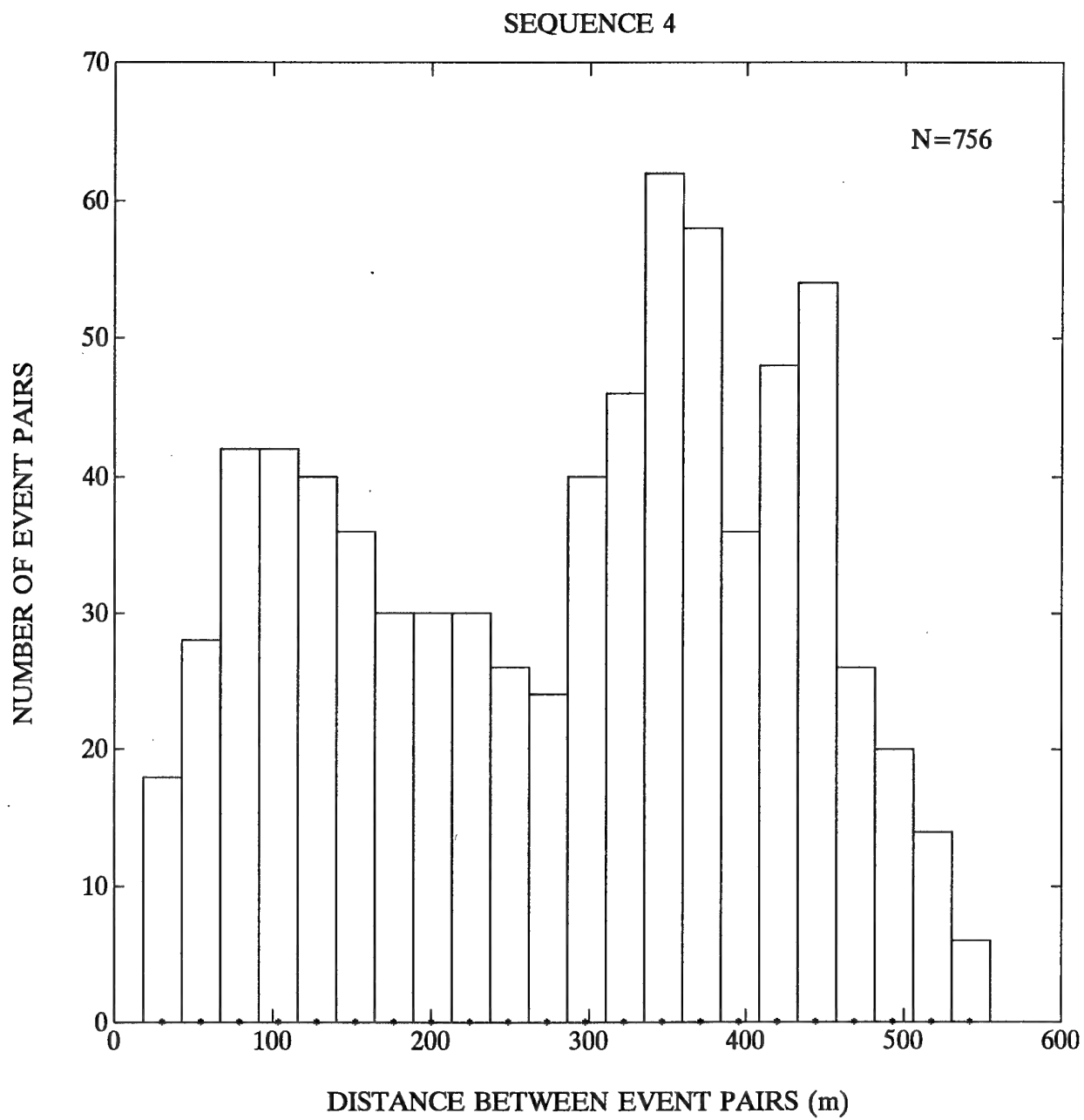


FIGURE 14. Histogram of distances between the pairs of events from sequence 4, used to estimate the fractal dimension of the sequence.

respectively, where the number of pairs is also indicated. The first sequence is the most extensive in space. The largest distance between two events is 650 m and the smallest distance is 13 m. There is one maximum in the histogram (Fig. 11) and the dominant distance is around 100 m. The second sequence is the most compact. The largest distance between two events is 480 m and the smallest distance is 12 m. The dominant distance is about 150 m and the histogram is of the most regular, bell-like shape (Fig. 12). The largest distance between two events from the third sequence is 580 m and the smallest distance is 2 m. The histogram is not regular and its maximum at 300 m is not distinct (Fig. 13). The largest distance between two events from the fourth sequence is 550 m and the smallest distance is 19 m. The histogram is irregular with two wide maxima at 100 and 350 m (Fig. 14).

The fractal dimension  $D$  was calculated by the linear regression of the correlation integral  $C(r)$  versus the distance  $r$  displayed on a logarithmic scale for each sequence. To construct such diagrams, selection of proper distance intervals  $\Delta r$ , for the pairs of hypocenters whose distances are smaller than  $r$ , is needed. The correlation integral versus the distance between the pairs of events from the first sequence for various distance intervals is shown in Fig. 15. From this figure it follows that the selection of the intervals is not critical and the values of fractal dimension  $D$  are similar for  $\Delta r$  equal to 12, 24 and 36 m. The circled points are used to estimate the fractal dimension. The deviation from the linearity at large distances is caused by the limited size of the aftershock volume, especially its thickness (Guo and Ogata, 1995). No deviation from the linearity at small distances is observed, which possibly confirms the high precision of the location of hypocenters.

The correlation integral versus the distance between the pairs of events from the four sequences is shown on a logarithmic scale in Fig. 16. The fractal dimension  $D$  and the number of pairs are also shown for each sequence. The selected distance intervals ranged from 18 to 24 m and the distances used to estimate the fractal dimension ranged from 21 to 144 m. The values of fractal dimension for the four sequences are significantly different. The first sequence is characterized by the lowest value of  $D=1.75$  and the second sequence is characterized by the highest value of  $D=2.4$ . The third and fourth sequences are characterized by the middle value of  $D=1.9$ .



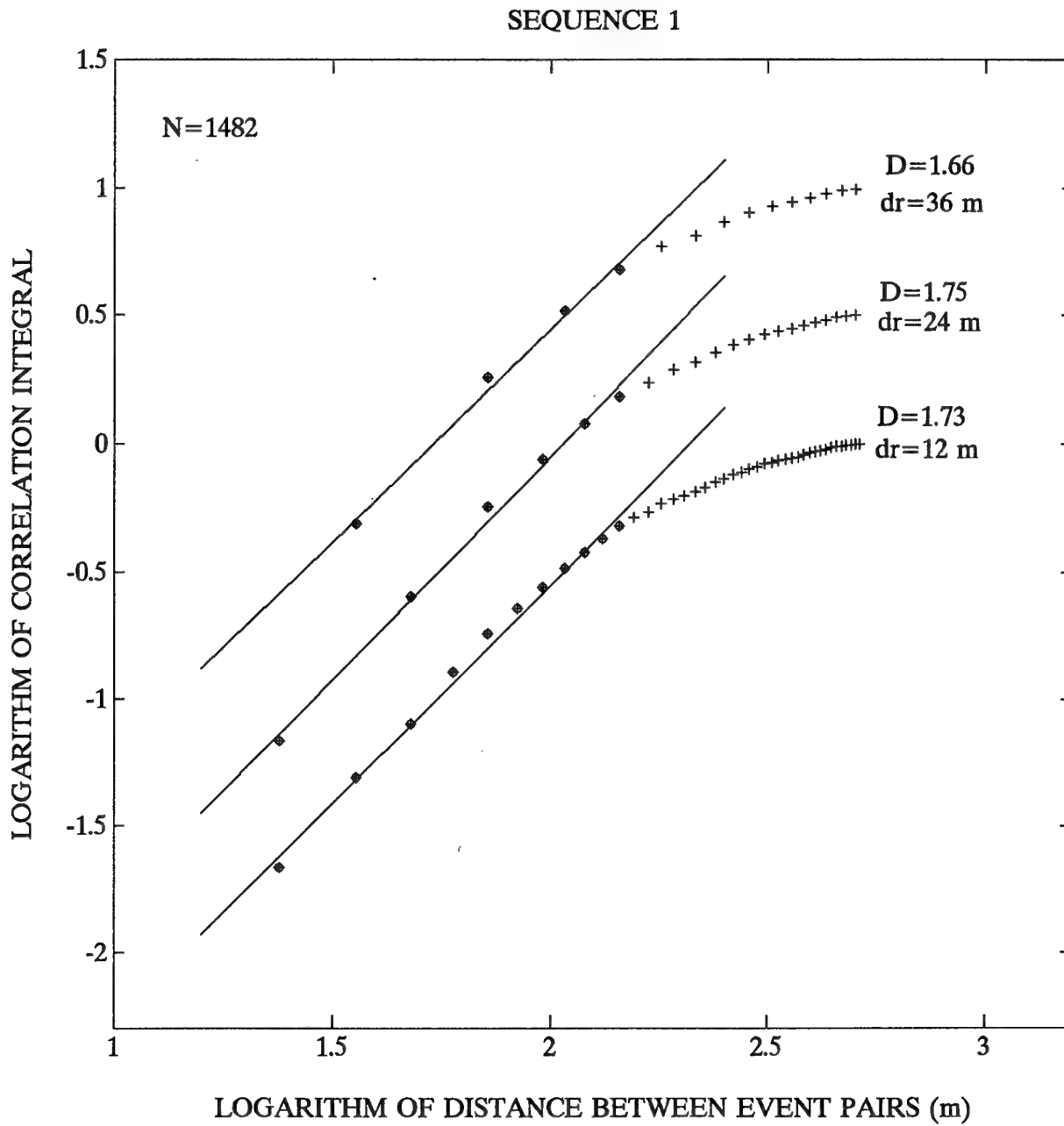


FIGURE 15. Logarithm of the correlation integral versus logarithm of the distance between the pairs of events from sequence 1 for various distance intervals  $dr$ . Circled points are used to estimate the fractal dimension  $D$  by the linear regression.

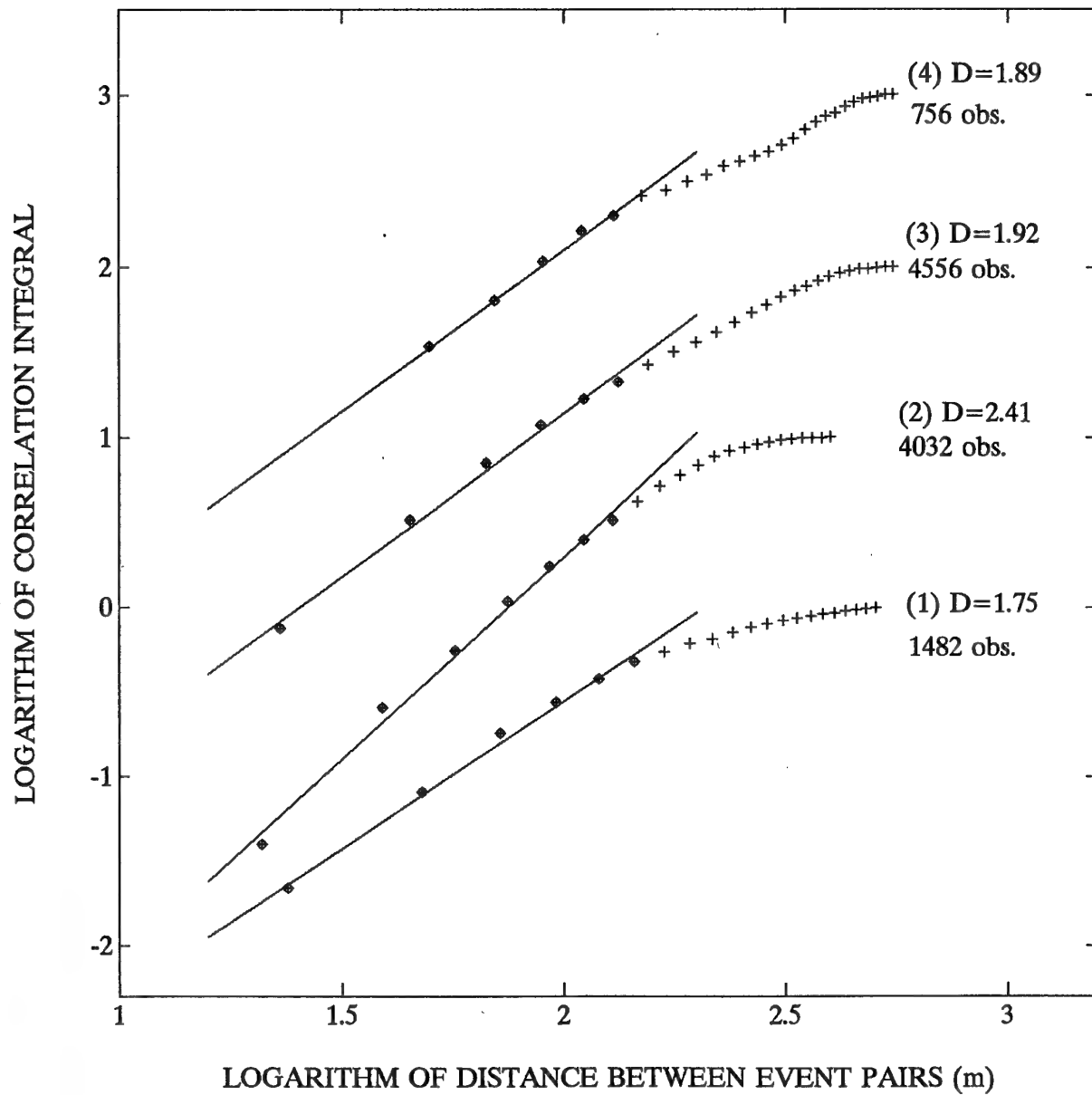


FIGURE 16. Logarithm of the correlation integral versus logarithm of the distance between the pairs of events from sequences 1, 2, 3, and 4. Circled points are used to estimate the fractal dimension  $D$  by the linear regression.

From the laboratory experiments on rock fracturing Hirata (1987) found that bursts of acoustic emissions decayed exponentially during the early stage of fracturing and changed to decay hyperbolically at the last stage. The decay of bursts in the rock may correspond to the decay of aftershocks (Ito, 1992). The transmission from the exponential decay to the hyperbolic decay indicates that fracture events at the early stage were rather independent but they became correlated with progressing fracturing. Hirata *et al.* (1987) also found that the space distribution of acoustic emissions had the fractal dimension of 2.75 and was almost homogeneous at the primary stage of fracturing and then it gradually organized to become a fractal with decreased dimension of 2.25 at the final stage of fracturing. The decreasing of fractal dimension indicates that fracture events became more strongly correlated with advancing fracturing (Ito, 1992).

Thus, the seismic events from our first, the best developed sequence are the most strongly correlated and are characterized by the lowest value of fractal dimension, whereas the events from the second sequence had no time for stronger correlation as a result of their interruption by the third sequence and are characterized by the highest value of fractal dimension. The third sequence was in turn interrupted by the fourth sequence but not as suddenly as the second sequence (Fig. 5) and is characterized by a middle value of fractal dimension. The fourth sequence was of short duration and rather irregular with the main shock composed in fact of three shocks.

Utsu (1961) introduced the relation  $p = 2b/\beta$  based on a model of residual strain energy of aftershock volume, where  $\beta$  is the slope coefficient of the linear relation between the logarithm of seismic energy and magnitude, usually accepted as close to 1.5. The values of parameter  $p$  against those of parameter  $b$  for our four sequences are displayed in Fig. 17.

The parameter  $b$  is considered to be proportional to the fractal dimension  $D$  in a form  $D = 3b/c$  (Aki, 1981), where  $c$  is the slope coefficient of the linear relation between the logarithm of seismic moment and magnitude equal to 1.5 (Kanamori and Anderson, 1975). The values of fractal dimension  $D$  versus those of parameter  $b$  for the four sequences are shown in Fig. 18. Our  $b$ -values are in general very low and the Aki's relation  $D = 2b$  was adjusted by a term +0.8 to fit our data. The modified relation is shown in Fig. 18 by the dashed line.

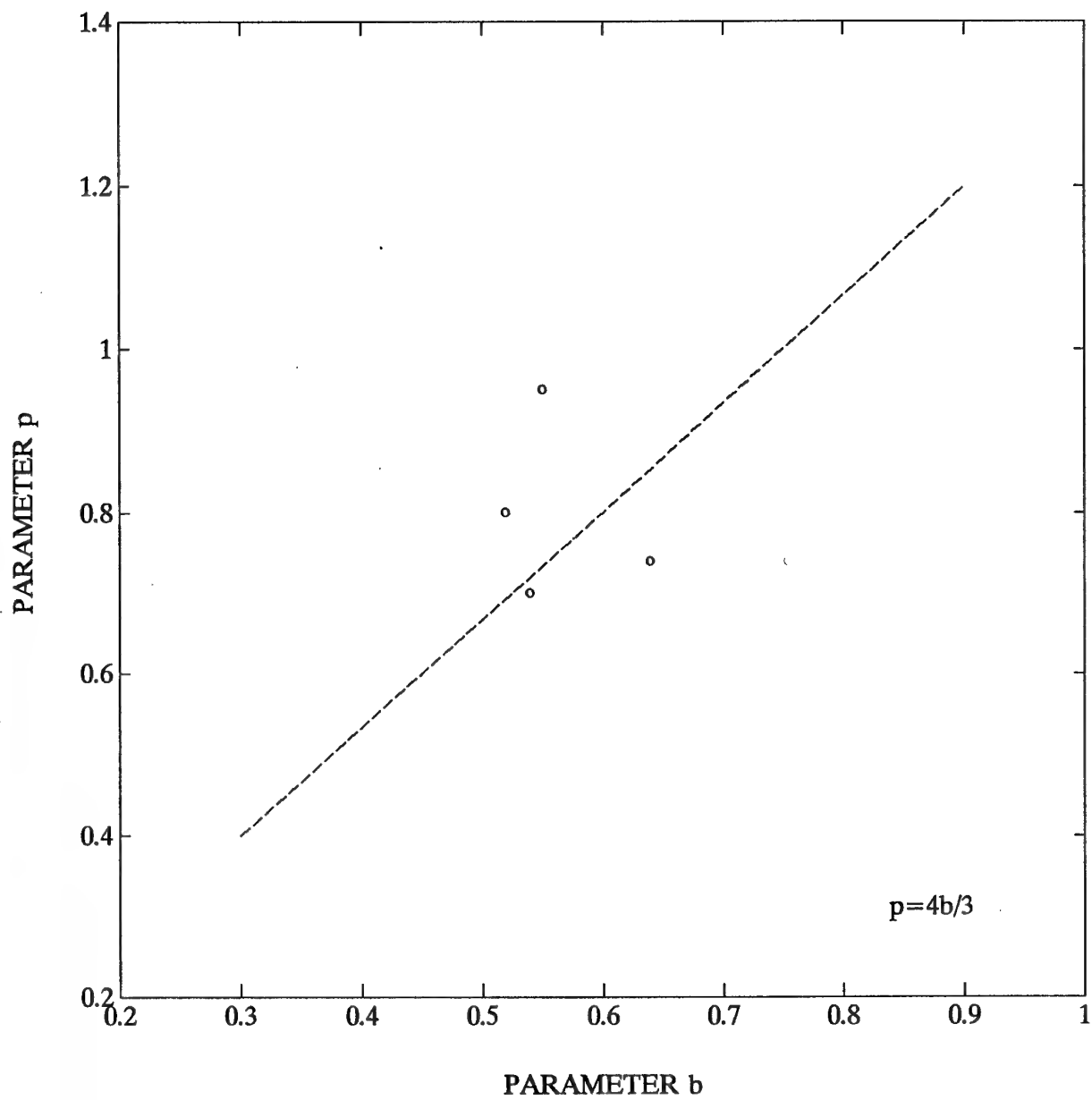


FIGURE 17. Parameter  $p$  versus parameter  $b$  for the four sequences. Utsu's relation  $p=4b/3$  is shown by the dashed line.

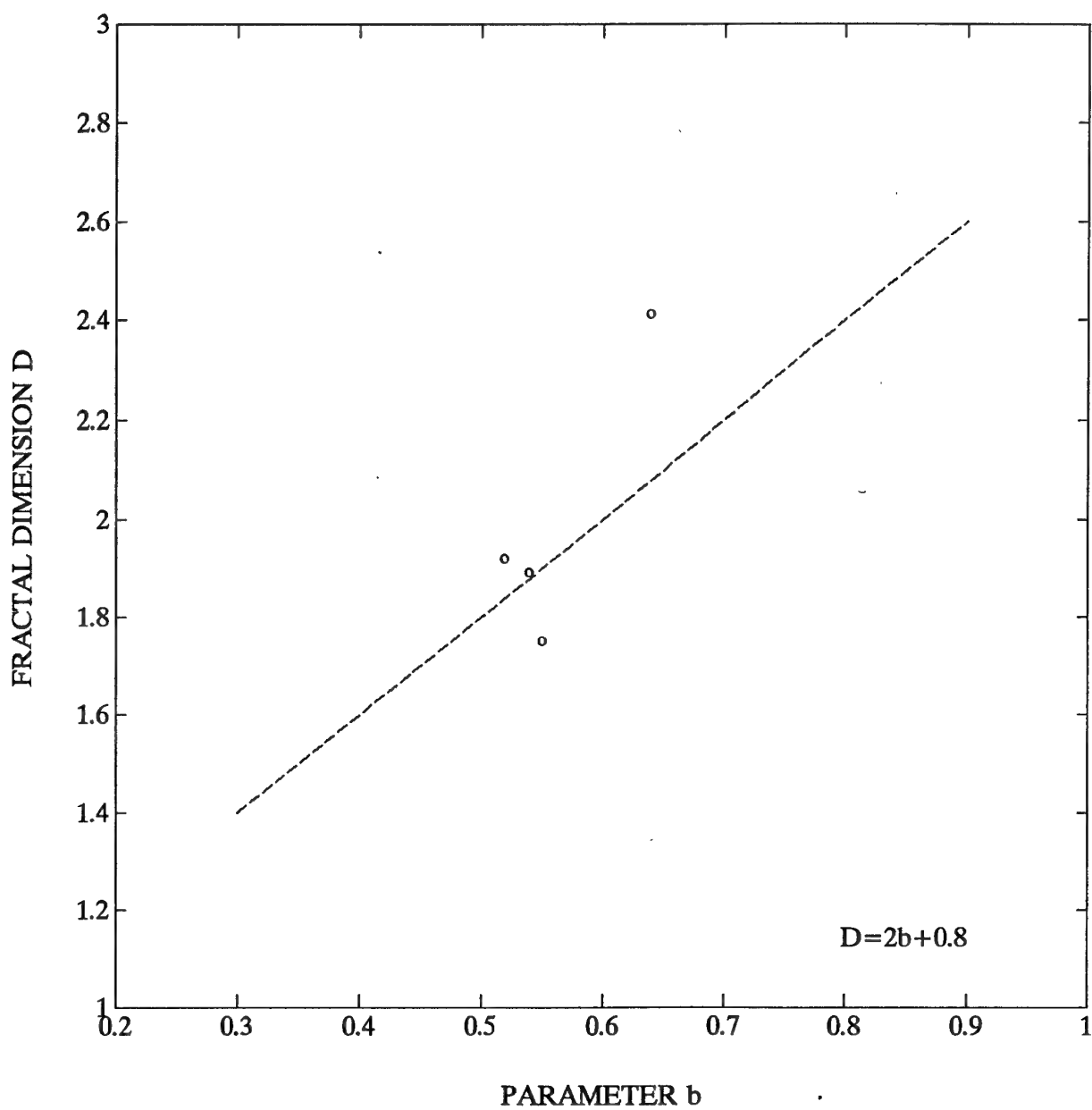


FIGURE 18. Fractal dimension  $D$  versus parameter  $b$  for the four sequences. Aki's relation  $D=2b$  is adjusted by a term  $+0.8$  and is shown by the dashed line.

## 4. SPECTRAL SOURCE PARAMETERS

### 4.1 Spectral analysis

Using the values of the azimuth and the angle of incidence, computed for each station, the traditional three-component seismograms N, E, Z can be rotated into the local ray coordinate system with one longitudinal component in the *P*-wave direction and the transverse components in the *SH* and *SV* directions (e. g., Plesinger *et al.*, 1986). The rotation of components is made to cut down the number of seismic pulses and spectra to be processed for each station from a single event, from six (*P* and *S* waves on three components each) to three (one component for *P* wave and two components for *SH* and *SV* waves).

A simpler and more direct approach is based on polarization analysis of *P*-wave pulses recorded on three components. Several techniques for polarization analysis are available, providing the required orientation of particle motion of *P* waves in terms of the azimuth and the angle of incidence, including algorithms in the time and frequency domains (e. g., Montalbetti and Kanasewich, 1970; Vidale, 1986; Park *et al.*, 1987).

Both approaches are used in the ISS data processing system. The second approach in the time domain is used for the rotation of seismograms selected for spectral analysis. The seismograms are filtered between the frequency of a given sensor, which is in our case 3 Hz, and the frequency corresponding to the sampling frequency divided by five, which is 400 Hz. The windows selected for *P* waves contain 10 cycles (or double zero-crossings), with an additional constraint added that the window cannot be longer than the *S-P* interval. The windows for *SH* and *SV* waves contain 15 cycles. The windows are set half a cycle before *P* or *S* first arrivals and they are centered before further processing.

In the ISS system the cosine 10% taper is used. The tapered windows are supplemented by zeros to the number of samples  $2^n$ , where the integer *n* is defined by the ratio of the sampling frequency to the lower cutoff frequency.

The spectra are calculated by a FFT routine and corrected for instrumental effect by dividing them by the frequency response of the recording system. The spectra of noise are also calculated in a similar manner.

The original seismograms provided by the underground seismic network at Western Deep Levels represent ground velocity records. It is a long-established practice in seismology that spectral and source parameters are estimated from displacement spectra rather than from ground velocity or acceleration spectra. The original ground velocity spectra, therefore, were transformed into the displacement spectra simply by their division by the angular frequency  $\omega = 2\pi f$ , where  $f$  is the frequency.

Since only global features of the spectra, described by a few spectral parameters, are of practical interest, the spectra were smoothed before further processing. In the ISS system, the spectra are smoothed by cepstral filtering, which is a powerful technique found to be highly efficient. The cepstrum is an inverse FFT of the spectrum natural logarithm. The filtering corresponds to cepstrum zeroing after the  $m$  zero-crossing. The number  $m$  can be set to a selected value and in the ISS procedure  $m = 4$  is accepted as the most satisfactory in most cases.

The observed spectra must be corrected for attenuation and scattering effects along the travel path of seismic waves. Such correction are of the utmost importance for the proper retrieval of source parameters of small seismic events, even if they are recorded at close distances (e. g., Rovelli *et al.*, 1991). The uncorrected spectra are often characterized by the decay coefficient distinctly higher than the most often observed value of 2. In contrast, the corrected spectra of mine tremors are well described by a  $f^{-2}$  fall-off (e. g., Gibowicz, 1990).

The attenuation rate of body waves is generally parametrized by the average quality factor  $Q$  (different for  $P$  and  $S$  waves) along the ray path. To correct for attenuation, the spectra are usually multiplied by the exponential term  $\exp(\omega R/2VQ)$ , where  $R$  is the distance between the source and the receiver and  $V$  is either  $P$ - or  $S$ -wave velocity. In the ISS system, the quality factor  $Q$  is one of a few parameters set free in the spectrum inversion procedure.

The simplest and most often used model of displacement spectra is that described by the low-frequency level  $\Omega_0$  and the corner frequency  $f_0$  above which the spectrum is assumed to fall off as a second power of frequency (Brune, 1970, 1971). Such a model is accepted in the ISS system and the model displacement spectrum for a given seismic station is multiplied by the exponential term correcting attenuation and scattering effects. The three free parameters  $\Omega_0$ ,  $f_0$  and  $Q$  are estimated by an iterative linear inversion of spectral data, expanding the model spectrum into a Taylor series around some trial estimate  $\mathbf{x}^* = (\Omega_0^*, f_0^*, Q^*)$  (e. g., Del Pezzo *et al.*, 1987; Scherbaum, 1990; Fehler and Phillips, 1991). A number of constraints is introduced into the inversion procedure, resulting from the accepted relations between the values of  $f_0$  and  $Q$  for  $P$  and  $S$  waves.

#### 4.2 Relations between various source parameters

From the inversion of seismic spectra, two independent spectral parameters  $\Omega_0$  and  $f_0$  are obtained from the three spectra of  $P$ ,  $SH$  and  $SV$  waves. The third parameter, the energy flux  $\epsilon$ , is also calculated from each spectrum at each station, and is used for the calculation of seismic energy of  $P$  and  $S$  waves. The energy flux of a plane wave is the product of the medium density  $\rho$ , the wave velocity  $V$ , and the integral  $I$  of the square of the ground velocity (e. g., Bullen and Bolt, 1985). The integral  $I$  was calculated using the method described by Snoke (1987), and the values of  $\rho = 2750 \text{ kg/m}^3$ ,  $V_p = 5700 \text{ m/s}$  and  $V_s = 3300 \text{ m/s}$  were accepted for the computation of the energy flux and other source parameters.

Quality indices for each spectral parameter and for the whole spectra are introduced, normalized to the values from 0 to 1 (Mendecki, 1993). It was found from experience that the spectra with the quality indices smaller than 0.5 were of irregular shape and could not be properly fitted by the model function. Such spectra are automatically rejected in the ISS system and are not taken into account for the calculation of source parameters.

Thus, the primary input quantities used for the determination of source parameters are the low-frequency spectral level  $\Omega_0$ , the corner frequency,  $f_0$ , and the energy flux  $\epsilon$ , calculated separately for  $P$  and  $S$  waves. From the



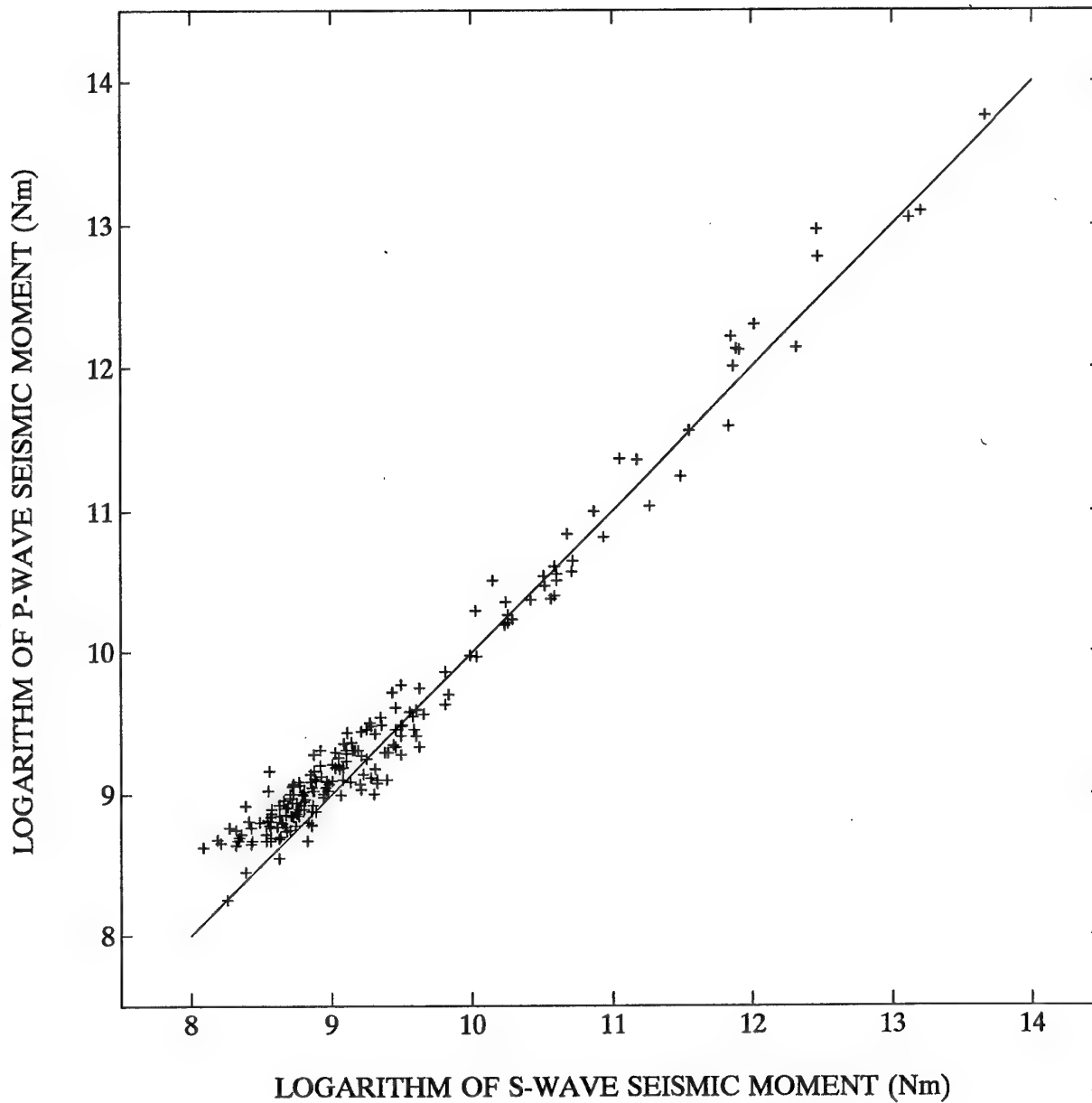


FIGURE 19. Logarithm of seismic moment estimated from *P*-wave spectra versus that estimated from *S*-wave spectra for the four sequences. The straight line corresponds to the same values of both estimates.

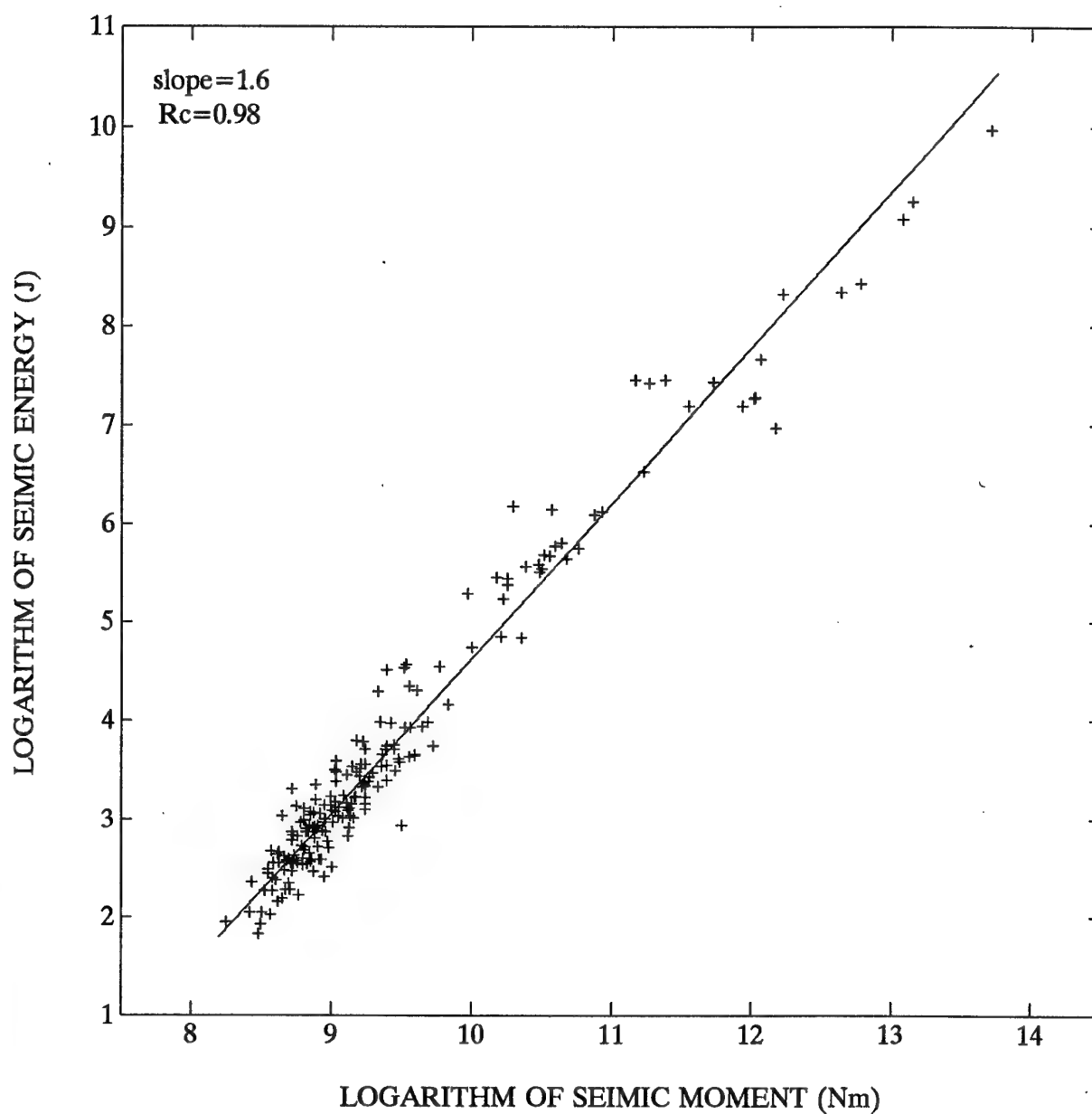


FIGURE 20. Logarithm of seismic energy versus logarithm of seismic moment. Linear regression slope coefficient and correlation coefficient  $R_c$  are also indicated.

low-frequency level of the far-field displacement spectrum either of  $P$  or  $S$  waves seismic moment  $M_0$  is computed, taking into account the radiation pattern, the free-surface amplification and the site correction for either  $P$  or  $S$  waves. When the focal mechanism was not determined, the *rms* averages of radiation coefficients over the whole focal sphere (Boore and Boatwright, 1984) were used. The free-surface effect is expressed by a factor of two for  $SH$  waves, whereas for  $SV$  and  $P$  waves it is a function of the angle of incidence and frequency. A free-surface correction can be neglected (i. e., assumed to be one) for sensors located in underground mines. Similarly, site corrections were also neglected for our sensors, though near-surface site response is an important factor in source studies based on sensors located at the surface of the Earth.

Logarithm of seismic moment estimated from  $P$  waves versus that estimated from  $S$  waves for all seismic events from the four sequences is shown in Fig. 19, where the straight line corresponds to the same value of both estimates. The differences between the two estimates are small and the average values from the two estimates were accepted as the final values of seismic moment. They range from  $1.8 \cdot 10^8$  to  $5.2 \cdot 10^{13}$  N·m. In recent years, moment magnitude  $M$  (equal to  $M_w$  used for large earthquakes) defined by Hanks and Kanamori (1979), instead of seismic moment itself, became an often used measure of the earthquake strength, simply as a matter of convenience. Its values for our events range from -0.5 to 3.1.

The energy radiated in the  $P$  and  $S$  waves was calculated from the relation between the energy and the energy flux, derived by Boatwright and Fletcher (1984), who neglected however directivity effects. To minimize the errors associated with these effects, the estimates of the energy flux (corrected for attenuation and scattering) were arithmetically averaged before correcting for the radiation pattern. Small errors in the radiation pattern coefficients for the events with known focal mechanism, in turn, can lead to large errors in estimates of the seismic energy. To reduce these effects, a lower bound or "waterlevel" for the radiation pattern was used. The total seismic energy is taken as a sum of  $P$ -wave and  $S$ -wave energy.

The values of total seismic energy range from  $6.6 \cdot 10^1$  to  $9.4 \cdot 10^9$  J. They are displayed on a logarithmic scale against the values of seismic moment in Fig. 20. The linear regression slope coefficient is 1.6 and the correlation

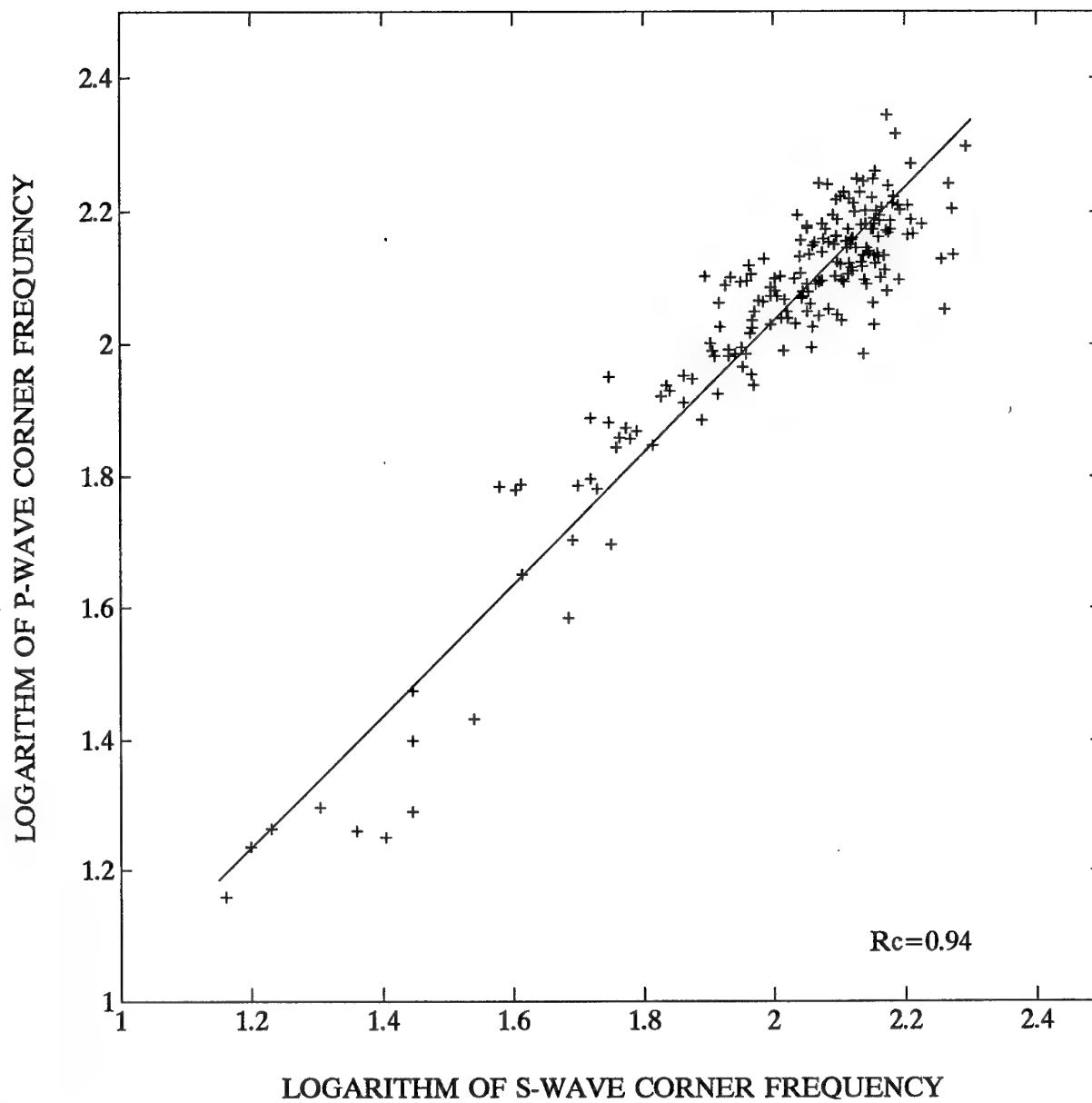


FIGURE 21. Logarithm of *P*-wave corner frequency versus logarithm of *S*-wave corner frequency. The slope coefficient of the linear regression is close to one.

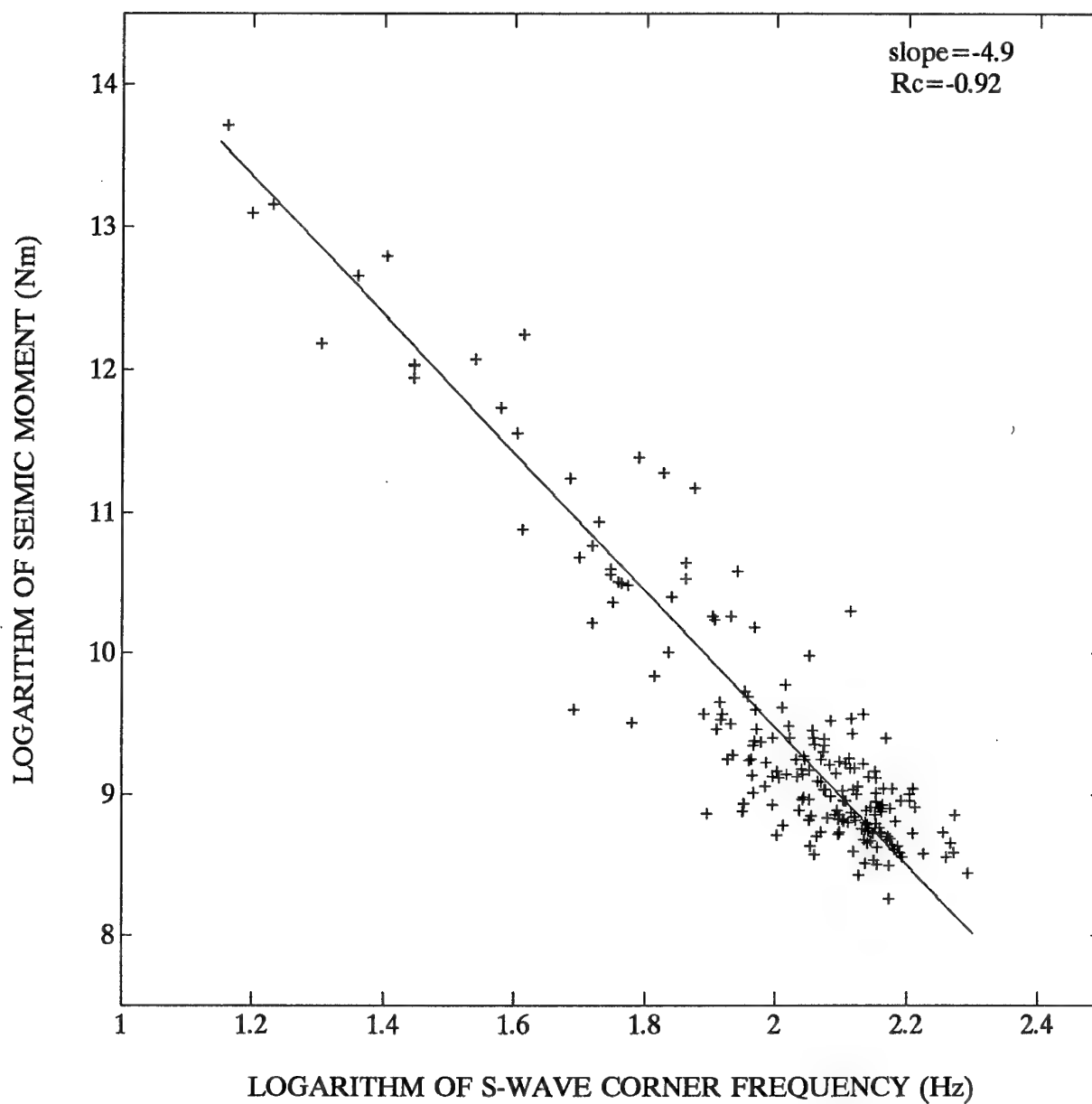


FIGURE 22. Logarithm of seismic moment versus logarithm of S-wave corner frequency.

coefficient is 0.98 which is significant with more than 99% confidence. The scatter of data is surprisingly small, in contrast with other observations that the energy of small mine tremors for a given seismic moment can vary as much as by a factor of 20 or more (e. g., Gibowicz *et al.*, 1990; Mendecki, 1993).

The corner frequencies of *P* and *S* waves are remarkably close to each other. They range for *P* waves from 14.4 to 220 Hz and for *S* waves from 14.5 to 197 Hz. The corner frequencies of *S* waves correspond to the source radius ranging from 6 to 85 m, based on the source model of Brune (1970, 1971). The values of *P*-wave corner frequency versus those of *S*-wave corner frequency are displayed on a logarithmic scale in Fig. 21. The correlation coefficient is 0.94 which is significant with more than 99% confidence. The slope of regression line is equal practically to one and the free term is equal to 0.04. This means that the *P*-wave corner frequencies are higher than those of *S* waves by a factor of 1.1. A similar result was obtained in a recent study based on a large number of observations from underground mines in South Africa, Europe and Canada (Gibowicz, 1995).

Walter and Brune (1993) considered two extreme values for the *P*- to *S*-wave corner frequency ratio. If a rupture occurs rapidly, almost instantaneously, then the *P*- and *S*-corner frequencies are proportional to the velocity divided by the fault dimension, and their ratio will be equal to the *P*- to *S*-velocity ratio. If, on the other hand, the effective duration of rupture is long in comparison to the fault radius divided by the wave velocity, then the corner frequencies might be determined by the rupture time, and their ratio will be equal to one. Our low value of 1.1 of the ratio, therefore, could possibly imply that the rupture velocity of seismic events induced by mining is relatively low. There other indications as well that mine tremors are probably slower events than natural earthquakes of the same magnitude (Gibowicz *et al.*, 1989).

The logarithm of seismic moment versus the logarithm of *S*-wave corner frequency is shown in Fig. 22. The correlation coefficient is -0.92 and is significant with more than 99% confidence. The slope coefficient is -4.9, which is large in comparison with the slope equal to -3, characterizing constant stress drop relations recently confirmed for large number of seismic events induced by mining, with seismic moment ranging from  $5 \cdot 10^3$  to  $2 \cdot 10^{15}$ .

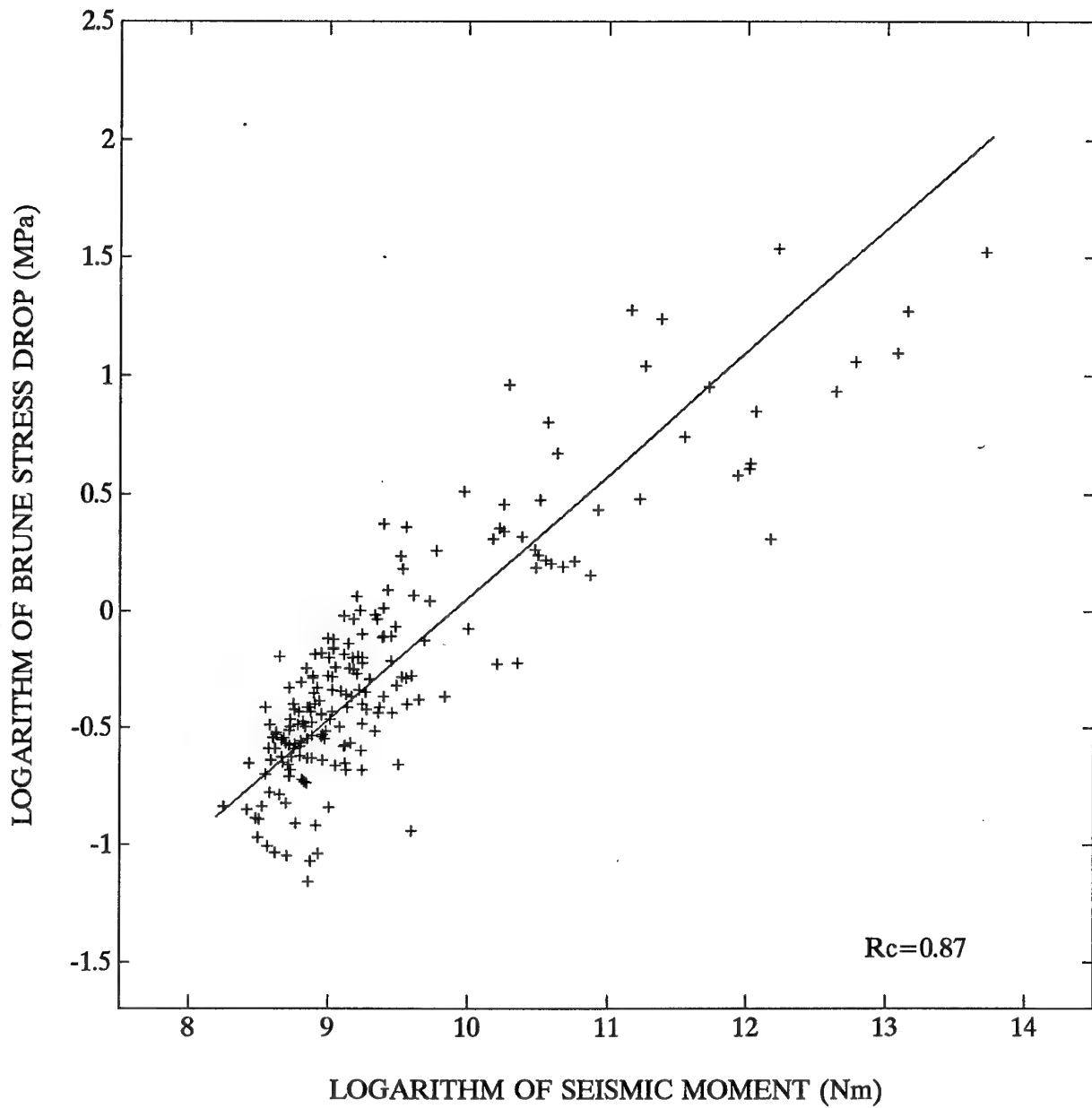


FIGURE 23. Logarithm of Brune stress drop versus logarithm of seismic moment.

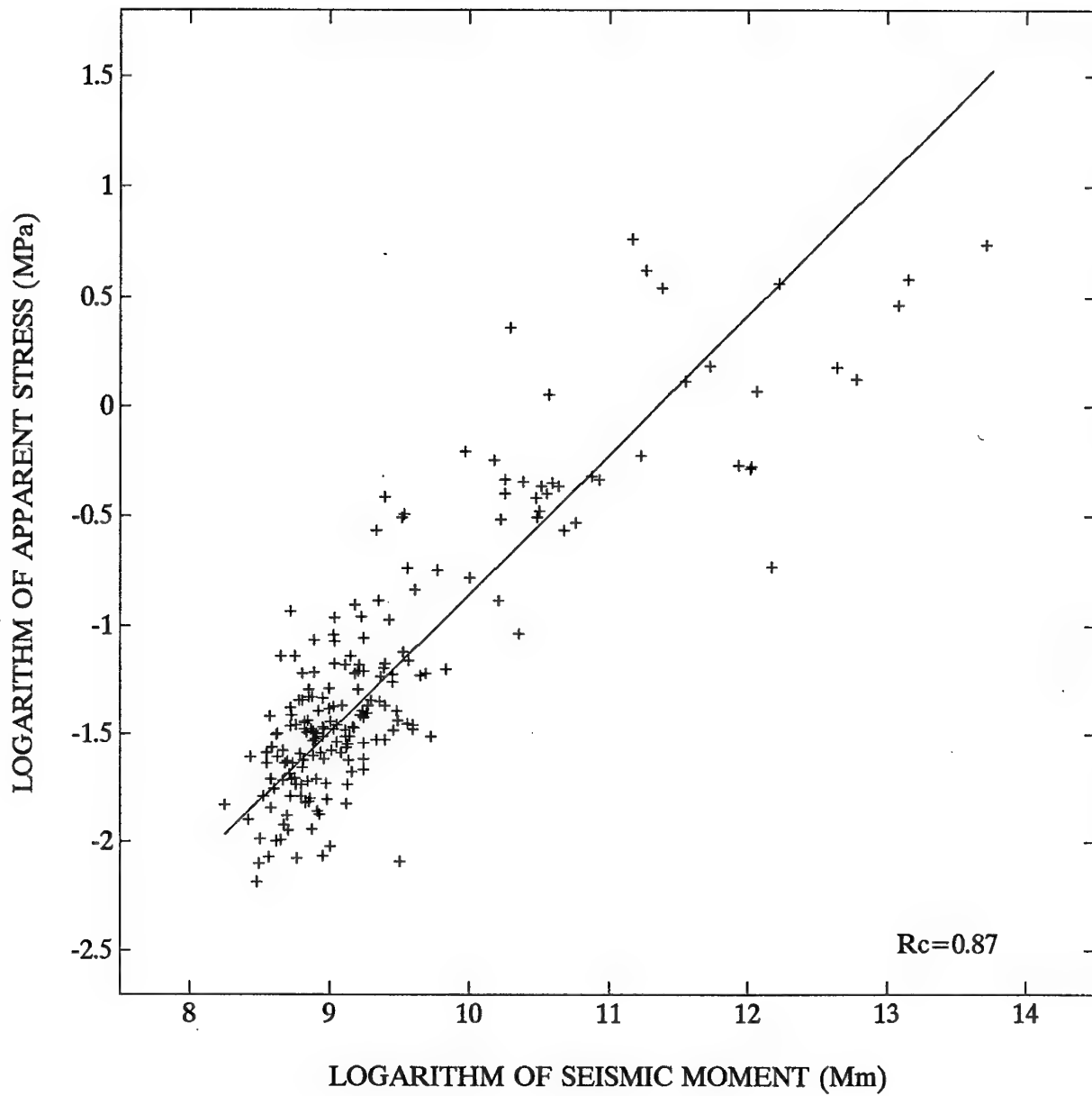


FIGURE 24. Logarithm of apparent stress versus logarithm of seismic moment.



N-m. The only distinct evidence for a breakdown in the similarity between large and small mine tremors was found for the smallest seismic events with moment magnitude below -2.5 (Gibowicz, 1995).

This non-similar behavior, shown in Fig. 22, is contradictory to the results described in the previous section as well. Spatial distribution of hypocenters was shown to be self-similar, with well determined fractal dimensions. The Gutenberg-Richter relation and the Omori formula, corresponding to the self-organized critical behavior of aftershocks, were also found as proper descriptions of our sequences. This discrepancy could possibly be explained by the dominant role played by small events in our data set, with smaller corner frequencies than those that would be expected for the events following constant stress drop relations. Such an effect could be related to the local rock mass structure with strong attenuation of high frequencies. The observations from larger events (Fig. 22) can be readily approximated by a straight line with the slope coefficient of -3.

The breakdown of constant stress drop scaling relations implies that the stress drop is dependent on the seismic moment. The stress drop, based on Brune's model and often called the Brune stress drop, is rather high, ranging from 0.07 to 34.4 MPa. The logarithm of Brune stress drop versus the logarithm of seismic moment is shown in Fig. 23. Although the correlation coefficient is high, equal to 0.87 and significant with more than 99% confidence, the small events again are dominant and their parameters are much stronger correlated than those from larger events. The apparent stress (Wyss and Brune, 1968), ranging from 0.0065 to 5.8 MPa, displays a similar pattern. Its values against those of seismic moment are displayed on a logarithmic scale in Fig. 24. Once again, the data from smaller events are strongly correlated, whereas the observations from larger events are widely scattered.

Madariaga (1976) has demonstrated that the apparent stress is proportional to the dynamic stress drop, but does not represent an actual stress difference. If the *P*-wave contribution to the seismic energy and the azimuthal dependence of the energy flux are neglected, the Brune stress drop is a constant multiple of the apparent stress (Snoke, 1987). In general, for mine tremors the energy of *P* waves cannot be neglected and the apparent stress becomes an independent parameter (Gibowicz *et al.*, 1990, 1991). The logarithm of apparent stress versus the logarithm of Brune stress drop is

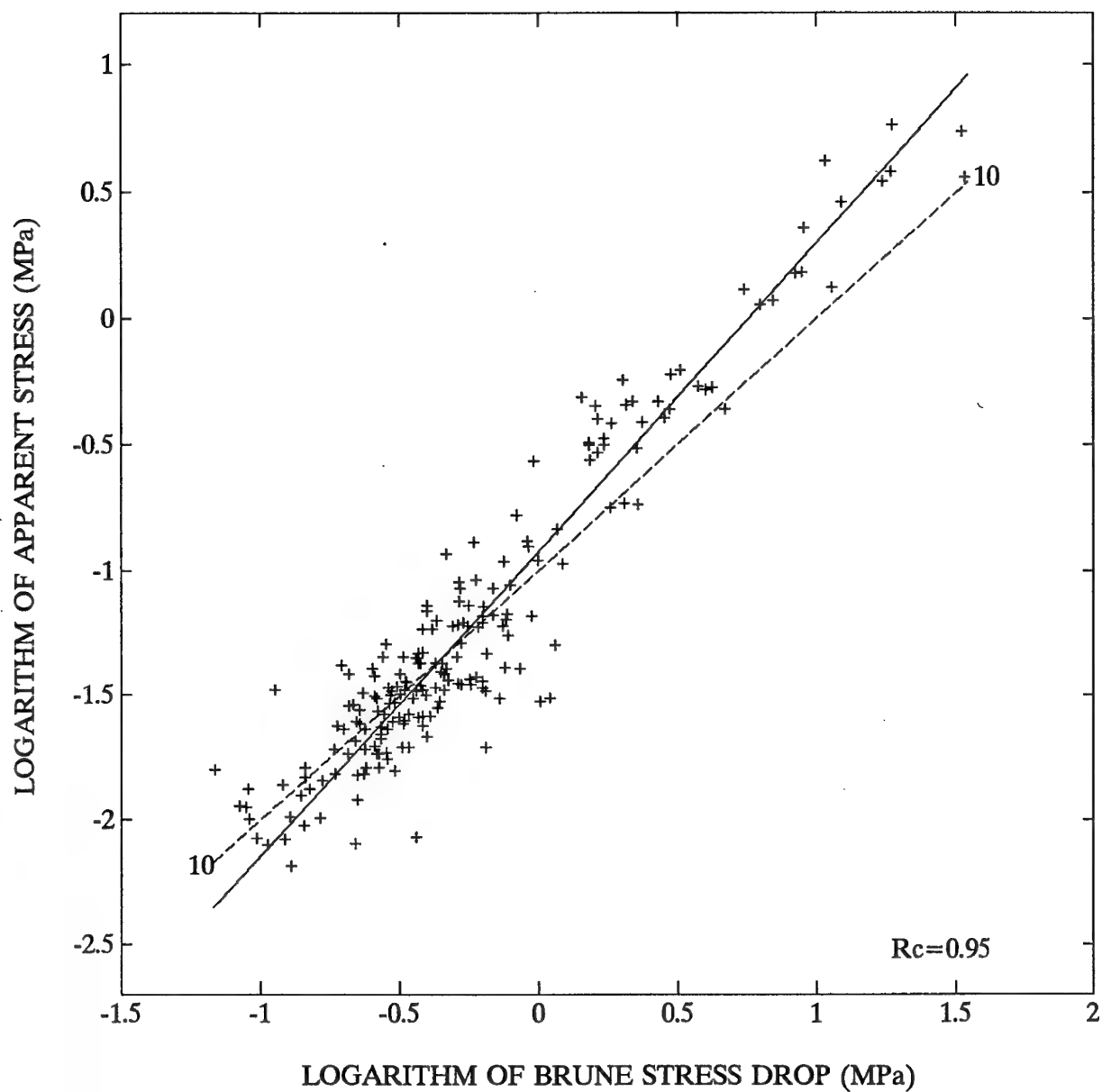


FIGURE 25. Logarithm of apparent stress versus logarithm of Brune stress drop. The ratio of Brune stress drop over apparent stress equal to 10 is shown by the dashed line.

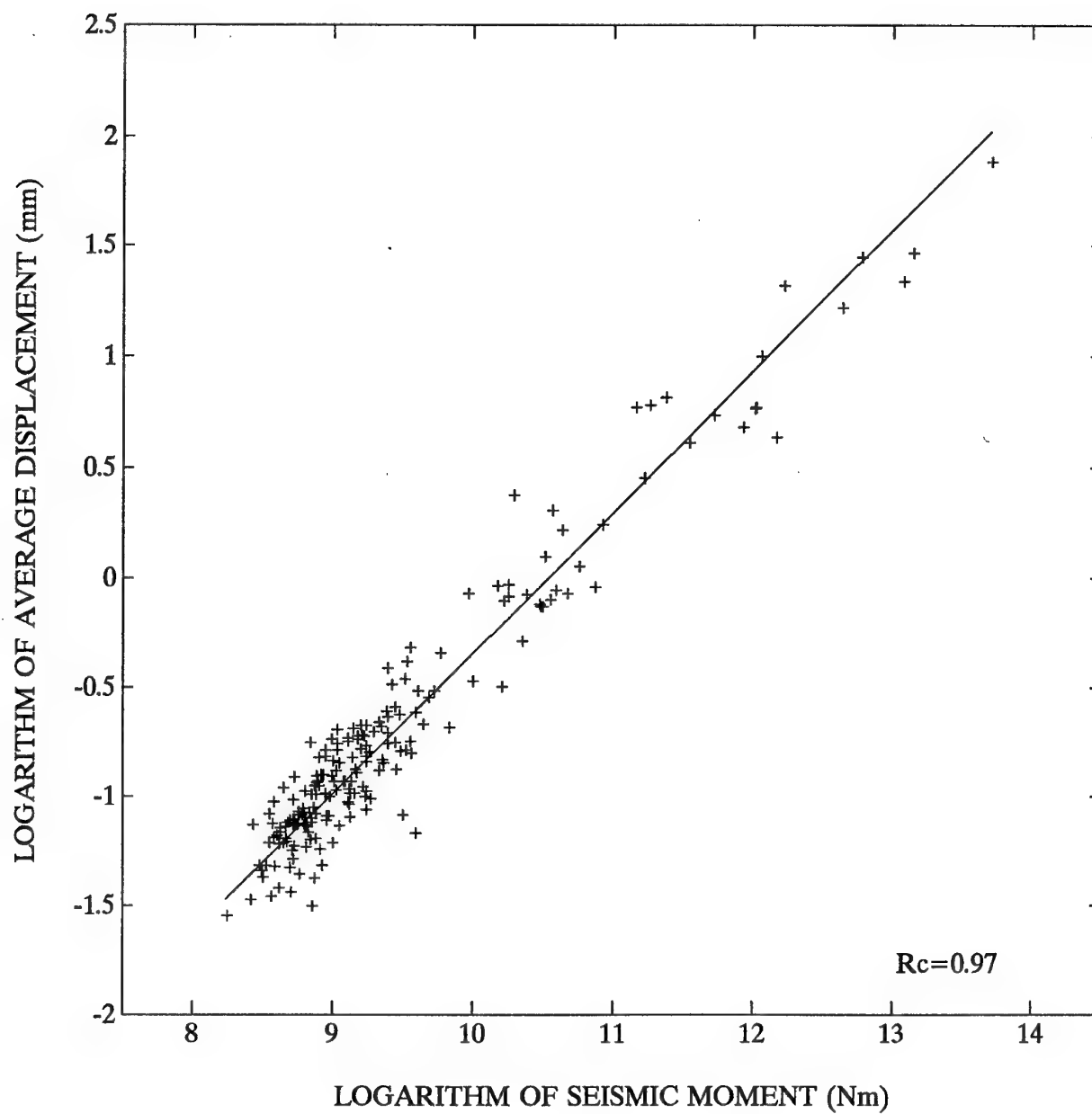


FIGURE 26. Logarithm of average displacement versus logarithm of seismic moment.

shown for our events in Fig. 25. The correlation coefficient is very high, equal to 0.95 and significant with more than 99% confidence. The values of apparent stress are approximately ten times lower than those of Brune stress drop, though the scatter of data is considerable.

The average displacement across the fault plane is another important source parameter, often used for the source characterization. This can be calculated directly from the original definition of seismic moment as a product of the shear modulus at the source by the average displacement and by the fault area (e. g., Aki and Richards, 1980). The values of the average displacement range for our events from 0.03 to 76 mm. They are displayed on a logarithmic scale against the values of seismic moment in Fig. 26. A very good correlation between these two parameters is observed, characterized by the correlation coefficient close to one and insignificant scatter of the data.

#### 4.3 P-wave energy versus S-wave energy

The ratio of S- to P-wave energy might be an important indicator of the type of focal mechanism responsible for the generation of seismic events in mines. There is a definite evidence from natural earthquakes that the energy radiated in P waves is a small fraction of that in S waves, with the ratio of S-wave over P-wave energy ranging between 10 and 30 (e. g., Boatwright and Fletcher, 1984; Boatwright and Quin, 1986). In contrast, it has been found that the energy ratio for small mine tremors in the Ruhr Basin, Germany, ranges from 1.5 to 30; for two thirds of the events the ratio was smaller than 10 (Gibowicz *et al.*, 1990). A similar result has also been reported from the Underground Research Laboratory in Manitoba, Canada, where extremely small seismic events induced by the excavation of a shaft in granite were observed (Gibowicz *et al.*, 1991) and from two coal mines in Poland (Gibowicz and Wiejacz, 1994). The observed energy depletion in S waves could possibly be explained by a non-double-couple mechanism of some mine tremors, enriching the energy radiated in P waves, and implying that tensile failures, or at least shear failures with tensile components, are often generated in mines.

P-wave energy versus S-wave energy from our seismic events is shown in Fig. 27, where the ratio of S-wave over P-wave energy equal to 1, 10 and 100

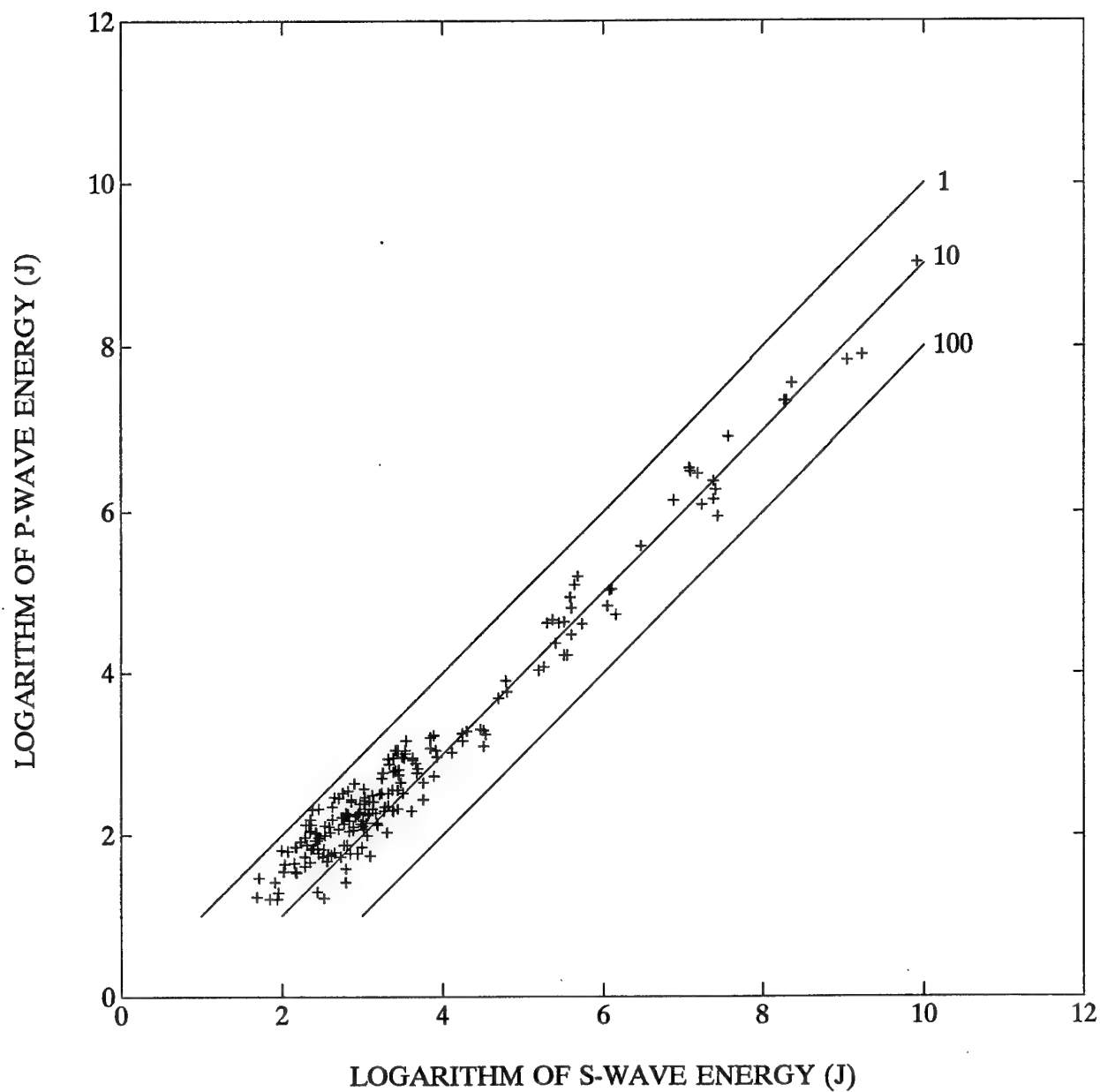


FIGURE 27. Logarithm of *P*-wave energy versus logarithm of *S*-wave energy. The ratio of *S*-wave energy over *P*-wave energy equal to 1, 10, and 100 is shown by straight lines.

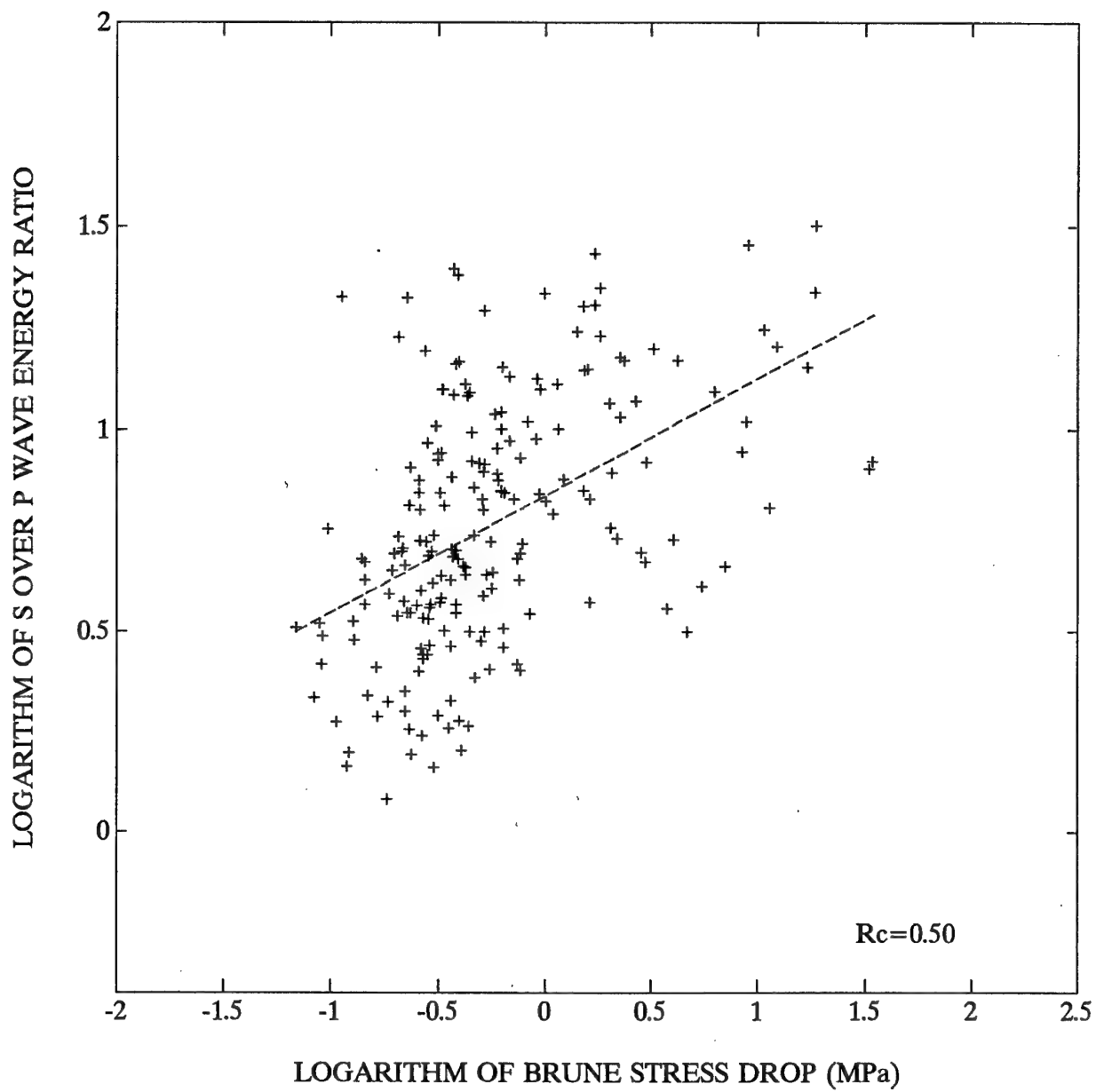


FIGURE 28. Logarithm of the ratio of S-wave energy over P-wave energy versus logarithm of Brune stress drop.

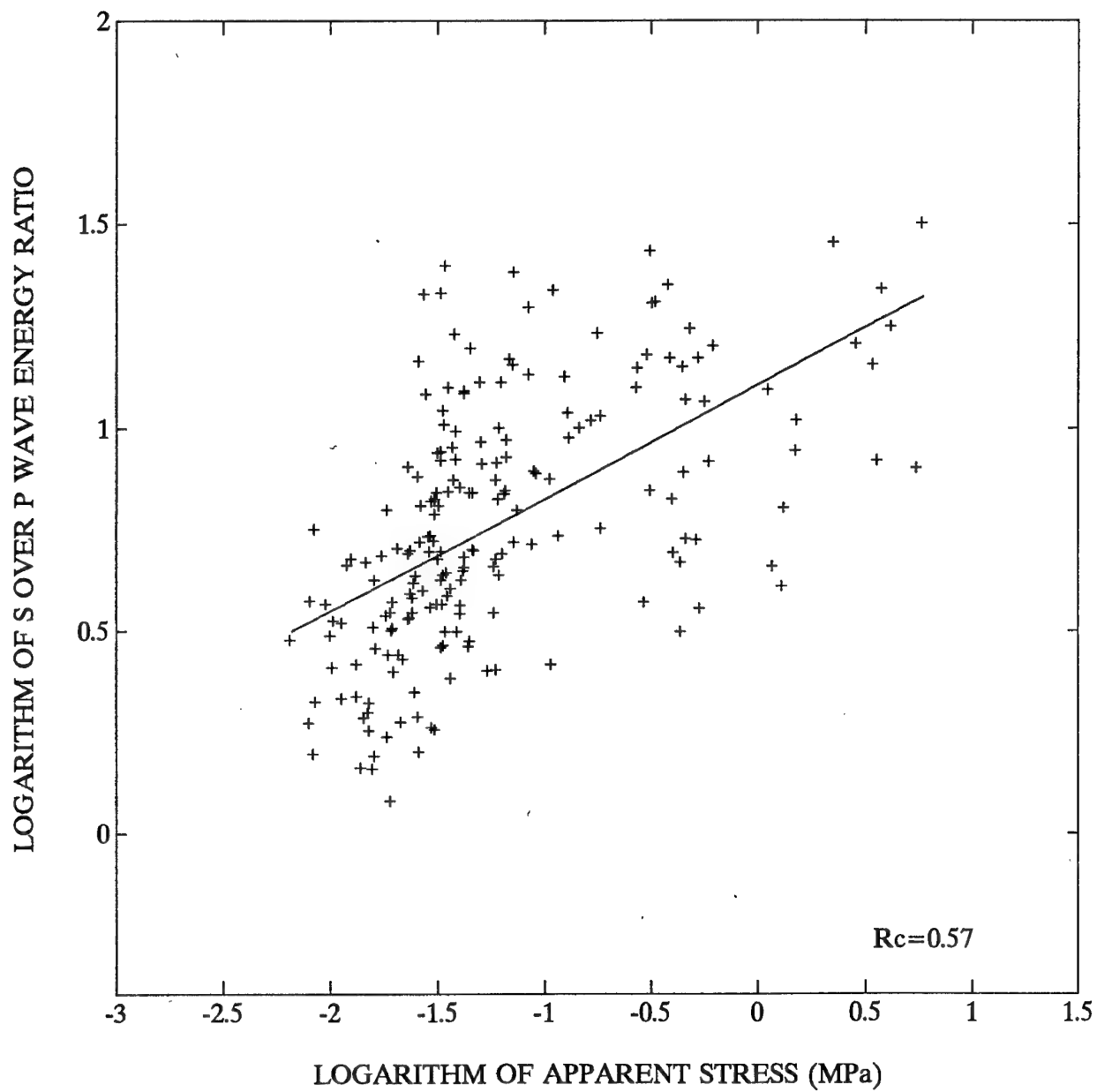


FIGURE 29. Logarithm of the ratio of S-wave energy over P-wave energy versus logarithm of apparent stress.

is also indicated by straight lines. The ratio ranges from about 1 to 30 and for about three quarters of events, especially for small events, it is less than 10. The values of the energy ratio are compared with the moment tensor solutions in Section 5.

It should be noted that the ratio of S-wave over P-wave energy correlates with stress release measurements: Brune stress drop and apparent stress. The energy ratio against the Brune stress drop is shown on a logarithmic scale in Fig. 28 and the ratio versus the apparent stress is displayed in Fig. 29. In both figures a positive correlation is observed: large stress release corresponds to high values of the energy ratio. In other words, the high stress drop events are characterized by the high S-wave energy, implying that shearing mechanism plays a dominant role in their generation. Although the correlation coefficient in both cases is only 0.5 and 0.6, it is significant with more than 99% confidence.

#### 4.4 Time distribution of the source parameters

An analysis of several source parameters as a function of time for the four sequences shows that the four main shocks are most distinctly marked by their source radius rather than by their seismic moment or seismic energy. The source radius versus the time after the occurrence of the first main shock is displayed in Fig. 30. The duration of the four sequences is highly diverse. The first sequence was the longest and lasted 169 hours and the second sequence, the shortest, lasted only 23 hours. The third and fourth sequences lasted 31 and 61 hours, respectively. Thus the distribution of their source parameters in real time is rather unclear as the time axis is too compressed for the sequences of short duration.

A better presentation of time distribution of the source parameters is achieved when the source parameters are displayed against the number of consecutive seismic events forming the four sequences. Such a presentation for the source radius is shown in Fig. 31. The four main shocks are clearly marked by the highest values of the source radius ranging from 50 to 85 m, while the source radius of all aftershocks is smaller than 30 m.



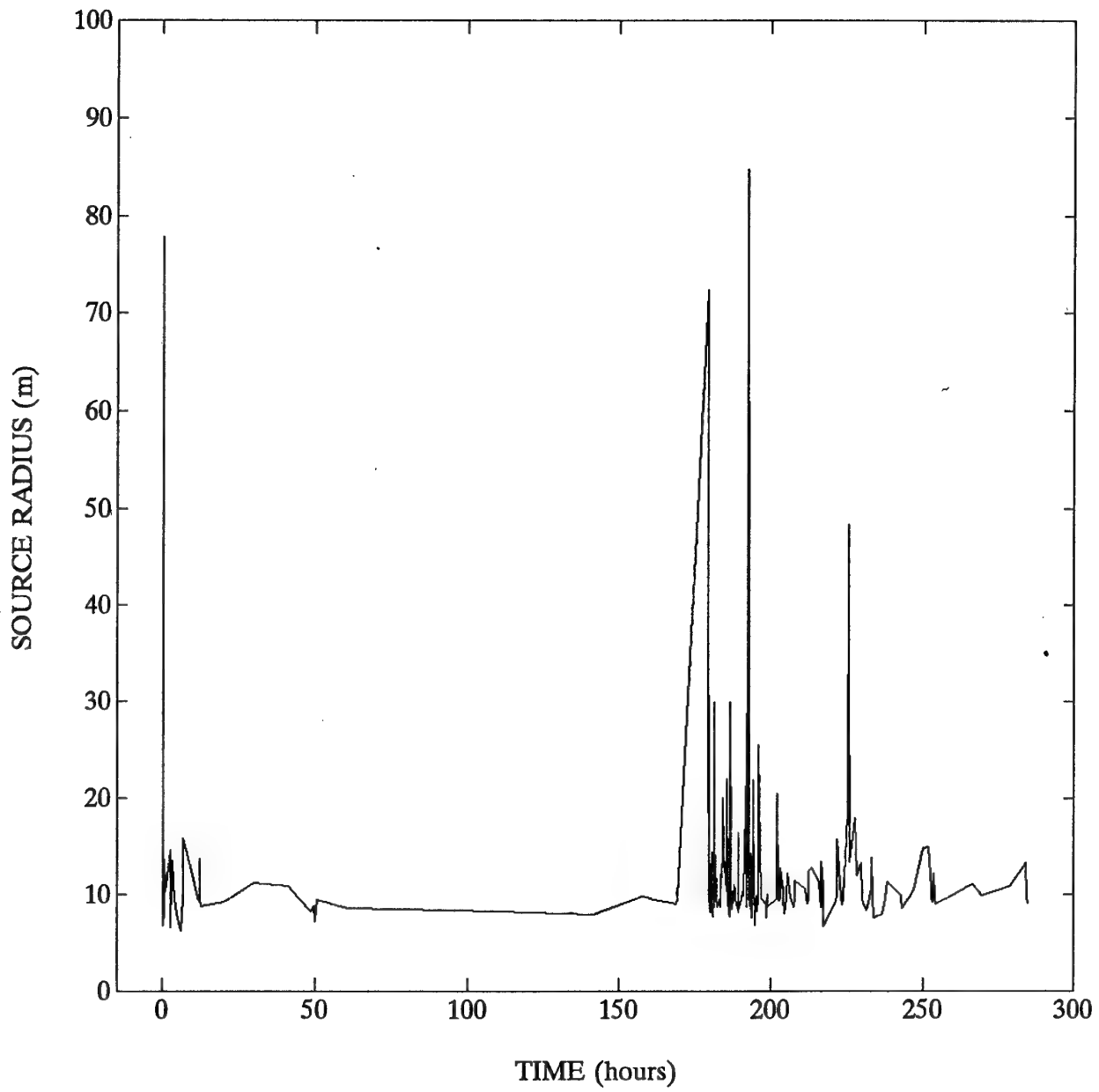


FIGURE 30. Source radius versus real time after the occurrence of the first main shock for the four sequences.

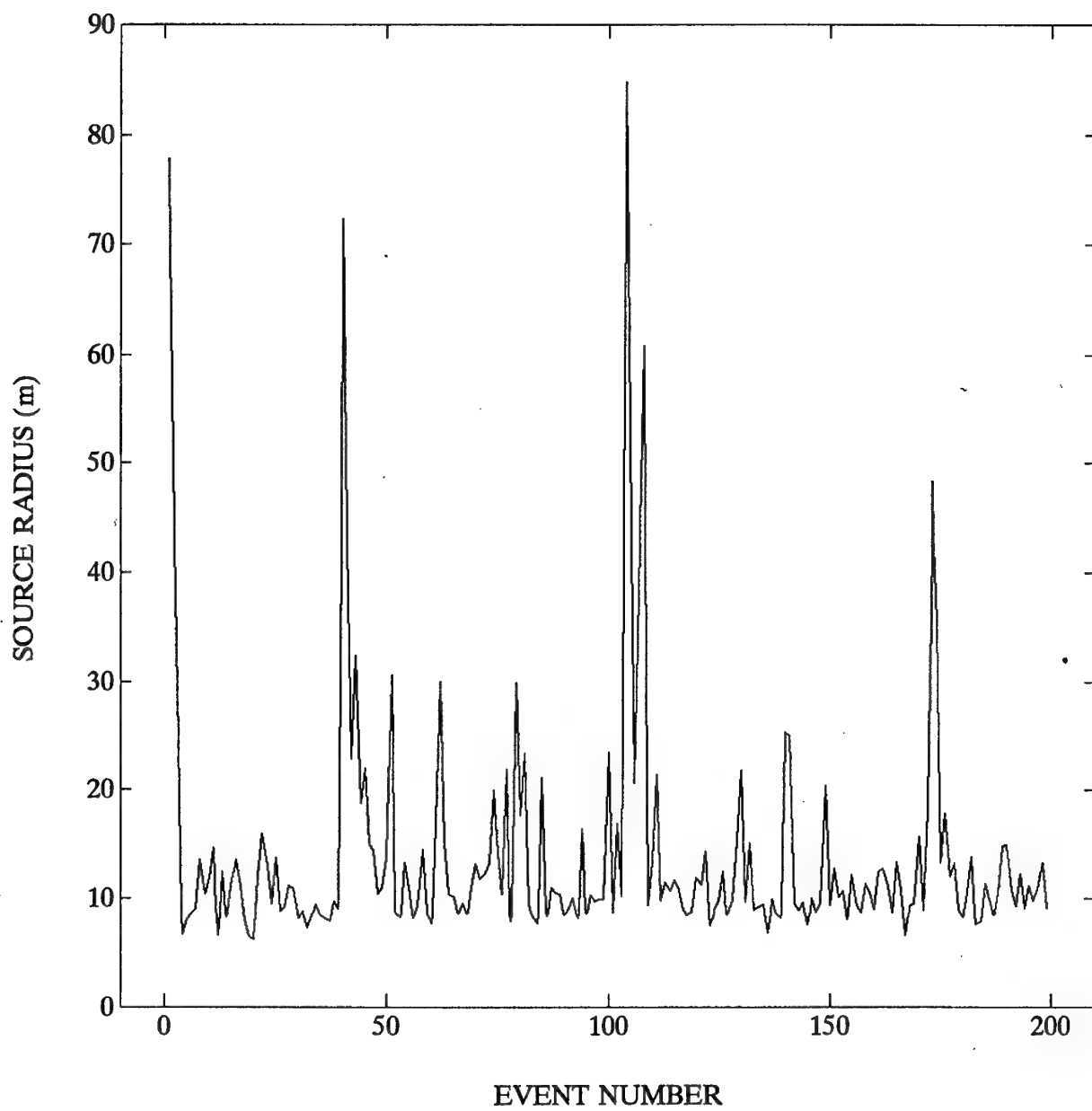


FIGURE 31. Source radius versus the number of consecutive seismic events forming the four sequences whose beginnings are clearly marked by the highest values of the source radius.

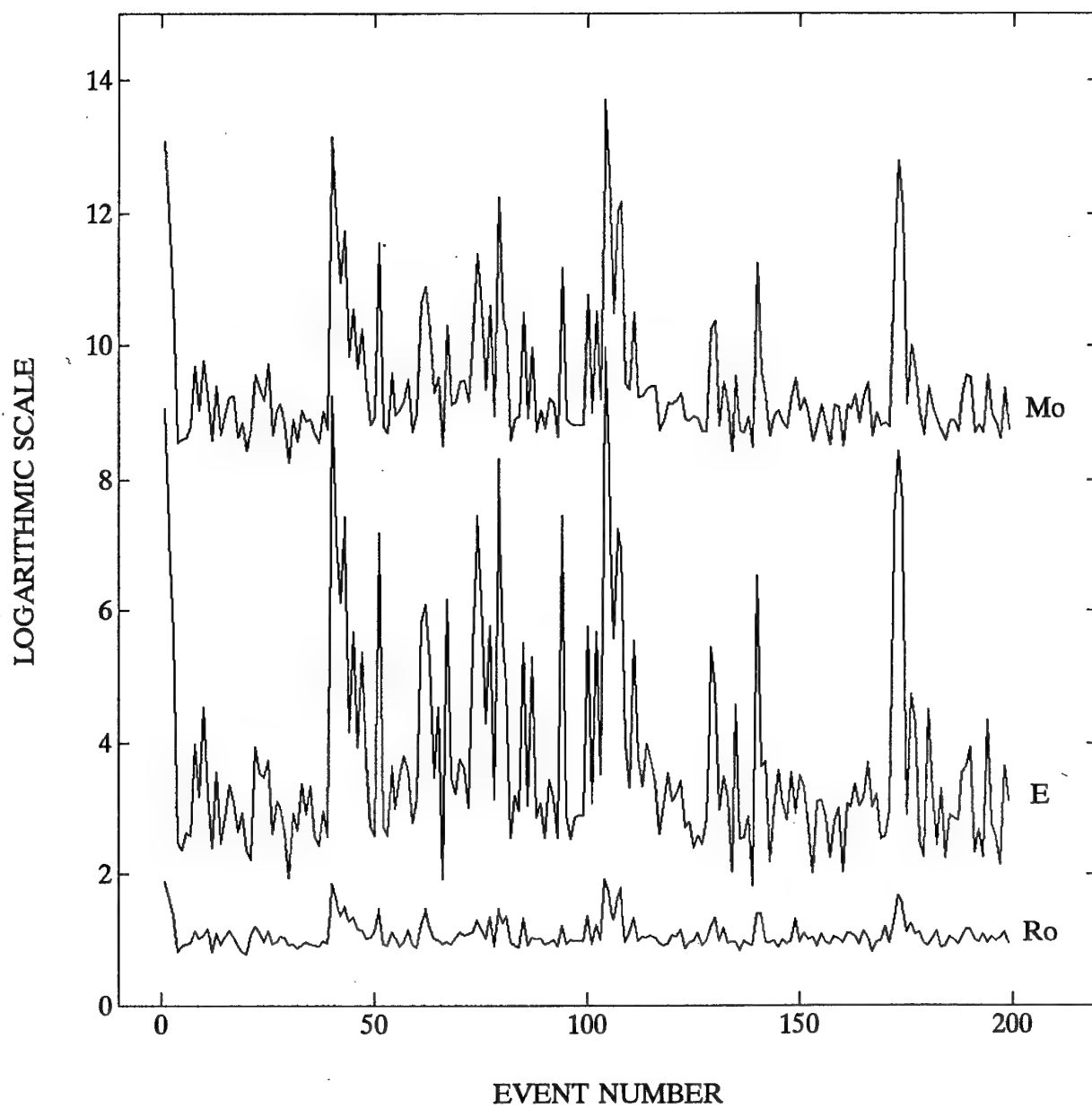


FIGURE 32. Logarithm of seismic moment  $M_o$  (in  $N \cdot m$ ), seismic energy  $E$  (in  $J$ ) and source radius  $R_o$  (in  $m$ ) versus the number of consecutive seismic events forming the four sequences.

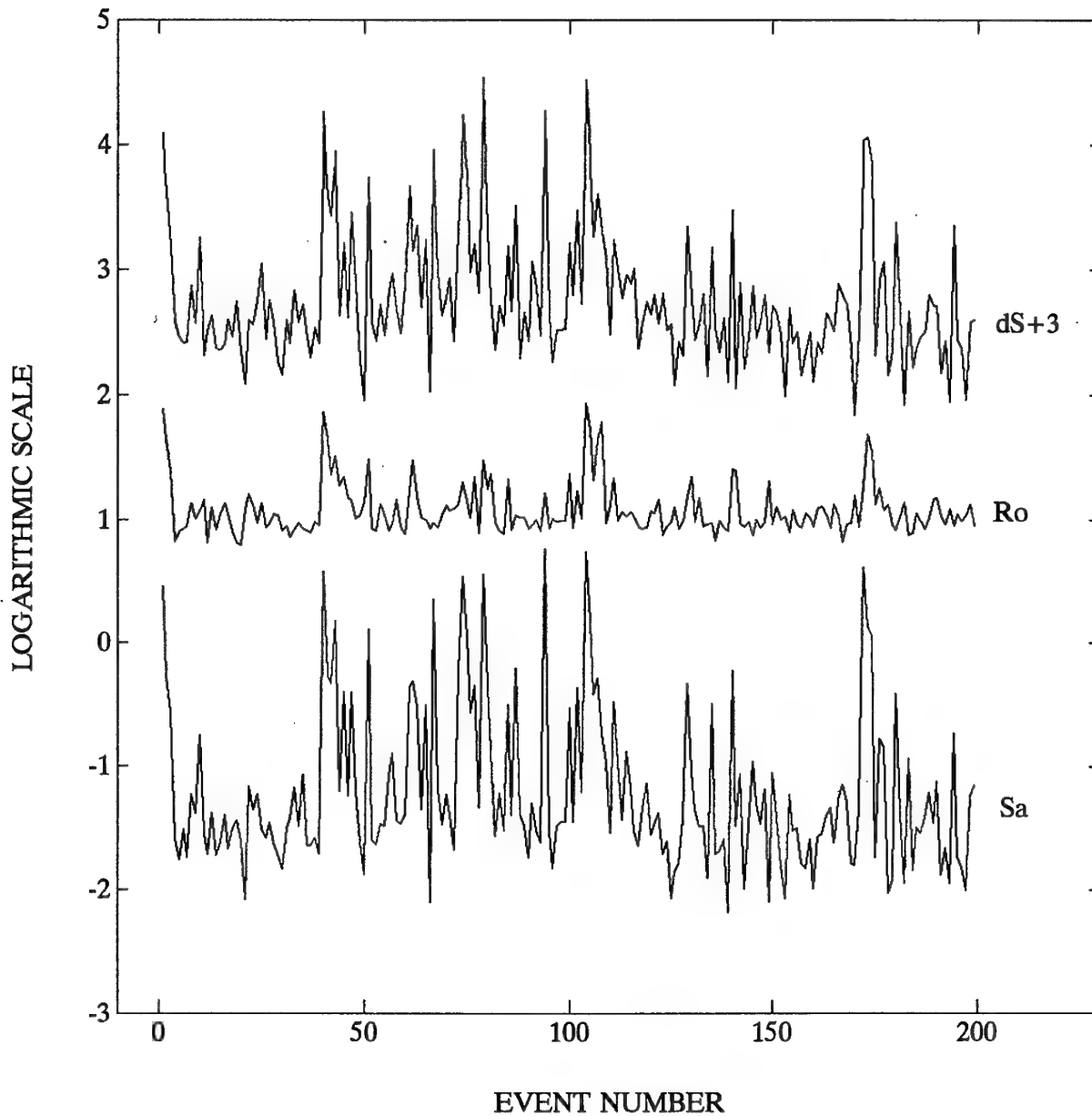


FIGURE 33. Logarithm of Brune stress drop  $dS$  (in MPa), source radius  $R_o$  (in m) and apparent stress  $S_a$  (in MPa) versus the number of consecutive seismic events forming the four sequences. The stress drop is moved up by 3 units for the sake of clarity.

A similar presentation for the seismic moment and seismic energy is shown on a logarithmic scale in Fig. 32, where the values of source radius are displayed again for comparison. The second sequence, which occurred in the middle of the volume containing the four sequences (Figs 3 and 4), is characterized by a number of large events in terms of their seismic moment and energy, not much smaller than the main shock. Thus the second sequence is more similar to a seismic swarm than to a main shock - aftershocks series. There are still a few large events in the third sequence, whereas the fourth sequence displays a regular main shock - aftershocks pattern similar to that characterizing the first sequence.

The logarithm of Brune stress drop and apparent stress against the event number is shown in Fig. 33. Here again the second sequence contains several large events with the stress release indicators of the same magnitude as that for the main shock.

## 5. MOMENT TENSOR INVERSION: SOURCE MECHANISM

There are various methods of inversion for moment tensor elements. The inversion can be done in the time or frequency domain, and different data can be used separately or in combination. The moment tensor inversion in the time domain can be based on the formulation describing the displacement as a linear function of the moment tensor elements and the terms related to the temporal convolution of Green's function and the source time function of a synchronous source (e. g., Gilbert, 1970; Stump and Johnson, 1977; Fitch *et al.*, 1980; Langston, 1981). This approach leads to a linear inversion in the time domain for which a number of fast computational algorithms are available (e. g., Lawson and Hanson, 1974; Press *et al.*, 1990). A detailed description of the procedure for solving appropriate equations using regional and local seismograms was given by Oncescu (1986). The application of moment tensor inversion to microseismic events was described by O'Connell and Johnson (1988).

The main difficulty in the moment tensor inversion is a proper calculation of Green's function for geologically complex media. Synthetic Green's functions are calculated taking into account geological structure between the source and the receiver. The source time function is often assumed to be a step function (Knopoff and Gilbert, 1959) or a ramp function (Haskell, 1964) and used in the inversion (e. g., Gilbert, 1970; Stump and Johnson, 1977; Kanamori and Given, 1981). The Green's function is in general different for different displacement components and takes different values for particular stations. The simplest approach in the time domain is to use directly the source radiation formulation for *P*, *SH* or *SV* waves. This approach was used, for example, by Fitch *et al.* (1980) and De Natale *et al.* (1987).

### 5.1 The method used in the ISS system

The inversion of moment tensor in the ISS system is done in the time domain. The source time function is assumed to be a step function. The

simplest approach for the calculation of Green's function is used, which is the source radiation formulation for  $P$ ,  $SH$  and  $SV$  waves. The input data for the inversion contain the polarities of  $P$  waves and the values of the spectral low-frequency level from  $P$ ,  $SH$  and  $SV$  waves. The polarities of  $P$  waves and their quality indices are determined automatically from the first motion of  $P$  arrivals. The quality index of polarity (see Mendecki, 1993) can take any value between 0 and 1 for compressions and between -1 and 0 for dilatations. Whenever the absolute value of the quality index is less than 0.5, the corresponding polarity is discarded and is not taken into further account. At least four polarities are needed to start the inversion.

The quality index of spectral amplitudes used for the moment tensor inversion is based on the quality index for the low-frequency level from  $P$ ,  $SH$  or  $SV$  waves at a given station, the quality index for the  $P$ -wave direction found from polarization analysis, and the difference between the angle of incidence found from  $P$ -wave polarization and that calculated geometrically from the source location (see Mendecki, 1993).

Normalized values of the quality index of spectral amplitudes are used as the weighting function for the inversion. In principle, all spectral amplitudes provided by the spectra with prescribed quality indices are accepted for the calculations. Seismic stations located at the surface are the only exceptions because of the free-surface and site effects. From such stations the spectral level from  $SH$  waves only is accepted, and the amplitude is divided by two to account for the free-surface enhancement. Stability of moment tensor solutions depends heavily on the number and distribution of seismic stations against the source location. Six stations with three spectral amplitudes of good quality are accepted in the ISS system as the minimum number of observations required for the inversion.

The difference in the angles of incidence of  $P$  waves, found from  $P$ -wave polarization and calculated geometrically from the source location, provides another criterion for the selection of input data. From a number of tests carried out on real observations it follows that the first arrivals correspond to direct  $P$  waves. The differences in the angles of incidence are randomly distributed against the distance between the source and the receiver implying that no refracted waves are observed as the first arrivals. It was also found from the tests that the difference in the incidence angles not

greater than 30 degrees is acceptable for the moment tensor inversion. Surface stations are again exceptional. They show, as a rule, large differences in the angles of incidence. The angles found from *P*-wave polarization are usually close to 90 degrees, whereas the angles calculated from straight-line seismic rays are much smaller. The observations are accepted regardless of the difference in their angles of incidence. The solutions are considerably constrained by the observations from surface stations as a result of improved vertical distribution of seismic stations.

It is convenient to characterize the moment tensor by the eigenvalues. This can be done by a rotation of the moment tensor from local topographic coordinates into its principal axes. For a general moment tensor all eigenvalues are different and they can be readily found following, for example, Kennett (1988). From several tests on real data it was found that the deviatoric moment tensor provides the most stable solution in terms of variable configuration of seismic stations and variable depth. In the ISS system, therefore, the deviatoric moment tensor solution is accepted as a starting point for the full moment tensor inversion and for the double-couple inversion in the automatic mode.

Seismic sources with no volume change can be obtained by constraining the moment tensor to have zero trace, and the deviatoric moment tensor contains 5 components to be found from the inversion. The non-isotropic constraint is linear. The initial deviatoric moment tensor components are found by solving by the singular value decomposition method the system of linear equations with the weights equal to the normalized values of the quality index of spectral amplitudes. During this preliminary stage of calculations the only spectral amplitudes accepted are those with the weights not smaller than 0.5. To constrain the initial solution as much as possible, four sets of observations are used to solve the equations. Besides the observed polarities of *P* waves, the polarities of *S* waves are prescribed to the two largest amplitudes observed usually at two stations, alternatively with the plus and minus signs. The best solution out of the four, in terms of norm  $L_1$  (the smallest sum of residuals), is then accepted as the initial solution for the moment tensor.

The initial solution is the starting point for the final deviatoric moment tensor inversion carried out by the simplex method. After the recovery of



moment tensor, its eigenvectors and eigenvalues are calculated. Then the moment tensor is presented in a diagonal or matrix form. The radiation pattern of *P* waves corresponding to a given moment tensor is displayed graphically on an equal-area lower-hemisphere projection, in terms of compressional (shaded) and dilatational (unshaded) areas separated by nodal lines. An example of such presentation for the first event from our series is shown in Fig. 34. The polarities at particular stations are also shown either by a plus or minus signs, and stations without polarity observations are marked by open circles. The surface stations, which supply only *SH* observations, are marked by small "s". The best double couple (Giardini, 1984) corresponding to a given moment tensor solution is calculated and its tension *T* and pressure *P* axes are determined; they are marked on a graphical display.

The quality index for the moment tensor is defined taking into account the quality index for the configuration of seismic stations, the numbers of components and stations used in the inversion, the correlation coefficient between the observed and the calculated spectral amplitudes, and the normalized sum of residuals corresponding to the first norm  $L_1$  (Mendecki, 1993). If the focal depth is not determined with sufficient precision, a linear inversion can be done for a number of trial depths. The most probable depth will minimize the corresponding error between observed and theoretical waveforms (e. g., Patton and Aki, 1979; Sipkin, 1982). In the ISS system, a provision is made for an interactive mode in which the depth can be changed, as well as the horizontal components of a given hypocenter.

For the moment tensor of the double-couple source, its determinant must vanish. The vanishing of the tensor determinant and tensor trace are therefore necessary and sufficient conditions for a double-couple source. The constraint of zero determinant on the moment tensor is nonlinear and the system must be solved iteratively until the determinant and the trace converge to zero. In the ISS system, two modes of operation for the moment tensor inversion are possible: the automatic mode and the interactive mode. In the automatic mode, the deviatoric moment tensor solution is taken as a starting point for the double-couple iterative inversion by the simplex technique. After the inversion, the double-couple solution is presented in the final printout in the numerical and graphical form (Fig. 34).

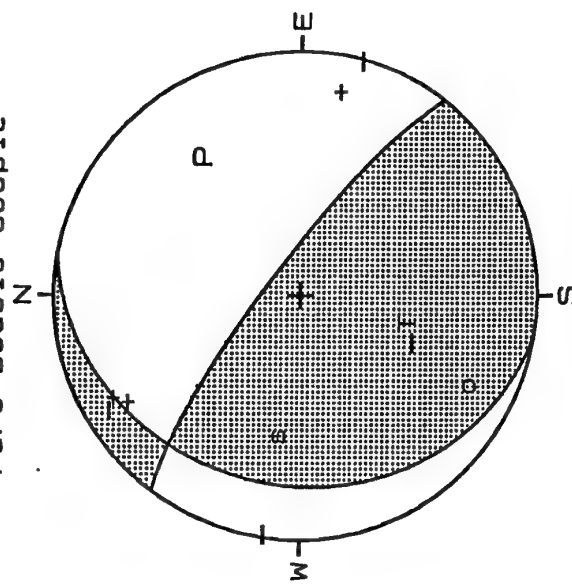
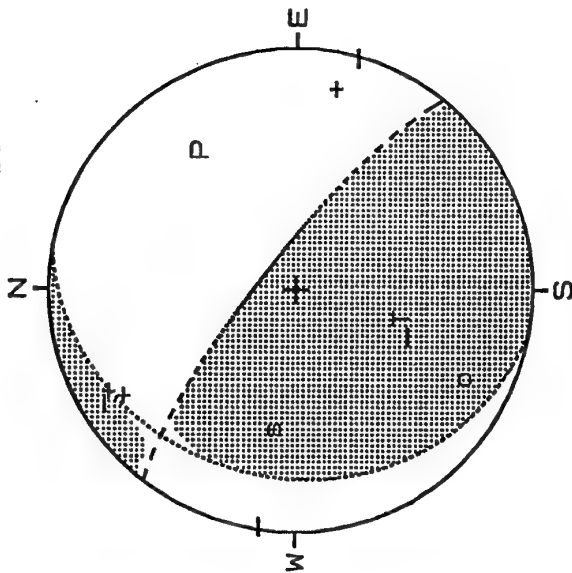
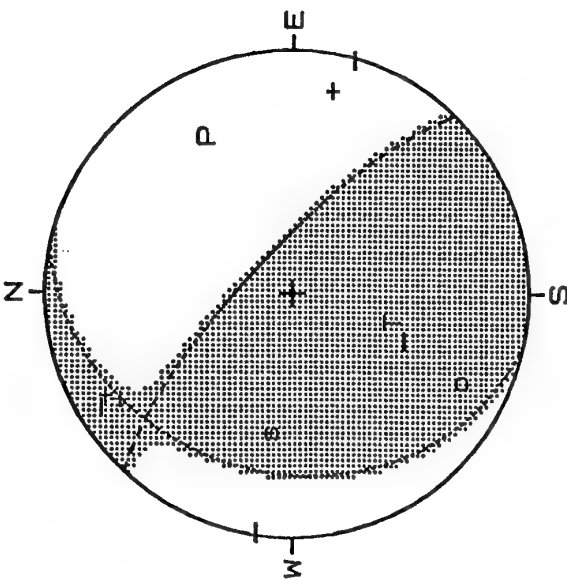
FIGURE 34.

Moment Tensor of Event Occurring at 09:09:35 on 93/04/07  
 Event Location: X = 26886, Y = 44074, Z = 2985

Full Tensor

Pure Deviatoric

Pure Double Couple



Tensor of Event Occurring at 09:08:12 on 93/04  
Event Location:  $X = 26655$ ,  $Y = 44070$ ,  $Z = 2941$

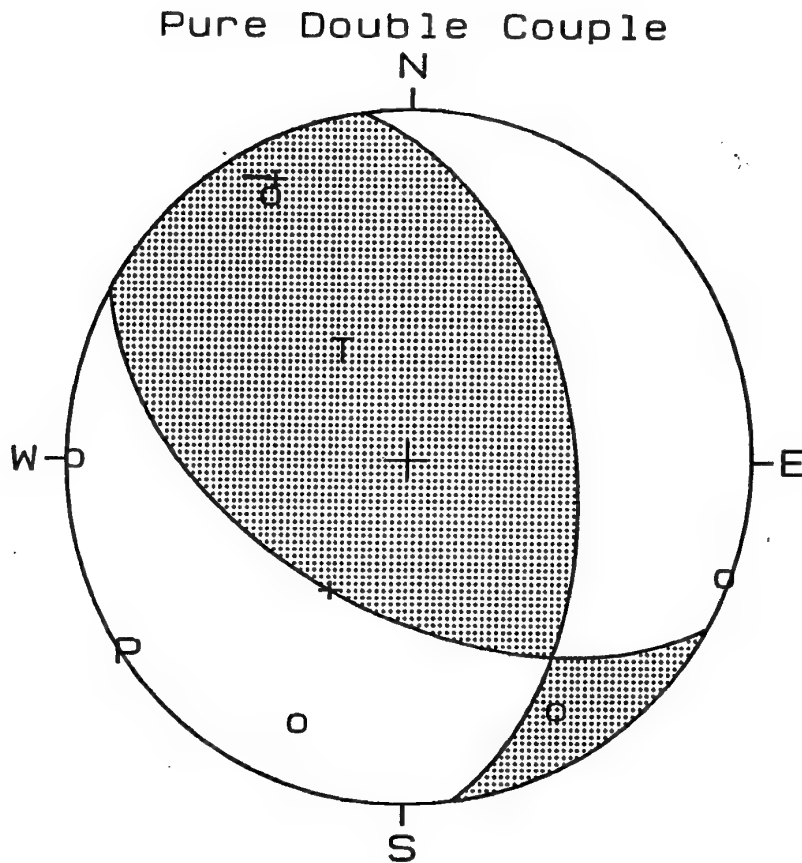


FIGURE 35. An example of the double-couple moment tensor solution for one of the events from the selected series. Full description is given in the text.

In the interactive mode, the double-couple solution can be obtained separately and independently from the general moment tensor inversion. There are 144 starting points for an iterative inversion by the simplex method, and the best solution is sought in terms of norm  $L_1$ , i. e. the smallest sum of residuals. The starting points are defined by the values of the strike, dip and rake angles of nodal planes (six for the strike angle, four for the dip angle and six for the rake angle) and the best double-couple solution in terms of norm  $L_1$  is accepted as the final solution and is presented numerically and graphically in the same form as the solution found from the inversion with the starting point prescribed by the deviatoric moment tensor. An example of graphical presentation of such a solution for one of the event from our series is shown in Fig. 35.

In the ISS system, the full moment tensor inversion can also be performed in the automatic and interactive modes. In the automatic mode, the starting point is provided by the deviatoric moment tensor, similarly as in the double-couple automatic inversion. The inversion for the six independent components of a full moment tensor is then carried out exactly in the same manner as in the case of deviatoric moment tensor. The initial moment tensor components are calculated by solving the system of linear equations by the singular value decomposition method and the final moment tensor is computed by the simplex technique. The manner of selection of the starting points for the inversion is the only difference between the automatic and interactive approaches. In the interactive mode, the four starting points are selected in the same way as those selected for the deviatoric moment tensor inversion.

The final moment tensor is decomposed into the isotropic component and two deviatoric components, the double couple and the compensated linear vector dipole components. The three components are presented in the final printout and the full moment tensor solution is also shown in a graphical form, similarly as that for the deviatoric moment tensor (Fig. 34).

## 5.2 Source mechanism

Out of 199 seismic events, forming our four sequences, full moment tensor solutions were found for 35 events (4 from the first and fourth sequences, 20 from the second, and 7 from the third sequence) and constrained double couple

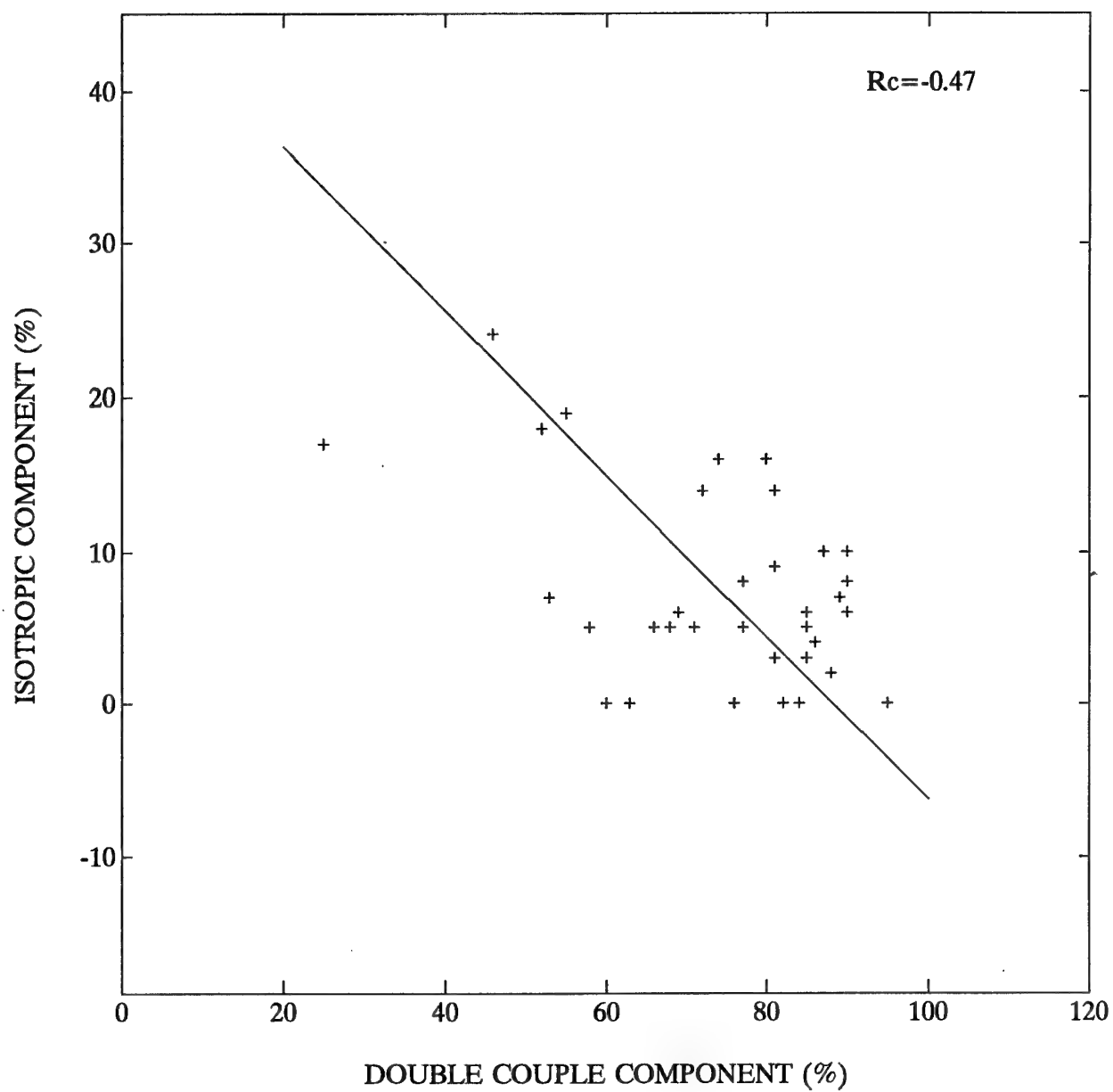


FIGURE 36. The isotropic component versus the double couple component of the general moment tensor solution for 35 seismic events from the four sequences. The correlation coefficient  $R_c$  is also indicated.

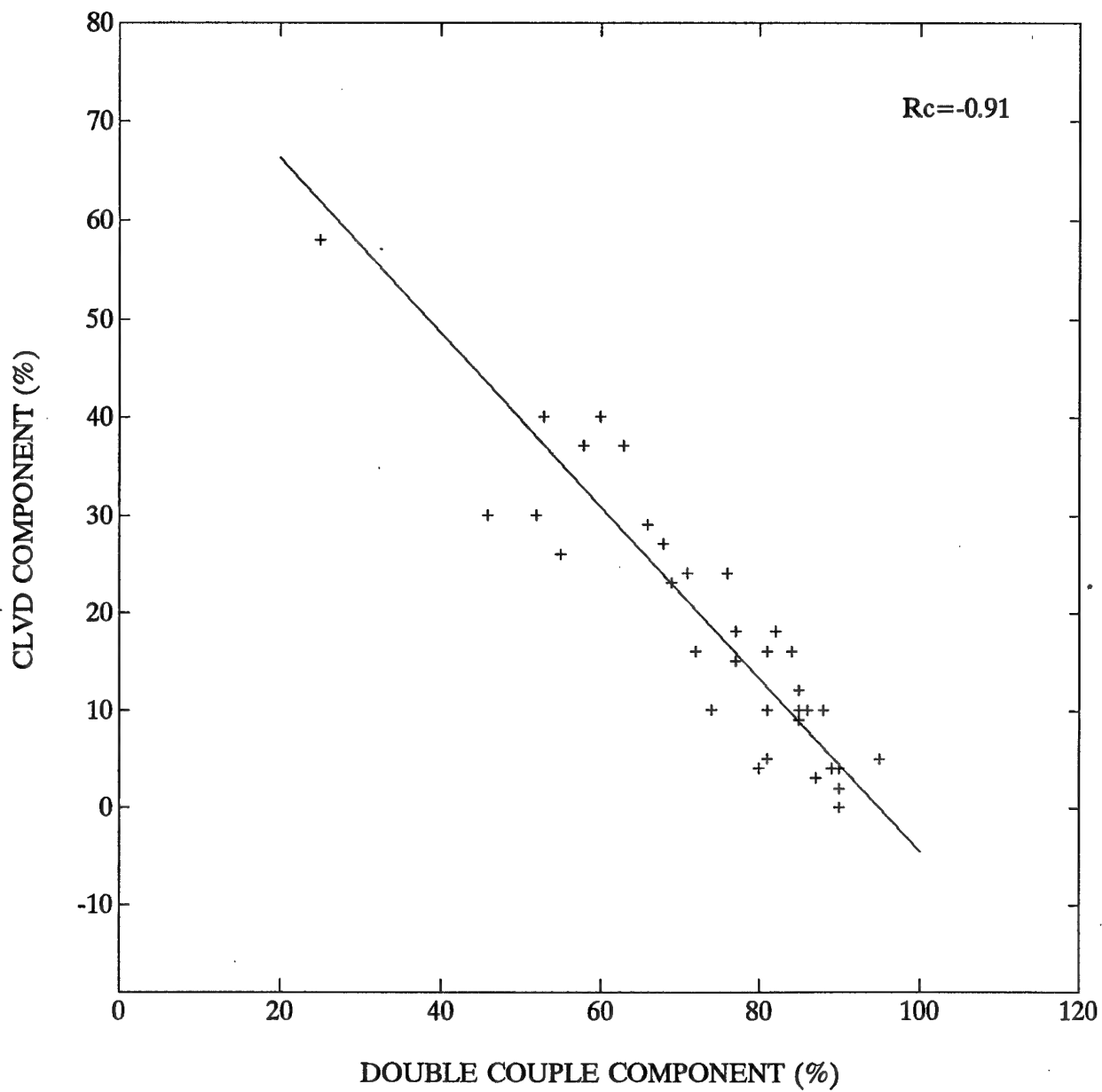


FIGURE 37. The CLVD component versus the double couple component of the general moment tensor solution for 35 seismic events from the four sequences.

solutions were obtained for another 11 events (5 from the second, 2 from the third, and 4 from the fourth sequences).

In most cases the shearing component of the source mechanism, represented by a double couple, is definitely dominant. It ranges from 60 to 90 percent of the solution for 80 percent of the events for which the general moment tensor solution was found. The isotropic component ranges from 0 to 15 percent of the solution for 83 percent of the events, and the CLVD component is the largest non-shearing component and it ranges from 0 to 40 percent of the solution in all cases but one.

The isotropic component versus the DC component is displayed in Fig. 36 and the CLVD component versus the DC component of the general solution is shown in Fig. 37. A negative correlation is observed in both presentations. The correlation coefficient in the first case is only about  $-0.5$ , but it is significant with 98 % confidence. In the second case, the correlation is rather distinct and is characterized by the correlation coefficient as high as  $-0.9$ , which is significant with more than 99 % confidence. Thus the components of the deviatoric tensor are well correlated and its non-shearing component is occasionally of considerable value, whereas the isotropic component of the general tensor appears to be small for almost all events.

### 5.3 Space distribution of P, T and B axes

The restrained double couple moment tensor solutions found for 46 events (4 for the first, 25 for the second, 9 for the third, and 8 for the fourth sequences), represented by normalized eigenvectors (length of 50 m) describing the P, T and B axes are shown on a horizontal projection in Fig. 38. The seismic events from the four sequences are marked by different symbols and the four main shocks are marked by circled points and numbered. There is no clear pattern in the distribution of the axes. The distribution seems to be rather chaotic, at least when the all three axes are presented jointly.

The horizontal distribution of each P, T and B axis is shown separately in Figs 39, 40 and 41, respectively. There is no distinct pattern in the distribution of P axes, though a tendency towards the E-W direction seems to be apparent. This tendency is more obvious in the distribution of T axes,

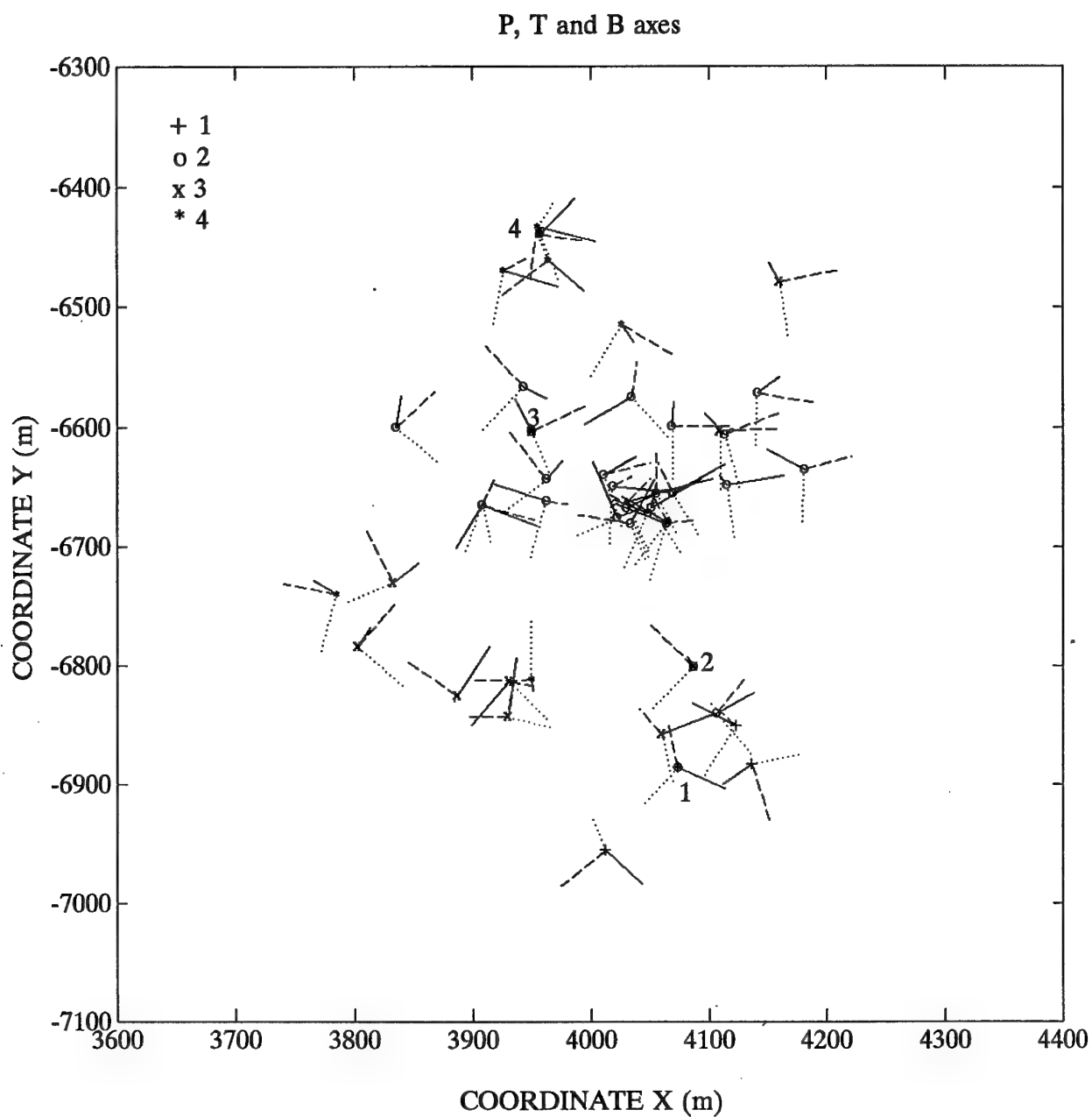


FIGURE 38. Horizontal distribution of normalized eigenvectors (length of 50 m) describing P (continuous lines), T (dashed lines) and B (dotted lines) axes from double couple moment tensor solutions obtained for 46 seismic events from the four sequences, marked by different symbols. The four main shocks are marked by circled points and numbered 1, 2, 3, 4.



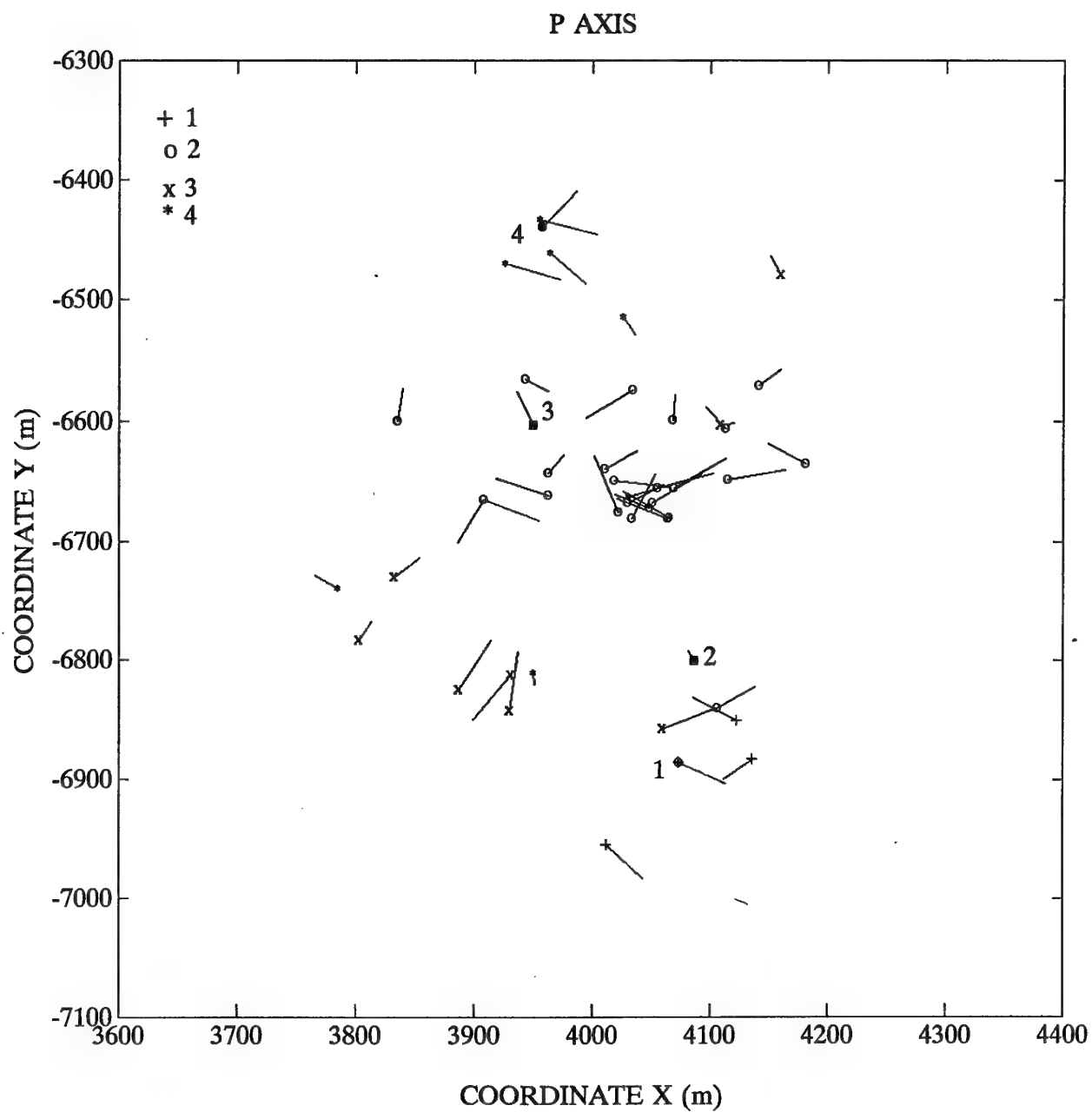


FIGURE 39. Horizontal distribution of P axes from 46 seismic events from the four sequences, marked by different symbols. The four main shocks are marked by circled points and numbered 1, 2, 3, and 4.

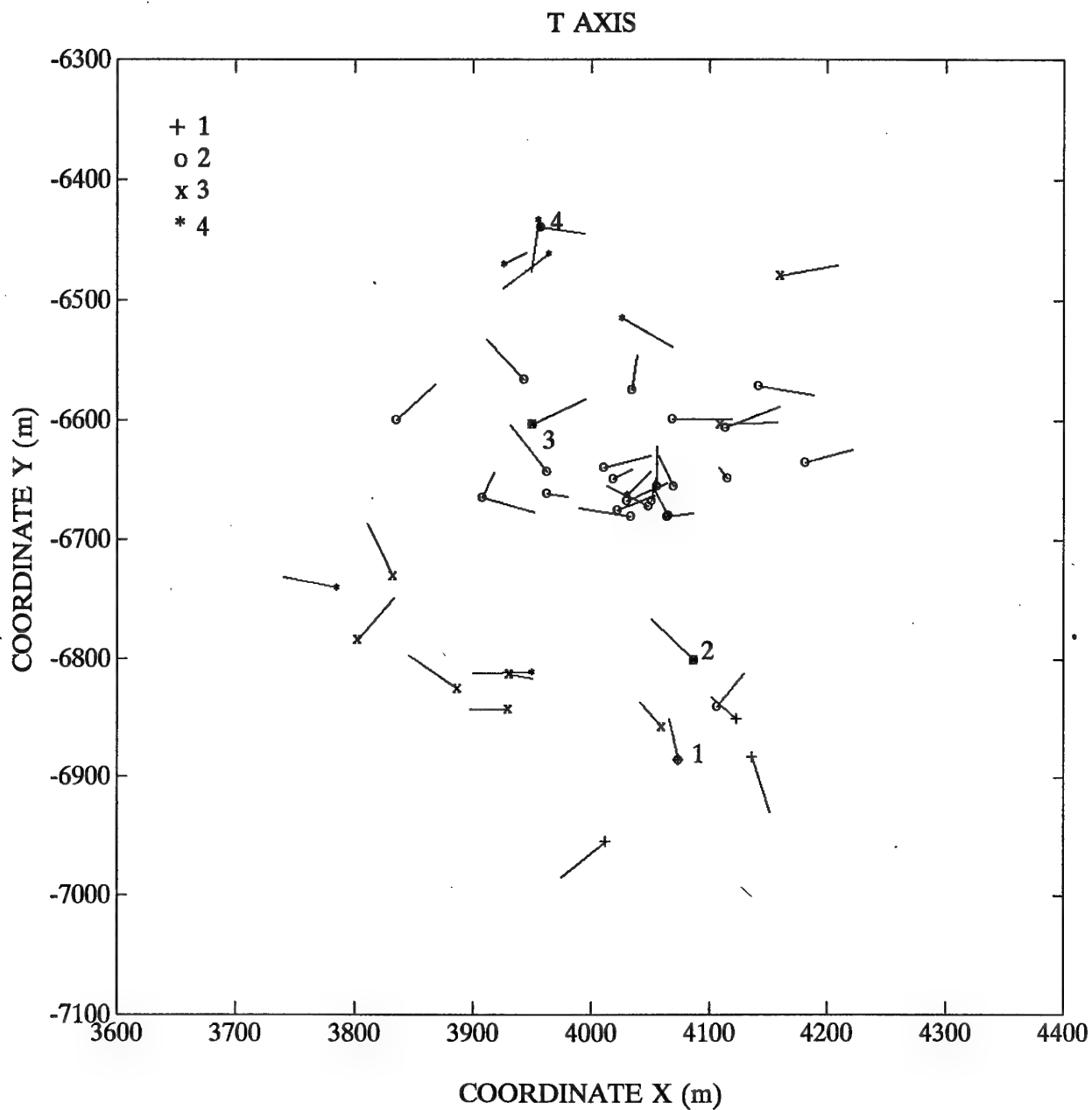


FIGURE 40. Horizontal distribution of T axes from 46 seismic events from the four sequences, marked by different symbols. The four main shocks are marked by circled points and numbered 1, 2, 3, and 4.

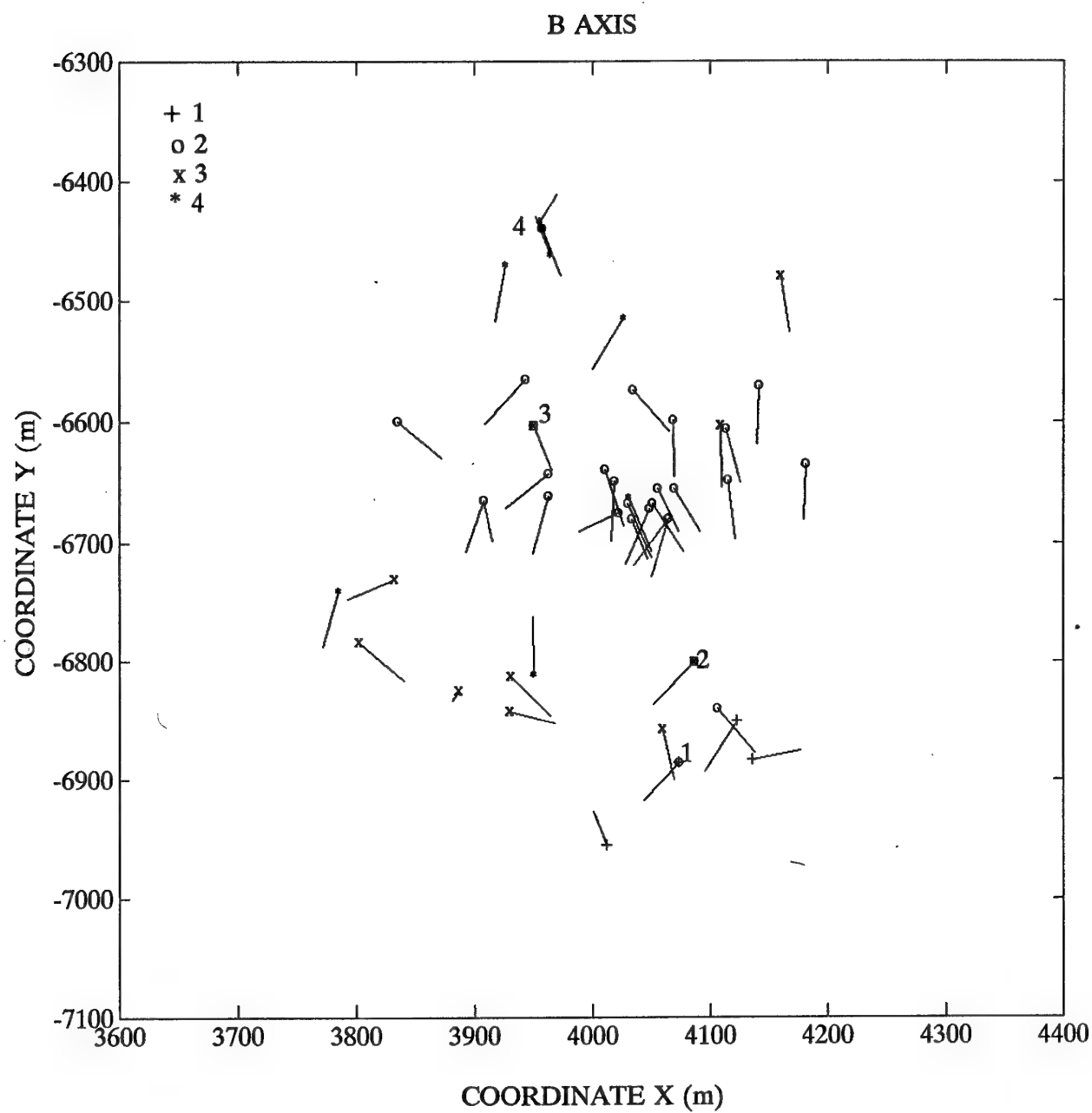


FIGURE 41. Horizontal distribution of B axes from 46 seismic events from the four sequences, marked by different symbols. The four main shocks are marked by circled points and numbered 1, 2, 3, and 4.

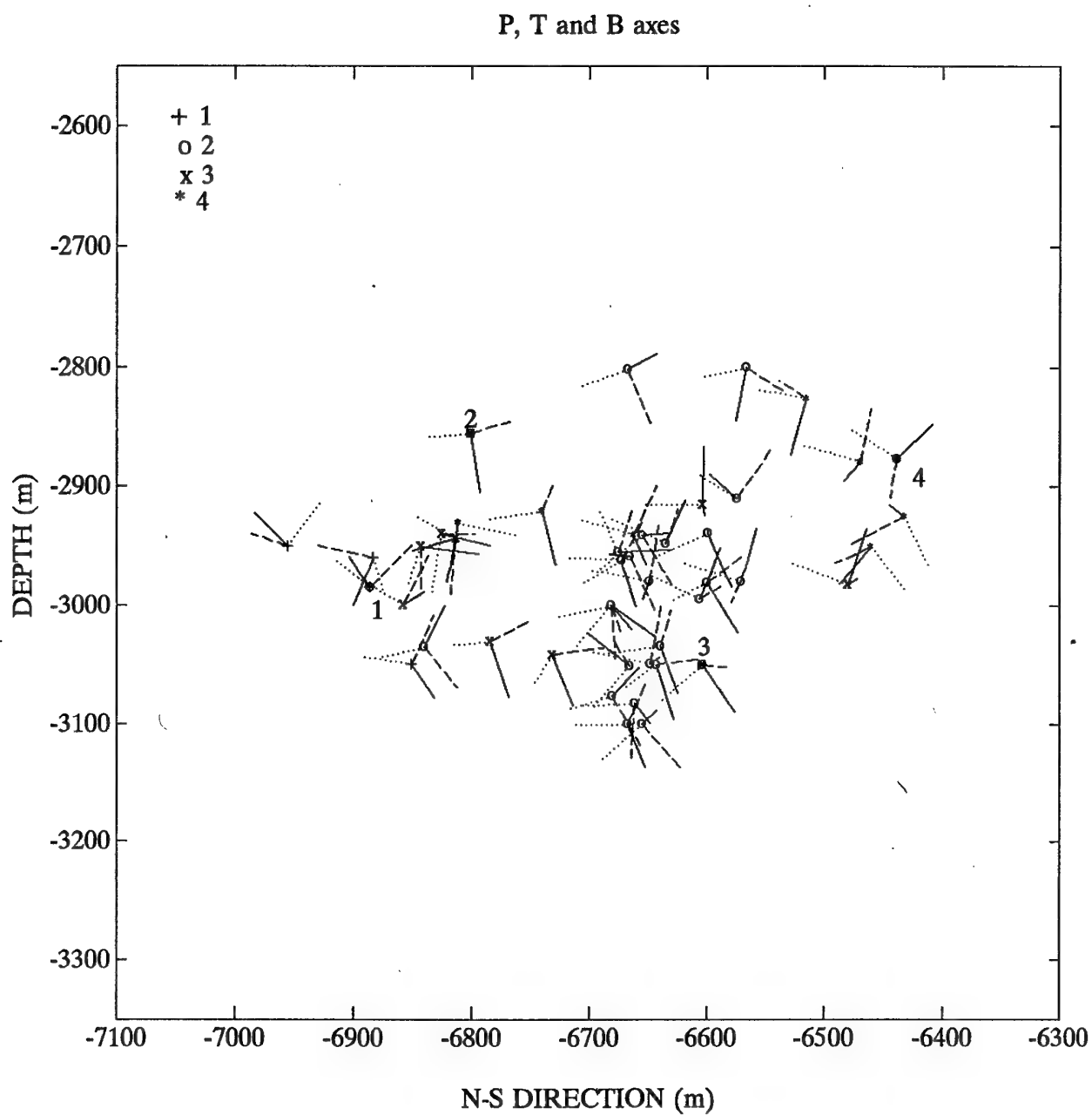


FIGURE 42. Vertical distribution along the N-S direction of P (continuous lines), T (dashed lines) and B (dotted lines) axes from 46 seismic events from the four sequences, marked by different symbols. The four main shocks are marked by circled points and numbered 1, 2, 3, and 4.

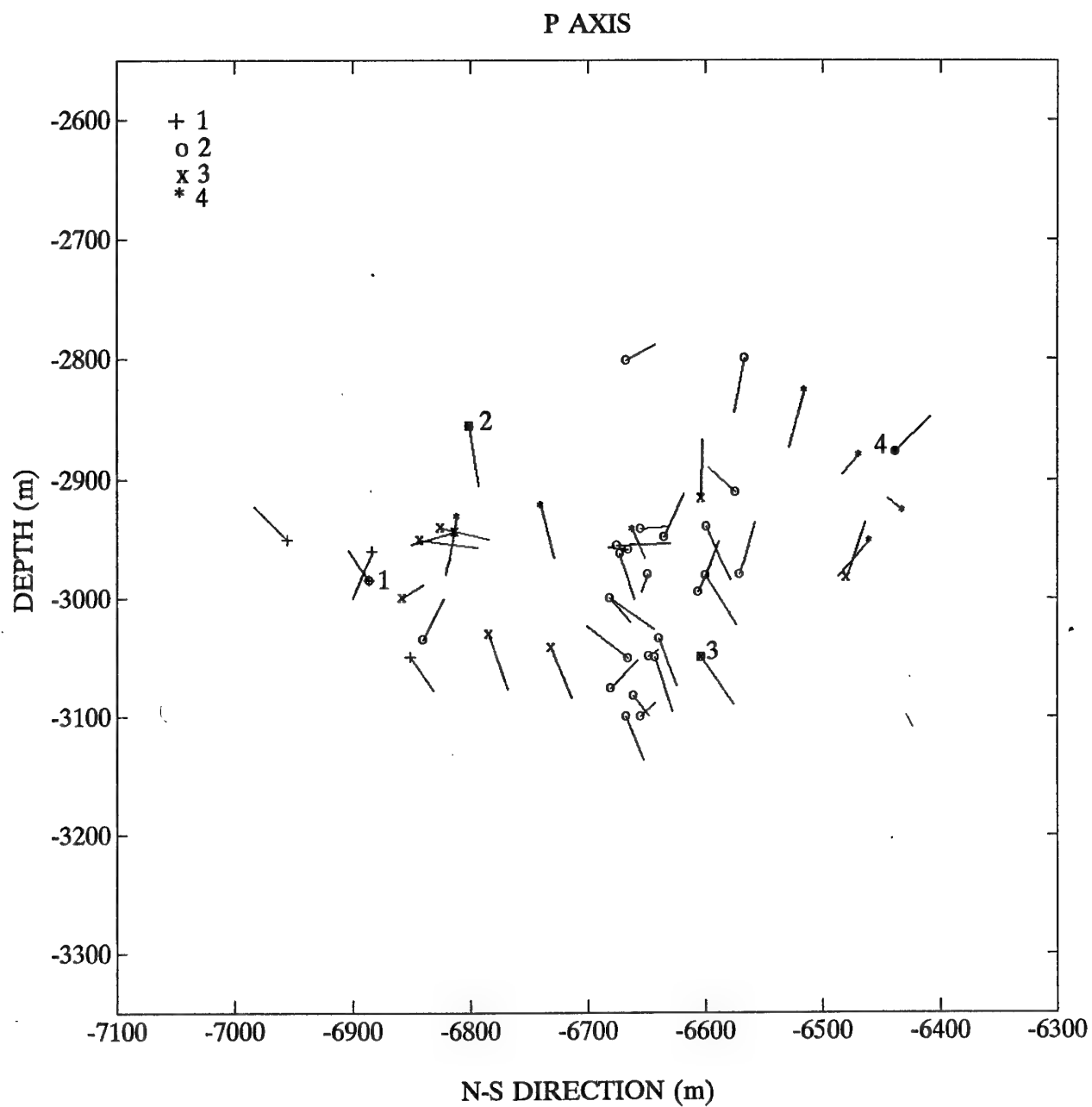


FIGURE 43. Vertical distribution along the N-S direction of P axes from 46 seismic events from the four sequences, marked by different symbols. The four main shocks are marked by circled points and numbered 1, 2, 3, and 4.

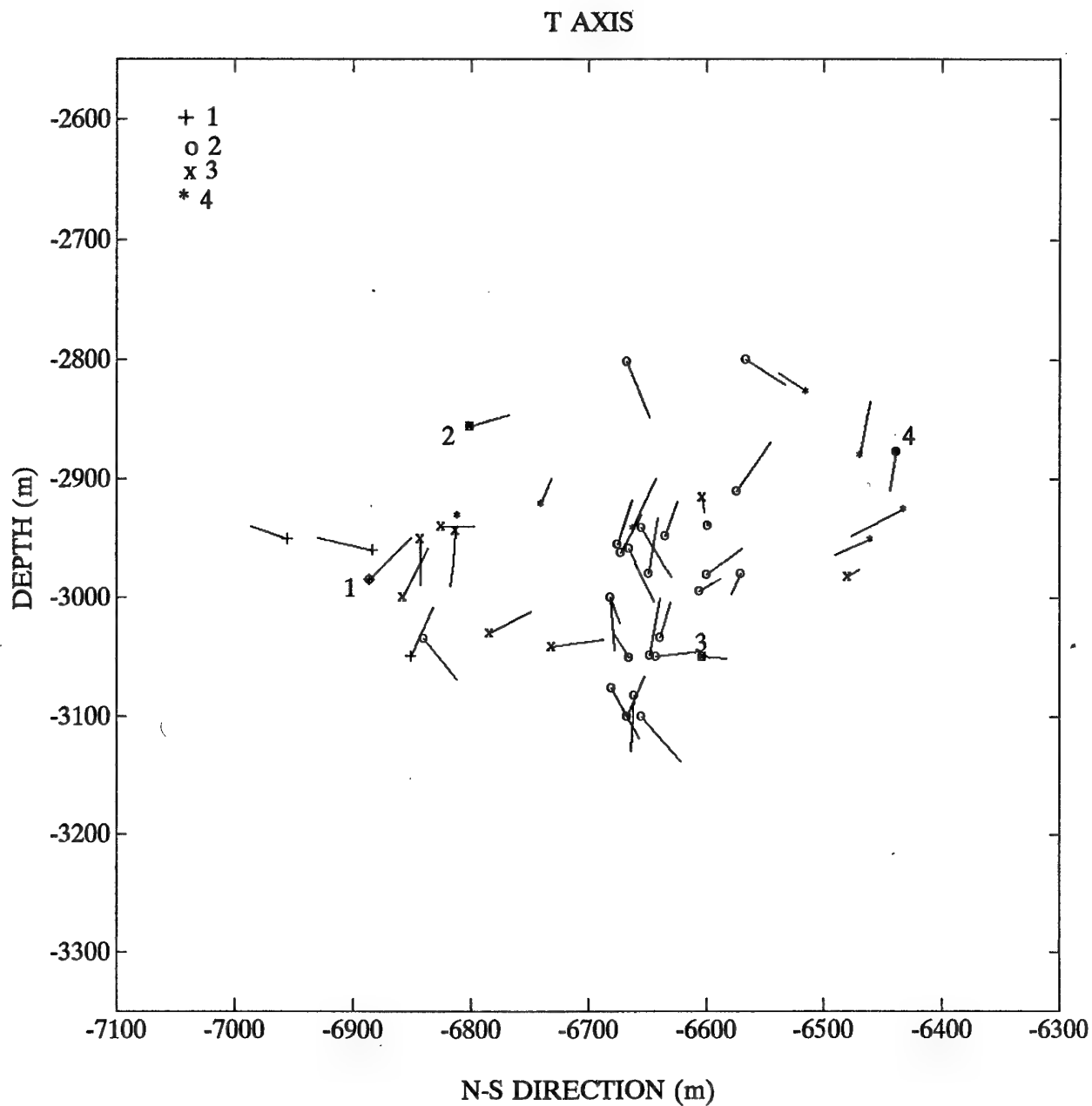


FIGURE 44. Vertical distribution along the N-S direction of T axes from 46 seismic events from the four sequences, marked by different symbols. The four main shocks are marked by circled points and numbered 1, 2, 3, and 4.

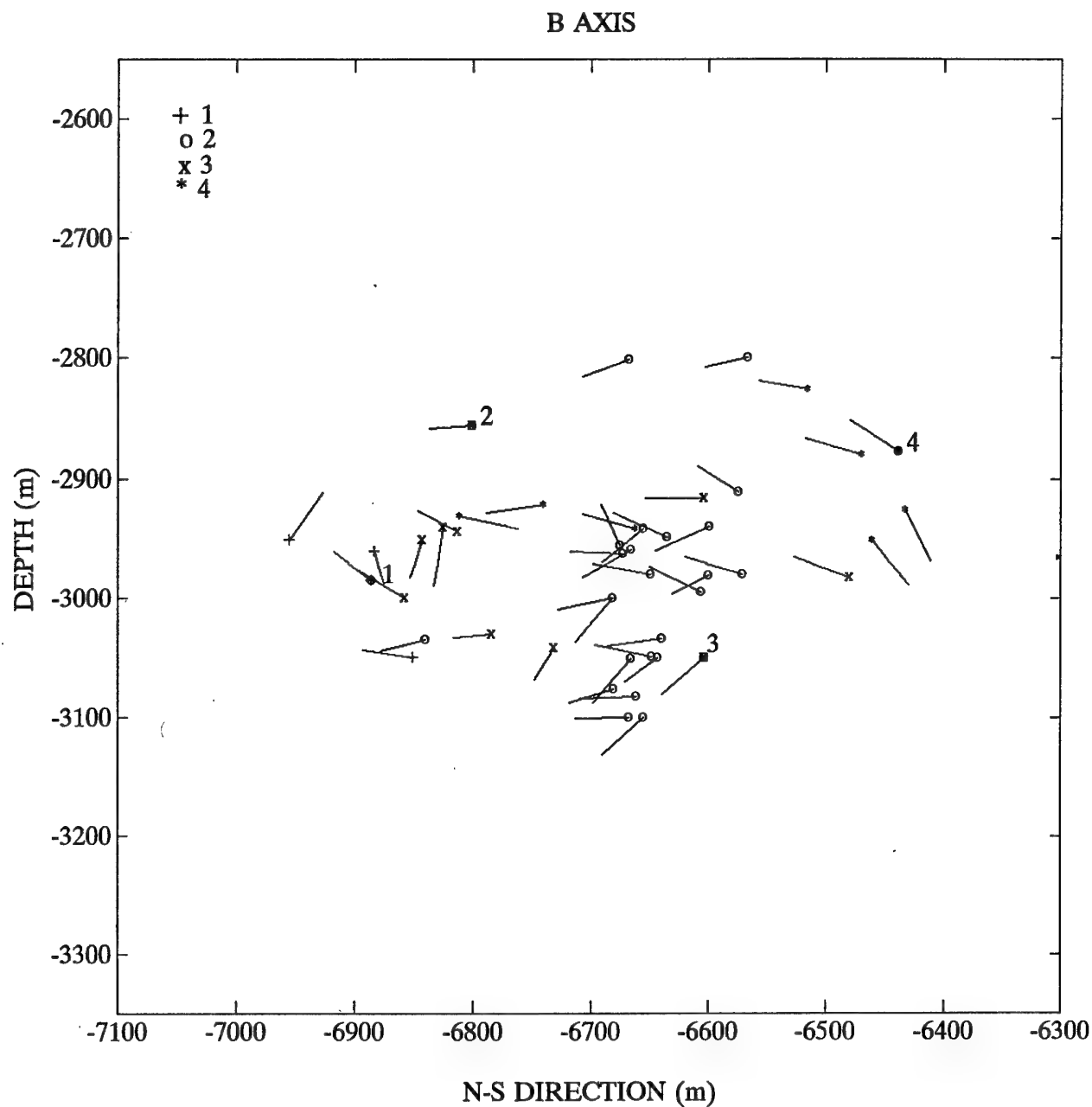


FIGURE 45. Vertical distribution along the N-S direction of B axes from 46 seismic events from the four sequences, marked by different symbols. The four main shocks are marked by circled points and numbered 1, 2, 3, and 4.

which is more regular with the dominant E-W direction. The distribution of null B axis displays the most regular pattern. Almost all B axes tend to act horizontally along the N-S direction from the north to the south, that is in the opposite direction to the movement of the four sequences from the south to the north (see Fig. 3).

The vertical distribution along the N-S direction of the all three axes is shown in Fig. 42. Once again, there is no clear pattern in their distribution displayed jointly. The vertical distribution along the N-S direction of each P, T and B axis is shown separately in Figs 43, 44 and 45, respectively. The P axes, with a few exceptions, tend to act vertically down, and the T axes tend to act vertically up, though some exceptional cases are also present. The distribution of B axes displays again the most regular pattern. Almost all B axes are distributed horizontally and are directed from the north to the south. The observed pattern is most probably connected with several pillars intersected by dykes present in the area.

#### 5.4 Time distribution of P, T and B axes

The change of the azimuth and plunge of the three axes with time is irregular. The azimuth of B, P and T axes as a function of "relative" time, that is the number of consecutive 46 seismic events, is shown in Fig. 46, where the P and T axes for the sake of clarity are separated from the B axis by 360 and 720 degrees, respectively. The beginning of the four sequences is marked by numbers on the B axis. No regular patterns are here apparent, except the dominance of the azimuth corresponding to the N-S direction for B axes and to the E-W direction for P and T axes during the whole series; the situation observed in Figs 39, 40 and 41.

The plunge of B, P and T axes against the number of consecutive seismic events is shown in Fig. 47, where the P and T axes for the sake of clarity are separated from the B axis by 180 and 360 degrees, respectively. Once again, no apparent trends are present, except those observed in Figs 43, 44 and 45, that is the dominance of the plunge corresponding to the horizontal distribution with depth of B axes and vertical distribution of P and T axes.



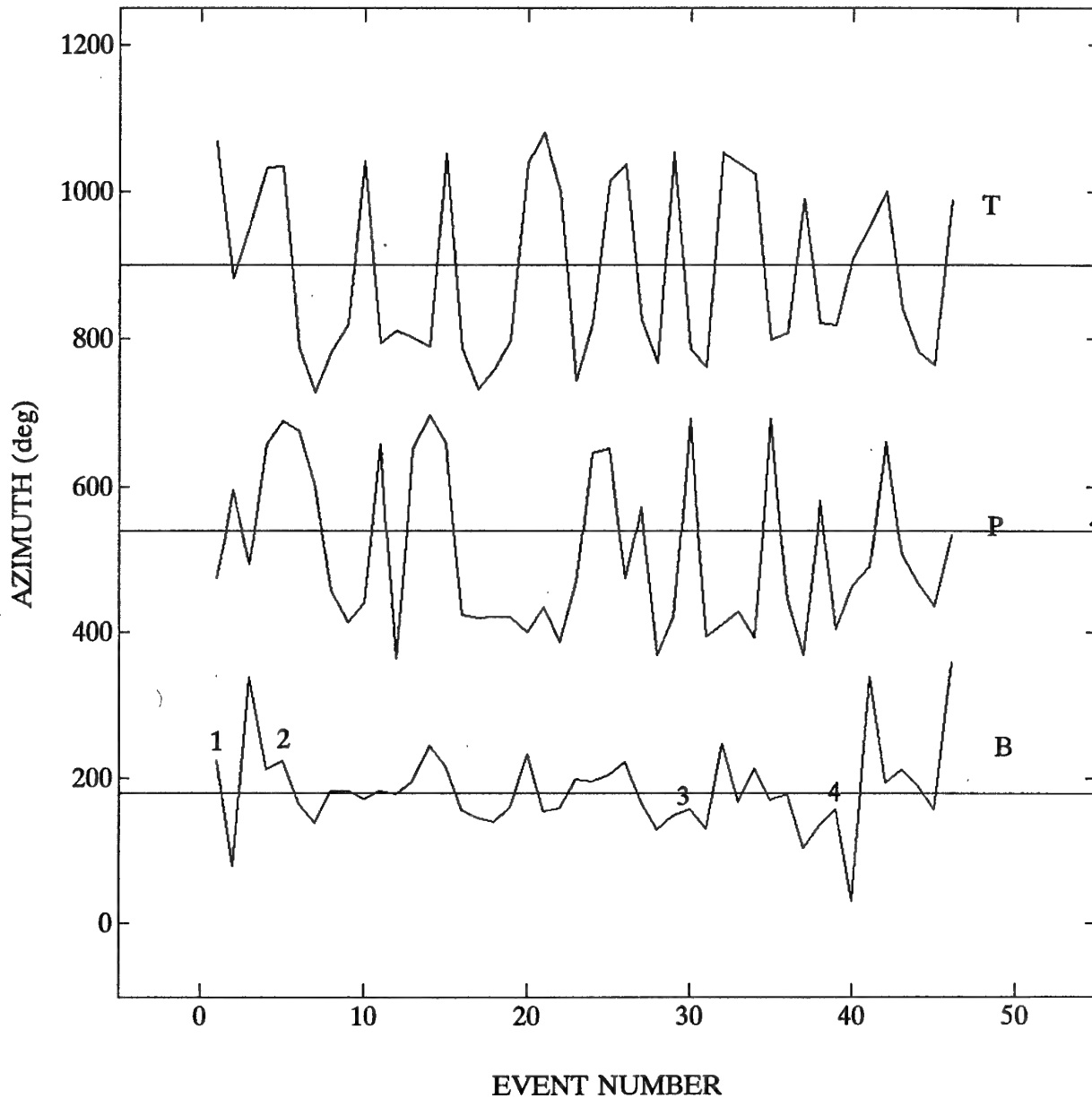


FIGURE 46. Azimuth of B, P and T axes versus the number of consecutive 46 seismic events from the four sequences. The azimuth ranges from 0 to 360 degrees. The P and T axes are separated from the B axis by 360 and 720 degrees, respectively, for the sake of clarity. The beginning of sequences is marked by numbers 1, 2, 3, and 4 on the B axis.

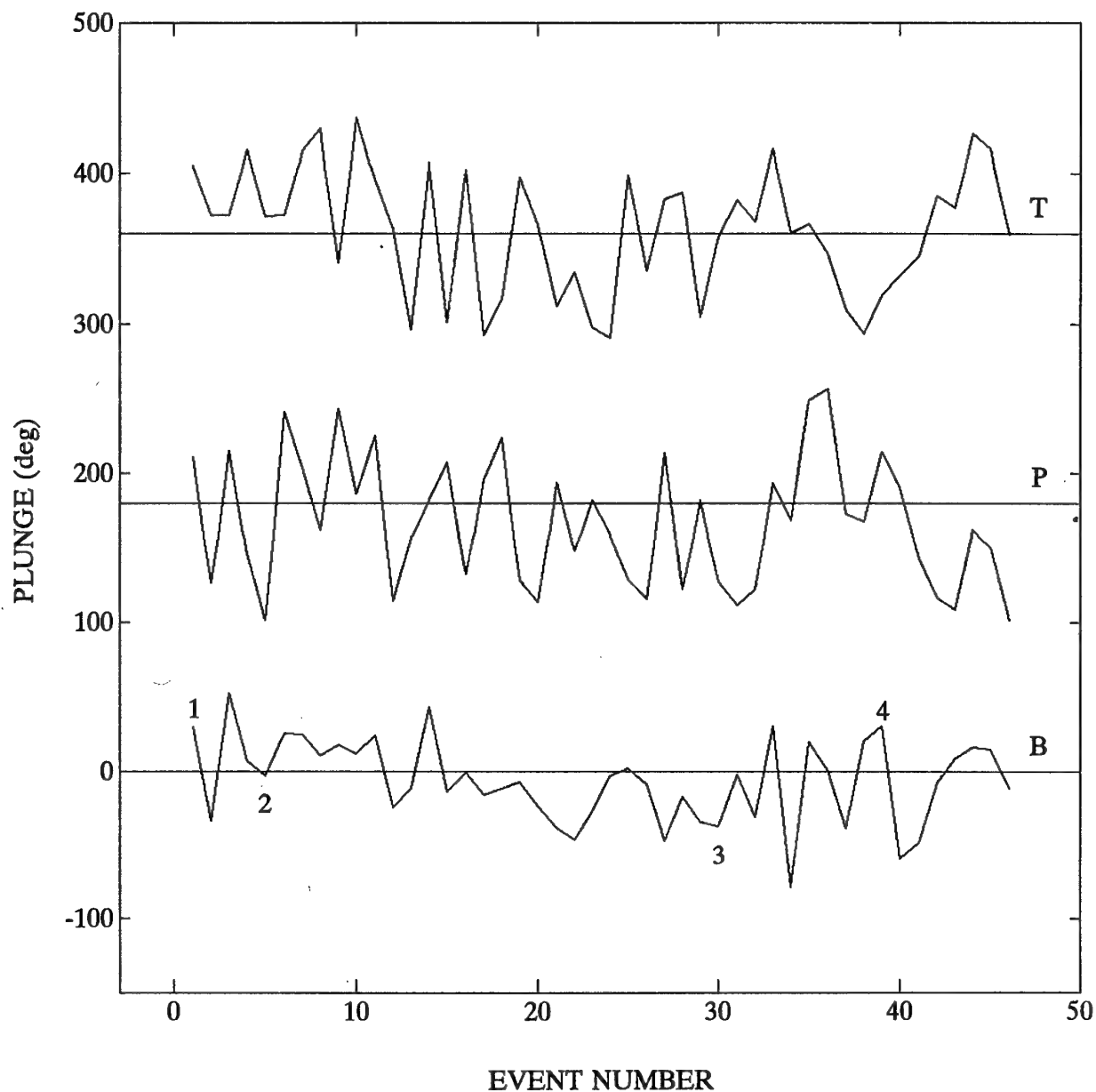


FIGURE 47. Plunge of B, P and T axes versus the number of consecutive 46 seismic events from the four sequences. The plunges ranges from -90 to +90 degrees. The P and T axes are separated from the B axis by 180 and 360 degrees, respectively, for the sake of clarity. The beginning of sequences is marked by numbers 1, 2, 3, and 4 on the B axis.

## 6. SPECTRAL AND MOMENT TENSOR SOURCE PARAMETERS

The values of scalar seismic moment calculated as the greatest eigenvalue of the double couple moment tensor solutions obtained for 46 seismic events versus the values of seismic moment calculated from the spectra of *P* and *S* waves are shown on a logarithmic scale in Fig. 48. There is an excellent agreement between the two sets of data, reflecting the high quality of three-component seismic spectra used for the inversion of moment tensor and for the calculation of source parameters.

The calculation of *P*- and *S*-wave energy, based on the energy flux and described in Section 4 (see Fig. 27), was repeated for the 46 events with known source mechanism. The average radiation coefficients were replaced by those found from the focal mechanism. The logarithm of *P*-wave energy against the logarithm of *S*-wave energy is shown in Fig. 49, where the ratio of *S*-wave over *P*-wave energy equal to 1, 10 and 100 is shown by straight lines. For over 60 % of the events the energy ratio is smaller than 10.

A comparison of the ratio of *S*-wave over *P*-wave energy with the indicators of either double couple or non-double couple components of the moment tensor solutions is highly interesting for a search of non-shearing components of the seismic source. It was found that the correlation between the logarithm of the energy ratio and the source mechanism is more distinct than that between the energy ratio and the mechanism.

The logarithm of the ratio of *S*-wave over *P*-wave energy versus the indicator of a double couple component in the general moment tensor solution for the 35 seismic events is shown in Fig. 50. The logarithm of the same ratio versus the indicator of a CLVD component is presented in Fig. 51, and the energy ratio versus the indicator of a volumetric component is shown in Fig. 52. The scattering of data is considerable and the correlation coefficient in the first case is 0.56 which is significant with 99 % confidence, in the second case it is -0.41 which is significant with 95 % confidence, and in the third case it is -0.47 which is significant with 95 %

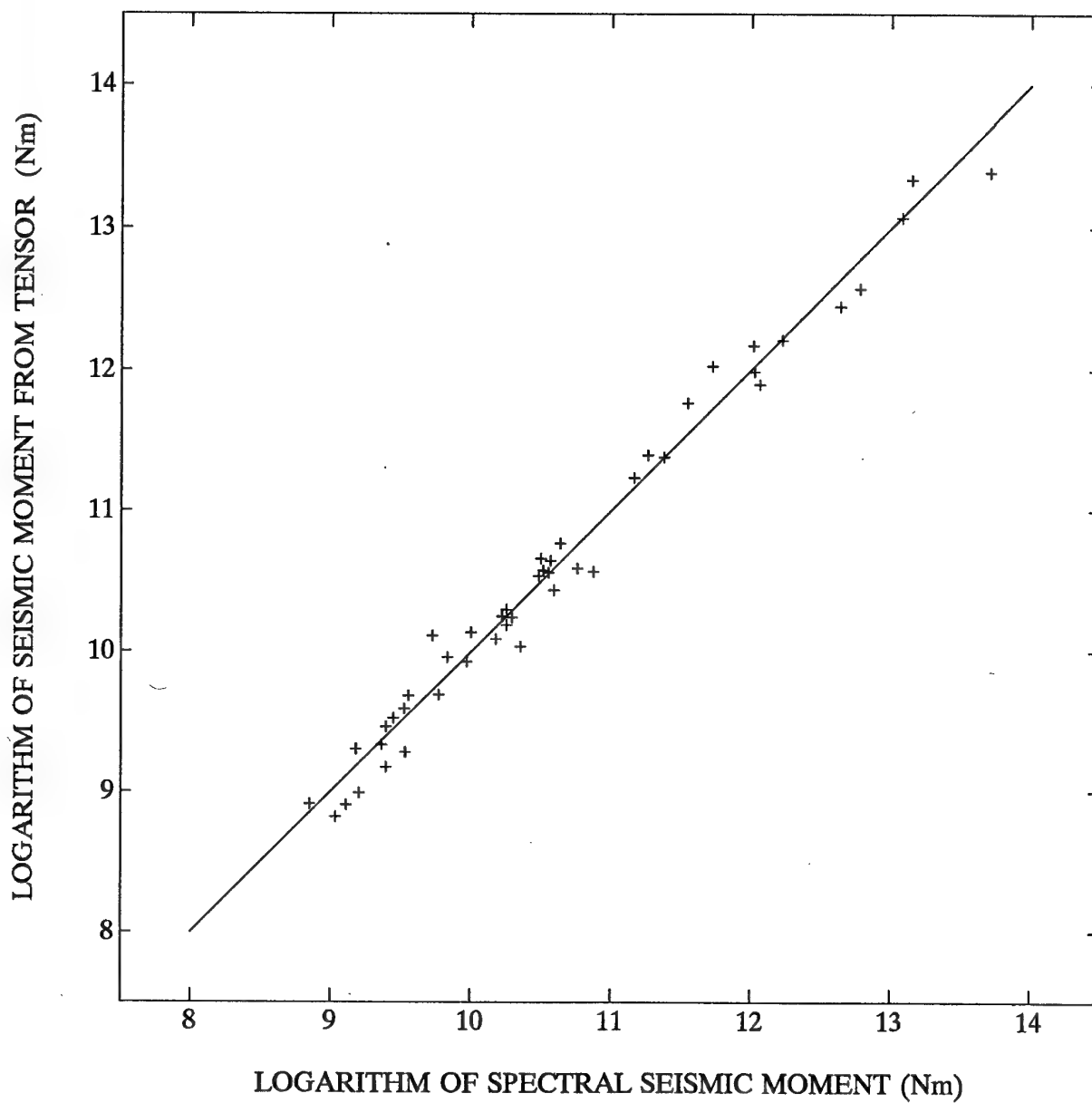


FIGURE 48. Logarithm of seismic moment estimated from the momet tensor inversion versus that estimated from the spectra for 46 seismic events for which source mechanizm is determined. The straigh line corresponds to the same values of both estimates.

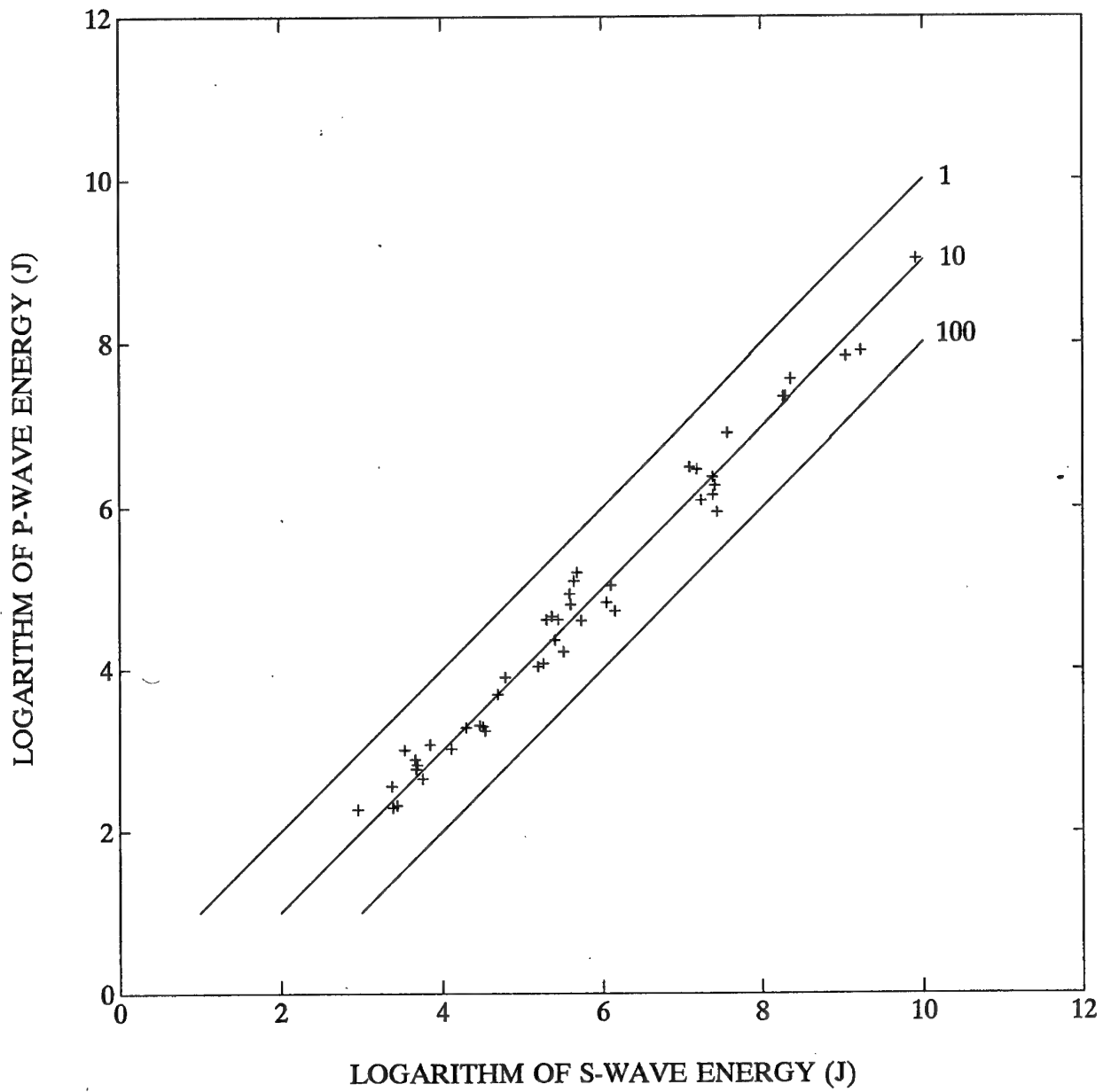


FIGURE 49. Logarithm of *P*-wave energy versus logarithm of *S*-wave energy for 46 seismic events for which source mechanism is determined. The ratio of *S*-wave energy over *P*-wave energy equal to 1, 10, and 100 is shown by straight lines.

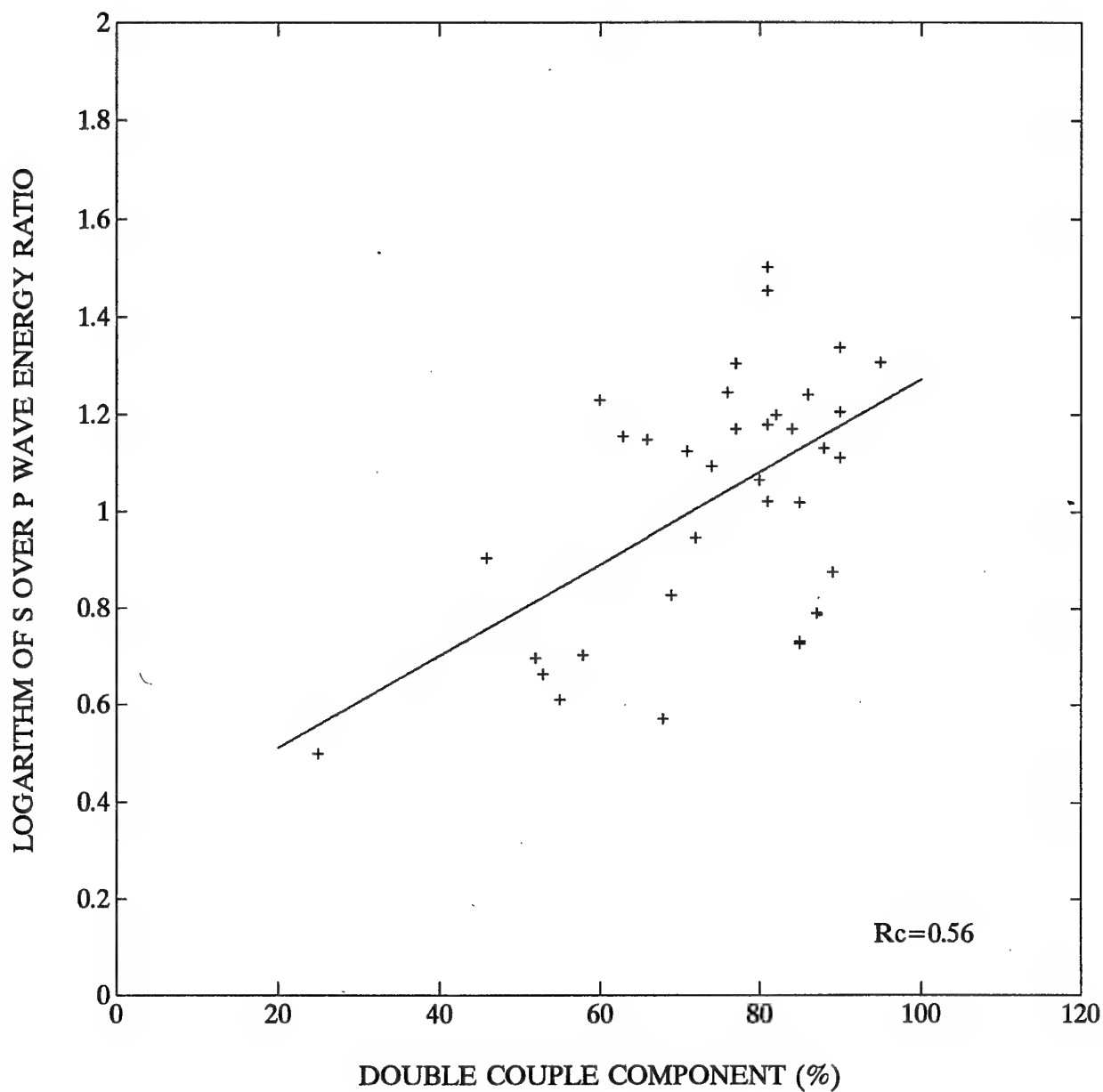


FIGURE 50. Logarithm of the ratio of S-wave over P-wave energy versus the double couple component of the general moment tensor solution for 35 seismic events from the four sequences.

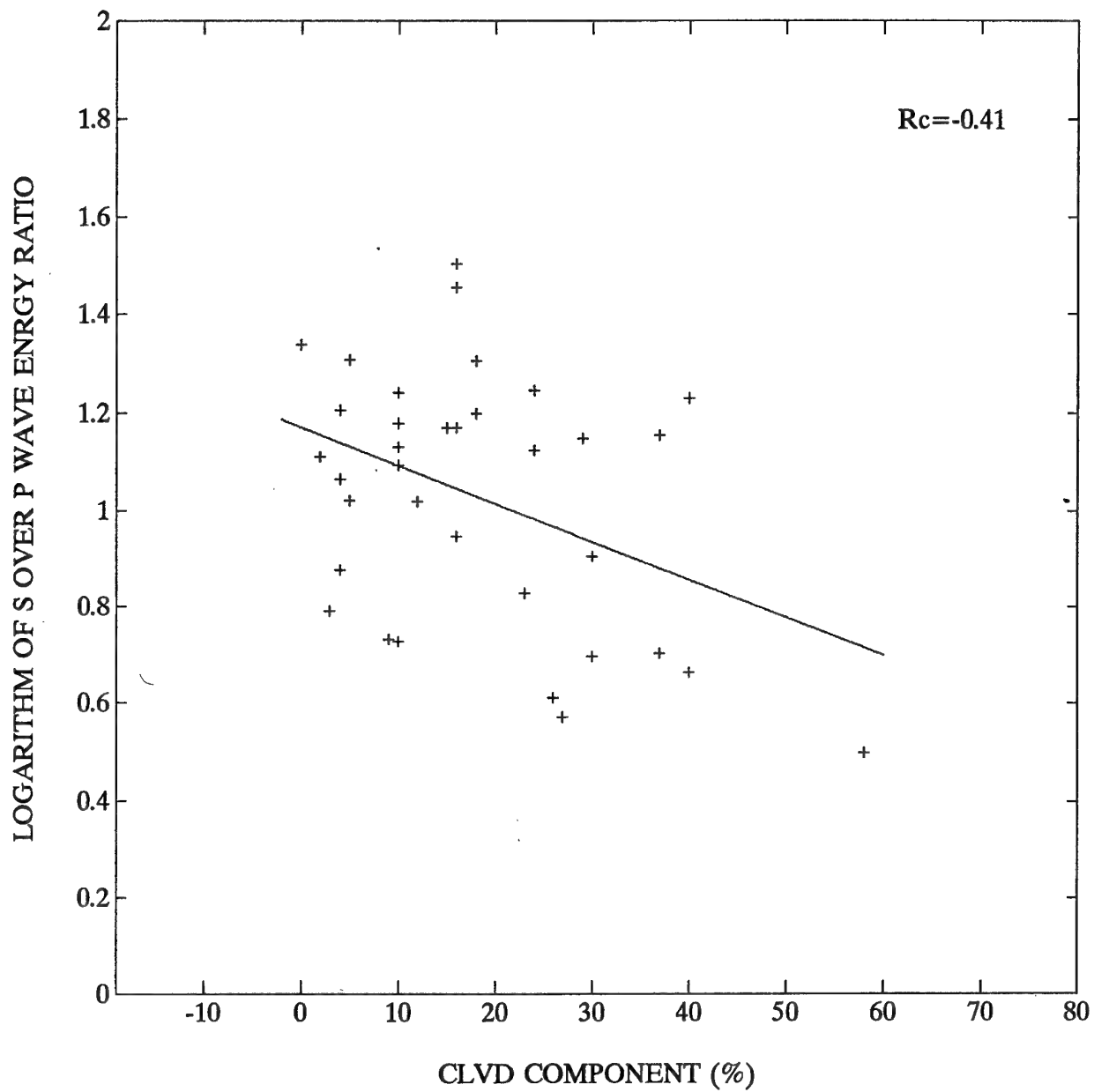


FIGURE 51. Logarithm of the ratio of S-wave over P-wave energy versus the CLVD component of the general moment tensor solution for 35 seismic events from the four sequences.

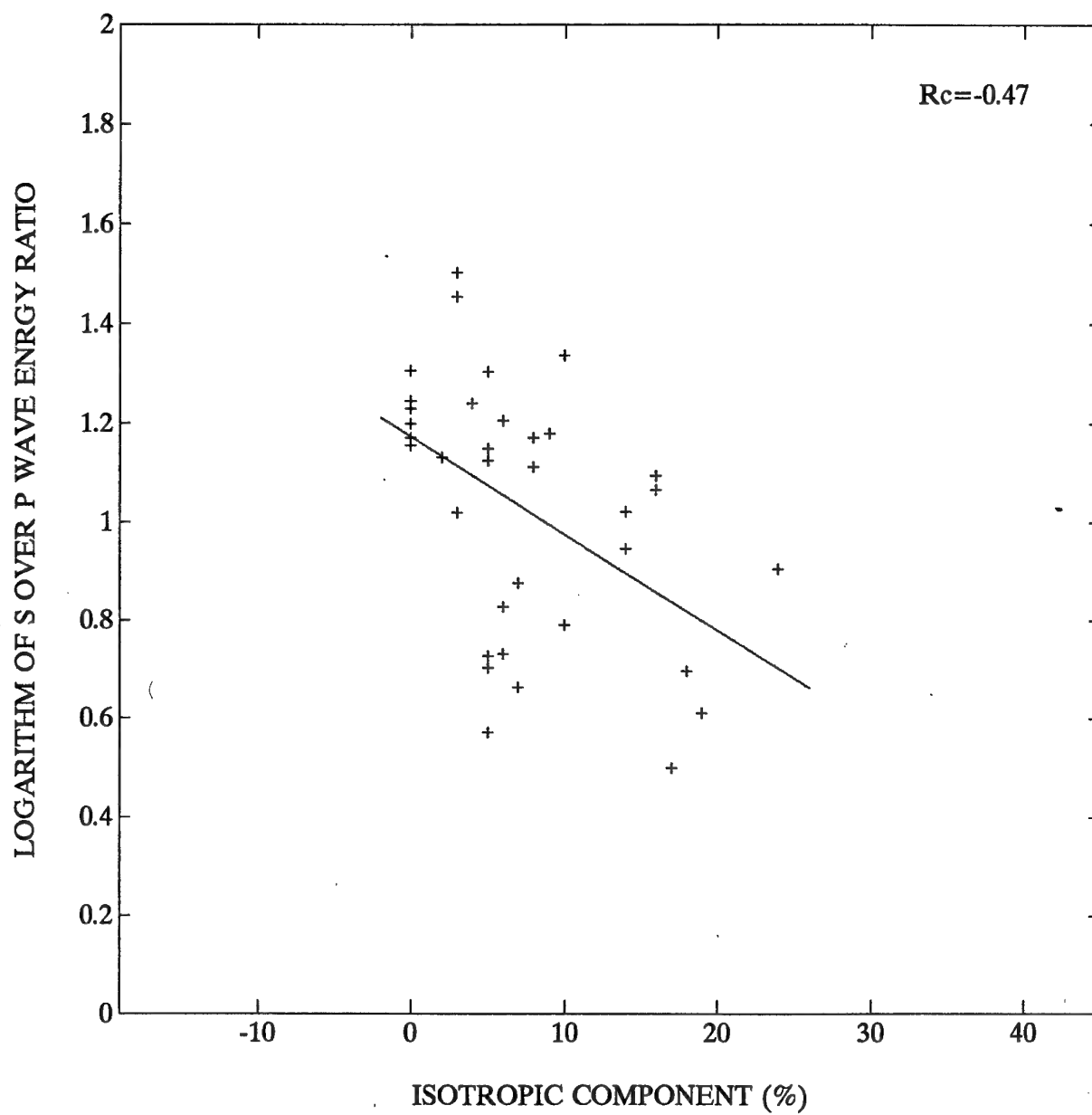


FIGURE 52. Logarithm of the ratio of *S*-wave over *P*-wave energy versus the isotropic component of the general moment tensor solution for 35 seismic events from the four sequences.



confidence. Although these values indicate that the relations between the ratio of *S*- over *P*-wave energy and the indicators of shearing and non-shearing components of the moment tensor are not as straightforward as it could be expected, the general tendency points into right direction. On the average, the high values of the *S*- over *P*-wave energy ratio are associated with seismic sources with dominant double couple components and its low values are associated with the sources characterized by large non-shearing components.

## 7. CONCLUSIONS

The objective of this research has been to investigate possible time variations of source parameters and source mechanism of seismic events forming sequences at a South African gold mine. To accomplish this objective we selected Western Deep Levels gold mine, situated in the Carletonville mining district, where the Integrated Seismic System is in operation with 22 three-component underground stations. On April 7, 1993, an interesting swarm-like sequence of seismic events occurred at a depth of 3 km. We selected this sequence for our study and collected and analyzed the available data.

The sequence lasted 12 days and was composed in fact of four main shock-aftershock sequences, following closely each other in space and time. Altogether 199 seismic events were recorded and located with moment magnitudes ranging from -0.5 to 3.1. The events were confined to a volume of rock extending to 630 m in the E-W direction, 670 m in the N-S direction, and 390 m in the vertical direction. The first sequence occurred at the southern edge of the rock volume, the second and third sequences occurred in the middle, and the main shock of the fourth sequence occurred at the northern edge of the volume, while their aftershocks moved back to the south.

The first sequence lasted 179 hours and had time for full development. The second sequence lasted only 13 hours and had no time for full development as it was followed immediately by the third sequence which lasted 33 hours and was in turn interrupted by the fourth sequence lasting 58 hours. The parameter  $p$ , describing the rate of occurrence of aftershocks with time, ranged from 0.7 for the second sequence to 1 for the first sequence. The parameter  $b$ , characterizing the frequency-magnitude relation, has the value of 0.6 for the whole series. The fractal dimension  $D$  for the four sequences is significantly different. The first sequence is characterized by the lowest value of  $D=1.75$  and the second sequence by the highest value of  $D=2.4$ . The third and fourth sequences are characterized by the middle value of  $D=1.9$ . The seismic events forming the first sequence are therefore the most strongly

correlated, whereas the events from the second sequence had no time for stronger correlation with advancing fracturing.

The corner frequencies of *P* and *S* waves are remarkably close to each other and they range from 14 to 220 Hz. The corresponding source radius ranges from 6 to 85 m. The Brune stress drop, ranging from 0.1 to 34 MPa, appears to be dependent on the seismic moment, but the small events are dominant and their source parameters are much stronger correlated than those from larger events. The seismic energy ranges from  $6.6 \cdot 10^1$  to  $9.4 \cdot 10^9$  J and the ratio of *S*-wave over *P*-wave energy ranges from 1 to 30. For about three quarters of events the energy ratio is less than 10, implying that tensile failures, or at least shear failures with tensile components, were responsible for generation of considered events. The energy ratio correlates also with stress drop and apparent stress. Large stress release corresponds to high values of the ratio of *S*- over *P*-wave energy.

An analysis of source parameters as a function of time shows that the four main shocks are most distinctly marked by their source radius rather than by their seismic moment or seismic energy. Their source radius ranges from 50 to 85 m, while the source radius of aftershocks is smaller than 30 m. The second sequence is characterized by a number of large events in terms of their seismic moment and energy, not much smaller than the main shock. There are a few large events in the third sequence, whereas the fourth sequence displays a regular main shock - aftershock pattern similar to that characterizing the first sequence.

Out of 199 seismic events forming the four sequences, full moment tensor solutions were found for 36 events and constrained double couple solutions were obtained for another 11 events. In most cases the shearing component of the source mechanism is dominant. It ranges from 60 to 90 percent of the solution for 80 percent of the events for which the general moment tensor solution was found. The isotropic component ranges from 0 to 15 percent of the solution for 83 percent of the events, and the CLVD component ranges from 0 to 40 percent of the solution. A negative correlation between the isotropic and double couple components and between the CLVD and double couple components is observed. The correlation coefficient in the first case is -0.5 but it is significant with 98 % confidence, and the correlation coefficient in the second case is as high as -0.9.

An analysis of space distribution of P, T and B axes from the restrained double couple moment tensor solutions, found for 46 events, shows that the distribution of B axis is the most regular. Almost all B axes tend to act horizontally from the north to the south, in the opposite direction to the movement of the four sequences. The P axes tend to act vertically down along the E-W direction and the T axes tend to act vertically up along the same direction, though their pattern is not as regular as that of B axes. The observed pattern is most probably associated with several pillars intersected by dykes present in the area. The change of the azimuth and plunge of the three axes with time is not regular.

The correlation coefficient between the logarithm of the ratio of S- over P-wave energy and the indicator of a double couple component in the general moment tensor solution is only 0.56 but it is significant with 99 % confidence. The correlation coefficient between the energy ratio and the indicator of a CLVD component is -0.41 which is significant with 95 % confidence, and the correlation coefficient between the ratio and the indicator of a volumetric component is -0.47 which is significant with 95 % confidence. Thus the relations between the ratio of S- over P-wave energy and the shearing and non-shearing components of the moment tensor tend to point into right direction. On the average, the high values of the energy ratio are associated with seismic sources with dominant double couple components and its low values are associated with the sources characterized by large non-shearing components.

## PART II: POLKOWICE COPPER MINE IN POLAND

### 1. INTRODUCTION

In contrast to South African gold mines, seismic sequences are seldom observed in Polish copper mines. The 1977 seismic event of magnitude 4.5, which occurred at the Lubin copper mine and was followed by a regular aftershock sequence (Gibowicz *et al.*, 1979), is an exception. The 1987 event of magnitude 4.3, which occurred at the same mine, was followed by a few small aftershocks and the level of seismicity after the event was lower than that during a few months preceding the event (Gibowicz *et al.*, 1989). Here is a major difference between seismic events induced by mining at some mining districts and natural shallow earthquakes always followed by aftershocks.

Polkowice copper mine, selected for our study, is situated in the Lubin copper mining district between Lubin and Rudna mines. Its underground digital seismic network is of good quality and we have ready access to the seismic records. Two mining sections G-32 and G-21 were selected, characterized by the highest level of seismicity in the mine and situated in different geological environments. Altogether 34 well recorded seismic events from section G-32 were selected. They occurred between May 1994 and May 1995 and their moment magnitude is from 1.2 to 2.7. The number of selected events from section G-21 is 56, with moment magnitude ranging from 1.2 to 3.0. They occurred between October 1994 and May 1995.

The search for regular seismic sequences at Polkowice mine, in a sense of notion used in earthquake seismology, was not successful. The selected seismic events, on the other hand, form close clusters in a sense that they occurred in small well defined areas, with the horizontal extension of about 600 m (Fig. 1), and within a defined time interval. They can be considered therefore as a series of closely related seismic events, reflecting current mining activity in sections G-32 and G-21 of the mine.

Spectral analysis of seismic waves and moment tensor inversion techniques are used to study the source parameters and source mechanism of selected seismic events. The spectral analysis provides the source parameters, such as seismic moment, seismic energy, source radius, stress drop, and apparent stress, to characterize individual events forming the series. The moment tensor inversion provides the source mechanism in the most general form. A moment tensor will be decomposed into an isotropic part corresponding to a volumetric change in the source, a compensated linear vectot dipole describing a sort of uniaxial compression or tension, and a double couplke corresponding to a shear failure. The main objective of this study is to investigate possible time variations of the source parameters and source mechanism during the series.

## 2. GEOLOGICAL STRUCTURE AND TECTONICS

The Lubin copper district is located in southwestern Poland within the Fore-Sudetic Monocline, which is part of a larger geological unit - the Fore-Sudetic Zone striking NW-SE. The Monocline forms an area morphologically subdued against the other part of the Zone - the Fore-Sudetic Block composed of crystalline rocks mainly of the Proterozoic age. The Fore-Sudetic Zone contains Permian and Triassic deposits overlying a crystalline basement and dipping gently towards NE at angles of 2 - 7 degrees. These deposits are separated from the basement by a stratigraphic break with angle and erosion disconformity. The Monocline is separated from the Fore-Sudetic Block by a wide zone of deep tectonic fractures - the dislocation system of the Odra River.

The copper ore area is located on the border of the Monocline, on the edge of the Odra River deep fracture zone. The area is composed of the Rotliegendes deposits overlying a crystalline basement, characterized by low values of the strength parameters. They are overlaid by the Zechstein deposits of considerable strength. Carbonate deposits, composing the floor of this rigid complex, also form the roof of mining works, and their lithological and structural features are of basic importance for mining operations, especially for the closing of excavated areas by the roof-fall technique. The carbonate deposits are able to accumulate large strains and then to release them suddenly. They are therefore easily susceptible to rockbursts.

The mined seam is composed from the top of dolomitic carbonates and marly dolomites, dolomitic schists, tarry slates and sandstones. The seam floor is composed of quartz fine-grained sandstones with carbonate cement changing gradually into argillaceous cement. The strength of top sandstone layers is only slightly lower than that of carbonate rocks. It decreases distinctly with depth as a result of changing cement.

The properties of rock mass reflect to a great degree upon tectonic deformations. The prevailing direction NW-SE of faults and fractures in the

area (parallel to the Odra River deep fracture zone) is one of the most important factors for mining operations, their techniques and direction of works. Normal faults of NW-SE direction and inverse faults of E-W direction played a dominant role in the formation of the geological structure of the copper ore area of the Fore-Sudetic Monocline (e. g., Salski, 1977).

The complex geological and tectonic pattern of the Fore-Sudetic Zone justifies the existence of natural low seismicity in the area. Unfortunately, macroseismic data from historical records are incomplete and sporadic. Nevertheless, from the catalogue of earthquakes in Poland from the year 1000 to 1970 (Pagaczewski, 1972) it follows that Sudeten and Fore-Sudetic Zone are, beside the Carpathians, the most seismic regions in Poland, where the highest observed intensities were within a range of 7 - 8 degrees of the MCS macroseismic scale. Even a sporadic occurrence of larger earthquakes in the Fore-Sudetic Zone implies that a natural tectonic component of the existing stress field should not be disregarded when seismicity induced by mining works is considered.



### 3. SEISMIC NETWORK AND DATA

Polkowice copper mine has a local digital seismic network composed of 24 stations located underground at a depth from 460 to 930 m below the surface and a single station at the surface. Three stations are composed of three-component sensors and 22 stations have single vertical sensors. Their horizontal distribution is shown in Fig. 1, where the single-component stations are marked by triangles and three-component stations are marked by squares. The seismic stations are numbered from 1 to 26 (there is no station number 12). The surface station, numbered 18, was dismantled in December 1994 and the station numbered 23 was moved to a new location in February 1995. Stations 2 and 26 have the same horizontal coordinates, but the single component station 2 is located 60 m below the three component station 26.

The digital network works under a system called ELOGOR C, manufactured in Lubin. Willmore seismometers MK-II and MK-III are used. The signal is transmitted to the central station in analog form with FM modulation by standard cables used in mining but independent from the telecommunication lines at the mine. The seismic signals are digitized at the central station; a 14-bit converter is used. The frequency band is from 0.5 to 150 Hz and the system dynamics is about 70 dB. The sampling frequency is 500 Hz. Digital registration on-line of seismic signals and data processing are based on IBM PC-486 computers. The system works in a triggering mode. The recorded data are written to files on a hard disk of the computer. The preliminary analysis of records contains location of the event, its energy estimate and determination of the first motion of *P*-wave arrivals at various stations.

For the purpose of this study, two mining sections were selected. Section G-32 is located near the center and section G-21 is situated in the southeastern part of the mine. The selected period of observation was from May 1994 to the end of May 1995 in section G-32 and from October 1994 to the end of May 1995 in section G-21. Seismic records of events with energy greater than  $10^3$  J were collected, excluding the events triggered by blasting.

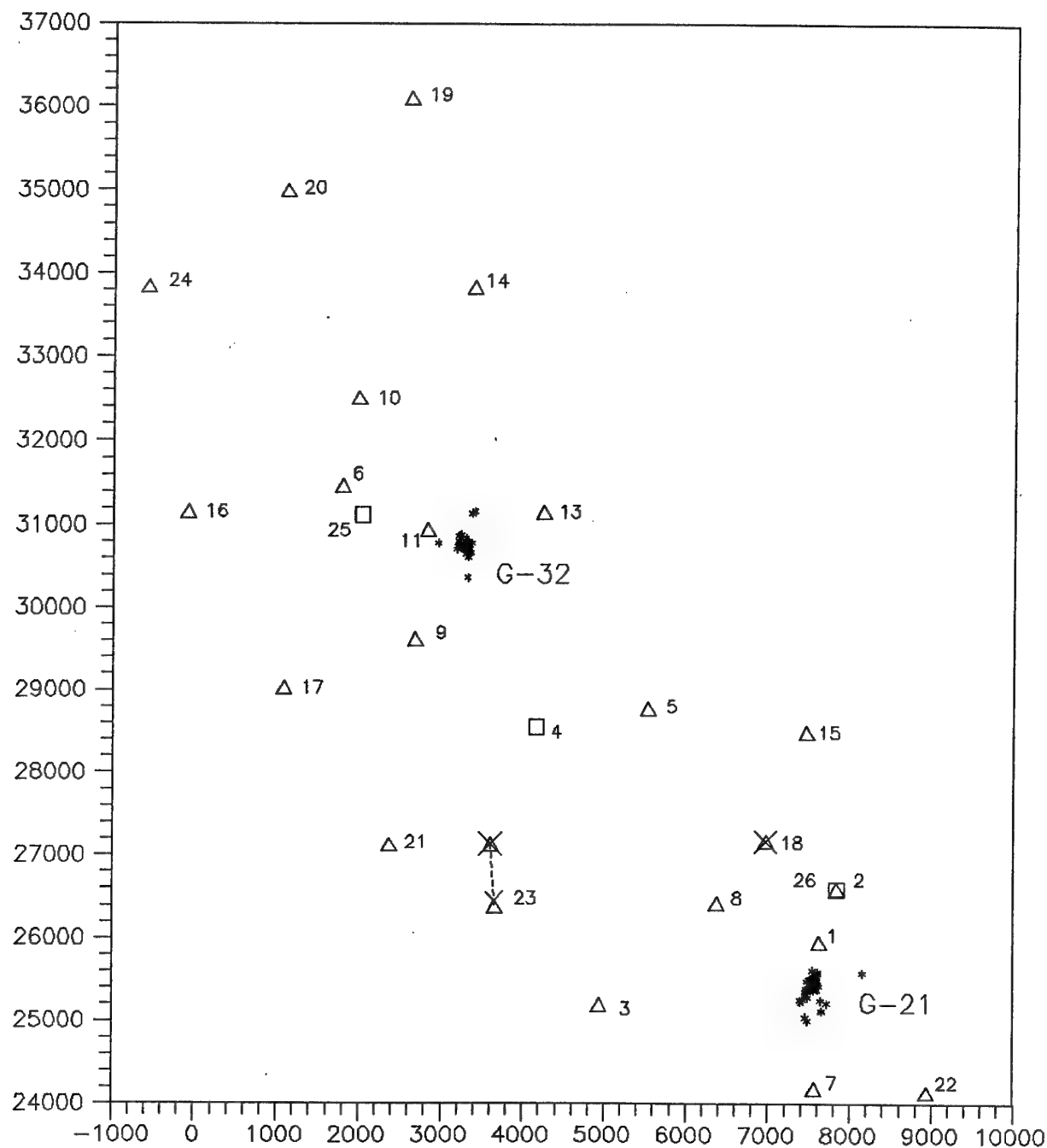


FIGURE 1. Horizontal distribution of seismic stations (single-component marked by triangles and three-components by squares) at Polkowice copper mine and selected seismic events (stars) at sections G-32 and G-21.

TABLE 1. ORIGIN TIME AND LOCATION OF SELECTED  
SEISMIC EVENTS AT POLKOWICE MINE SECTION G-32.

Event number	Date			Local time h m	Hypocenter coordinates		
	y	m	d		X (m)	Y (m)	Z (m)
1	1994	05	11	02 44	30873	3202	-633
2	1994	05	17	06 56	30884	3229	-679
3	1994	06	17	12 48	31163	3395	-684
4	1994	06	21	07 20	30747	3188	-676
5	1994	07	05	13 44	30808	3198	-676
6	1994	07	09	17 21	31141	3363	-686
7	1994	07	30	14 13	30814	3272	-672
8	1994	08	10	05 09	30843	3285	-678
9	1994	09	17	13 34	30809	3295	-671
10	1994	09	29	23 36	30762	3282	-695
11	1994	09	30	01 13	30817	3279	-671
12	1994	10	29	04 14	30790	3304	-682
13	1994	11	13	21 14	30784	2950	-698
14	1994	11	17	15 29	30766	3288	-670
15	1994	11	18	14 59	30807	3207	-666
16	1994	11	23	15 43	30766	3328	-675
17	1994	12	02	09 19	30725	3249	-672
18	1994	12	08	13 31	30725	3233	-667
19	1994	12	11	07 00	30767	3272	-667
20	1995	01	02	07 52	30735	3294	-669
21	1995	01	04	21 41	30745	3295	-670
22	1995	01	12	00 42	30677	3319	-674
23	1995	01	27	23 06	30724	3278	-669
24	1995	01	28	14 45	30710	3178	-665
25	1995	02	08	02 08	30786	3355	-673
26	1995	02	09	21 30	30706	3305	-668
27	1995	02	25	14 07	30715	3301	-666
28	1995	03	09	13 31	30668	3323	-713
29	1995	03	23	01 00	30670	3346	-671
30	1995	04	14	19 46	30667	3337	-667
31	1995	04	20	22 27	30619	3317	-673
32	1995	04	29	14 08	30650	3289	-671
33	1995	05	08	04 33	30675	3307	-670
34	1995	05	13	15 11	30368	3309	-670

TABLE 2. ORIGIN TIME AND LOCATION OF SELECTED  
SEISMIC EVENTS AT POLKOWICE MINE SECTION G-21.

Event number	Date			Local time			Hypocenter coordinates		
	y	m	d	h	m		X (m)	Y (m)	Z (m)
1	1994	10	02	06	00		25371	7549	-515
2	1994	10	06	11	34		25284	7482	-498
3	1994	10	08	23	07		25379	7597	-518
4	1994	10	15	04	01		25448	7589	-529
5	1994	10	19	17	44		25317	7470	-510
6	1994	11	02	22	36		25545	7555	-516
7	1994	11	04	10	40		25479	7597	-507
8	1994	11	05	20	17		25251	7386	-502
9	1994	11	26	05	25		25246	7637	-499
10	1994	12	02	12	24		25485	7582	-514
11	1994	12	03	11	50		25230	7397	-496
12	1994	12	11	20	01		25459	7582	-515
13	1994	12	29	23	16		25547	7589	-517
14	1994	12	30	09	26		25402	7527	-514
15	1995	01	03	06	47		25214	7717	-503
16	1995	01	08	03	46		25526	7549	-532
17	1995	01	12	02	44		25397	7509	-526
18	1995	01	13	06	01		25409	7535	-513
19	1995	01	13	13	43		25311	7454	-498
20	1995	01	17	18	36		25439	7517	-536
21	1995	01	24	19	02		25546	7583	-512
22	1995	01	30	02	26		25431	7517	-516
23	1995	02	01	02	45		25391	7463	-515
24	1995	02	01	06	52		25585	8145	-521
25	1995	02	11	04	53		25411	7537	-515
26	1995	02	11	04	54		25381	7525	-508
27	1995	02	22	15	26		25500	7566	-522
28	1995	02	26	18	58		25572	7577	-516
29	1995	03	12	16	24		25123	7649	-491
30	1995	03	13	20	19		25004	7475	-492
31	1995	03	14	02	52		25495	7591	-524
32	1995	03	17	08	01		25401	7519	-512
33	1995	03	21	05	27		25504	7522	-522
34	1995	03	22	11	11		25587	7597	-510
35	1995	03	26	00	37		25360	7456	-554
36	1995	03	26	18	01		25547	7582	-546
37	1995	03	31	18	58		25615	7542	-520
38	1995	04	04	00	24		25407	7489	-516
39	1995	04	05	22	52		25501	7499	-520
40	1995	04	09	00	50		25370	7512	-514
41	1995	04	13	18	46		25045	7456	-495
42	1995	04	14	10	32		25515	7525	-530
43	1995	04	14	15	40		25259	7418	-494
44	1995	04	15	04	31		25438	7604	-525
45	1995	04	15	15	53		25394	7503	-519

TABLE 2. ORIGIN TIME AND LOCATION OF SELECTED SEISMIC EVENTS AT POLKOWICE MINE SECTION G-21.

Event number	Date			Hypocenter coordinates		
	y	m	d	X (m)	Y (m)	Z (m)
46	1995	04	19	25474	7563	-519
47	1995	04	21	25367	7440	-494
48	1995	04	26	25426	7545	-513
49	1995	04	27	25421	7613	-527
50	1995	04	28	25589	7603	-518
51	1995	04	28	25365	7518	-497
52	1995	05	06	25571	7600	-503
53	1995	05	06	25481	7473	-527
54	1995	05	16	25450	7498	-515
55	1995	05	22	25367	7465	-509
56	1995	05	26	25120	7648	-494

Altogether, 54 such events were recorded from section G-32 and 58 from section G-21. Many of the events, however, were too small for proper analysis, in the sense that there were too few seismic records with the first *P*-wave onsets suitable for moment tensor inversion. Finally, 34 events with moment magnitude from 1.2 to 2.7 from section G-32 and 56 events with magnitude from 1.2 to 3.0 from section G-21 were analyzed. Their location is shown in Fig. 1 and they are listed in Table 1 and 2, respectively.

For one rather large event from section G-21, numbered 47, moment tensor inversion could not be executed due to electronic trigger failure, however the latter part of the signal is suitable for spectral analysis and it was retained in the database with a comment that moment tensor data are not available for this event. Similarly, the records of event 17 from section G-32 were distorted and their spectral analysis was not successful, but the first *P*-wave arrivals are well recorded and were used for the moment tensor inversion for this event.

#### 4. MINING WORKS, SEISMICITY AND FRACTAL DIMENSION

##### 4.1 Section G-32

Mining section G-32 is located in the northwestern part of the mining area granted to the Polkowice mine. The works are carried out in a stabilising pillar at a depth from 840 to 860 m. The ore deposits contain the floor part of Zechstein carbonate series and their thickness is on the average 3 m. There are gray and light dolomites and a thin layer of slates in the floor of dolomites. The roof directly above the deposits is formed by consolidated lime and dolomite rock series about 3.5 m thick and is composed of several layers of thickness from 0.05 to 2 m. The main roof is formed by highly consolidated dolomites without layering. In the floor of the ore deposits fine-grained gray sandstones are present with clay-dolomitic cement. The compressional strength of the rocks forming the deposits is from 82 to 160 MPa, those forming the deposit floor is from 16 to 86 MPa, and those from the roof is from 98 to 250 MPa.

The deposits are mined out by pillar-chamber and roof-fall techniques used to cut large pillars, established earlier, into smaller ones. The mining is done by blasting, which is carried out once a day. After the blasting an eight-hour period of watching is observed before the miners enter the area.

Section G-32 is one of the most seismic areas at Polkowice mine. Although the number of seismic events in the area is high at any time of mining activity, the number of selected events for this study is rather limited. Our aim is to search for time changes of the source parameters and source mechanism rather than to look at statistical properties of seismic events.

The only statistical approach used here is determination of fractal dimension of the selected set of 34 events, containing practically all larger events which occurred between May 1994 and May 1995. The correlation fractal dimension was determined in a similar way as it was done by Guo and Ogata

POLKOWICE G - 32

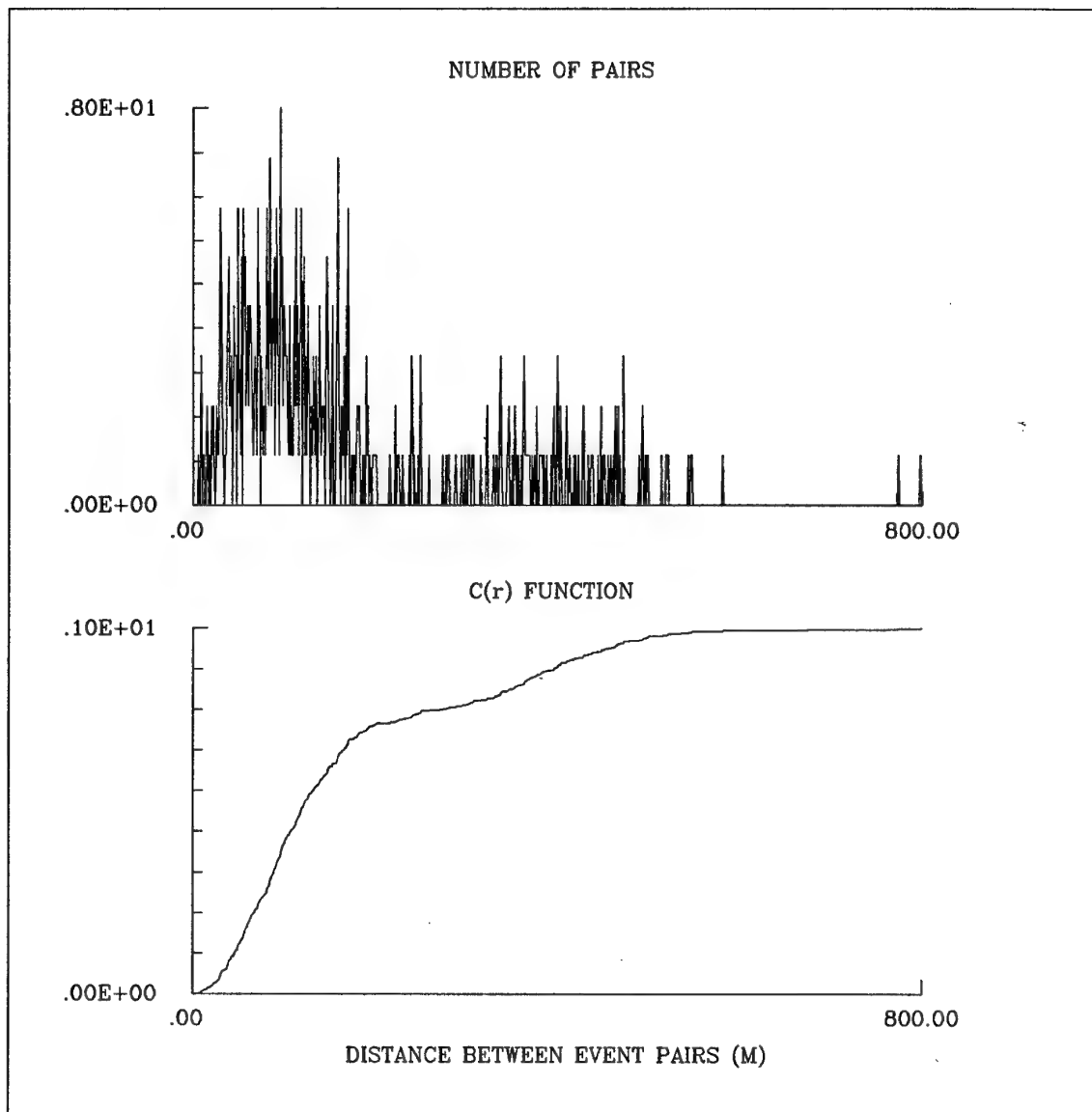


FIGURE 2. Histogram of distances between the pairs of seismic events from section G-32 (top) and the correlation integral  $C(r)$  versus the distance (bottom), used to estimate the fractal dimension of the events.

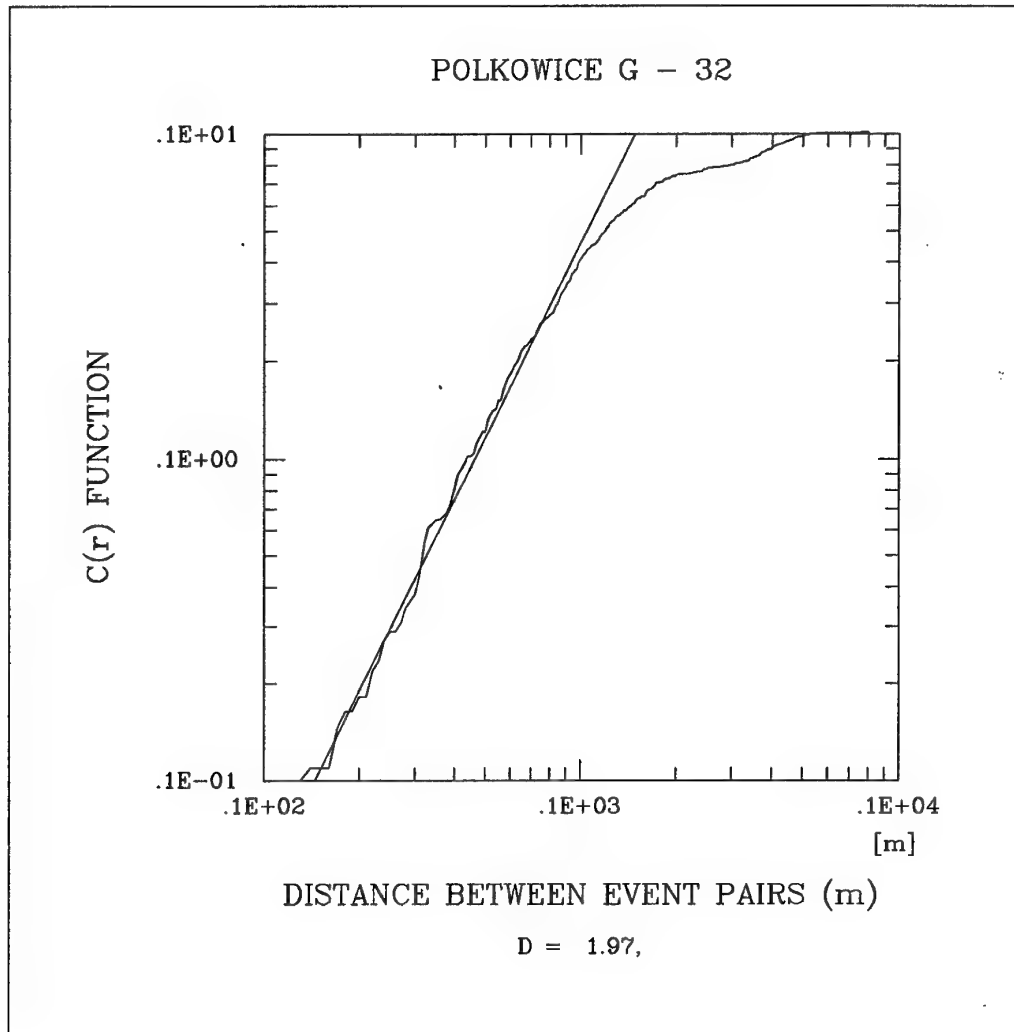


FIGURE 3. Linear approximation of the correlation integral  $C(r)$  as a function of the distance between the pairs of events from section G-32. The fractal dimension  $D$  is also indicated.



(1995) and in Part I of this report where seismicity at WDL in South Africa is described. The correlation integral  $C(r) = 2N(r)/N(N-1)$ , where  $N(r)$  is the number of pairs of hypocenters whose distances are smaller than  $r$  and  $N$  is the total number of selected seismic events, is considered to determine the fractal dimension of a given set of hypocenters. If the distribution has a fractal structure, then the correlation integral should be proportional to  $r^D$ , where  $D$  is the fractal dimension.

The distances between the pairs of hypocenters were calculated for the selected set of events and their histogram and the correlation integral  $C(r)$  are shown in Fig. 2. The fractal dimension  $D$  was calculated by the linear regression of the correlation integral against the distance between event pairs, shown in Fig. 3. The deviation from the linearity at large distances is caused by the limited size of the volume in which seismic events originated (Guo and Ogata, 1995). Our set of events is characterized by a low value of the fractal dimension  $D=2.0$  in comparison with those from natural aftershocks (e. g., Guo and Ogata, 1995). The decreasing of fractal dimension indicates that fracture events became more strongly correlated with advancing fracturing (Ito, 1992).

#### 4.2 Section G-21

Mining section G-21 is located in the southeastern part of the Polkowice mining area. The works are carried out at a depth from 660 to 710 m. The ore deposits are on the average 5.5 m thick and they are located between Zechstein and Rotliegendes sediments in carbonate rocks, slates and sandstones. The deposit strike direction is NW-SE and its dip is 3-5 degrees to NW. The deposits are composed mainly of fractured lime dolomites and fine-grained quartz sandstones. The roof directly above the deposits is formed by strongly consolidated and fractured dolomites and lime dolomites. The main roof contains rocks of Zechstein carbonate series, from 70 to 75 m thick. In the floor of the ore deposits fine-grained gray Rotliegendes quartz sandstones are present with clay cement. The compressional strength of the dolomites forming the deposits is from 97 to 181 MPa and that of sandstones is from 47 to 71 MPa. The strength of rocks forming the deposit floor is from 34 to 79 MPa and those from the roof is from 35 to 253 MPa.

POLKOWICE G - 21

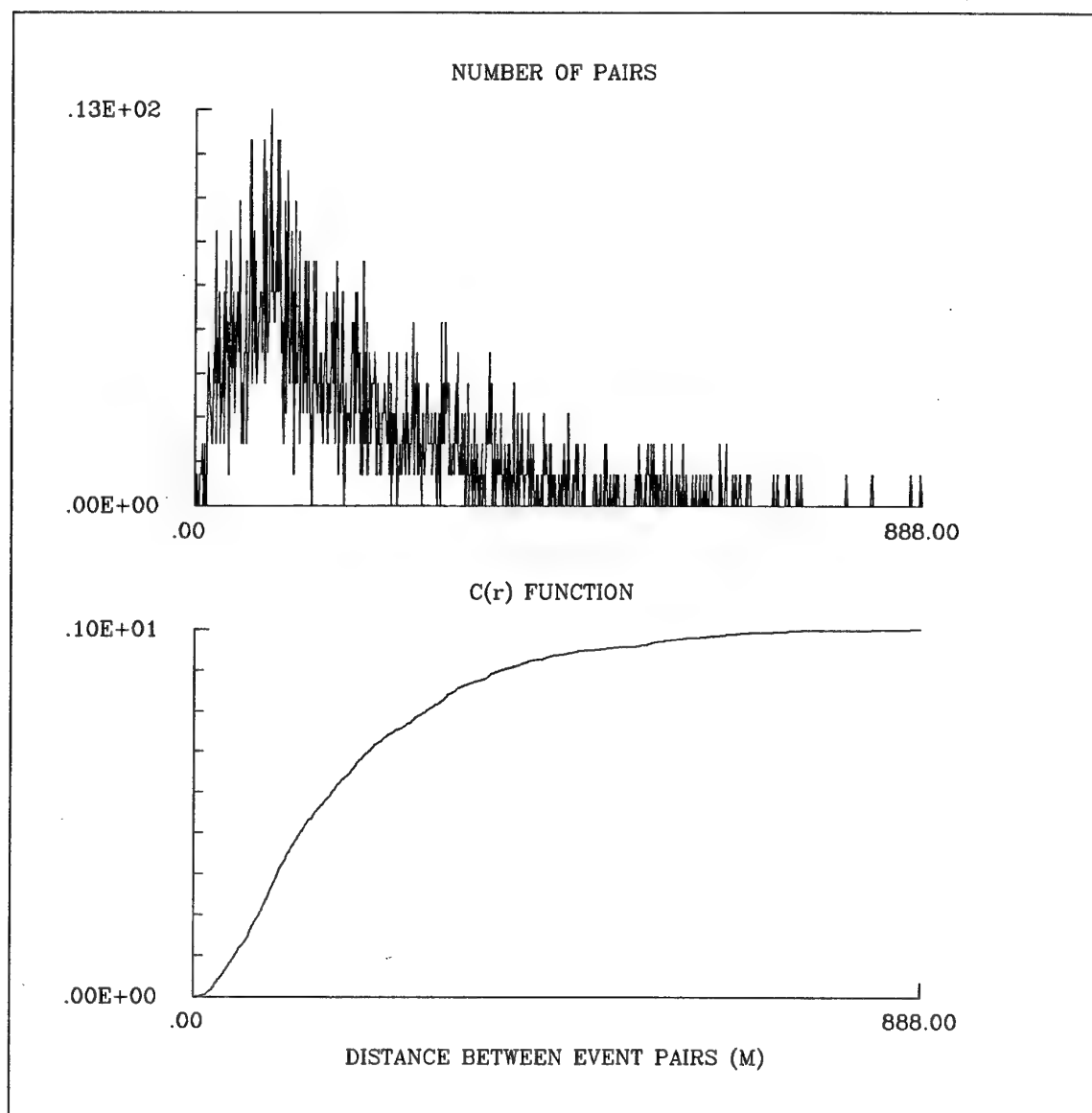


FIGURE 4. Histogram of distances between the pairs of seismic events from section G-21 (top) and the correlation integral  $C(r)$  versus the distance (bottom), used to estimate the fractal dimension of the events.

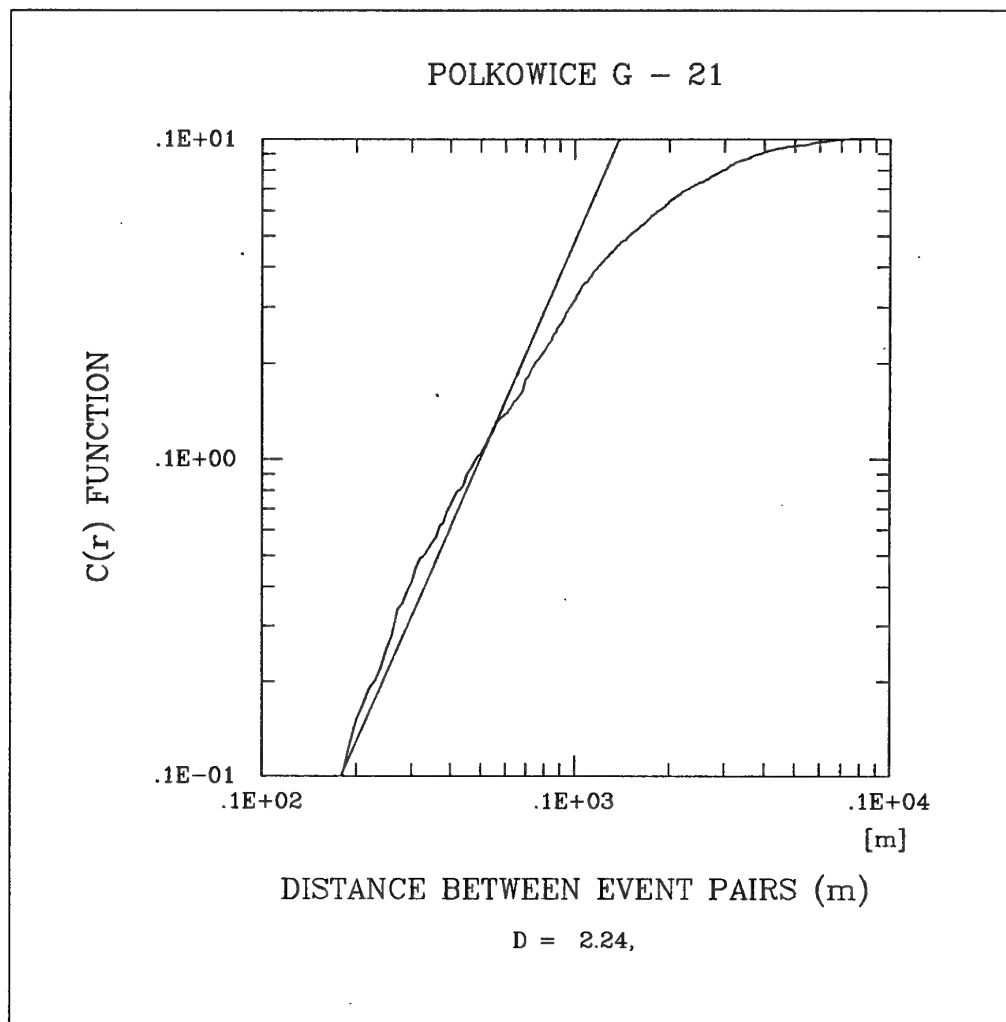


FIGURE 5. Linear approximation of the correlation integral  $C(r)$  as a function of the distance between the pairs of events from section G-21. The fractal dimension  $D$  is also indicated.

A fault with the strike direction of NW-SE and a throw from 3 to 4 m towards NE confines section G-21 from the north-east. Numerous fractures are present with the dominant strike direction of NW-SE.

The deposits are mined out by one-phase pillar-chamber technique used to cut rock mass into small pillars with dimensions of about 8 by 12 m. A so-called wide opening of the deposit roof is used to ensure its gentle bending. The mining is done by blasting, which is carried out after each working shift. A so-called limited roof-fall technique, enforced by blasting, is used to fill the worked-out areas.

Similarly as section G-32, section G-21 is one of the most seismic areas at Polkowice mine. The set of selected 56 seismic events contains all larger events which occurred between October 1994 and May 1995. The correlation fractal dimension was determined for this set by calculating the distance  $r$  between the pairs of hypocenters and the corresponding correlation integral  $C(r)$ . The histogram of the distances and the function  $C(r)$  are shown in Fig. 4. The fractal dimension  $D$  was calculated by the linear regression of  $C(r)$  against  $r$  on a logarithmic scale, shown in Fig. 5. Our set of events is characterized by a relatively low value of the fractal dimension  $D=2.2$ , which is only slightly higher than that found for seismic events from section G-32. This value could possibly mean that the selected seismic events are strongly correlated.

## 5. SPECTRAL SOURCE PARAMETERS

### 5.1 Spectral analysis

After single integration of all original seismograms, representing the records of ground velocity, the displacement records were obtained. The spectral analysis was carried out using interactive computer graphics allowing the choice and rapid change of signal windows on various ground displacement traces. Windows containing *P* and *S* pulses with a variable length were selected in each case. The time series was tapered using a cosine taper affecting a tenth of the window. The ground displacement spectra were then calculated by an FFT routine and corrected for instrumental response. The instrumental response is flat for frequencies above 0.5 Hz and below 150 Hz, and the Nyquist frequency is 250 Hz. The observed corner frequencies are well within this interval. The effects of the bandwidth limitation on the estimates of source parameters can be significant when the corner frequencies are not in the middle of the selected frequency band (Di Bona and Rovelli, 1988).

The observed spectra must be corrected for attenuation and scattering effects along the travel path of seismic waves. Such corrections are important for the proper retrieval of source parameters of small earthquakes, even recorded at close distances (e.g., Rovelli *et al.*, 1991). To correct for attenuation, the displacement spectra were multiplied by the exponential term  $\exp(\omega R / c Q_c)$ , where *R* is the hypocentral distance, *c* is either *P*- or *S*-wave velocity,  $Q_c$  is the quality factor of either *P* or *S* waves, and  $\omega = 2\pi f$ , in which *f* is the frequency. The *P*-wave velocity of 5.7 km/s and the *S*-wave velocity of 3.3 km/s, representing the average values at Polkowice mine, were accepted for the calculations. Since the attenuation properties of the Polkowice rock mass are not known, an assumption that  $Q_p = (9/4)Q_s$  (e. g., Burdick, 1978) was accepted and an approximate value of the quality factor for *S* waves equal to 200 was chosen for the attenuation correction. The attenuation corrections were found to be not significant.

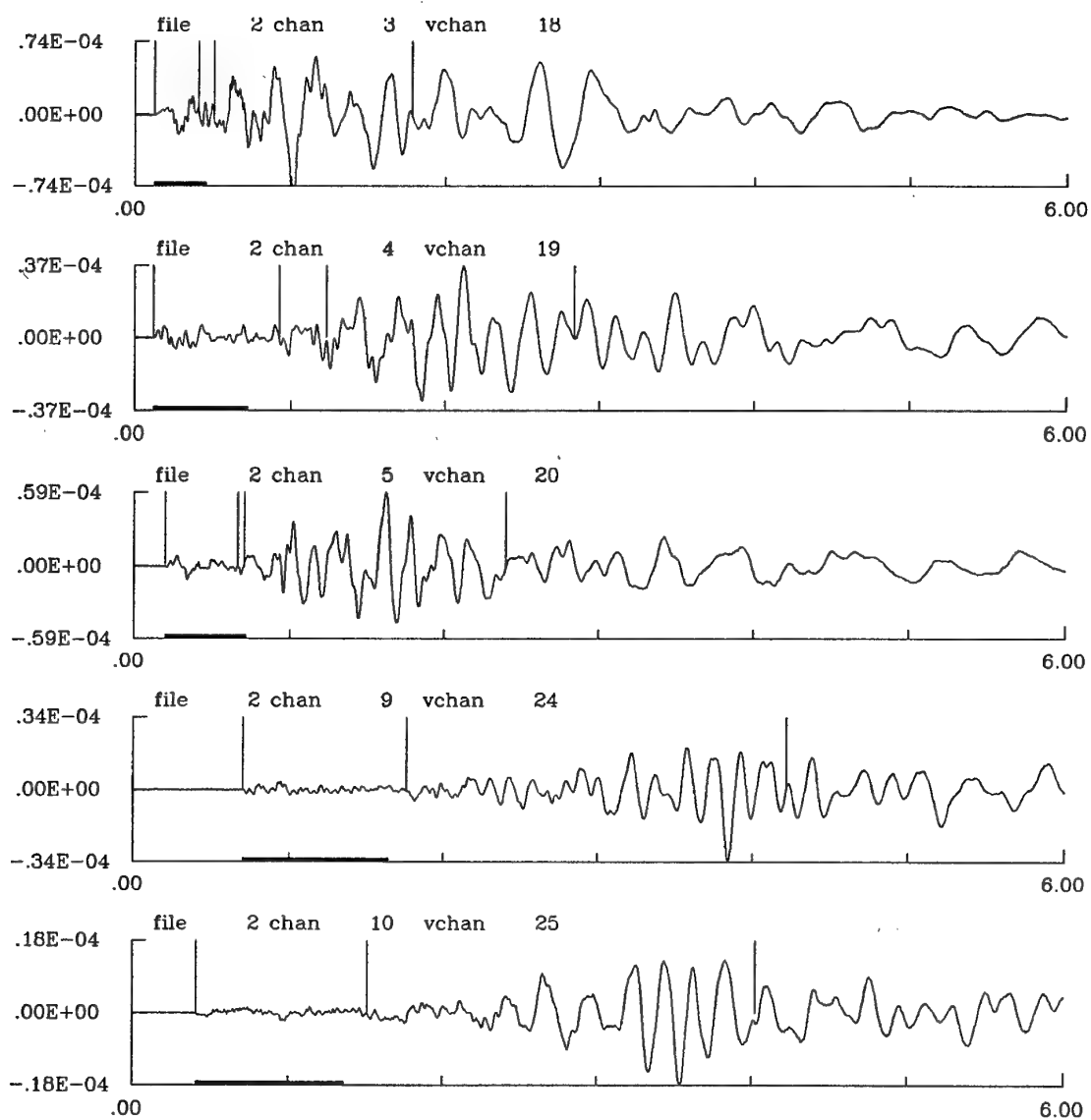
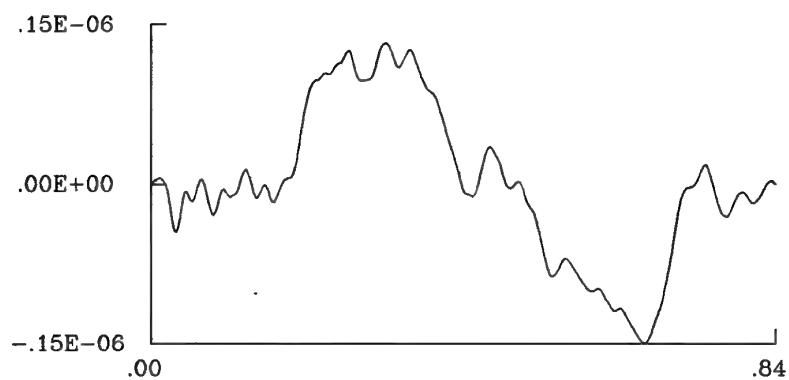


FIGURE 6. Example of typical seismograms recorded at Polkowice mine from the seismic event of October 6, 1994 with moment magnitude  $M=2.2$ , which occurred at section G-21. The vertical bars show the windows selected for spectral analysis of  $P$  and  $S$  waves, and the time axis is in seconds.



Kan 3 - 3 Z                      Fala P   file   5 kanal   3  
 Kopalnia Polkowice  
 1994.11.23-15.43.25.00000- 327                      23G15432.MIN

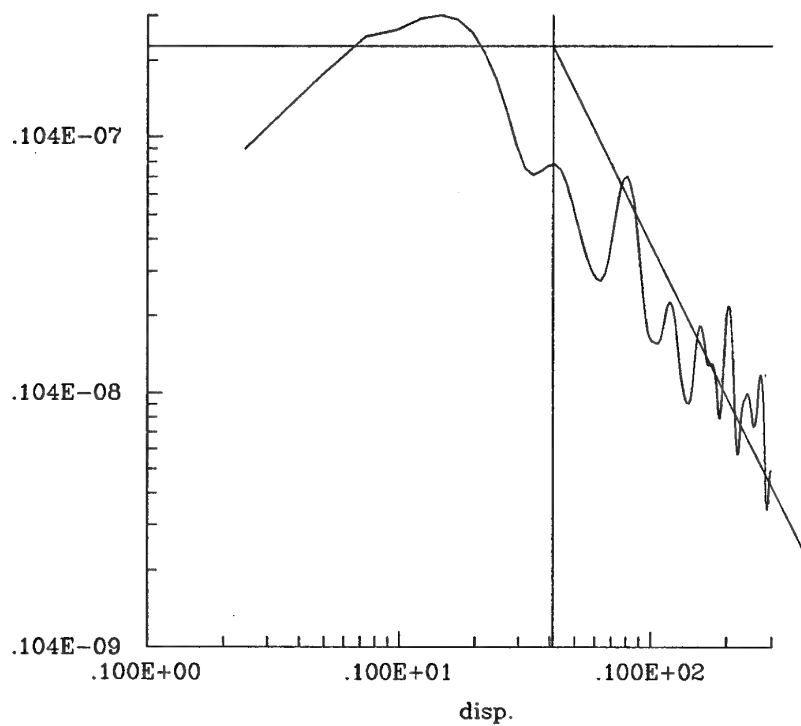
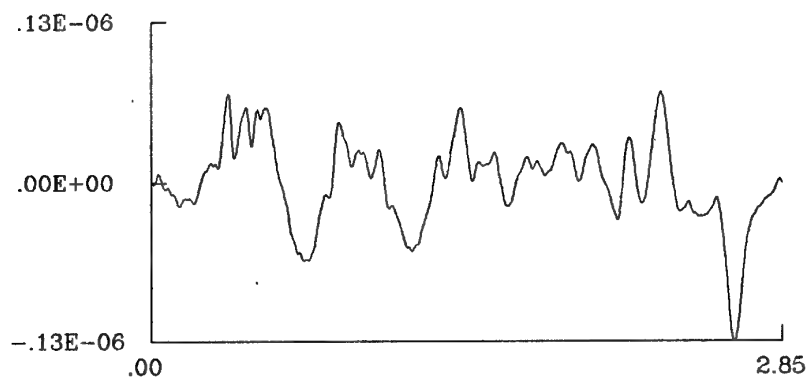


FIGURE 7. Example of a *P*-wave displacement spectrum from the seismic event of November 23, 1994 with moment magnitude 1.7, which occurred at section G-32. The spectrum is approximated by two straight lines. The corresponding *P*-wave record is shown at the top.



Kan 22 - 22 Z                      Fala S   file 32 kanal 22  
 Kopalnia Polkowice  
 1994.09.29-23.36.15.00000- 272                      29E23361.MIN

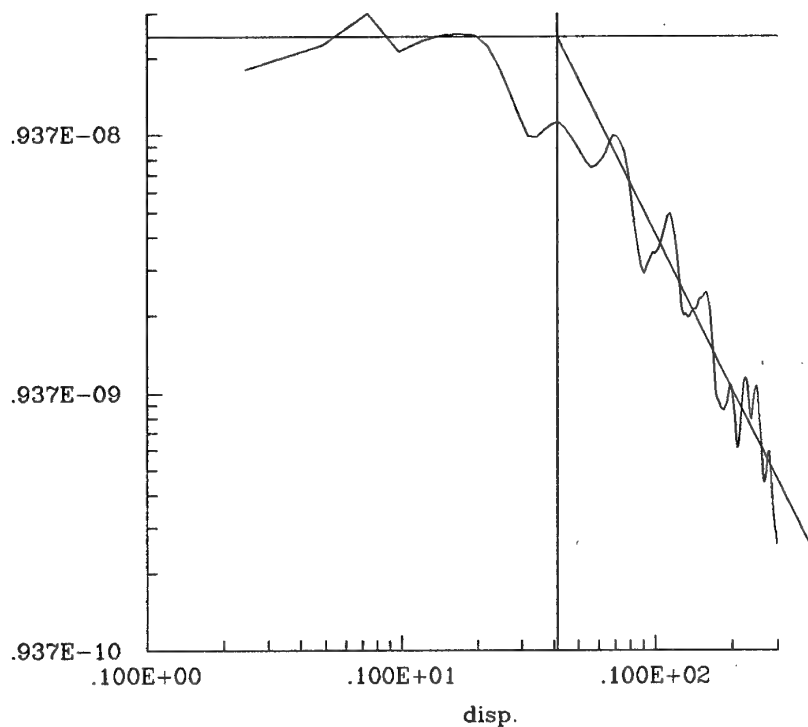


FIGURE 8. Example of a S-wave displacement spectrum from the seismic event of September 23, 1994 with moment magnitude 1.8, which occurred at section G-32. The spectrum is approximated by two straight lines. The corresponding S-wave record is shown at the top.



The noise level was considerably lower than the signal level in all cases and at all frequencies. An example of typical seismograms recorded at Polkowice mine is shown in Fig. 6. These are the records of the seismic events of October 6, 1984 with moment magnitude  $M=2.2$ , which occurred at section G-21. The vertical bars show the windows selected for spectral analysis of  $P$  and  $S$  waves. Various methods are used for the accurate and objective interpretation of seismic spectra to provide reliable estimates of source parameters. The simplest and most often used spectral model is that described by the low-frequency spectral level  $\Omega_0$  and the corner frequency  $f_0$ , above which the spectrum is assumed to fall off as a second power of frequency (Brune, 1970, 1971).

Our displacement spectra, corrected for attenuation and instrumental effects, were approximated by two asymptotes, describing the flat and decreasing portions of the spectra. The two asymptotes were determined automatically by computing the integral of the square of ground displacement and of ground velocity (Andrews, 1986). Examples of  $P$ - and  $S$ -wave displacement spectra and their approximation by the two asymptotes are shown in Fig. 7 and 8, respectively. The corresponding  $P$ - and  $S$ -wave records are shown at the top of each figure. The examples are related to the seismic event of November 23, 1994 with moment magnitude 1.7 and of September 23, 1994 with magnitude 1.8. The two events occurred at section G-32.

The integral  $J$  of the square of ground velocity is a direct measure of the energy flux of  $P$  or  $S$  waves as well. The energy flux, in turn, is a measure of the energy radiated in the  $P$  or  $S$  waves, which can be calculated from the relation derived by Boatwright and Fletcher (1984). The simplest calculation of the energy flux is done in the frequency domain, following the method described by Snoke (1987). Thus, two independent parameters  $\Omega_0$  and  $J_c$  were calculated directly from the spectra;  $\Omega_0$  is the value of the low-frequency level of the spectrum, and  $J_c$  is the integral of the square of ground velocity of either  $P$  or  $S$  waves. From the low-frequency level  $\Omega_0$  and the energy flux  $J_c$ , the corner frequency  $f_c$  was calculated (Snoke, 1987). Thus our input data for the calculation of source parameters are  $\Omega_0$ ,  $J_c$ , and  $f_c$ , from  $P$  and  $S$  waves recorded by several seismometers at Polkowice copper mines.

## 5.2 Relations between various source parameters

The values of full-displacement vector  $\Omega_0$  are needed for proper estimates of seismic moment. To account for this, our values  $\Omega_0$ , obtained from single-component records, were divided by direction cosines which were calculated assuming a straight-line ray geometry between the sources and the sensors. The values of the radiation coefficient, calculated from the double-couple solutions of the moment tensor inversion (described in Chapter 6) for each sensor and for both  $P$  and  $S$  waves, were used for the computation of seismic moment. The density of the source material of  $2700 \text{ kg/m}^3$  was accepted. Seismic moment estimated from  $S$  waves versus that estimated from  $P$  waves for seismic events from section G-32 is shown in Fig. 9 and for seismic events from section G-21 is presented in Fig. 10. The values of seismic moment from  $S$  waves are consistently larger than those estimated from  $P$  waves. The accepted values of seismic moment  $M_0$ , averaged from the values from  $P$  and  $S$  waves, for the seismic events at section G-32 are listed in Table 3 and for those at section G-21 are given in Table 4. The values of moment magnitude  $M$ , defined by Hanks and Kanamori (1979), are also listed in Tables 3 and 4.

Estimates of the source size are heavily model dependent. In Polish mines, it was found that whenever the size and geometry of underground damage caused by rockbursts could be estimated, its radius was considerably smaller than that predicted by Brune's model (e. g., Gibowicz, 1984; Gibowicz *et al.*, 1989). Similarly, the Brune model provides unrealistic estimates of the source size in French coal mines (Revalor *et al.*, 1990). The quasi-dynamic model of Madariaga (1976), on the other hand, provides reasonable results in good agreement with independent observations in mines and this model was used to estimate the source radius at Polkowice mine, listed in Tables 3 and 4. The corner frequency of  $P$  waves ranges there from 2.2 to 13 Hz and the corner frequency of  $S$  waves ranges between 2.8 and 7.3 Hz. The values of  $S$ -wave corner frequency versus those of  $P$ -wave corner frequency are displayed on a logarithmic scale for seismic events from section G-32 in Fig. 11 and for the events from section G-21 in Fig. 12. The corner frequency of  $P$  waves is consistently higher than that of  $S$  waves. The range of observations, however, is too limited for further consideration.

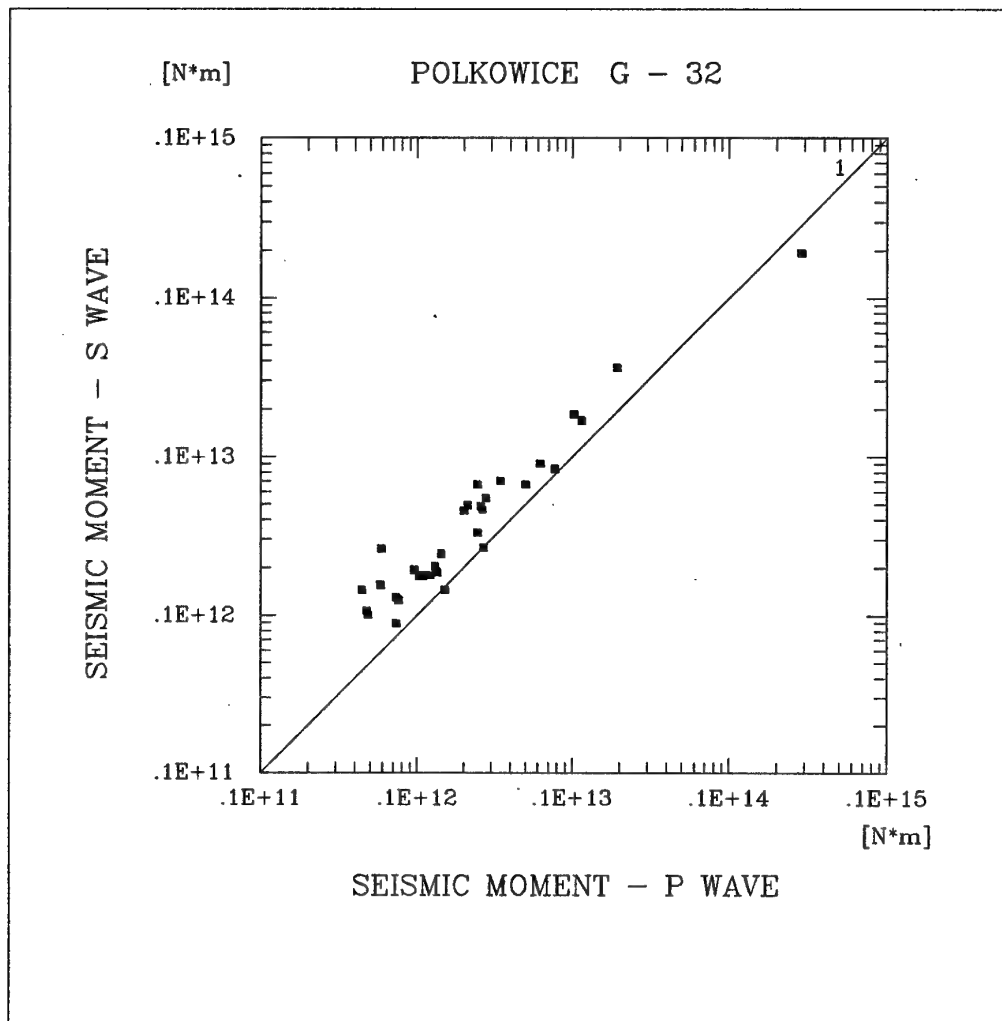


FIGURE 9. Seismic moment estimated from S-wave spectra versus that estimated from P-wave spectra for seismic events from section G-32. The straight line corresponds to the same value of both estimates.

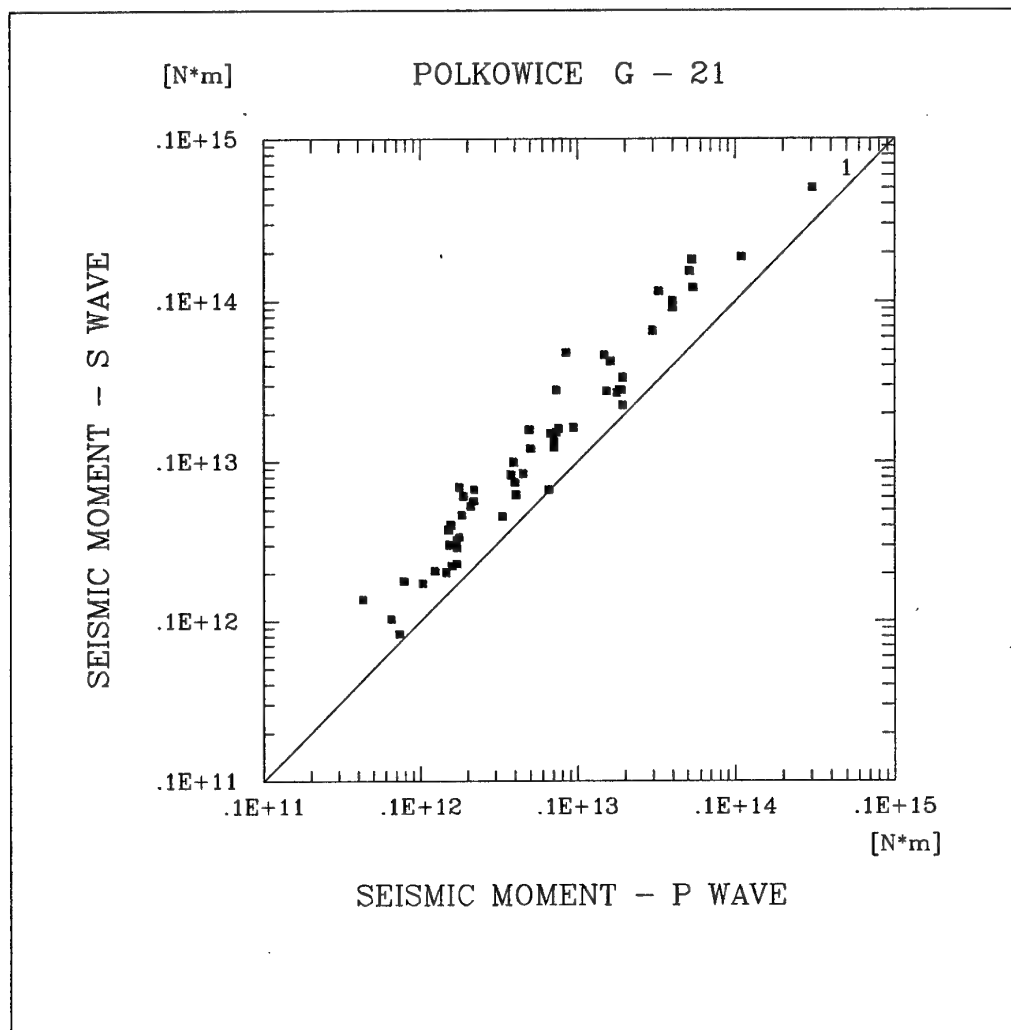


FIGURE 10. Seismic moment estimated from S-wave spectra versus that estimated from P-wave spectra for seismic events from section G-21. The straight line corresponds to the same value of both estimates.

TABLE 3. SEISMIC MOMENT AND SOURCE RADIUS OF SEISMIC

## EVENTS AT POLKOWICE MINE SECTION G - 32.

Event number	Seismic moment M <sub>0</sub> (N·m)	Moment magnitude M	P-wave frequency f <sub>p</sub> (Hz)	S-wave frequency f <sub>s</sub> (Hz)	Source radius r <sub>0</sub> (m)
1	.145E+12	1.42	8.97	6.51	96.4
2	.147E+12	1.42	7.03	6.07	115.3
3	.149E+12	1.39	7.66	7.16	102.0
4	.763E+11	1.22	9.93	7.12	89.4
5	.169E+12	1.45	5.86	5.50	138.0
6	.102E+12	1.31	8.87	6.36	100.0
7	.152E+12	1.43	7.68	6.16	112.0
8	.459E+12	1.69	6.64	4.80	151.2
9	.373E+12	1.67	5.67	4.69	153.0
10	.332E+12	1.63	8.39	5.38	114.4
11	.146E+12	1.42	8.62	6.72	99.9
12	.283E+13	2.25	4.41	4.11	192.3
13	.242E+14	2.65	2.18	2.78	313.9
14	.417E+12	1.70	6.86	6.33	119.7
15	.109E+12	1.28	11.58	7.27	82.5
16	.815E+12	1.92	4.94	5.59	152.7
17					
18	.821E+11	1.26	8.63	6.24	106.3
19	.368E+12	1.67	6.24	5.48	137.2
20	.780E+11	1.21	12.08	6.82	82.9
21	.532E+12	1.78	5.28	4.68	159.2
22	.271E+12	1.60	6.86	5.84	127.5
23	.142E+12	1.40	7.69	6.57	104.4
24	.953E+11	1.25	10.83	6.82	87.7
25	.162E+12	1.39	9.34	6.82	95.1
26	.103E+12	1.32	9.84	7.10	87.5
27	.144E+13	2.08	4.22	4.85	176.9
28	.357E+12	1.67	6.48	5.77	127.1
29	.593E+12	1.82	6.51	5.58	128.6
30	.293E+12	1.62	8.00	5.78	113.2
31	.163E+12	1.45	5.17	5.64	142.2
32	.772E+12	1.90	4.18	4.50	188.4
33	.147E+13	2.06	5.32	5.21	152.9
34	.197E+12	1.50	7.18	5.56	121.9

TABLE 4. SEISMIC MOMENT AND SOURCE RADIUS OF SEISMIC

## EVENTS AT POLKOWICE MINE SECTION G - 21.

Event number	Seismic moment Mo (N·m)	Moment magnitude M	P-wave frequency fp (Hz)	S-wave frequency fs (Hz)	Source radius ro (m)
1	.266E+12	1.58	9.45	5.40	103.0
2	.228E+13	2.22	3.76	3.48	210.9
3	.485E+13	2.41	4.55	3.48	188.1
4	.132E+13	2.06	4.71	3.73	176.5
5	.236E+13	2.23	3.64	3.40	216.2
6	.115E+13	1.98	6.54	3.80	151.9
7	.149E+14	2.72	3.03	2.83	261.9
8	.104E+13	1.98	5.95	3.46	168.9
9	.120E+13	2.00	5.71	3.90	159.9
10	.251E+12	1.58	6.98	4.71	129.9
11	.581E+12	1.81	11.27	5.65	95.5
12	.749E+13	2.45	4.88	2.88	207.4
13	.911E+11	1.24	10.01	4.75	111.0
14	.851E+11	1.27	12.78	6.03	84.9
15	.204E+12	1.52	9.16	5.64	104.8
16	.312E+13	2.25	4.29	3.31	200.8
17	.371E+12	1.68	7.84	4.79	119.8
18	.612E+12	1.82	6.51	3.89	150.5
19	.269E+13	2.26	4.21	3.42	201.6
20	.231E+12	1.54	7.94	4.59	123.3
21	.983E+12	1.96	6.40	4.54	145.9
22	.654E+12	1.84	7.21	4.17	136.7
23	.702E+12	1.83	8.80	5.03	112.7
24	.864E+12	1.90	8.34	4.83	123.3
25	.241E+13	2.22	4.66	3.35	210.1
26	.103E+14	2.58	4.53	3.00	215.4
27	.396E+12	1.67	7.25	3.48	158.6
28	.131E+12	1.35	9.18	4.76	117.0
29	.177E+12	1.47	9.91	5.42	103.6
30	.213E+13	2.19	4.65	3.91	180.0
31	.141E+12	1.38	11.88	6.27	87.6
32	.401E+12	1.71	7.76	5.34	113.6
33	.235E+12	1.54	8.59	4.69	124.2
34	.106E+13	1.94	7.58	3.93	141.5
35	.709E+13	2.49	4.11	3.11	212.9
36	.166E+12	1.45	8.71	5.40	111.9
37	.438E+12	1.68	8.14	4.21	127.9
38	.331E+12	1.62	7.69	4.74	122.4
39	.261E+12	1.56	9.38	5.06	112.5
40	.298E+13	2.24	5.55	3.83	167.3
41	.790E+11	1.24	13.10	7.30	75.7
42	.521E+12	1.76	8.51	5.66	110.0
43	.218E+13	2.20	4.96	2.71	206.3
44	.179E+13	2.07	5.59	3.26	174.8

TABLE 4. SEISMIC MOMENT AND SOURCE RADIUS OF SEISMIC

## EVENTS AT POLKOWICE MINE SECTION G - 21.

Event number	Seismic moment $M_0$ ( $N \cdot m$ )	Moment magnitude $M$	P-wave frequency $f_p$ (Hz)	S-wave frequency $f_s$ (Hz)	Source radius $r_0$ (m)
45	.398E+12	1.65	8.84	4.72	114.8
46	.110E+13	1.94	6.23	4.22	159.7
47	.666E+13	2.48	5.30	3.63	173.8
48	.285E+12	1.57	9.60	4.96	107.3
49	.289E+13	2.17	5.95	2.71	189.1
50	.409E+14	3.03	2.32	1.91	372.1
51	.449E+12	1.71	8.39	4.82	115.8
52	.403E+12	1.68	11.05	4.70	109.2
53	.888E+13	2.57	4.16	3.28	203.1
54	.667E+12	1.83	6.29	4.38	173.2
55	.119E+14	2.64	4.35	2.69	224.4
56	.192E+12	1.50	10.09	5.70	98.5

Seismic moment versus source radius for seismic events from section G-32 and G-21 is shown in Fig. 13 and 14, respectively, where a linear approximation of the data and the lines of constant stress drop are also marked. The slope coefficient of linear regression is 3.8 and 4.2, which is larger than the slope equal to 3 characterizing constant stress drop relations recently confirmed for seismic events induced by mining (Gibowicz, 1995), but the range of observations is again too limited for further evaluation.

The radiated seismic energy of either  $P$  or  $S$  waves can be estimated directly from the energy flux of either  $P$  or  $S$  waves. The loss of energy from attenuation is accounted for in the calculation of the energy flux. The values of the seismic energies  $E_p$  and  $E_s$  of the  $P$  and  $S$  pulses were readily calculated by applying individual values, divided by the RMS averages (e. g., Boatwright and Fletcher, 1984), of the radiation coefficient corresponding to various seismic sensors. The values of  $E_p$  and  $E_s$  for the selected seismic events at section G-32 are listed in Table 5, together with the values of the total seismic energy  $E = E_p + E_s$ . Similarly, the values of the energy for the events at section G-21 are given in Table 6.

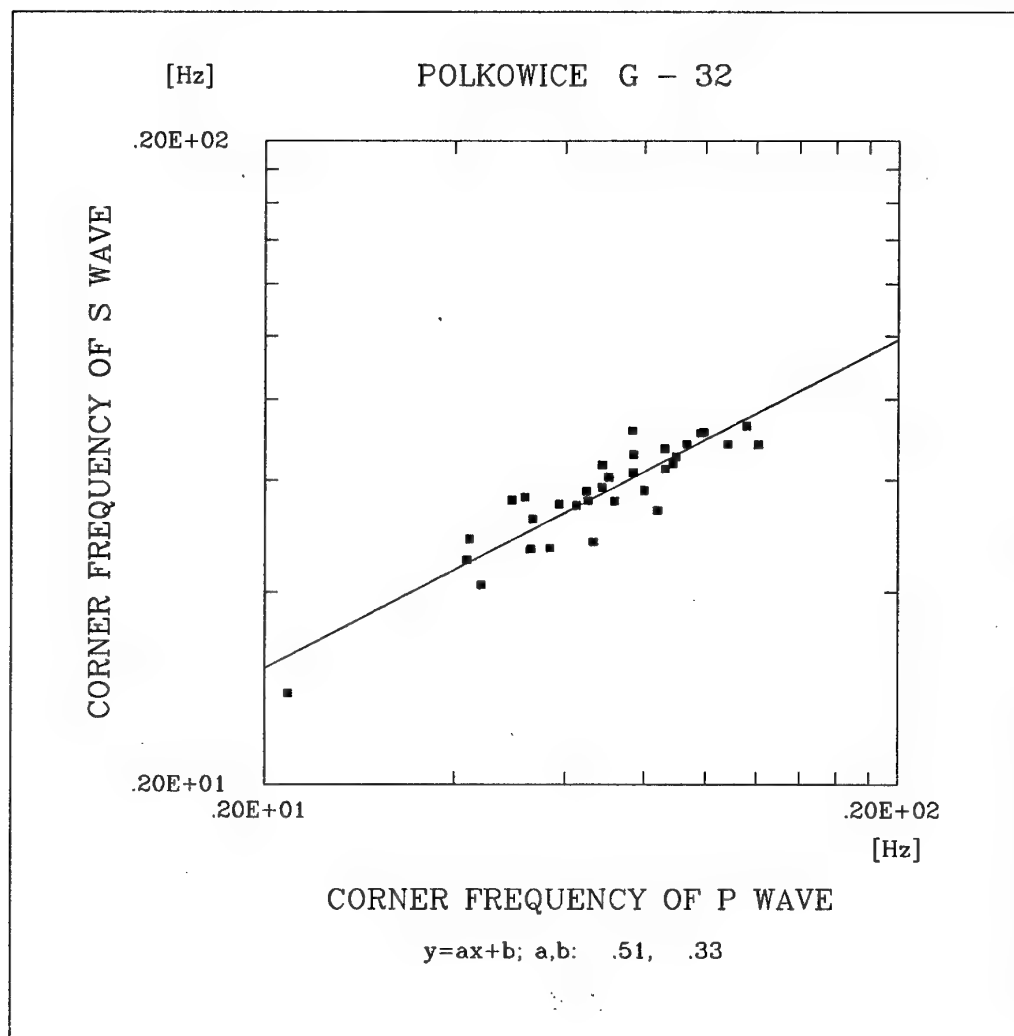


FIGURE 11. S-wave corner frequency versus *P*-wave corner frequency for seismic events from section G-32.



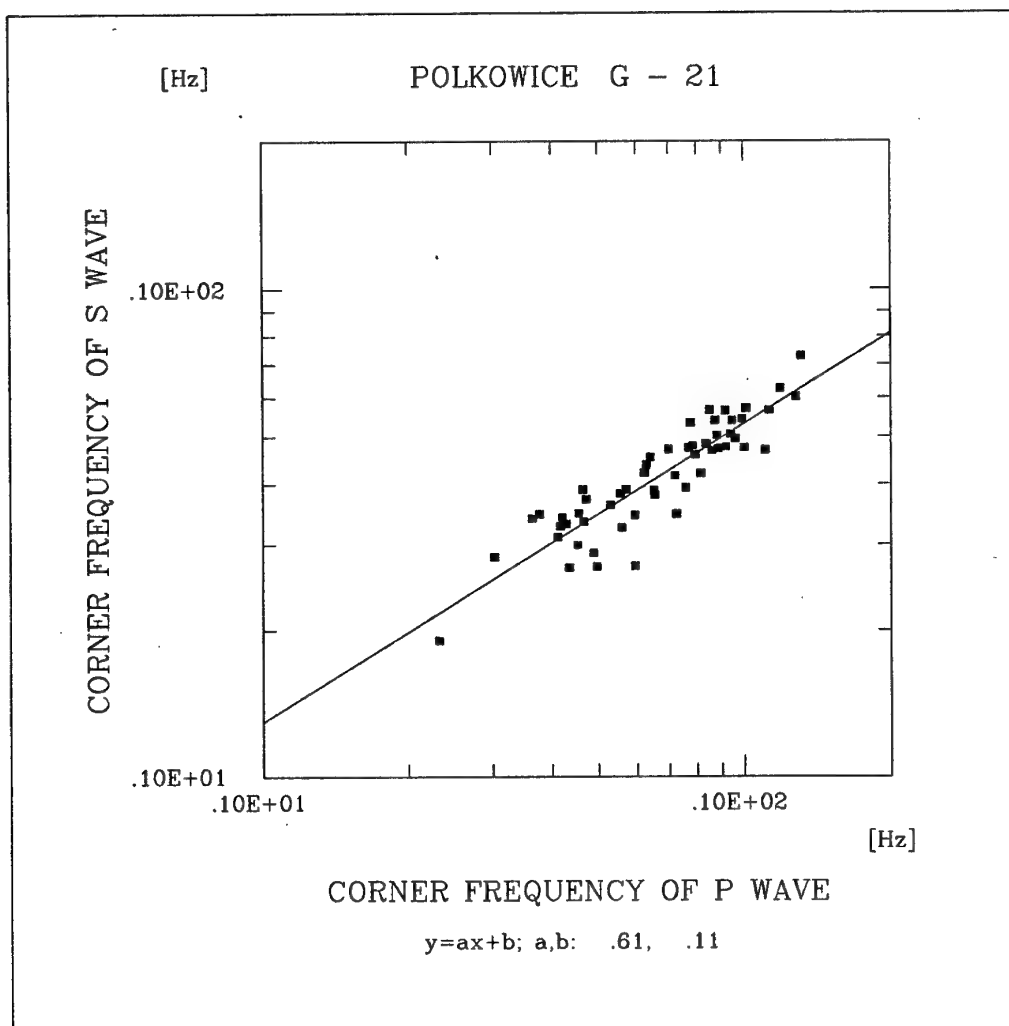


FIGURE 12. S-wave corner frequency versus *P*-wave corner frequency for seismic events from section G-21.

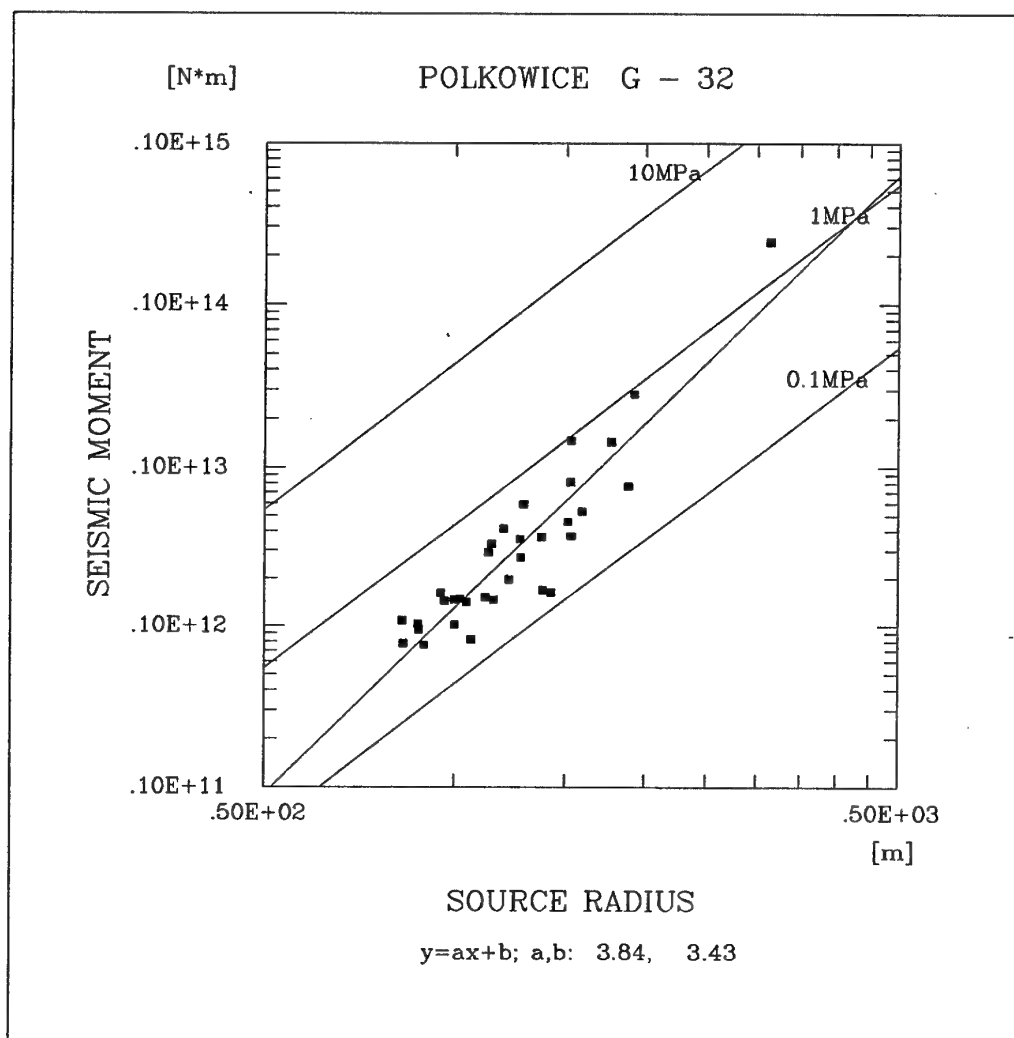


FIGURE 13. Seismic moment versus source radius for seismic events from section G-32. The lines of constant stress drop are also indicated.

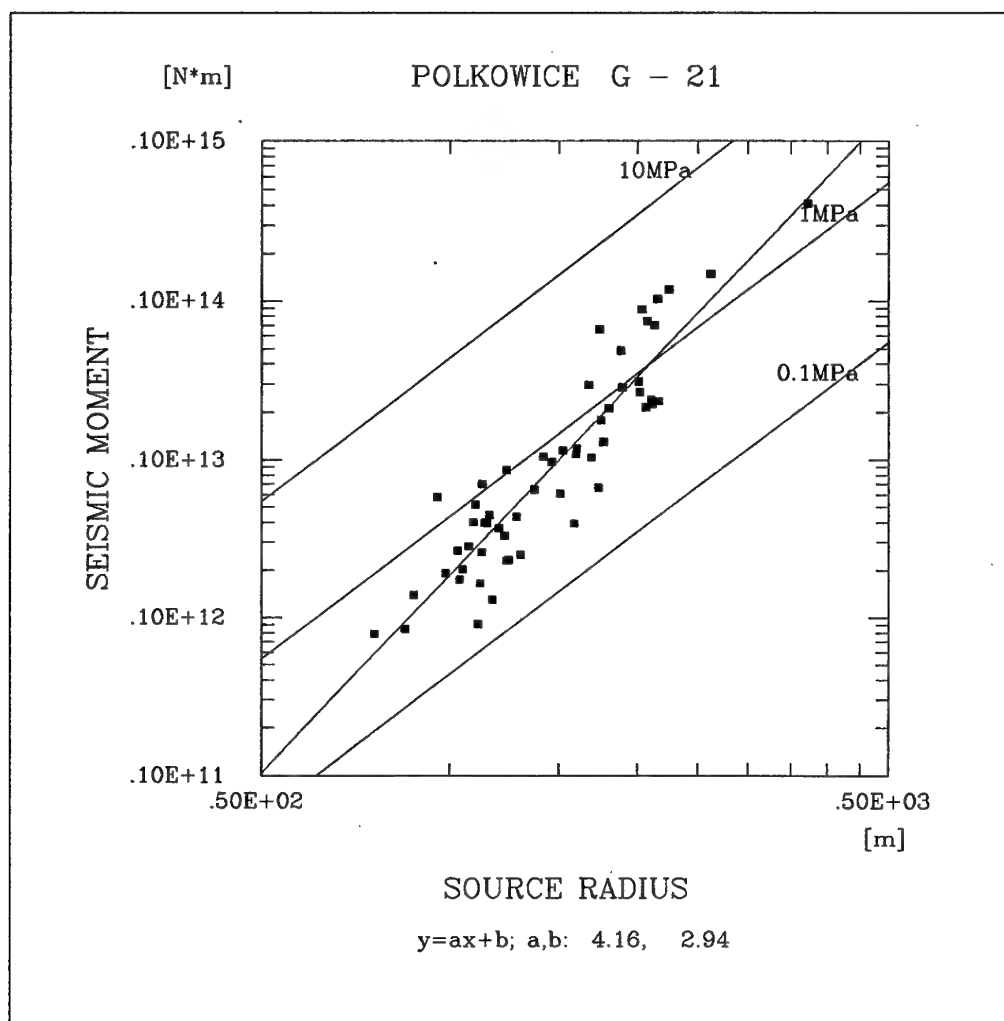


FIGURE 14. Seismic moment versus source radius for seismic events from section G-21. The lines of constant stress drop are also indicated.

TABLE 5. SEISMIC ENERGY AND STRESS-RELEASE ESTIMATE FOR

## SEISMIC EVENTS AT POLKOWICE MINE SECTION G - 32.

Event number	P-wave energy $E_p$ (J)	S-wave energy $E_s$ (J)	Total seismic energy $E$ (J)	Stress drop $\delta\sigma$ (MPa)	Apparent stress $\delta a$ (MPa)
1	.141E+04	.470E+05	.484E+05	.071	.007
2	.711E+03	.414E+05	.421E+05	.042	.006
3	.304E+04	.642E+05	.672E+05	.061	.010
4	.336E+03	.205E+05	.208E+05	.047	.006
5	.444E+03	.343E+05	.348E+05	.028	.004
6	.713E+03	.186E+05	.193E+05	.045	.004
7	.127E+04	.439E+05	.452E+05	.047	.006
8	.147E+04	.234E+06	.236E+06	.058	.011
9	.150E+04	.119E+06	.121E+06	.046	.007
10	.425E+04	.183E+06	.188E+06	.097	.012
11	.103E+04	.616E+05	.626E+05	.064	.009
12	.386E+05	.380E+07	.384E+07	.174	.029
13	.348E+07	.693E+08	.727E+08	.343	.063
14	.399E+04	.395E+06	.399E+06	.106	.020
15	.800E+03	.481E+05	.489E+05	.085	.009
16	.107E+05	.693E+06	.703E+06	.100	.018
17					
18	.537E+03	.107E+05	.112E+05	.030	.003
19	.222E+04	.187E+06	.190E+06	.062	.011
20	.557E+03	.183E+05	.188E+05	.060	.005
21	.303E+04	.254E+06	.257E+06	.058	.010
22	.283E+04	.736E+05	.764E+05	.057	.006
23	.862E+03	.450E+05	.458E+05	.055	.007
24	.391E+03	.411E+05	.415E+05	.062	.009
25	.471E+03	.979E+05	.984E+05	.082	.013
26	.995E+03	.315E+05	.325E+05	.067	.007
27	.166E+05	.162E+07	.164E+07	.114	.024
28	.221E+04	.258E+06	.261E+06	.076	.015
29	.109E+05	.392E+06	.402E+06	.122	.014
30	.463E+04	.110E+06	.115E+06	.088	.008
31	.430E+03	.273E+05	.277E+05	.025	.004
32	.433E+04	.378E+06	.382E+06	.050	.010
33	.231E+05	.212E+07	.215E+07	.180	.031
34	.104E+04	.569E+05	.579E+05	.048	.006

TABLE 6. SEISMIC ENERGY AND STRESS-RELEASE ESTIMATE FOR  
SEISMIC EVENTS AT POLKOWICE MINE SECTION G - 21.

Event number	P-wave energy $E_p$ (J)	S-wave energy $E_s$ (J)	Total seismic energy $E$ (J)	Stress drop $\delta\sigma$ (MPa)	Apparent stress $\delta a$ (MPa)
1	.395E+04	.102E+06	.106E+06	.107	.008
2	.338E+05	.141E+07	.145E+07	.106	.013
3	.150E+06	.960E+07	.975E+07	.319	.042
4	.188E+05	.697E+06	.716E+06	.105	.011
5	.285E+05	.157E+07	.160E+07	.102	.014
6	.322E+05	.613E+06	.645E+06	.144	.012
7	.580E+06	.410E+08	.415E+08	.363	.059
8	.207E+05	.390E+06	.410E+06	.095	.008
9	.208E+05	.745E+06	.766E+06	.128	.014
10	.193E+04	.555E+05	.574E+05	.050	.005
11	.447E+05	.443E+06	.488E+06	.292	.018
12	.221E+06	.145E+08	.147E+08	.367	.041
13	.252E+03	.855E+04	.880E+04	.029	.002
14	.153E+04	.105E+05	.120E+05	.061	.003
15	.428E+04	.466E+05	.508E+05	.078	.005
16	.341E+05	.435E+07	.438E+07	.169	.030
17	.415E+04	.142E+06	.146E+06	.095	.008
18	.799E+04	.178E+06	.186E+06	.079	.006
19	.543E+05	.207E+07	.212E+07	.144	.017
20	.234E+04	.380E+05	.403E+05	.054	.004
21	.391E+05	.666E+06	.705E+06	.138	.015
22	.178E+05	.234E+06	.252E+06	.112	.008
23	.172E+05	.540E+06	.557E+06	.214	.017
24	.399E+05	.825E+06	.865E+06	.202	.021
25	.472E+05	.149E+07	.154E+07	.114	.013
26	.269E+06	.240E+08	.243E+08	.452	.050
27	.291E+04	.475E+05	.504E+05	.043	.003
28	.817E+03	.170E+05	.178E+05	.036	.003
29	.427E+04	.368E+05	.410E+05	.069	.005
30	.840E+05	.117E+07	.126E+07	.160	.012
31	.423E+04	.376E+05	.418E+05	.092	.006
32	.983E+04	.153E+06	.163E+06	.120	.009
33	.322E+04	.364E+05	.396E+05	.054	.004
34	.159E+05	.812E+06	.828E+06	.164	.017
35	.193E+06	.145E+08	.147E+08	.321	.044
36	.200E+04	.301E+05	.321E+05	.052	.004
37	.312E+04	.181E+06	.184E+06	.092	.009
38	.307E+04	.109E+06	.112E+06	.079	.007
39	.378E+04	.594E+05	.632E+05	.080	.005
40	.690E+05	.469E+07	.476E+07	.279	.034
41	.231E+04	.166E+05	.189E+05	.080	.005
42	.167E+05	.336E+06	.352E+06	.171	.014
43	.589E+05	.647E+06	.706E+06	.109	.007
44	.171E+05	.134E+07	.136E+07	.147	.016

TABLE 6. SEISMIC ENERGY AND STRESS-RELEASE ESTIMATE FOR  
SEISMIC EVENTS AT POLKOWICE MINE SECTION G - 21.

Event number	P-wave energy $E_p$ (J)	S-wave energy $E_s$ (J)	Total seismic energy $E$ (J)	Stress drop $\delta\sigma$ (MPa)	Apparent stress $\delta a$ (MPa)
45	.671E+04	.164E+06	.171E+06	.115	.009
46	.132E+05	.606E+06	.619E+06	.118	.012
47	.349E+06	.180E+08	.184E+08	.555	.058
48	.462E+04	.849E+05	.895E+05	.101	.007
49	.281E+05	.198E+07	.201E+07	.187	.015
50	.179E+07	.101E+09	.103E+09	.347	.053
51	.658E+04	.208E+06	.215E+06	.127	.010
52	.923E+04	.156E+06	.165E+06	.136	.009
53	.397E+06	.238E+08	.242E+08	.463	.058
54	.101E+05	.155E+06	.165E+06	.056	.005
55	.357E+06	.259E+08	.263E+08	.460	.047
56	.498E+04	.352E+05	.402E+05	.088	.004

The values of total seismic energy range from  $1 \cdot 10^4$  to  $1 \cdot 10^8$  J. They are displayed against the values of seismic moment for seismic events from section G-32 and G-21 in Fig. 15 and 16, respectively. The scatter of data is rather small and the slope coefficient of linear regression is about 1.5 in both cases; the well-known value from classic magnitude-energy relations.

Two estimates of stress release are applied here: the modified Brune (1970, 1971) stress drop, based on the source radius from the model of Madariaga (1976) and called here the stress drop  $\delta\sigma$  and the apparent stress  $\delta_a$ , an independent parameter because of the *P*-wave contribution to the seismic energy, occasionally considered as an estimate of the dynamic stress drop (Boatwright, 1984). The values of the two estimates of stress release for seismic events at section G-32 are listed in Table 5 and those for the events at section G-21 are listed in Table 6. The stress drop ranges from 0.025 to 0.56 MPa and the apparent stress ranges from 0.002 to 0.063 MPa. The stress drop against seismic moment for seismic events from section G-32 and G-21 is shown in Fig. 17 and 18, respectively. Although the dependence of stress drop on seismic moment seems to be rather distinct, the range of stress drop values is highly limited. The apparent stress correlates quite well with seismic energy. Its values against those of seismic energy for seismic events from both sections are shown in Fig. 19 and 20, respectively.

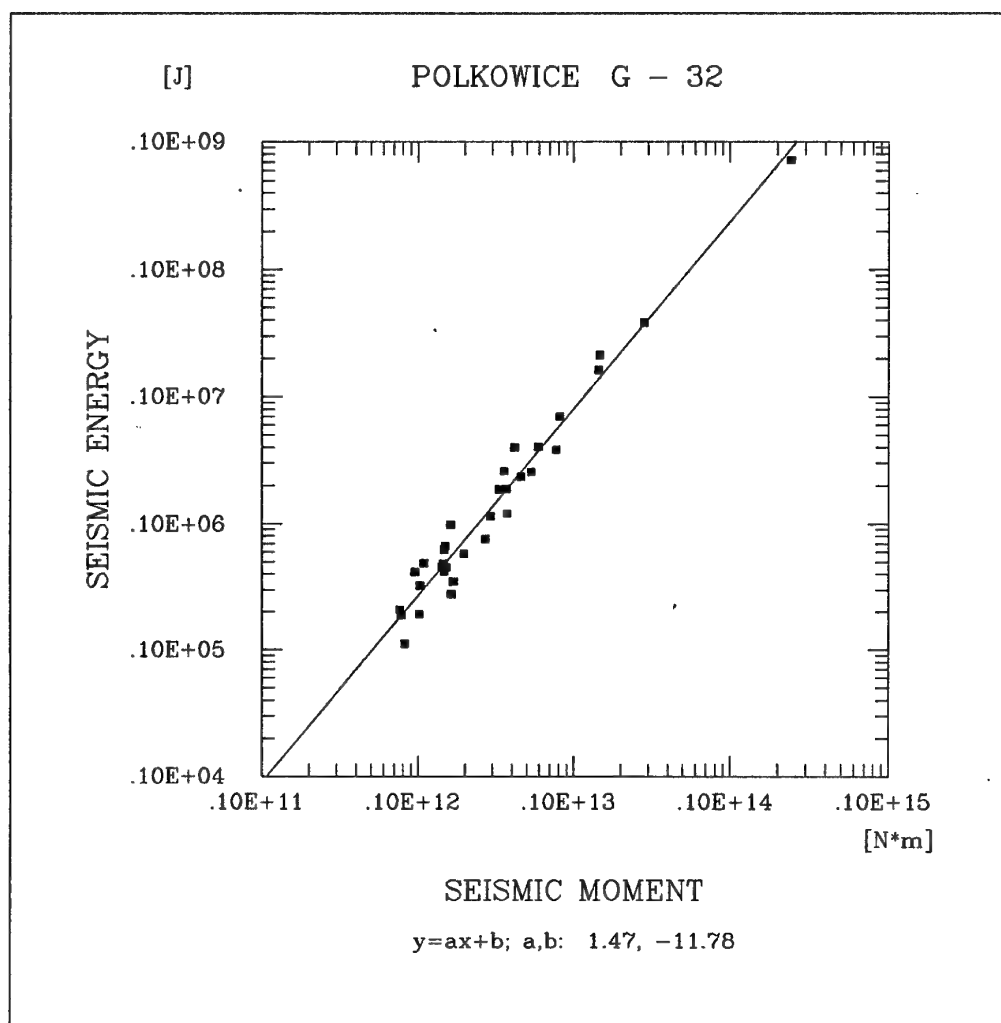


FIGURE 15. Seismic energy versus seismic moment for events from section G-32.  
The approximation of data by linear regression is also shown.

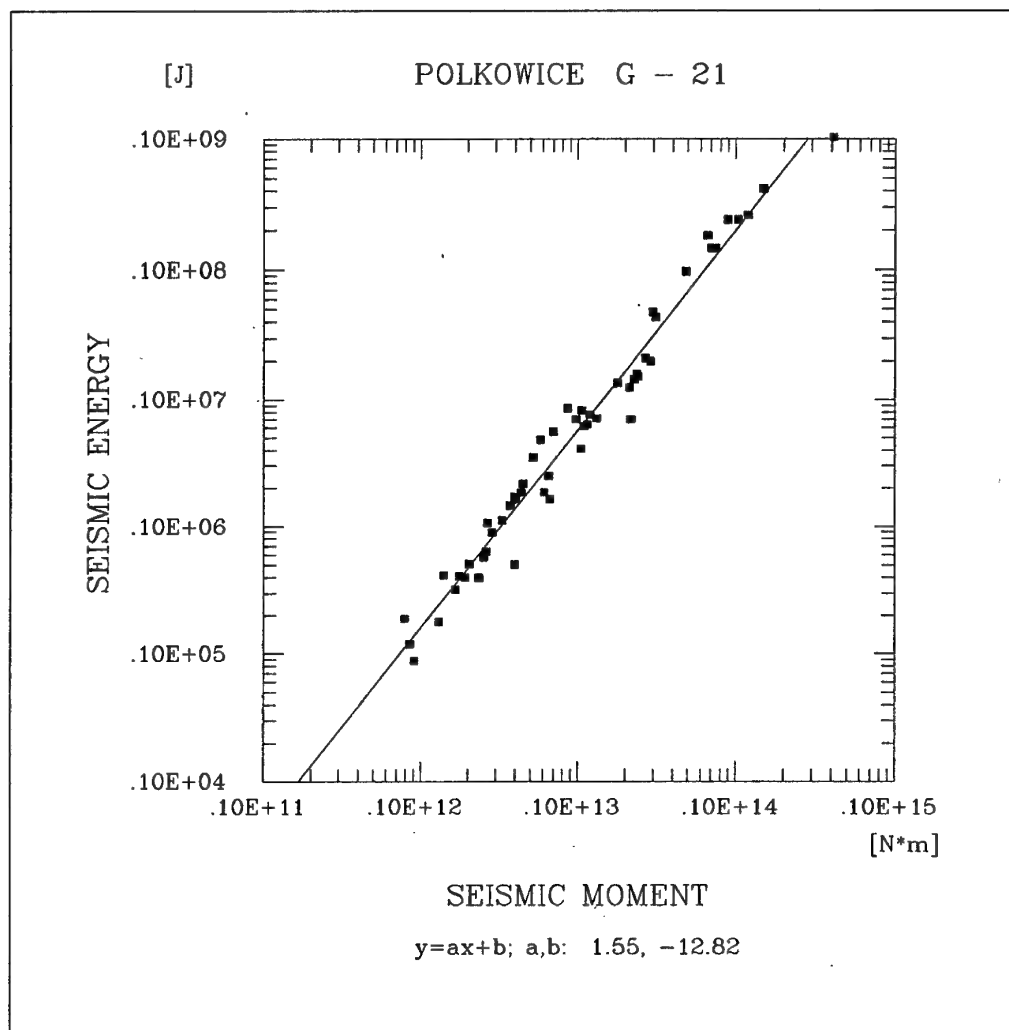


FIGURE 16. Seismic energy versus seismic moment for events from section G-21.  
The approximation of data by linear regression is also shown.



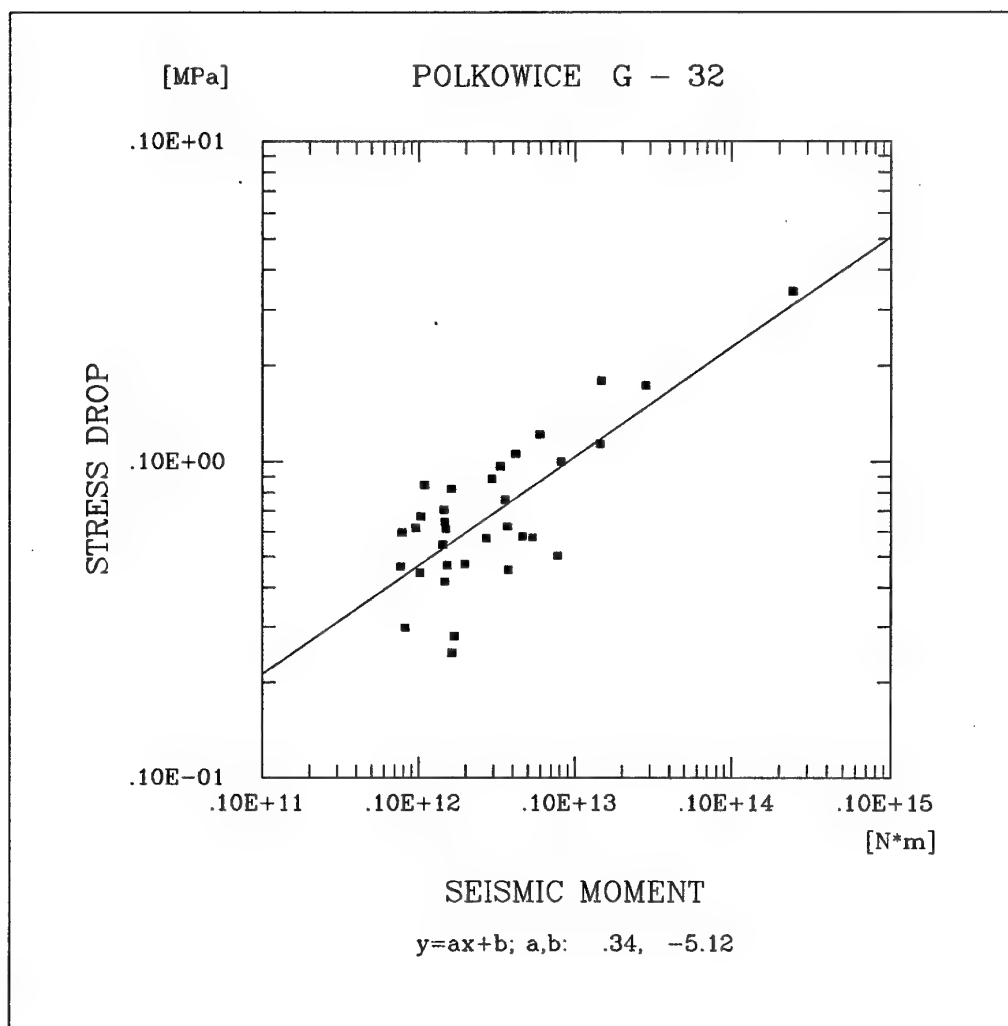


FIGURE 17. Stress drop versus seismic moment for seismic events from section G-32.

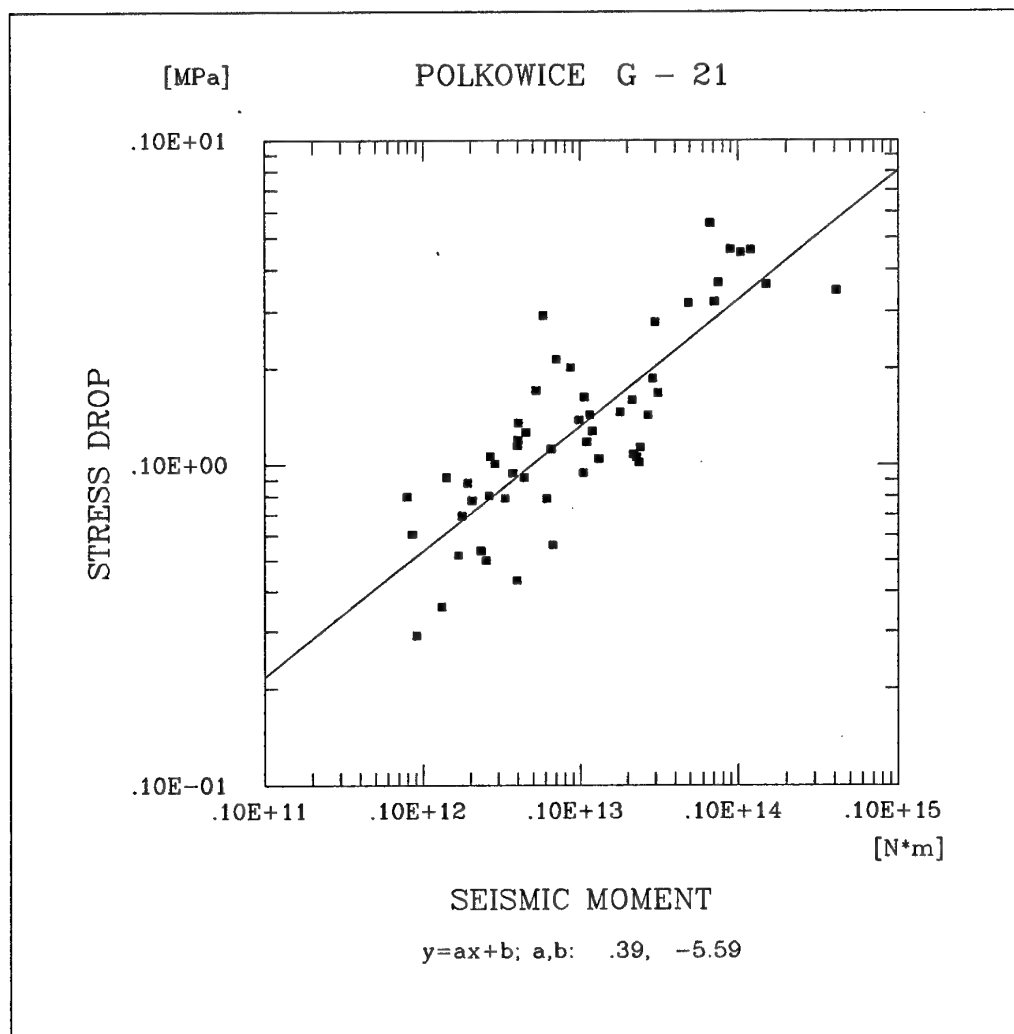


FIGURE 18. Stress drop versus seismic moment for seismic events from section G-21.

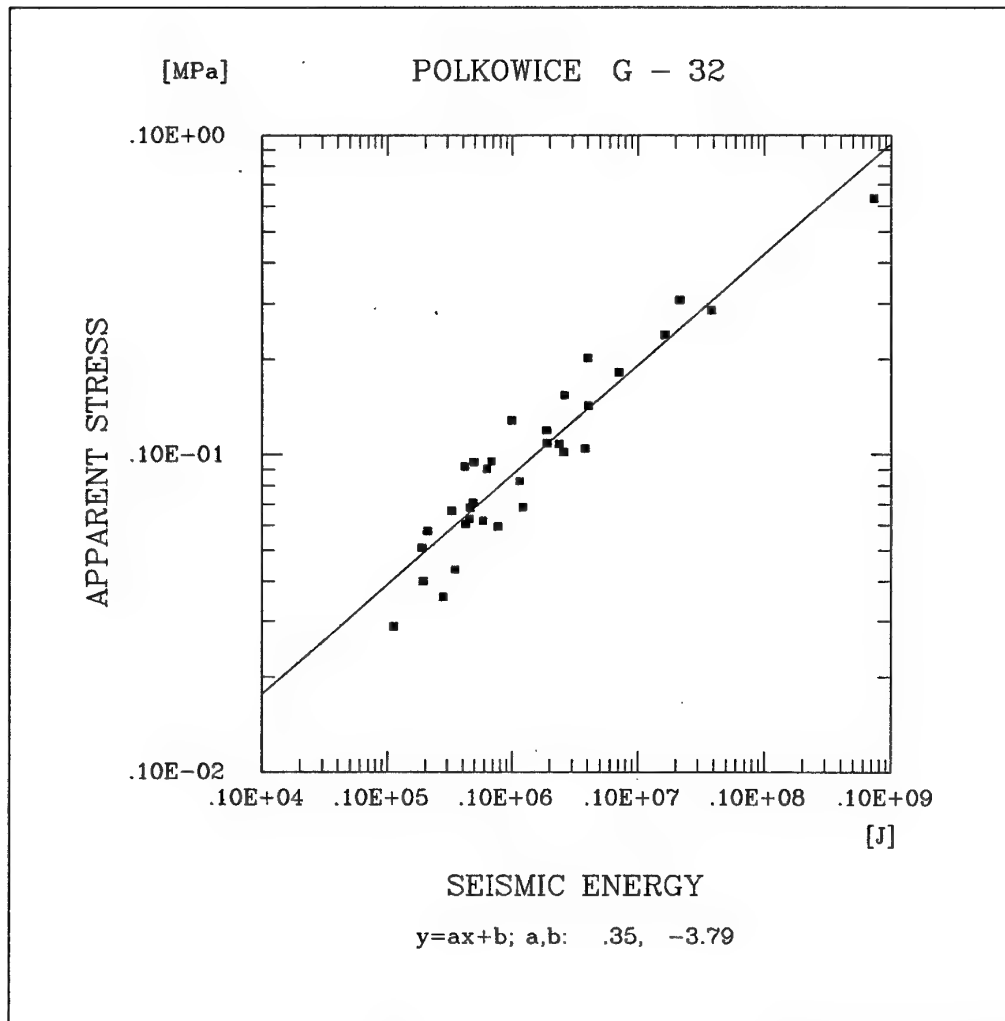


FIGURE 19. Apparent stress versus seismic energy for seismic events from section G-32.

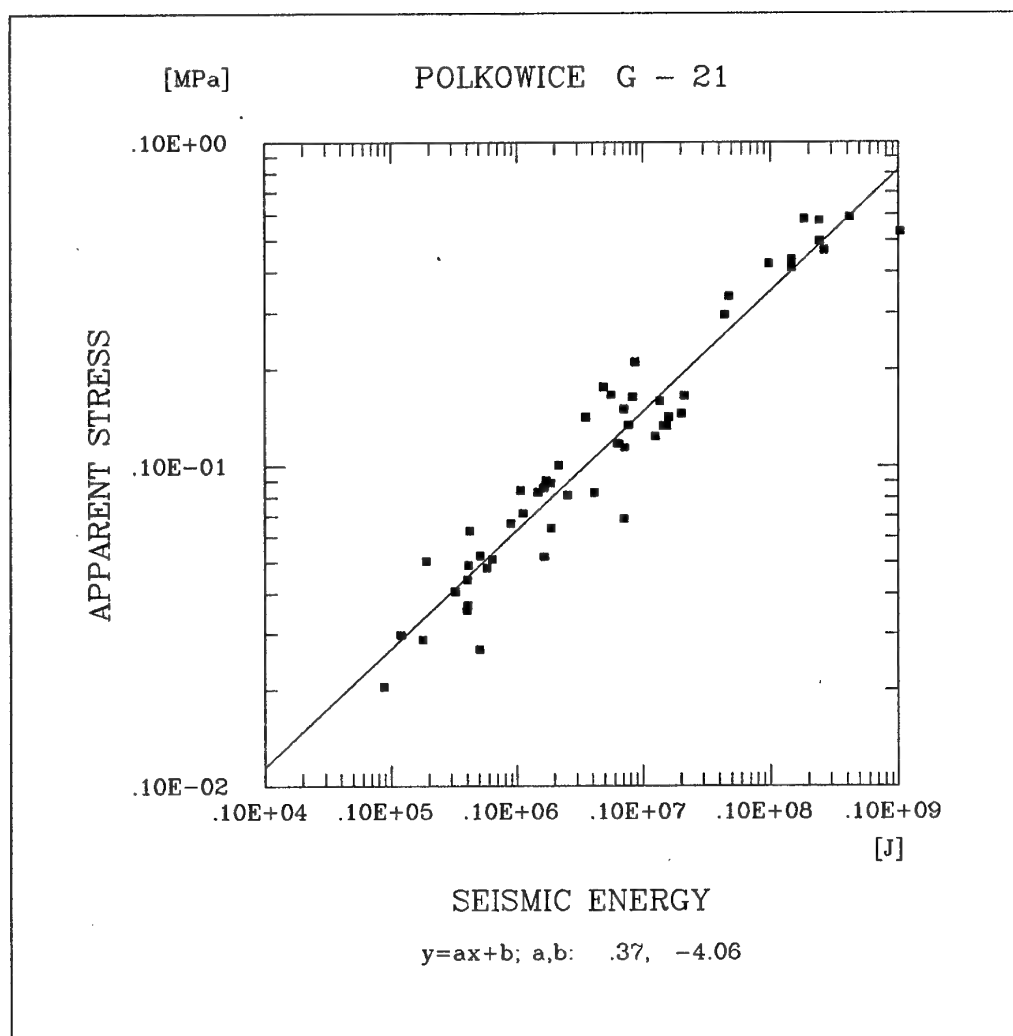


FIGURE 20. Apparent stress versus seismic energy for seismic events from section G-21.

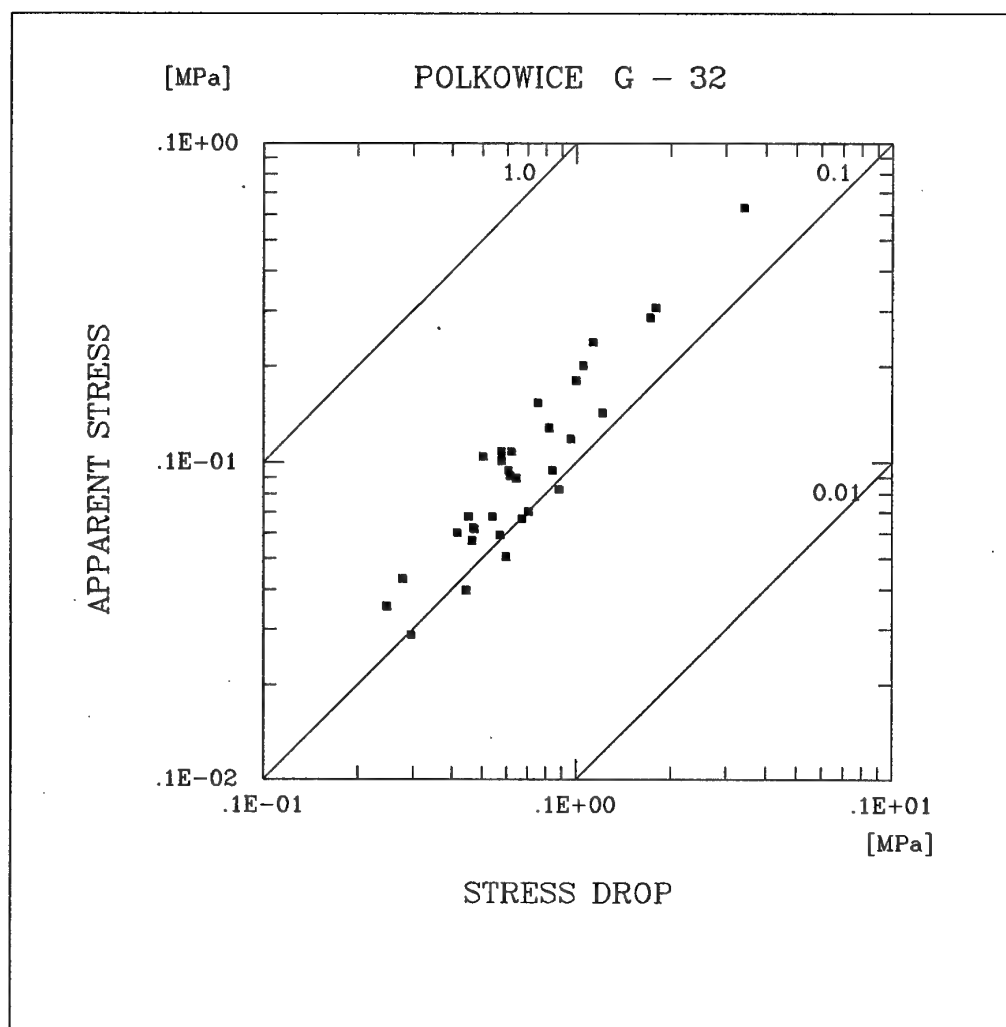


FIGURE 21. Apparent stress versus stress drop for seismic events from section G-32. The lines of constant ratio of apparent stress over stress drop are also marked.

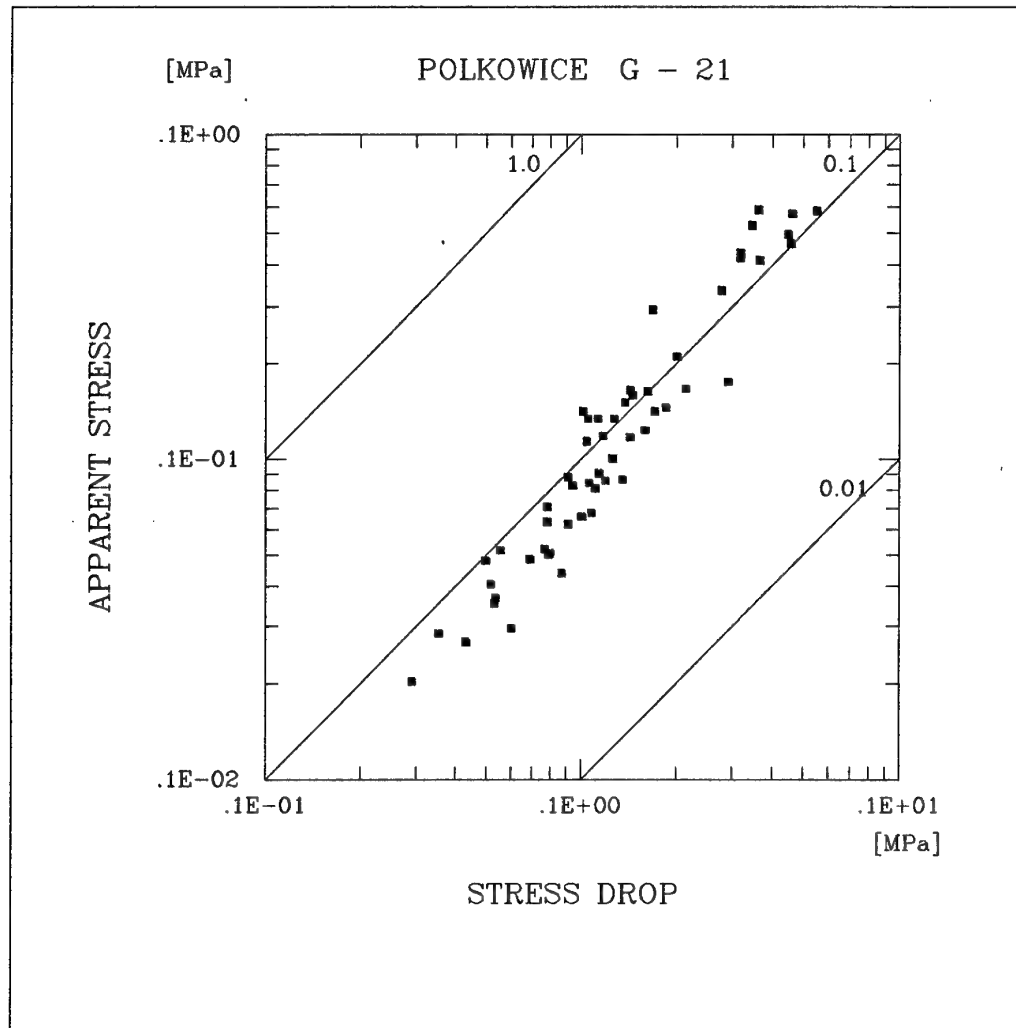


FIGURE 22. Apparent stress versus stress drop for seismic events from section G-21. The lines of constant ratio of apparent stress over stress drop are also marked.

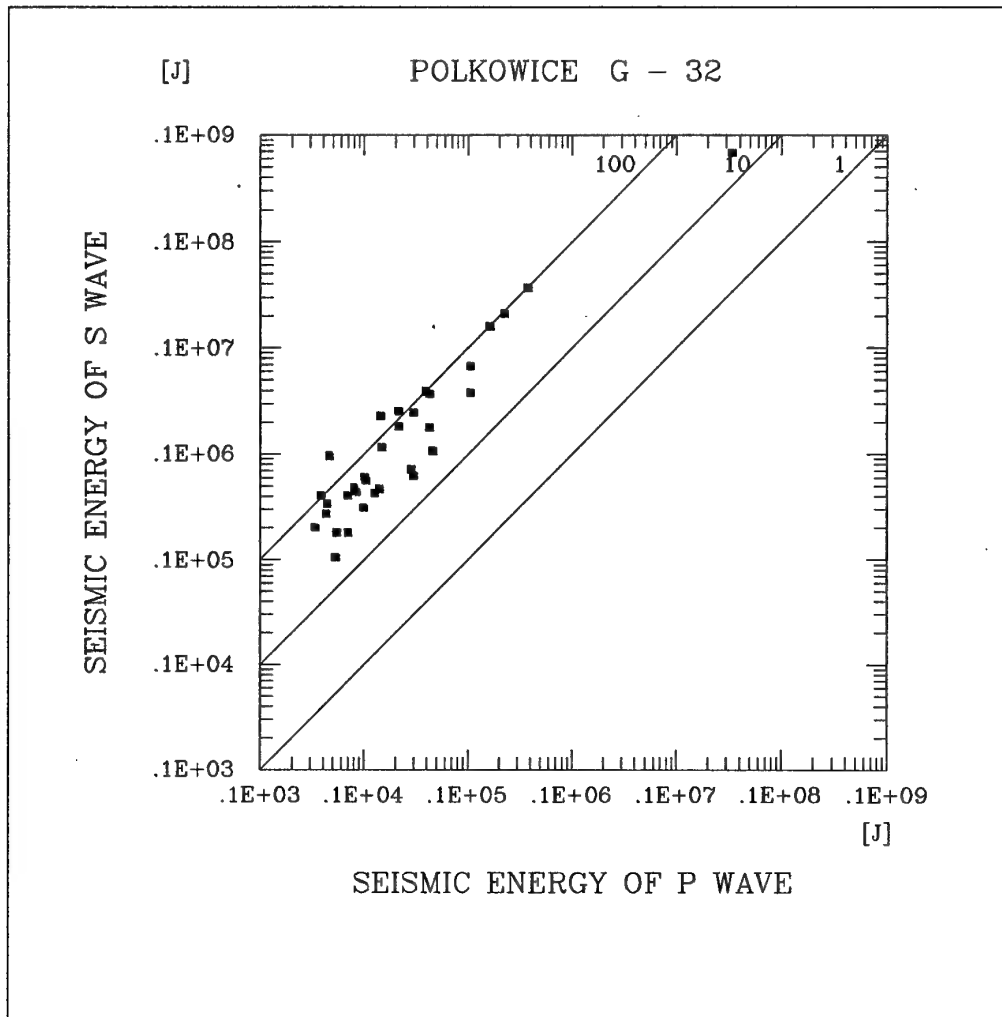


FIGURE 23. S-wave energy versus P-wave energy for seismic events from section G-32. The ratio of S- over P-wave energy equal to 1, 10, and 100 is shown by straight lines.

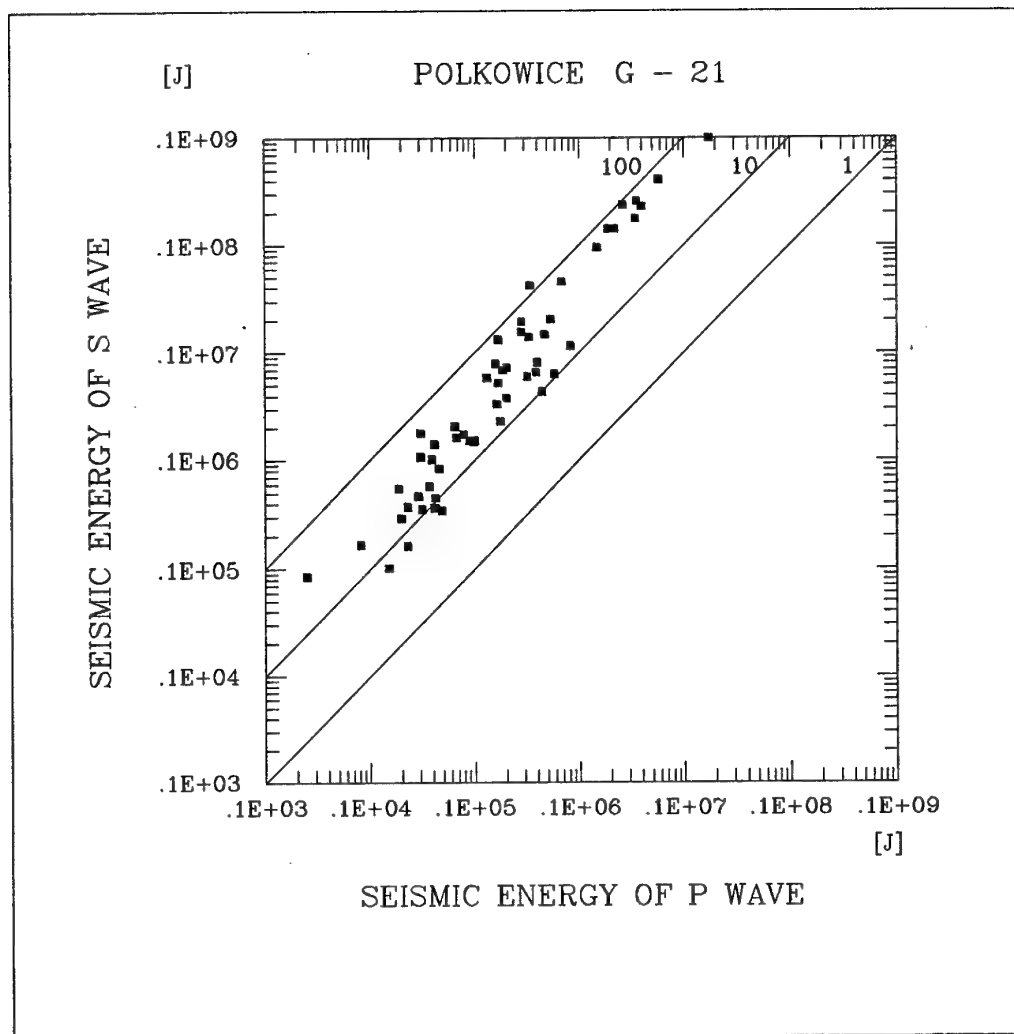


FIGURE 24. S-wave energy versus *P*-wave energy for seismic events from section G-21. The ratio of S- over *P*-wave energy equal to 1, 10, and 100 is shown by straight lines.



The display, on a logarithmic scale, of the apparent stress against stress drop for seismic events from section G-32 and G-21 is shown in Fig. 21 and 22, respectively, where the values of their ratio are indicated by straight lines. The apparent stress is roughly ten times lower than the stress drop in both cases; the result similar to that found at Western Deep Levels. S-wave energy versus P-wave energy for seismic events from section G-32 and G-21 is presented in Fig. 23 and 24, respectively, where the ratio of S-wave over P-wave energy equal to 1, 10 and 100 is also indicated by straight lines. The energy ratio from seismic events at section G-32 ranges from about 20 to 100 and that from tremors at section G-21 ranges from about 10 to 100. Surprisingly, only a few events from section G-21 are characterized by the energy ratio smaller than 10; the result considerably different from that found at Western Deep Levels.

### 5.3 Time distribution of the source parameters at section G-32

All computed source parameters of seismic events from section G-32 show similar distribution in time. There is one outstanding event with moment magnitude of 2.7, which occurred in the middle of the series on November 13, 1994 (number 13 in Tables 1, 3 and 5), preceded by an event of magnitude 2.3. Their source parameters have the highest values, while those of the other events are randomly distributed in time. The distribution of seismic moment, seismic energy and source radius versus time is shown in Fig. 25. Since the time intervals between the occurrence of consecutive events is irregular, a better presentation of time distribution of the source parameters is achieved when the source parameters are displayed against the number of consecutive seismic events forming the selected series. Such a presentation for the seismic moment, energy and source radius is shown in Fig. 26 and for the seismic moment, stress drop and apparent stress is given in Fig. 27. A similar presentation for the seismic energy of P and S waves and for the total seismic energy is shown in Fig. 28. The only pattern observed in these figures is the presence of small seismic events, characterized by low values of their source parameters, following directly the main event and forming a kind of quiescent interval before the occurrence of larger events at the end of our series.

POLKOWICE G - 32

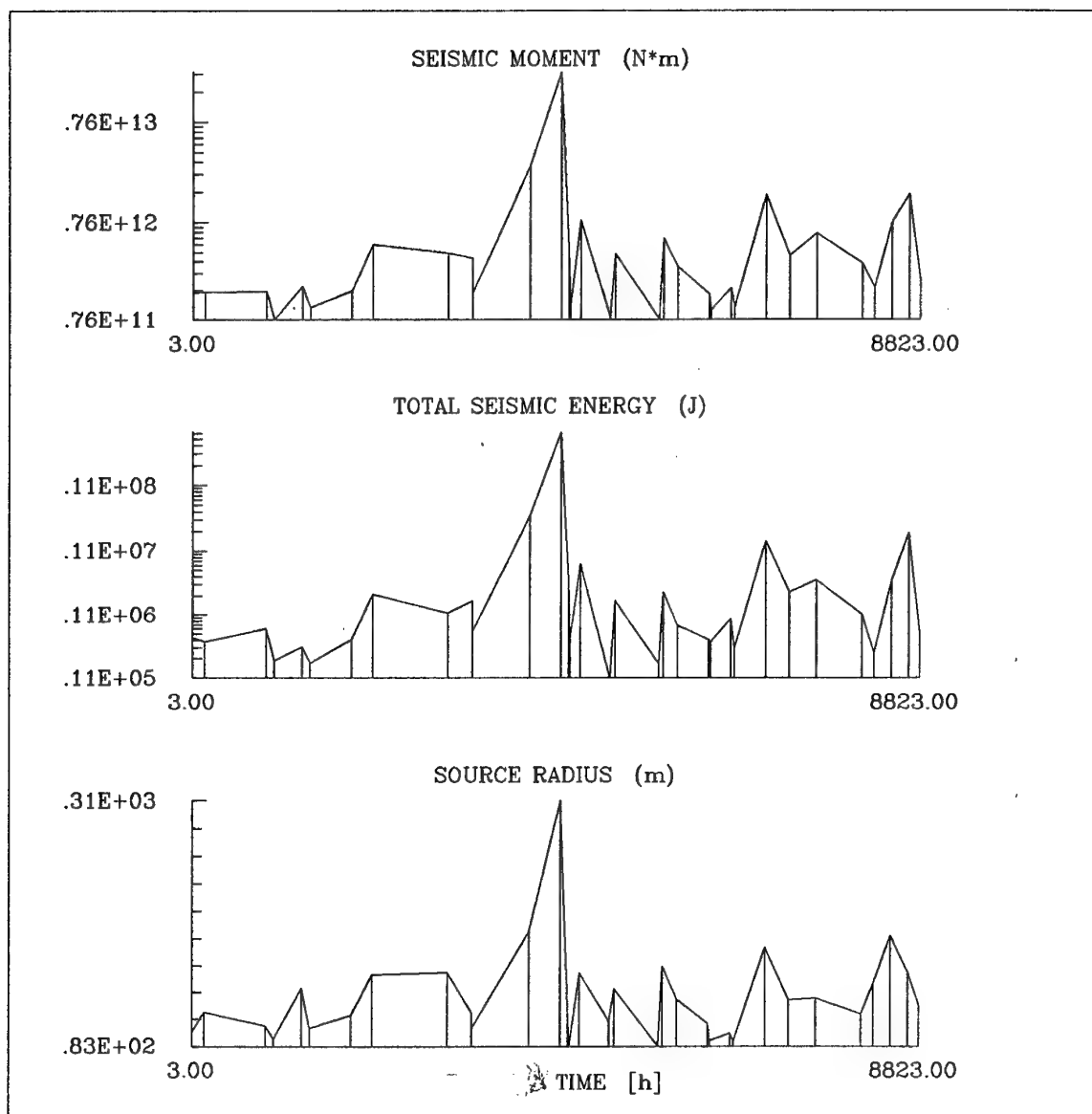


FIGURE 25. Seismic moment, seismic energy and source radius versus time for seismic events from section G-32.

POLKOWICE G - 32

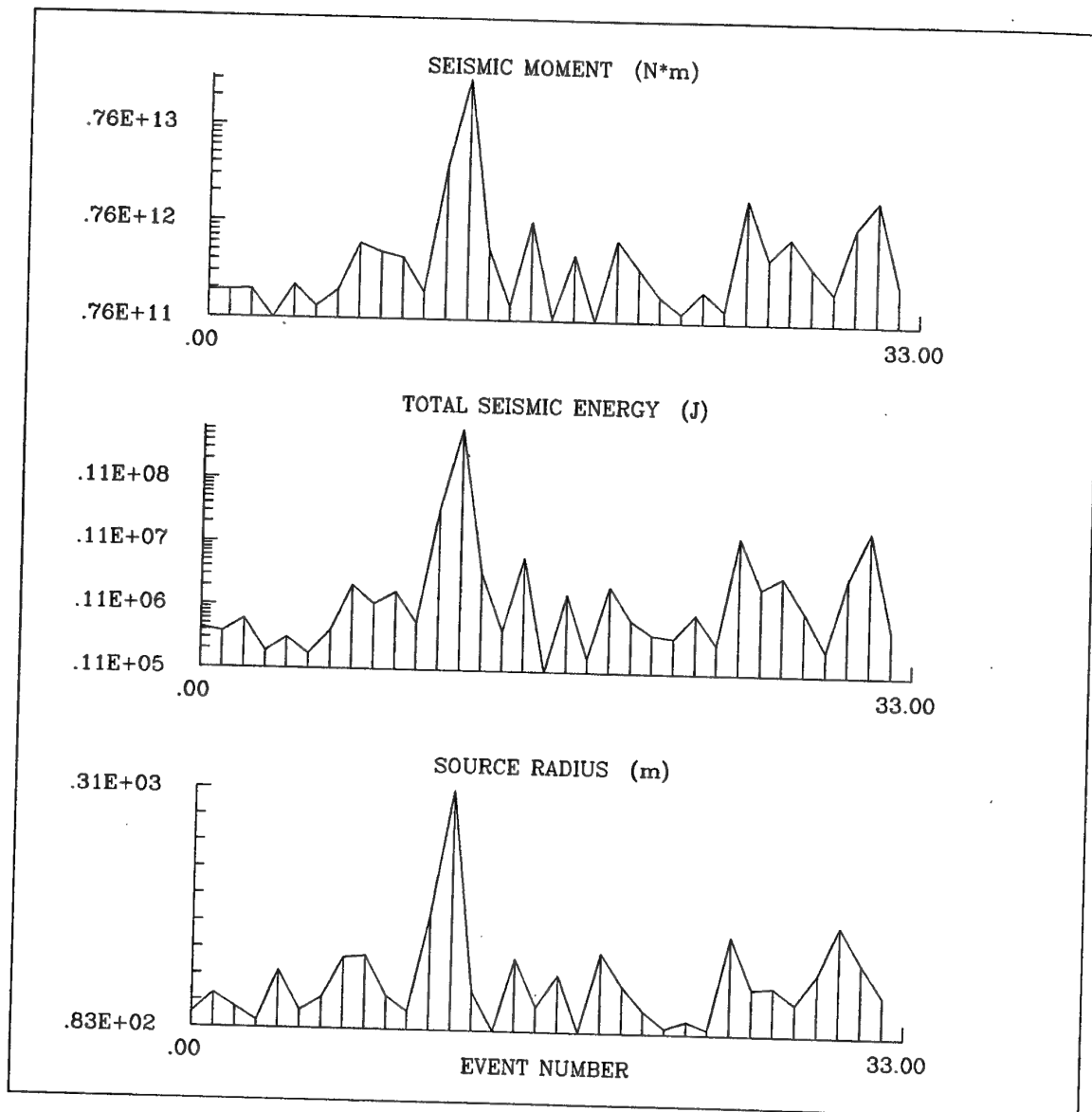


FIGURE 26. Seismic moment, seismic energy and source radius versus the number of consecutive seismic events from section G-32.

POLKOWICE G - 32

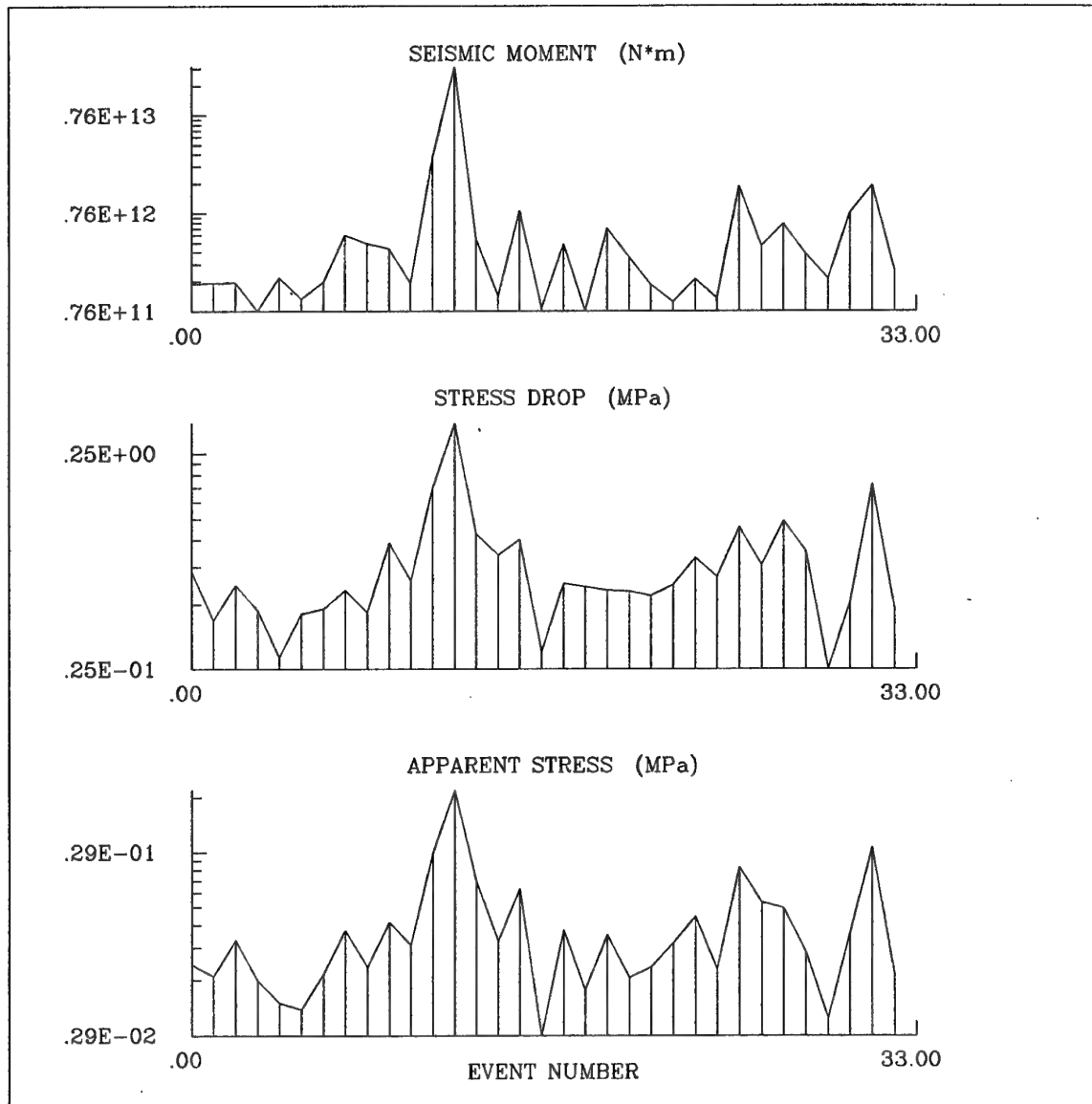


FIGURE 27. Seismic moment, stress drop and apparent stress versus the number of consecutive seismic events from section G-32.

# POLKOWICE G - 32

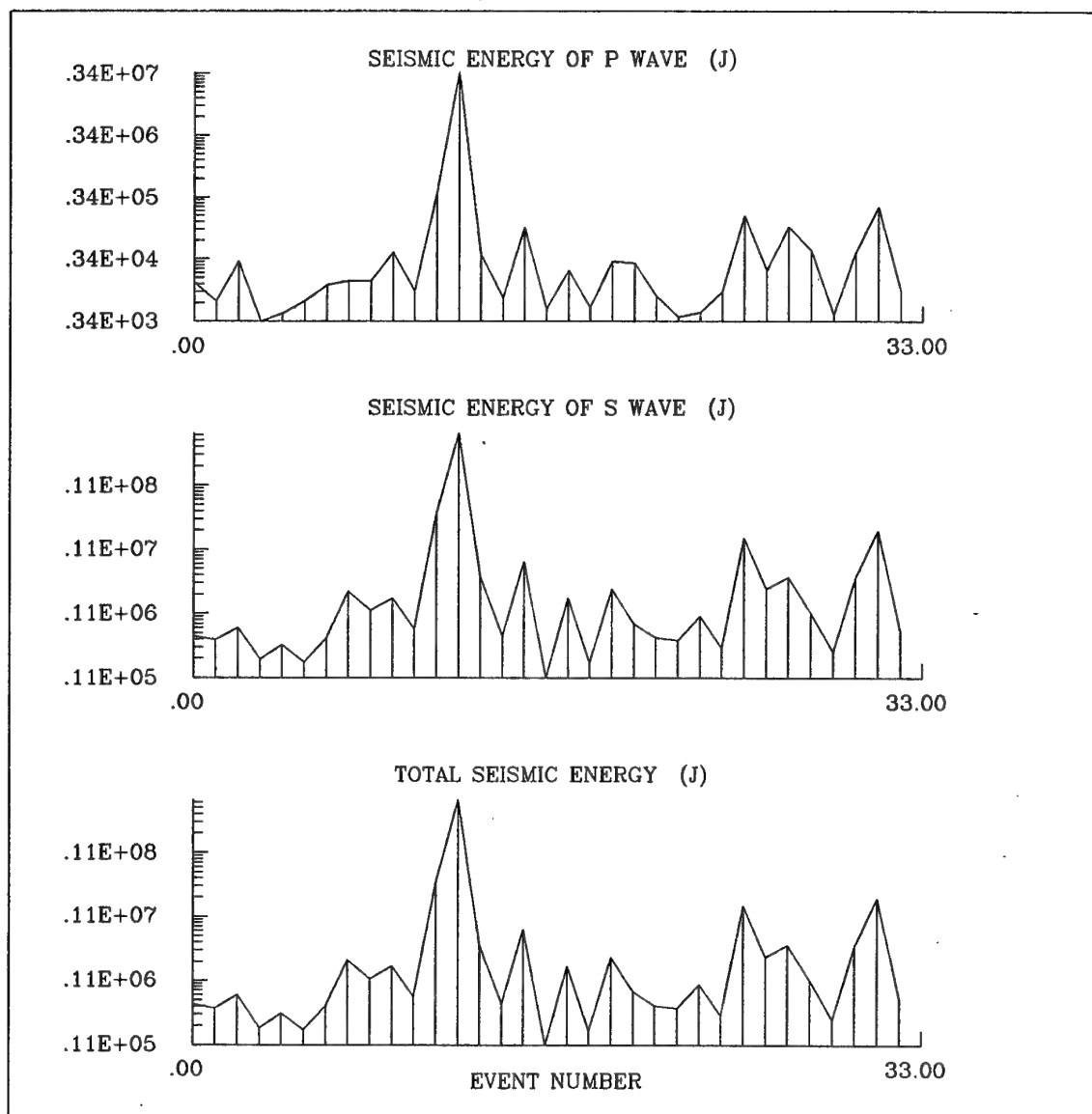


FIGURE 28. P-wave energy, S-wave energy and total seismic energy versus the number of consecutive seismic events from section G-32.

POLKOWICE G - 21

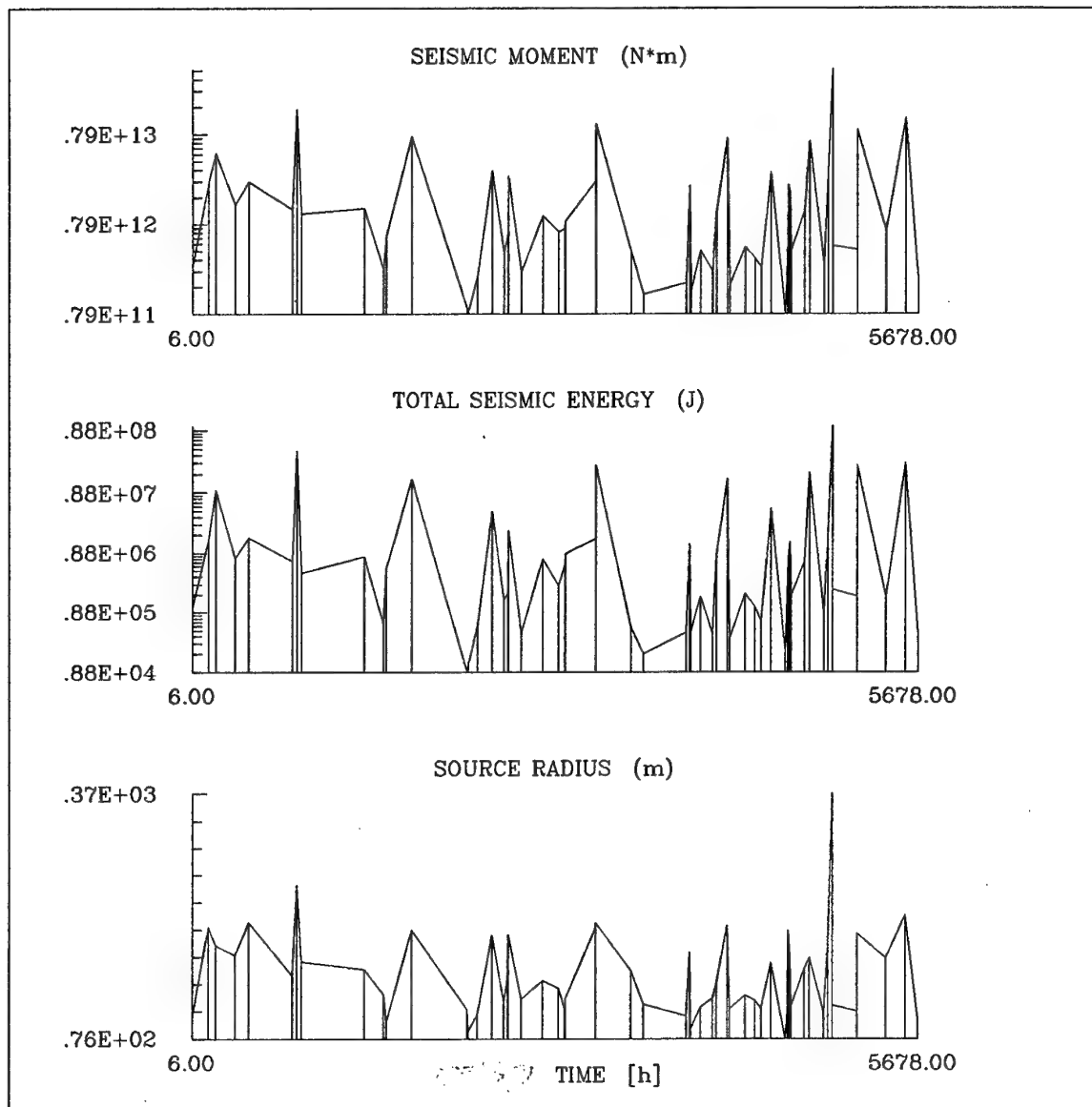


FIGURE 29. Seismic moment, seismic energy and source radius versus time for seismic events from section G-21.

POLKOWICE G - 21

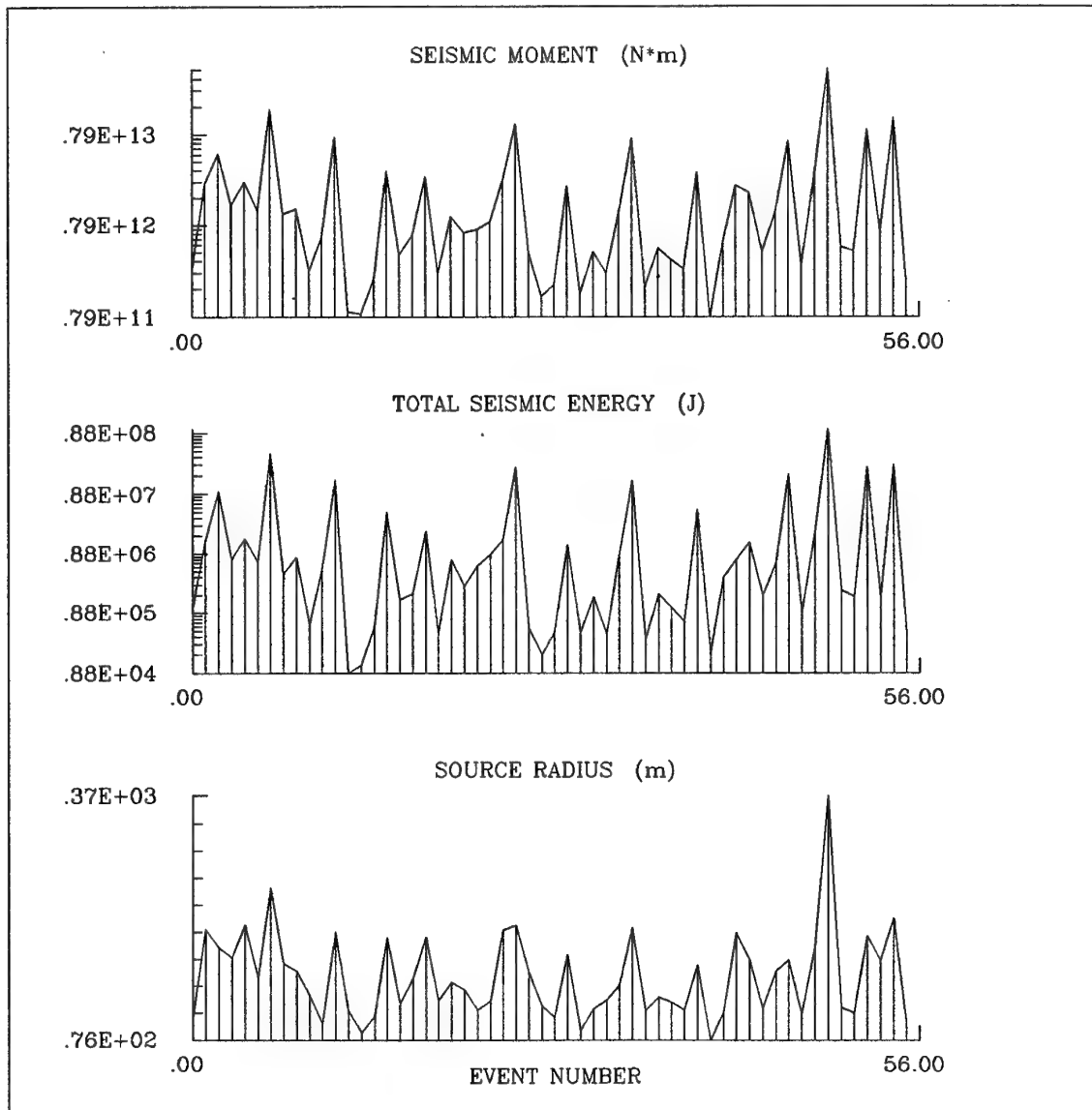


FIGURE 30. Seismic moment, seismic energy and source radius versus the number of consecutive seismic events from section G-21.

POLKOWICE G - 21

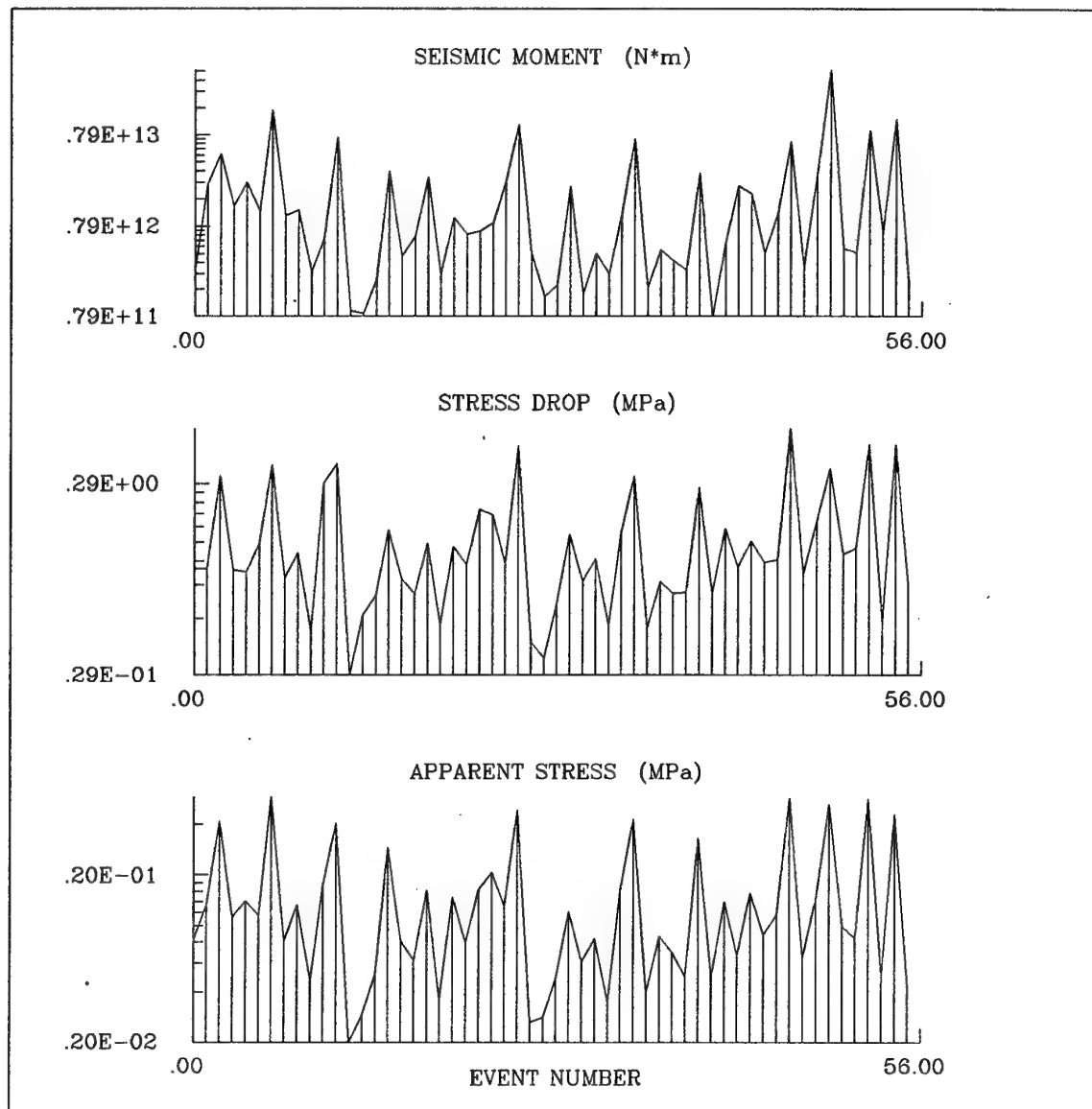


FIGURE 31. Seismic moment, stress drop and apparent stress versus the number of consecutive seismic events from section G-21.



POLKOWICE G - 21

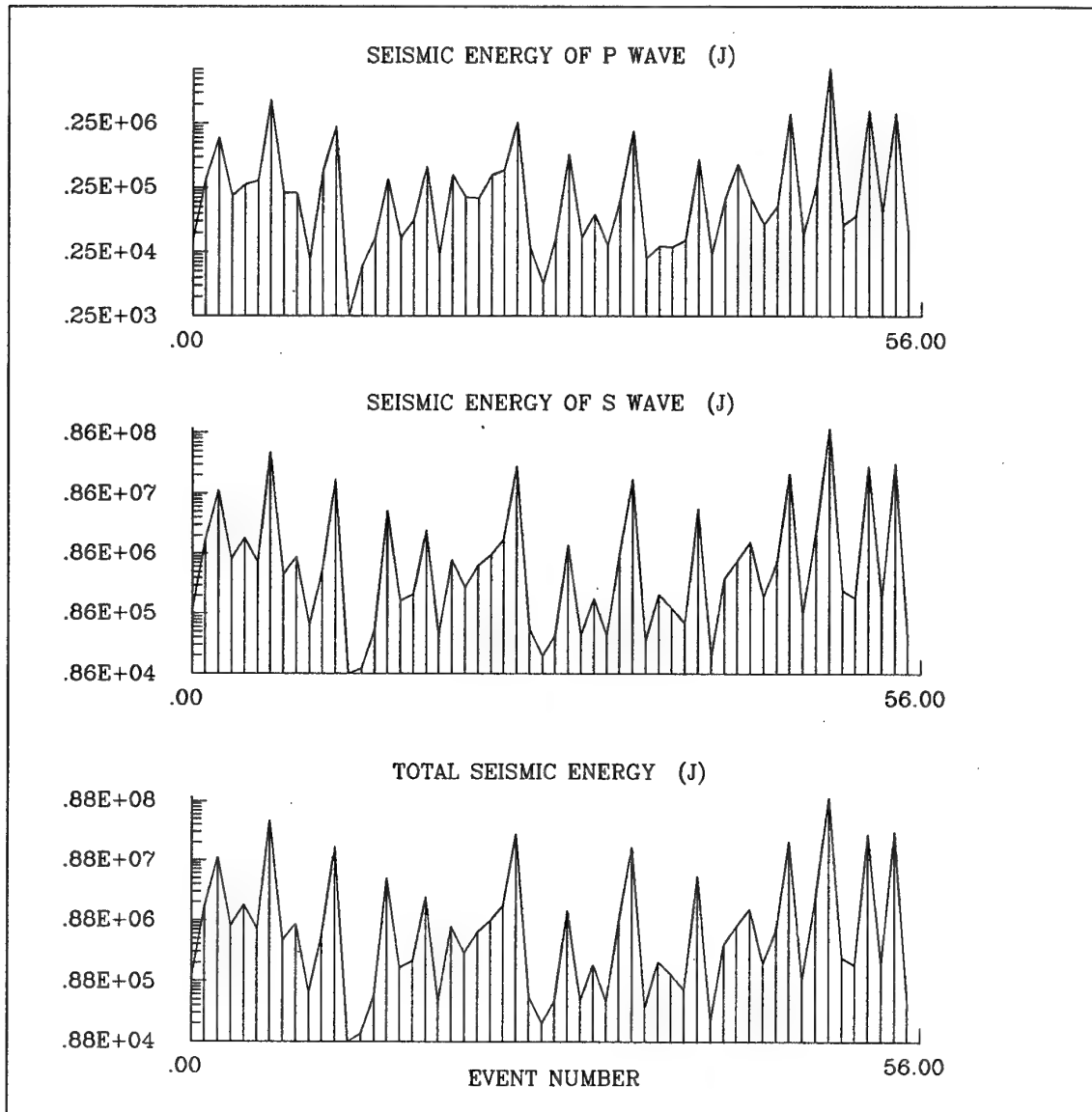


FIGURE 32. P-wave energy, S-wave energy and total seismic energy versus the number of consecutive seismic events from section G-21.

#### 5.4 Time distribution of the source parameters at section G-21

The time distribution of the source parameters of seismic events from section G-21 is less regular even than that from section G-32. There are eight seismic events with moment magnitude not smaller than 2.5 and one outstanding event with magnitude 3.0, which occurred at the end of the series on April 28, 1995 (number 50 in Tables 2, 4 and 6). The second largest event of magnitude 2.7 occurred at the beginning of the series on November 4, 1994 (number 7 in Tables 2, 4 and 6).

The two events are more distinctly marked by their source radius rather than by their seismic moment or seismic energy. The distribution of seismic moment, seismic energy and source radius versus time is shown in Fig. 29. The same distribution against the number of consecutive events forming the series is shown in Fig. 30. The distribution of stress drop and apparent stress against the number of consecutive events is shown in Fig. 31. Their values are of the same order for the all largest events. Similar situation is also observed in Fig. 32 where the distribution of *P*- and *S*-wave energy and total seismic energy against the number of consecutive events is presented.

## 6. MOMENT TENSOR INVERSION

### 6.1 The method

There are various methods of inversion for moment tensor components. The inversion can be done in the time or frequency domain, and different data can be used separately or in combination. These problems were recently reviewed by Gibowicz (1993).

In many applications a point source approximation may be quite satisfactory. If the source dimensions are small in comparison to the observed wavelengths of seismic waves, and assuming that all components of the time dependent seismic moment tensor  $M_{ij}$  have the same time dependence  $s(t)$ , the case known as synchronous source (Silver and Jordan, 1982), the displacement  $u_k(\mathbf{x}, t)$  can be written as

$$u_k(\mathbf{x}, t) = M_{ij} [G_{ki,j} * s(t)], \quad (1)$$

where  $G_{ki,j}$  are the Green's functions containing the propagation effects between the source and the receiver and the comma between indices denotes partial derivatives with respect to the coordinates after the comma,  $s(t)$  is often called the source time function, and the asterisk  $*$  denotes the temporal convolution. Thus the displacement  $u_k$  is a linear function of the moment tensor elements and the terms in the square brackets.

The displacement in the frequency domain, corresponding to the formulation in (1), can be written as

$$u_k(\mathbf{x}, f) = M_{ij}(f) G_{ki,j}(f) \quad (2)$$

for each frequency  $f$ . Both approaches (1) and (2) lead to linear inversions

in the time or frequency domain, respectively, for which a number of fast computational algorithms are available.

Both equations either (1) or (2) can be written in a matrix form as

$$\mathbf{u} = \mathbf{G} \mathbf{m}, \quad (3)$$

where in the time domain, the vector  $\mathbf{u}$  consists of  $n$  sampled values of the observed ground displacement at various stations,  $\mathbf{G}$  is a  $n \times 6$  matrix containing the Green's functions calculated using an appropriate algorithm and earth model, and  $\mathbf{m} = (M_{11}, M_{12}, M_{22}, M_{13}, M_{23}, M_{33})$  is a vector containing the six moment tensor elements to be determined. In the frequency domain, equations (3) are written separately for each frequency.

The inversion of moment tensor in the time domain is used here. In the time domain the source time function  $s(t)$  must be specified in advance, since the matrix  $\mathbf{G}$  in the time domain contains the Green's functions derivatives convolved with the source time function. For the source time function  $s(t)$ , two forms are used most commonly: the Haskell (1964) type

$$s(t) = \begin{cases} 0 & \text{for } t < 0 \\ t/T & \text{for } 0 \leq t \leq T \\ 1 & \text{for } t > T \end{cases} \quad (4)$$

and the Brune (1970) type

$$s(t) = \begin{cases} 0 & \text{for } t \leq 0 \\ 1 - \exp(-t/\tau) & \text{for } t > 0 \end{cases} \quad (5)$$

where  $T$  or  $\tau$  are parameters associated with the duration of the rupture. The source time function of the Haskell type is used here. Its time derivatives

$$\dot{s}(t) = \begin{cases} 1/T & \text{for } 0 < t < T \\ 0 & \text{for } t < 0 \text{ and } t > T \end{cases} \quad (6)$$

are simpler to use than the time derivatives of Brune's function, and in practical applications the Haskell function fits the data equally well as the Brune function. The parameter  $T$  can be estimated from the time interval between the first onset of the wave and its maximum amplitude.

The main difficulty in the moment tensor inversion is a proper calculation of Green's functions for geologically complex media. The simplest approach in the time domain is to use directly the source radiation formulation for  $P$ ,  $SV$  or  $SH$  waves. This approach was used by Fitch *et al.* (1980), De Natale *et al.* (1987), Wiejacz (1992, 1995), and others, and is used here. The displacement amplitudes of the first arrivals of  $P$  and  $SV$  waves are given by (e. g., Fitch *et al.*, 1980; De Natale *et al.*, 1987)

$$u^P(\mathbf{x}, t) = \frac{1}{4\pi\rho\alpha^3 r} \left[ \bar{\gamma} M \dot{s} (t - r/\alpha) \bar{\gamma} \right] \bar{l}, \quad (7)$$

$$u^{SV}(\mathbf{x}, t) = \frac{1}{4\pi\rho\beta^3 r} \left[ \bar{p} M \dot{s} (t - r/\beta) \bar{\gamma} \right] \bar{p}, \quad (8)$$

where  $\dot{s}$  is the time derivative of the source time function;  $\rho$  is the density of the medium;  $\alpha$  and  $\beta$  are the velocities of  $P$  and  $S$  waves, respectively;  $r$  is the distance between the source and sensor; and  $\bar{\gamma}$ ,  $\bar{l}$ , and  $\bar{p}$  are unitary vectors;  $\bar{\gamma}$  is the direction the wave leaves the source,  $\bar{l}$  is the direction of propagation of the wave as it arrives at the seismometer, and  $\bar{p}$  is perpendicular to  $\bar{l}$  in the vertical plane containing  $\bar{l}$ . Once the displacements  $u$  are known, the calculation of the unitary vectors  $\bar{\gamma}$ ,  $\bar{l}$ , and  $\bar{p}$  must be performed, which may be done after adoption of a specific velocity model.

Finding a moment tensor requires solution of a set of  $n$  equations of type (7) or (8). Since the moment tensor has six independent components, there must be at least six such equations, but usually more than that are needed. Additional constraints may be imposed on the solution. The most common constraints require that either the trace of the moment tensor or the trace

and the determinant of the tensor vanish. The condition of zero trace automatically excludes the volume change type mechanism, and since zero trace means also that  $M_{33} = -(M_{11} + M_{22})$ , only five components remain independent. The constraint of zero trace and zero determinant limits the solution to the double-couple source. The null determinant condition is nonlinear, forcing the use of the Lagrange multiplier scheme in order to find the solution (e. g., Oncescu, 1986).

Typically the number of equations (7) and (8) greatly exceeds the number of unknown variables. If we rewrite the set of equations into a  $A m = u$  form, the best solution of this over-determined problem is normally expected to be such  $m_0$ , for which

$$S_2 = \sum_{i=1}^n \left[ u_{z(i)}^c - (A m_0) \right]^2 = \min, \quad (9)$$

where  $c$  is either  $P$  or  $SV$ . Such solution is commonly referred to as a L2-norm solution. A series of tests run on synthetic data has shown, however, that such solutions may be prone to considerable errors; a single erroneous observation, if its value is large, may affect the whole solution. In some cases it is safer therefore to use the L1-norm solution, which requires that

$$S_1 = \sum_{i=1}^n \left| u_{z(i)}^c - (A m_0) \right| = \min. \quad (10)$$

## 6.2 Space distribution of the source mechanisms at section G-32

The first  $P$ -wave motion amplitudes were inverted in the time domain to produce three types of seismic moment tensors: the full tensor, the deviatoric tensor, and the double couple tensor. The inversion was performed using L2 norm. L1-norm calculations, which have been performed for selected events, provided similar results.

For some events, the full moment tensor solutions are different from the other two, often having a large non-shearing components and most, if not all,

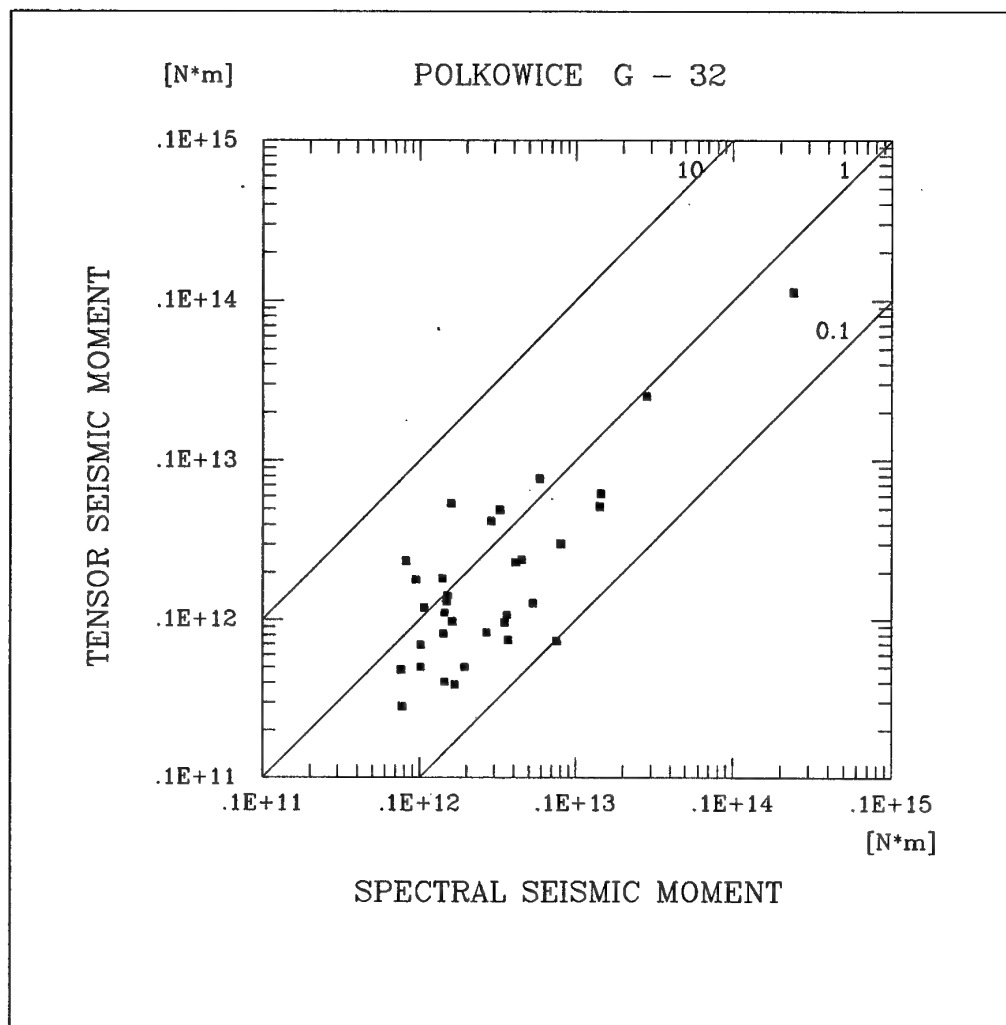


FIGURE 33. Seismic moment estimated from the moment tensor inversion versus that estimated from the spectra for seismic events from section G-32.

TABLE 7. FULL MOMENT TENSOR SOLUTIONS FOR SEISMIC EVENTS AT SECTION G-32

#	Seismic moment tensor components							t0	M0	ERR				P-axis		T-axis		B-axis		QI
	M11	M12	M13	M22	M23	M33	ISO%				CLVD%	DC%	ΦP	δP	ΦT	δT	ΦB	δB		
1	2.3	4.4	1.2	5.3	-3.3	-5.0	12.2	7.8	.35	10.2	3.6	86.2	129.8	62.8	237.0	8.7	331.1	25.6	.44	
2	-2.0	1.9	.7	1.0	-2.7	1.8	11.0	3.9	.42	6.7	2.5	90.8	145.4	21.6	259.8	46.2	38.8	35.9	.27	
3	-11.1	4.8	4.0	-1.0	2.0	7.7	19.7	11.6	1.12	-9.3	-7.0	83.7	160.3	8.4	49.3	87.5	253.5	20.8	.48	
4	1.6	1.0	.7	-.1	-1.5	-4.3	11.2	3.8	.22	-13.5	-14.2	72.3	115.6	68.8	25.3	.1	295.3	21.2	.39	
5	-3.6	-.3	1.3	.2	1.8	2.8	14.3	3.5	.26	-4.8	6.9	88.2	189.3	13.1	71.9	63.2	285.0	23.0	.28	
6	-5.0	1.8	.5	-2.6	2.1	1.8	14.6	3.5	.58	-31.9	10.5	57.6	329.3	4.8	69.4	64.6	237.1	24.9	.47	
7	4.9	4.2	3.7	8.7	2.0	-15.6	16.2	13.9	.75	-3.0	-13.8	83.2	198.0	80.1	55.6	7.8	324.8	5.9	.58	
8	-14.6	-2.8	1.9	-13.0	.1	27.6	15.1	16.8	.83	.2	65.1	34.7	216.7	2.0	358.3	87.4	126.7	1.6	.54	
9	-4.3	-4.9	2.4	-3.0	-2.2	3.4	15.8	7.3	1.08	-14.5	-2.6	82.9	220.4	2.2	313.5	53.9	128.8	36.0	.45	
10	8.1	-4.4	-.5	5.8	-8.1	-52.2	15.9	38.7	1.28	-15.0	-18.7	66.3	82.7	82.0	319.2	4.4	228.7	6.6	.57	
11	-4.7	5.7	3.3	-6.3	-.3	6.4	14.0	9.8	.63	-11.3	-7.9	80.8	132.5	7.9	19.3	70.7	225.0	17.5	.34	
12	78.2	24.2	26.1	2.1	-18.3	-254.0	20.9	192.0	7.04	-15.7	-15.0	69.3	136.9	83.5	15.3	3.4	285.0	5.6	.67	
13	-323.0	-72.4	635.0	-39.8	-31.6	-764.0	31.0	869.0	94.50	-20.6	-16.7	82.7	181.4	54.5	334.5	32.4	72.8	12.8	.62	
14	8.3	2.9	9.1	.8	4.9	-20.1	17.3	18.8	1.50	-11.9	-11.7	76.3	211.8	72.3	21.2	17.5	112.2	3.1	.58	
15	4.3	1.2	2.5	-.4	7.5	-9.6	12.4	10.9	.76	-8.9	-17.4	73.6	259.8	61.1	35.7	21.6	133.3	18.2	.39	
16	8.5	6.8	22.2	-.8	2.9	-22.4	18.0	28.9	2.09	-13.0	-4.8	82.1	177.6	62.3	19.7	26.0	285.2	9.0	.66	
17	4.0	4.4	7.0	3.7	3.1	-15.1	13.8	14.4	1.18	-11.1	-10.2	78.7	195.1	72.4	40.1	16.0	308.0	7.0	.49	
18	-15.4	-.3	-5.2	-1.1	-3.9	24.3	16.8	21.4	.82	12.1	19.9	68.0	3.0	7.6	228.7	79.1	94.0	7.7	.61	
19	-3.8	3.0	4.4	-1.6	1.9	9.9	15.8	9.5	.55	16.1	25.7	58.2	150.8	10.1	33.5	68.8	244.2	18.5	.67	
20	-.4	.1	1.3	.4	1.8	-1.6	10.0	2.6	.27	-14.7	-7.4	78.0	226.5	55.8	64.4	32.9	329.0	8.3	.20	
21	11.7	3.1	5.6	-2.4	-1.9	-10.1	18.5	11.4	1.10	-2.0	15.1	82.8	133.6	68.6	9.7	12.3	275.8	17.2	.60	
22	.4	4.2	3.6	1.0	-6.1	.8	13.7	4.9	.86	4.6	-18.7	76.7	130.7	36.7	261.4	41.2	18.1	27.2	.44	
23	3.9	9.4	12.8	-3.3	9.3	.4	18.5	12.4	1.12	3.1	82.9	14.0	236.7	51.7	35.1	36.3	133.0	10.6	.42	
24	3.5	-3.5	9.6	-.3	-5.3	12.4	13.3	14.7	.35	40.0	56.7	3.3	189.9	29.6	330.5	53.8	88.5	19.1	.35	
25	3.6	-.7	28.3	.6	-2.6	39.7	14.3	40.0	2.83	35.5	34.4	30.1	176.5	28.8	354.4	61.2	86.0	.9	.21	
26	1.1	4.0	2.3	5.2	-1.8	-4.0	13.0	6.8	.46	10.0	2.7	87.3	146.6	57.4	239.2	1.7	330.2	32.5	.47	
27	-12.9	3.2	41.0	6.9	-4.6	-23.5	24.0	45.7	5.14	-10.4	-18.2	71.4	172.9	48.5	357.0	41.4	265.1	2.0	.59	
28	5.4	-.1	6.7	-2.2	3.3	-6.5	15.1	9.5	1.34	-10.2	.7	89.1	223.6	59.9	7.8	25.2	105.2	15.4	.40	
29	9.8	5.6	9.2	-1.4	22.0	-72.0	18.8	56.9	2.59	-17.7	-17.1	65.2	252.6	73.8	33.5	12.7	125.7	9.9	.60	
30	14.2	-.6	9.9	-1.8	8.8	-38.5	14.9	32.0	.67	-14.6	-14.7	70.8	231.0	74.2	3.5	10.8	95.7	11.4	.52	
31	1.4	.3	5.2	-.3	4.7	-5.4	13.8	8.1	.69	-11.1	-11.8	77.1	226.9	57.0	33.6	32.3	127.5	6.1	.33	
32	2.7	-.6	2.2	-1.7	2.6	-6.3	13.5	6.1	.72	-16.7	-12.0	71.3	242.5	63.5	.0	13.0	95.6	22.7	.47	
33	37.0	4.5	6.1	-8.8	-.6	-71.5	21.2	57.8	5.13	-17.6	-6.3	76.1	166.9	86.7	5.5	3.1	275.5	1.1	.59	
34	-.4	.4	.2	2.3	.6	-5.5	12.7	4.3	.28	-16.9	-10.9	72.3	241.6	85.3	80.7	4.4	350.5	1.5	.47	

=====

M11,M12,M13,M22,M23,M33 - moment tensor components in units of  $10^{10}$  N·m

t0 - estimated rupture time in milliseconds

M0 - seismic moment in units of  $10^{10}$  N·mERR - error of seismic moment in units of  $10^{10}$  N·m

ISO% - volume change component in %

CLVD% - compensated linear vector dipole component in %

DC% - double couple component in %

 $\phi_P, \delta_P$  - trend and plunge of pressure axis $\phi_T, \delta_T$  - trend and plunge of tension axis $\phi_B, \delta_B$  - trend and plunge of null axis

QI - solution quality index



TABLE 8. DEVIATORIC MOMENT TENSOR SOLUTIONS FOR SEISMIC EVENTS AT SECTION G-32

#	Seismic moment tensor components						t0	M0	ERR	CLVD%	DC%	P-axis		T-axis		B-axis		QI
	M11	M12	M13	M22	M23	M33						$\phi_P$	$\delta_P$	$\phi_T$	$\delta_T$	$\phi_B$	$\delta_B$	
1	2.4	3.8	1.6	2.8	-2.5	-5.2	12.2	6.4	.38	-4.3	95.7	130.3	62.4	227.8	3.9	319.8	27.2	.51
2	-1.8	1.8	.8	.2	-2.5	1.6	11.0	3.5	.44	-4.3	95.7	140.7	22.6	261.0	50.5	36.5	30.5	.35
3	-13.0	6.7	5.0	-.1	3.5	13.1	19.7	15.5	1.14	-3.7	96.3	158.8	6.6	52.7	67.4	251.4	21.5	.58
4	.7	1.8	1.1	1.0	-.2	-1.7	11.2	2.4	.22	15.7	84.3	148.3	56.8	44.7	8.7	309.3	31.7	.45
5	-3.8	-.1	1.4	.5	1.9	3.3	14.3	4.0	.26	8.8	91.2	185.9	11.9	71.1	63.3	281.2	23.5	.38
6	-7.0	3.9	1.2	-1.6	2.8	8.6	14.6	9.1	.61	6.3	93.7	331.9	.8	64.2	71.5	241.6	18.5	.58
7	4.2	4.8	4.1	9.4	2.7	-13.5	16.2	13.0	.76	-8.9	91.1	200.1	78.0	57.5	9.6	326.3	7.2	.63
8	-14.5	-2.8	1.9	-13.0	.0	27.5	15.1	16.7	.83	65.0	35.0	217.2	2.0	357.4	87.4	127.1	1.6	.59
9	-6.9	-4.7	2.8	-2.6	-1.6	9.6	15.8	10.0	1.09	4.3	95.7	211.4	4.5	317.0	73.8	120.1	15.6	.53
10	6.8	-3.1	10.3	6.7	-4.3	-13.6	15.9	14.0	2.10	-15.8	84.2	163.0	67.4	324.8	21.5	57.3	6.4	.55
11	-4.9	5.8	4.2	-6.3	-1.1	11.2	14.0	12.0	.71	1.9	98.1	133.4	9.1	4.0	75.8	225.1	10.8	.43
12	69.2	29.4	47.1	7.7	15.9	-76.9	20.9	91.3	7.31	4.4	95.6	195.5	73.8	21.4	16.1	290.9	1.6	.68
13	-309.0	-30.9	882.0	-29.4	259.0	339.0	31.0	958.0	101.00	3.5	96.5	193.3	35.3	19.1	54.6	285.2	2.8	.66
14	6.8	3.3	9.2	1.3	2.0	-8.0	17.3	12.4	1.69	.2	99.8	183.7	64.7	20.8	24.3	287.8	6.6	.59
15	3.8	1.4	2.9	-.2	5.6	-3.6	12.4	6.8	.99	-11.5	88.5	256.9	54.3	36.5	28.6	137.6	19.4	.43
16	6.9	7.9	23.0	-.5	2.2	-6.5	18.0	24.2	2.25	9.3	90.7	167.8	51.2	19.5	34.3	278.4	15.8	.68
17	2.7	4.8	6.7	4.3	.6	-7.0	13.8	9.9	1.27	-6.5	93.5	165.9	60.4	42.0	17.6	304.2	23.0	.52
18	-15.2	-.2	-6.6	-1.2	-2.0	16.4	16.8	16.6	.80	8.1	91.9	2.4	11.5	207.4	77.3	93.5	5.2	.65
19	-3.4	2.6	3.7	-1.8	1.7	5.2	15.8	5.8	.52	27.1	72.9	151.0	12.4	36.2	62.5	246.7	24.2	.68
20	-.6	.1	1.3	.5	1.1	.1	10.0	1.8	.35	5.0	95.0	202.9	40.8	56.8	43.9	308.9	17.7	.27
21	11.7	3.2	5.6	-2.4	-2.0	-9.3	18.5	11.5	1.12	17.2	82.8	132.2	67.1	9.7	12.8	275.3	18.7	.64
22	.6	4.1	3.7	1.0	-6.0	-1.6	13.7	6.1	.80	-20.7	79.3	129.8	41.7	251.5	30.6	4.3	33.2	.52
23	3.9	9.3	12.4	-3.3	9.4	-.7	18.5	11.8	1.11	80.7	19.3	239.6	52.2	35.4	35.3	133.9	11.8	.49
24	2.8	-3.3	3.3	.1	-3.2	-2.9	13.3	5.2	.43	37.8	62.2	115.4	62.6	323.6	24.6	228.3	11.4	.42
25	.0	.2	10.3	1.5	4.0	-1.5	14.3	10.5	2.87	-8.4	91.6	198.3	47.4	25.0	42.4	291.9	3.3	.24
26	2.2	3.3	3.0	4.3	-.7	-6.4	13.0	6.8	.48	-8.9	91.1	156.0	68.4	51.5	5.7	319.4	20.7	.53
27	-15.7	5.2	41.5	8.0	-5.6	7.7	24.0	39.2	5.31	-13.5	86.5	170.4	36.9	355.7	53.0	262.3	2.5	.62
28	5.1	.0	6.8	-2.1	2.8	-3.0	15.1	7.9	1.40	15.6	84.4	222.4	54.8	8.6	30.4	108.3	16.1	.44
29	3.1	6.3	16.5	.7	5.6	-3.8	18.6	17.2	3.94	16.9	83.1	182.1	51.2	29.3	35.5	289.5	13.5	.53
30	13.3	-.2	16.0	-1.3	3.9	-12.0	14.9	20.4	1.28	3.7	96.3	203.7	62.6	4.4	26.1	98.3	7.9	.56
31	.6	.4	5.2	.1	3.2	-.7	13.8	6.1	.68	2.0	98.0	211.7	48.7	31.4	41.3	121.5	.2	.40
32	2.3	-.6	2.6	-1.5	.5	-.7	13.5	2.7	.75	37.8	62.2	231.2	46.0	356.9	29.4	105.4	29.4	.43
33	33.1	4.9	11.0	-7.5	-11.8	-25.6	21.2	33.6	5.79	4.9	95.1	112.2	62.0	3.9	9.5	269.2	26.0	.58
34	-1.3	.4	.3	3.5	.0	-2.3	12.7	2.3	.32	52.5	47.5	174.7	74.2	84.7	.0	354.7	15.8	.49

=====

M11,M12,M13,M22,M23,M33 - moment tensor components in units of  $10^{10}$  N·m

t0 - estimated rupture time in milliseconds

M0 - seismic moment in units of  $10^{10}$  N·m

ERR - error of seismic moment in units of  $10^{10}$  N·m

CLVD% - compensated linear vector dipole component in %

DC% - double couple component in %

$\phi_P, \delta_P$  - trend and plunge of pressure axis

$\phi_T, \delta_T$  - trend and plunge of tension axis

$\phi_B, \delta_B$  - trend and plunge of null axis

QI - solution quality index

TABLE 9. DOUBLE COUPLE MOMENT TENSOR SOLUTIONS FOR SEISMIC EVENTS AT SECTION G-32

#	Seismic moment tensor components						t0	M0	ERR	P-axis		T-axis		N-axis		fault type	QI
	M11	M12	M13	M22	M23	M33				$\Phi_P$	$\delta_P$	$\Phi_T$	$\delta_T$	$\Phi_N$	$\delta_N$		
1	2.3	3.9	1.4	2.7	-2.3	-5.1	12.2	6.4	.38	130.1	63.0	227.8	3.9	319.7	26.7	normal	.58
2	-1.7	1.7	.7	.2	-2.5	1.6	11.0	3.5	.43	140.1	22.9	261.0	50.5	35.9	30.2	reverse	.44
3	-12.4	6.4	4.9	-.7	3.7	13.0	19.7	15.5	1.15	158.2	6.3	52.7	67.4	250.7	21.6	reverse	.62
4	.7	1.5	1.2	1.0	-.3	-1.6	11.2	2.4	.24	148.3	56.8	45.0	8.6	309.6	31.8	normal	.52
5	-3.7	-.2	1.4	.7	1.6	3.1	14.3	4.0	.26	185.9	11.9	70.5	63.8	281.1	23.0	reverse	.47
6	-6.9	4.1	1.1	-1.3	2.5	8.1	14.6	9.1	.62	331.9	.8	64.2	71.4	241.6	18.5	reverse	.64
7	3.0	5.5	3.8	8.9	2.6	-12.0	16.2	13.0	.74	195.8	77.2	57.5	9.6	326.0	8.4	normal	.68
8	-10.5	-8.1	1.5	-6.1	-.1	16.6	15.1	16.7	.98	217.2	2.0	338.0	86.1	127.1	3.3	reverse	.65
9	-6.9	-4.8	2.7	-2.3	-1.5	9.2	15.8	10.0	1.10	211.4	4.5	316.9	73.6	120.1	15.7	reverse	.59
10	6.2	-5.1	8.6	3.8	-4.3	-10.1	15.9	14.0	2.16	161.8	67.6	324.8	21.5	57.1	5.9	normal	.60
11	-4.8	5.9	4.2	-6.2	-1.2	11.0	14.0	12.0	.72	133.4	9.1	4.0	75.8	225.1	10.8	reverse	.36
12	67.7	25.5	46.4	9.5	14.9	-77.2	20.9	91.3	7.26	195.5	73.8	20.2	16.1	289.8	1.3	normal	.72
13	-314.0	-48.6	870.0	-3.3	243.0	317.0	31.0	958.0	102.00	193.3	35.3	17.9	54.6	284.8	2.2	reverse	.70
14	6.8	3.3	9.2	1.3	2.0	-8.0	17.3	12.4	1.69	183.7	64.7	20.8	24.3	287.8	6.6	normal	.64
15	3.3	2.0	3.1	-.3	4.8	-3.0	12.4	6.8	.95	256.0	54.7	36.5	28.6	137.2	18.9	normal	.50
16	5.6	7.0	22.2	1.3	1.2	-7.0	18.0	24.2	2.23	167.8	51.2	19.1	34.4	278.1	15.6	normal	.72
17	2.7	5.0	6.2	3.9	.9	-6.6	13.8	9.9	1.27	165.9	60.4	42.0	17.6	304.3	23.0	normal	.58
18	-15.2	-.3	-6.4	.1	-1.7	15.1	16.8	16.6	.83	2.4	11.5	206.9	77.4	93.4	5.1	reverse	.70
19	-3.4	2.9	3.0	-.9	.8	4.3	15.8	5.8	.54	151.0	12.4	35.5	63.1	246.5	23.5	reverse	.72
20	-.6	.1	1.3	.5	1.1	.1	10.0	1.8	.35	202.4	40.8	56.2	43.9	308.3	17.7	reverse	.36
21	9.9	2.3	5.4	-.8	-2.7	-9.1	18.5	11.5	1.04	132.2	67.1	7.8	13.5	273.2	18.2	normal	.69
22	-.9	3.0	1.1	2.0	-4.8	-1.1	13.7	6.1	.81	129.8	41.7	251.5	30.6	4.3	33.2	normal	.29
23	3.9	1.8	7.4	-.5	8.2	-3.4	18.5	11.8	1.44	239.6	52.2	36.4	35.5	134.6	11.3	normal	.54
24	2.5	-1.6	2.5	.6	-3.1	-3.2	13.3	5.2	.40	114.9	62.6	323.0	24.6	227.7	11.4	normal	.50
25	.3	.8	9.7	.6	3.8	-.9	14.3	10.5	2.81	197.7	47.3	25.0	42.4	291.7	3.6	normal	.33
26	1.8	3.6	2.5	4.0	-.4	-5.8	13.0	6.8	.45	156.0	68.4	51.5	5.7	319.4	20.7	normal	.42
27	-10.2	3.2	37.3	-.7	-4.7	10.9	24.0	39.2	5.47	170.0	36.8	355.7	53.0	262.0	2.8	reverse	.66
28	4.3	-.5	6.2	-1.0	2.9	-3.2	15.1	7.9	1.40	221.8	54.8	8.0	30.4	107.7	16.1	normal	.51
29	2.0	4.6	15.5	2.6	4.1	-4.6	18.6	17.2	3.87	181.5	51.2	28.8	35.5	288.9	13.5	normal	.57
30	12.7	-.3	15.7	-.6	4.0	-12.1	14.9	20.4	1.26	203.7	62.6	4.4	26.1	98.3	7.9	normal	.44
31	.6	.3	5.2	.2	3.2	-.8	13.8	6.1	.68	211.7	48.7	31.4	41.3	121.5	.2	normal	.24
32	1.6	-.8	2.0	-.8	1.0	-.8	13.5	2.7	.77	231.2	46.0	355.3	28.5	103.8	30.4	normal	.48
33	31.5	4.5	10.8	-6.2	-12.6	-25.3	21.2	33.6	5.73	112.2	62.0	3.4	9.7	268.6	26.0	normal	.62
34	-.1	-.3	.6	2.3	.0	-2.2	12.7	2.3	.37	174.7	74.2	84.0	.2	354.0	15.8	normal	.54

=====

M11,M12,M13,M22,M23,M33 - moment tensor components in units of  $10^{10}$  N·m

t0 - estimated rupture time in milliseconds

M0 - seismic moment in units of  $10^{10}$  N·mERR - error of seismic moment in units of  $10^{10}$  N·m $\Phi_P, \delta_P$  - trend and plunge of pressure axis $\Phi_T, \delta_T$  - trend and plunge of tension axis $\Phi_N, \delta_N$  - trend and plunge of null axis

QI - solution quality index

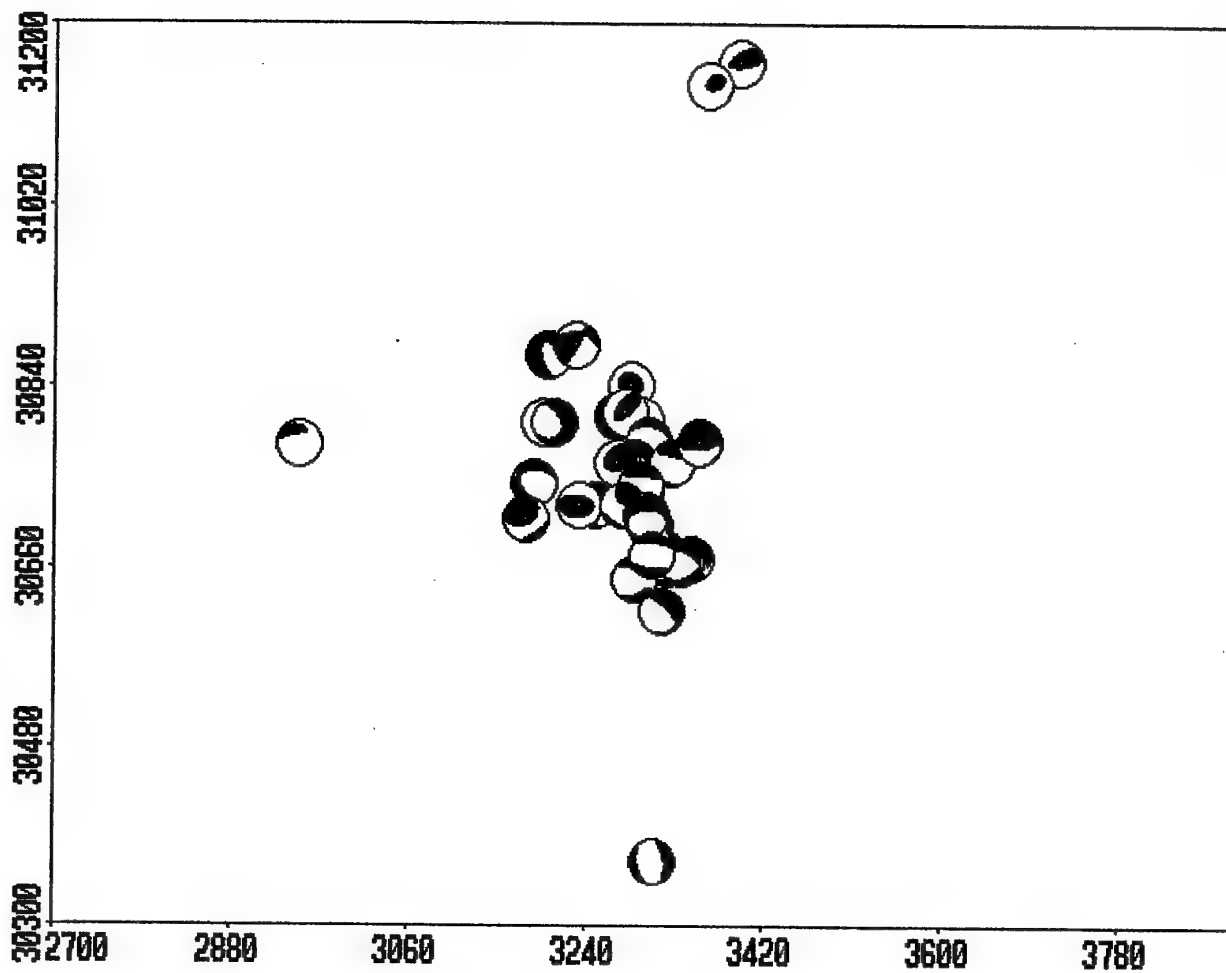


FIGURE 34. Horizontal distribution of full moment tensor solutions for seismic events at section G-32. Equal-area lower-hemisphere projection is used.

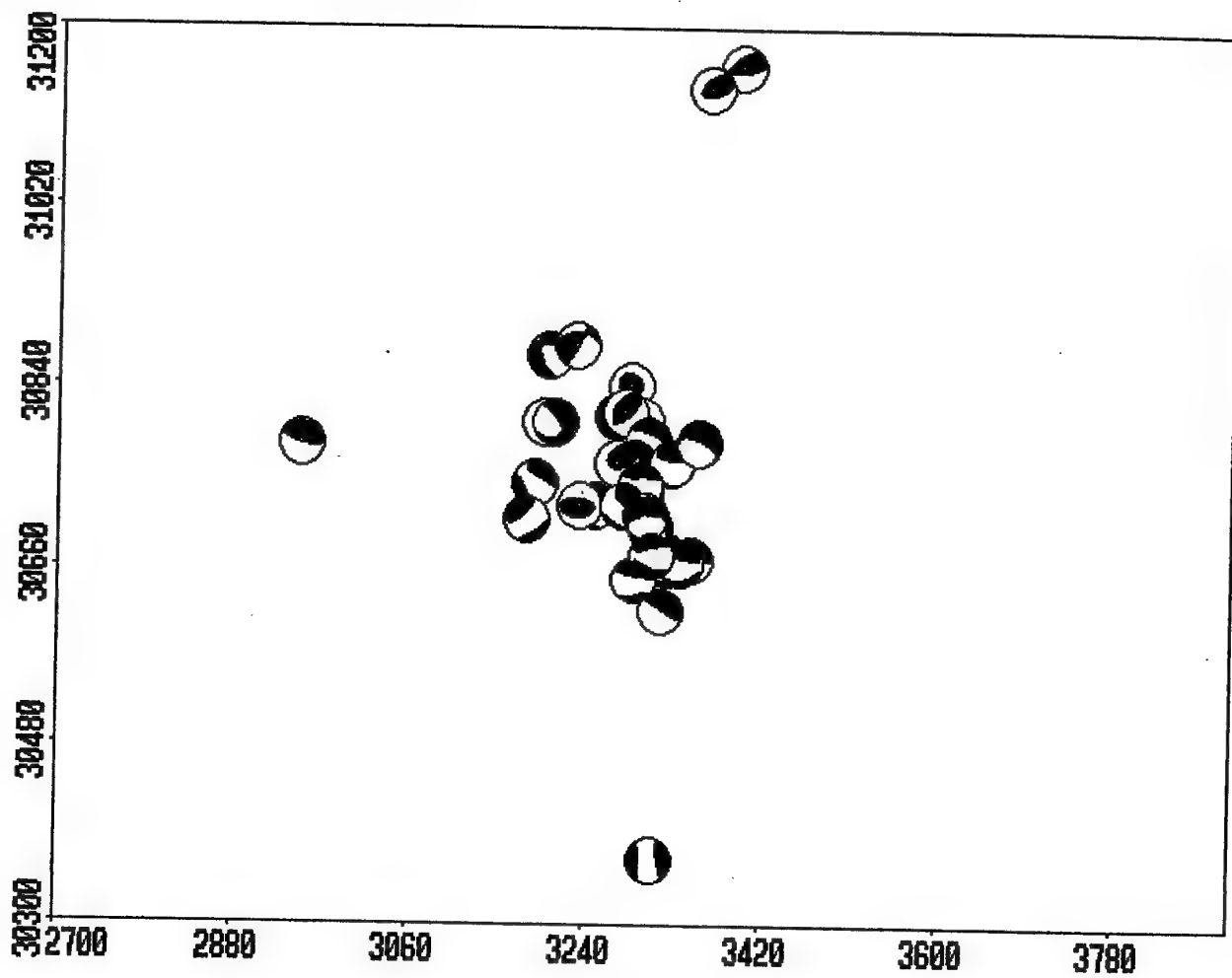


FIGURE 35. Horizontal distribution of deviatoric moment tensor solutions for seismic events at section G-32. Equal-area lower-hemisphere projection is used.

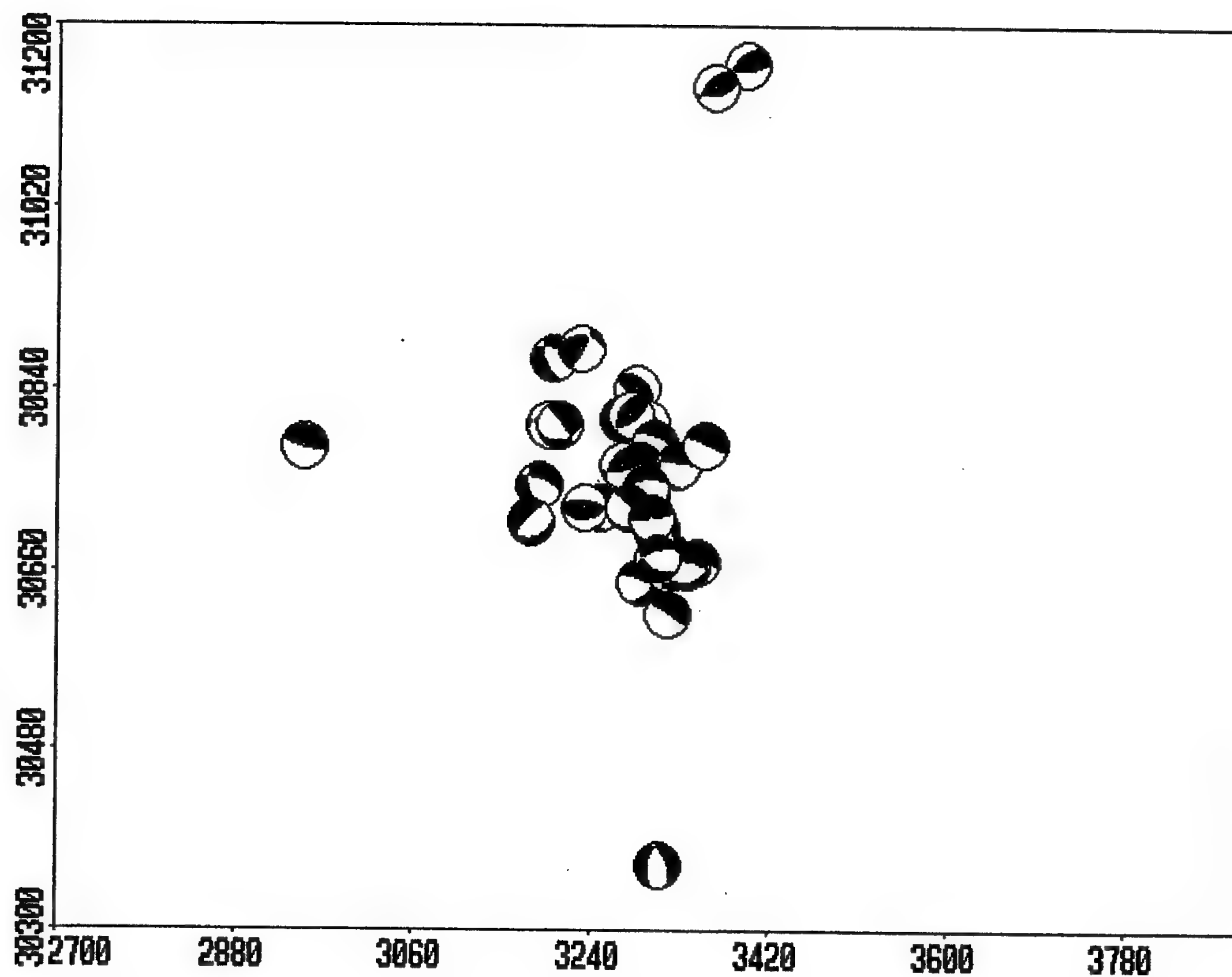


FIGURE 36. Horizontal distribution of double couple moment tensor solutions for seismic events at section G-32. Equal-area lower-hemisphere projection is used.

of the seismic stations located at or near the nodal lines on the mechanism diagrams. This results from the unfavorable distribution of seismic stations on the focal sphere. Under the specific geological conditions at Polkowice mine, only a few closest stations record direct P waves from the source. Most of the stations record diffracted waves, which start at takeoff angles of near 53 or 58 degrees. The full moment tensor solutions are most sensitive to this problem because of the larger number of numerical degrees of freedom than in the case of deviatoric and double couple solutions.

The values of scalar seismic moment calculated as the greatest eigenvalue of the double couple moment tensor solutions versus the values of seismic moment calculated from the spectra of P and S waves, for seismic events at section G-32, are shown in Fig. 33. On the average, the values from the moment tensor inversion are slightly lower than those estimated from the spectra, though the scattering of data is considerable. Nevertheless, the differences between the two sets of values, calculated by two independent techniques, are not large and the presented results are reasonable.

The numerical results from the moment tensor inversion are listed in Table 7 for the full tensor solutions, in Table 8 for the deviatoric tensor solutions, and in Table 9 for the double couple tensor solutions. The explanation of the used symbols is given below the tables.

The horizontal distribution of the full moment tensor solutions for our seismic events at section G-32 is shown in Fig. 34, where equal-area lower-hemisphere projection is used. The deviatoric tensor solutions are shown in Fig. 35 and the double couple tensor solutions are presented in Fig. 36. The deviatoric and double couple solutions are to great extent similar. Many seismic events in the central part of the section have similar focal mechanism with one nodal plane running in the E-W direction and the pressure quarter of the focal sphere situated to the south of this plane. The non-shearing components are usually small. In the deviatoric solutions, a 20 percent or larger non-shearing components are observed for seven events. In the full tensor solutions, the non-shearing components are only slightly greater than those from the deviatoric tensor solutions. A direct comparison, however, is not completely meaningful as a result of the above-mentioned problem with the unsuitable distribution of seismic stations for a proper inversion of the full moment tensor.

### 6.3 Space distribution of the source mechanisms at section G-21

The values of scalar seismic moment calculated as the greatest eigenvalue of the double couple moment tensor solutions versus the values of seismic moment calculated from the spectra of *P* and *S* waves, for seismic events at section G-21, are shown in Fig. 37. On the average, the values from the moment tensor inversion are similar to those estimated from the spectra, though the scatter of data is rather large. Nevertheless, the presented values, obtained by two independent methods, seem to be reasonable. Their differences are of random character, without a systematic component.

The numerical results from the moment tensor inversion are listed in Table 10 for the full tensor solutions, in Table 11 for the deviatoric tensor solutions, and in Table 12 for the double couple tensor solutions. The explanation of the used symbols is given below Tables 7, 8 and 9. The isotropic and CLVD components range from 0 to 30 percent of the full tensor solutions, which are highly sensitive however to the geometry of seismic network. The constraint deviatoric tensor solutions show also occasionally large non-shearing components, but in most cases their contribution to the focal mechanism is smaller than 20 percent of the solution.

The horizontal distribution of the full moment tensor solutions for our seismic events at section G-21 is shown in Fig. 38, where equal-area lower-hemisphere projection is used. The deviatoric tensor solutions are shown in Fig. 39 and the double couple tensor solutions are presented in Fig. 40. The deviatoric and double couple solutions are in many cases similar. A number of seismic events, especially in the active area of the section, have similar focal mechanism which can be interpreted as a reverse fault with the N-S strike. In the deviatoric tensor solutions, the non-shearing components are generally larger than those in the events from section G-32. How far the regular, to some extent, pattern observed in the space distribution of focal mechanisms is associated with mining works in the area is difficult to assess. For this a detailed information on daily mining activity would be needed, while only general background information related to mining was available from the management of Polkowice mine.

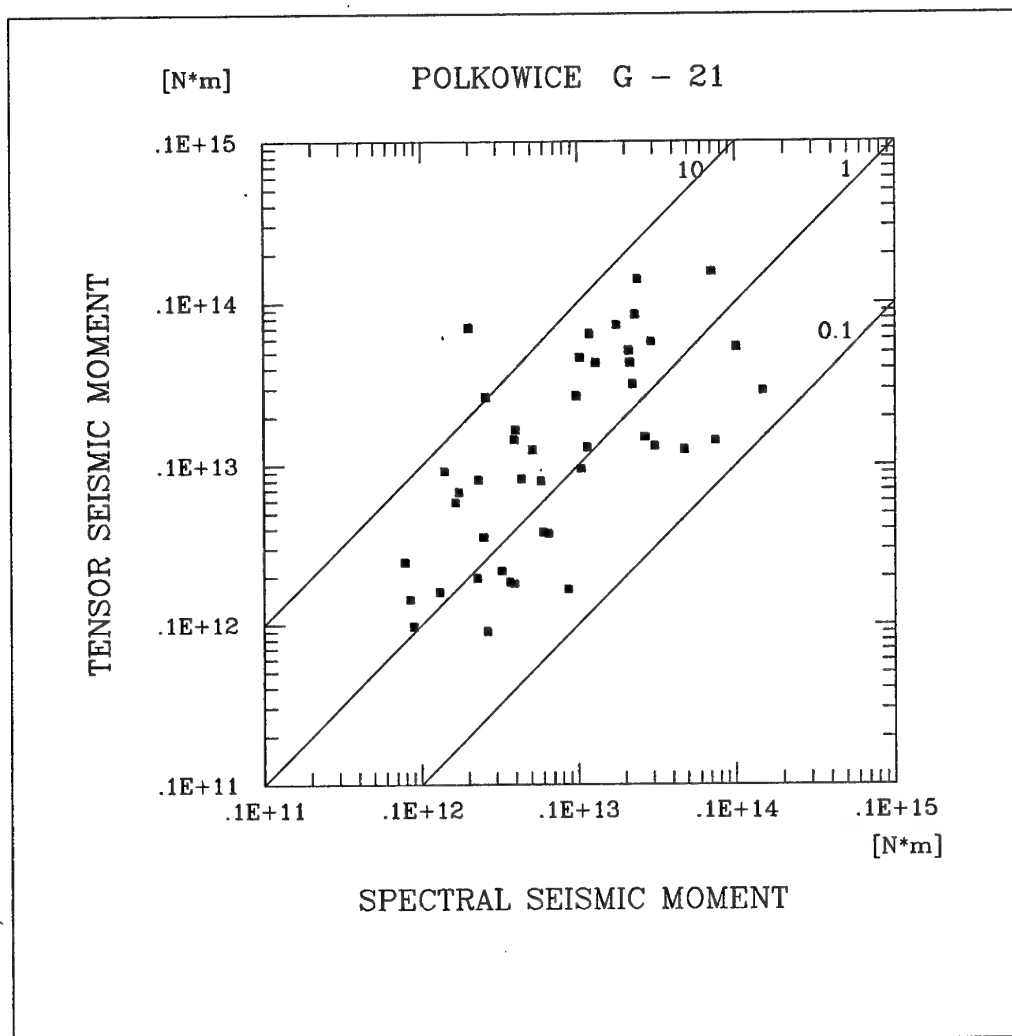


FIGURE 37. Seismic moment estimated from the moment tensor inversion versus that estimated from the spectra for seismic events from section G-32.



TABLE 10. FULL MOMENT TENSOR SOLUTIONS FOR SEISMIC EVENTS AT SECTION G-21

#	Seismic moment tensor components						t0	M0	ERR	ISO%	CLVD%	DC%	P-axis		T-axis		B-axis		QI
	M11	M12	M13	M22	M23	M33							OP	DP	OT	DT	OB	DB	
1	2.5	5.7	-1.6	-6.7	1.1	-5.1	18.2	5.4	1.30	-30.9	15.0	54.1	296.8	19.2	204.9	5.5	99.4	70.0	.41
2	41.5	-55.7	153.0	-14.7	-800.0	-2390.0	27.3	1870.0	12.10	-18.6	-18.8	62.6	99.5	72.9	294.6	16.6	203.3	4.2	.58
3	-9.7	-14.3	-35.2	5.2	-123.0	2.5	20.4	128.0	7.76	-.5	.2	99.3	66.8	43.9	261.1	45.2	163.8	7.2	.63
4	-21.3	-9.5	-86.1	-43.7	340.0	-197.0	34.9	379.0	27.00	-14.6	-10.0	75.4	282.5	51.3	107.1	38.6	15.3	2.3	.55
5	11.6	-6.6	-156.0	-758.0	-81.7	445.0	35.8	646.0	15.20	-11.3	-7.1	81.6	88.7	4.0	191.2	71.9	357.4	17.6	.63
6	-24.4	49.4	-19.6	44.9	94.2	-101.0	25.4	135.0	7.63	-16.1	-2.3	81.6	302.3	57.2	72.0	22.4	171.9	22.6	.66
7	-8.5	-146.0	-102.0	-383.0	125.0	45.8	32.5	349.0	38.90	-22.5	-6.1	71.3	254.1	10.6	152.8	46.4	353.6	41.7	.56
8	-126.0	169.0	55.7	433.0	391.0	-303.0	32.5	477.0	23.30	.2	35.2	64.6	277.0	66.0	75.9	22.5	169.2	7.8	.66
9	-10.8	-38.4	-224.0	-1110.0	81.8	465.0	37.3	883.0	27.00	-16.1	-8.7	75.1	268.6	2.8	171.6	68.1	359.7	21.7	.67
10	.1	1.6	14.4	-1.8	15.2	-79.5	23.0	60.0	1.41	-20.2	-18.4	61.4	227.2	76.2	39.3	13.7	129.7	1.8	.49
11	31.6	-12.0	-27.6	-46.2	47.0	-69.1	24.3	84.0	5.32	-23.3	-5.1	71.6	280.3	53.1	162.2	19.5	60.5	30.0	.65
12	-10.6	-23.7	-37.2	123.0	80.4	-117.0	30.0	143.0	10.50	-1.0	6.6	92.3	308.9	70.4	102.3	17.6	194.9	8.2	.64
13	-3.5	6.9	-1.2	-5.2	2.7	10.2	14.7	9.1	1.25	3.0	-12.1	85.0	311.0	7.4	92.2	80.6	220.3	5.9	.26
14	-4.4	1.8	6.5	-.4	2.1	-16.6	18.4	14.1	1.31	-26.7	-13.6	59.7	189.7	66.7	55.1	16.8	320.3	15.7	.38
15	-3.7	-26.1	-231.0	-551.0	-217.0	467.0	25.3	528.0	6.61	-4.8	7.9	87.3	82.5	12.9	205.5	67.2	348.1	18.5	.49
16	-30.9	22.0	-142.0	43.6	-81.1	41.3	28.7	172.0	6.85	9.8	5.1	85.1	14.0	39.8	222.7	46.4	116.7	14.7	.65
17	-5.5	13.9	-1.4	3.2	12.1	1.9	24.5	19.1	4.08	-.6	-1.9	97.5	316.9	23.6	61.9	30.8	196.1	49.5	.39
18	-2.8	5.4	-9.2	-37.2	-.2	39.1	22.7	37.1	.90	-.9	9.5	89.7	278.9	.9	184.6	77.9	9.1	12.0	.57
19	22.5	-16.6	-106.0	-28.6	57.2	-170.0	30.6	173.0	9.83	-20.8	-9.5	69.6	328.1	64.3	157.8	25.3	66.0	3.8	.60
20	-4.0	15.0	2.4	-32.9	4.4	59.4	17.6	50.6	2.03	13.8	10.0	76.2	292.8	1.8	48.2	85.7	202.7	3.9	.35
21	24.7	-81.9	-10.6	-140.0	146.0	-311.0	32.6	295.0	13.10	-29.7	-8.5	61.8	261.4	58.8	151.3	11.8	54.8	28.4	.62
22	-11.3	4.3	16.5	1.4	36.5	-17.5	24.0	36.5	4.96	-18.7	6.7	74.6	242.6	51.9	68.1	38.0	336.0	2.7	.43
23	-2.5	4.1	-14.6	5.7	24.6	-15.3	22.5	31.2	4.81	-7.9	-13.0	79.1	308.4	51.8	104.8	35.8	203.3	11.6	.39
24	-4.5	-.2	-47.4	7.7	-20.1	48.7	23.2	62.3	9.41	24.9	15.9	59.2	17.0	31.5	206.2	58.2	109.6	4.1	.42
25	-308.0	613.0	-715.0	-1610.0	-363.0	2360.0	41.1	2270.0	39.80	7.0	21.1	71.9	111.2	1.1	204.8	73.3	20.9	16.6	.58
26	-100.0	-20.5	-333.0	582.0	-79.2	-579.0	39.2	678.0	60.60	-3.4	-10.7	85.9	7.5	62.7	269.8	3.9	177.8	27.0	.61
27	-1.7	10.5	3.9	-16.9	5.1	25.6	17.8	24.9	1.37	8.6	.2	91.1	296.3	3.4	39.8	75.9	205.5	13.7	.39
28	-9.1	20.3	19.1	-17.0	19.5	56.2	16.8	54.1	1.89	18.6	26.8	54.6	308.0	2.3	43.1	65.9	217.0	24.0	.40
29	.0	-34.8	-53.9	-76.4	-25.1	12.1	21.8	87.9	1.60	-18.6	-3.4	78.0	61.0	22.0	176.8	47.3	314.9	34.5	.65
30	-51.4	329.0	-255.0	364.0	7.9	-370.0	37.3	489.0	42.20	-3.5	9.6	86.9	339.5	53.8	238.9	7.6	143.5	35.1	.62
31	-27.1	74.9	-50.1	-165.0	-17.5	297.0	18.0	258.0	6.60	13.1	14.4	72.5	293.8	.5	201.0	80.0	23.9	10.0	.35
32	-32.3	104.0	-37.9	-145.0	58.2	204.0	27.0	189.0	10.90	3.3	-7.3	89.4	300.9	9.3	125.9	80.6	31.0	.8	.53
33	-3.2	8.8	23.1	-70.9	22.9	65.6	19.2	66.5	3.50	-3.8	9.8	86.4	274.2	8.6	29.4	70.5	181.5	17.4	.50
34	-8.1	-7.8	-5.3	-37.9	91.9	-121.0	21.3	129.0	10.70	-20.6	-16.6	62.8	270.2	57.2	109.2	31.3	13.9	8.7	.52
35	-93.1	230.0	-213.0	-879.0	469.0	66.3	35.8	844.0	90.40	-18.2	-15.3	66.6	287.0	22.7	136.9	64.2	21.9	11.6	.62
36	-13.1	61.2	5.4	-37.5	15.6	56.7	26.7	58.3	3.37	1.4	-18.8	79.8	309.0	3.5	45.7	62.6	217.2	27.1	.58
37	-11.1	18.7	48.4	16.2	-79.6	-135.0	35.8	136.0	7.37	-15.5	-17.0	67.5	127.3	61.8	272.4	23.7	8.8	14.3	.34
38	19.3	23.5	149.0	-431.0	-770.0	-1480.0	22.6	1340.0	8.14	-20.6	-18.9	60.4	99.1	61.9	333.8	17.1	236.9	21.5	.22
39	-17.9	27.5	-24.3	-230.0	32.0	201.0	23.6	220.0	15.10	-6.6	.3	93.2	277.7	4.6	146.3	83.1	8.1	5.1	.34
40	30.8	-51.1	185.0	-462.0	211.0	298.0	21.9	483.0	18.50	-7.7	-3.6	88.7	259.4	16.2	25.8	63.9	163.4	19.9	.64
41	2.5	9.0	-12.8	-22.6	-9.2	22.2	14.4	28.2	1.34	2.6	14.0	83.3	104.5	6.8	206.3	59.7	10.7	29.4	.35
42	-9.6	14.3	48.0	7.5	44.4	-165.0	19.0	135.0	14.40	-21.0	-14.8	64.2	219.6	71.7	53.6	17.8	322.3	4.2	.37
43	-157.0	269.0	-162.0	-275.0	44.6	476.0	30.5	478.0	18.90	2.5	-4.0	93.4	310.2	8.0	186.7	75.7	41.9	11.7	.59
44	-198.0	676.0	-998.0	-1630.0	-832.0	3110.0	31.1	2890.0	74.00	15.3	28.0	56.7	108.3	5.4	213.5	70.2	16.5	19.0	.35
45	-1.9	-7.5	-45.8	-124.0	-39.3	99.9	26.6	117.0	2.00	-6.6	5.1	88.2	82.9	10.9	202.4	68.7	349.3	18.1	.52
46	-15.7	29.9	-45.7	-84.0	-35.7	96.1	19.2	93.5	4.09	-1.2	27.8	70.9	106.9	6.2	210.9	66.0	14.3	23.1	.40
47	N O T A V A I L A B L E						N.A.	N.A.	N.A.	N.A.	N.A.	N.A.	N.A.	N.A.	N.A.	N.A.	N.A.	N.A.	.00
48	-5.3	9.7	-19.5	-70.8	-4.5	65.0	22.8	62.9	2.03	-5.1	7.7	87.2	98.0	.7	190.8	75.0	7.8	15.0	.40
49	-16.8	31.0	-102.0	88.3	-85.7	2.2	22.7	151.0	12.80	14.8	7.3	77.9	16.5	45.8	239.2	35.6	131.9	22.7	.33
50	-21.3	31.8	-57.1	134.0	-90.7	23.3	21.8	148.0	5.67	29.1	28.0	42.9	14.2	41.3	253.2	30.4	140.1	33.7	.68
51	-2.8	5.8	-11.9	-65.9	-4.3	60.7	21.0	61.9	2.94	-4.0	2.9	93.1	94.9	1.5	192.7	79.3	4.6	10.6	.54
52	1.0	-13.0	2.6	-13.2	16.0	5.9	18.0	22.7	1.42	-5.0	-17.0	78.0	243.6	24.6	121.5	49.2	349.0	30.2	.55
53	185.0	-173.0	115.0	-595.0	823.0	-250.0	31.6	972.0	56.10	-10.2	-20.0	69.8	259.8	38.5	98.3	50.0	357.2	9.2	.65
54	-108.0	186.0	-106.0	-176.0	-4.4	401.0	27.7	384.0	16.60	9.4	2.5	88.0	311.0	5.1	198.9	76.6	42.1	12.3	.54
55	-32.7	-20.5	-109.0	122.0	2.8	-175.0	23.4	189.0	8.65	-8.5	-15.2	76.3	2.5	61.5	100.3	4.2	192.5	28.1	.58
56	10.1	12.4	-8.6	27.6	-.6	-38.1	19.2	34.7	3.09	-.3	-10.2	89.5	352.2	79.8	241.8	3.6	151.2	9.5	.49

=====

Explanation of symbols same as for Table 7.

TABLE 11. DEVIATORIC MOMENT TENSOR SOLUTIONS FOR SEISMIC EVENTS AT SECTION G-21

#	Seismic moment tensor components						t0	M0	ERR	CLVDX	DCX	P-axis		T-axis		B-axis		QI
	M11	M12	M13	M22	M23	M33						OP	DP	OT	DT	OB	DB	
1	1.4	10.4	-.6	-10.6	1.0	9.2	18.2	9.2	1.29	-23.5	76.5	299.9	2.6	122.4	87.3	29.9	.1	.52
2	-37.1	-27.5	-311.0	-13.1	-82.3	50.2	27.3	325.0	22.40	.3	99.7	18.0	40.5	191.7	49.3	285.3	3.1	.60
3	-9.7	-14.2	-35.3	5.2	-122.0	4.5	20.4	128.0	7.76	.7	99.3	66.7	43.7	260.9	45.5	163.6	7.2	.67
4	-24.4	-3.3	-87.5	-32.9	446.0	57.3	34.9	443.0	27.80	5.9	94.1	280.5	42.2	101.7	47.8	11.0	.6	.61
5	-13.2	78.1	-147.0	-846.0	-57.2	859.0	35.8	855.0	19.50	3.7	96.3	95.1	1.5	193.6	80.2	4.8	9.6	.68
6	-30.4	70.9	-11.0	70.6	108.0	-40.1	25.4	131.0	7.99	17.8	82.2	310.4	44.7	70.6	26.9	180.0	33.2	.69
7	-35.8	-71.7	-156.0	-241.0	173.0	276.0	32.5	295.0	39.60	34.1	65.9	263.5	15.1	142.5	62.4	360.0	22.5	.59
8	-125.0	167.0	54.5	429.0	389.0	-304.0	32.5	473.0	23.30	34.8	65.2	277.3	86.0	75.9	22.6	169.2	7.8	.70
9	-15.6	201.0	-211.0	-548.0	226.0	563.0	37.3	653.0	29.40	-3.6	96.4	290.8	13.0	152.4	72.9	23.4	11.0	.71
10	-5.4	4.4	-7.6	4.2	36.7	1.1	23.0	36.4	1.80	8.6	91.4	291.8	44.5	93.8	44.0	192.7	9.1	.54
11	27.2	-9.9	-50.9	-46.0	55.4	18.9	24.3	80.9	5.89	11.2	88.8	282.6	33.2	151.9	45.0	31.8	26.7	.69
12	-11.1	-21.8	-37.9	123.0	79.4	-112.0	30.0	143.0	10.50	7.4	92.6	310.8	69.8	101.8	17.9	194.8	9.2	.69
13	-3.3	6.2	-1.1	-6.1	2.8	9.4	14.7	9.9	1.29	-10.5	89.5	308.1	7.8	91.4	80.3	217.3	5.7	.35
14	-7.9	10.2	6.1	15.2	4.3	-7.3	18.4	14.6	1.81	39.8	60.2	166.5	34.3	67.7	12.7	320.4	52.8	.44
15	-7.9	1.4	-293.0	-650.0	-273.0	658.0	25.3	710.0	6.78	14.7	85.3	84.9	12.3	207.6	68.0	350.9	17.9	.57
16	-22.8	7.4	-122.0	22.0	-61.1	.8	28.7	135.0	6.41	-4.4	95.6	18.1	43.4	216.6	45.1	117.1	9.4	.69
17	-5.6	14.0	-1.5	3.0	12.0	2.6	24.5	18.8	4.08	-3.6	96.4	317.0	22.9	61.9	31.4	197.5	49.5	.45
18	-3.0	5.7	-9.5	-37.8	-.4	40.8	22.7	38.7	.89	10.3	89.7	279.3	.8	185.6	78.1	9.5	11.9	.63
19	27.0	-52.0	-213.0	-128.0	57.7	101.0	30.6	153.0	10.40	92.5	7.5	16.2	36.6	164.1	48.7	273.6	16.3	.64
20	-1.7	7.7	6.6	-15.4	9.0	17.1	17.6	19.8	2.15	13.0	87.0	289.8	9.6	40.0	63.9	195.5	24.0	.41
21	-7.9	-15.2	-66.6	-11.0	275.0	18.8	32.6	276.0	15.70	5.4	94.6	280.5	43.8	106.3	46.1	13.2	2.9	.66
22	-13.9	14.2	19.4	-16.2	38.0	30.0	24.0	38.0	4.96	55.8	44.2	280.1	26.6	56.7	55.5	179.4	20.4	.50
23	-2.6	5.2	-12.2	7.8	31.2	-5.2	22.5	33.6	4.76	-5.0	95.0	302.3	47.3	98.2	40.1	198.7	12.2	.46
24	-6.1	-1.5	-18.1	10.2	-7.7	-4.1	23.2	16.8	8.63	-19.2	80.8	14.7	43.8	233.9	39.0	126.1	20.8	.28
25	-206.0	397.0	-513.0	-1280.0	-211.0	1490.0	41.1	1410.0	37.50	17.8	82.2	107.9	.9	200.6	72.3	17.6	17.7	.63
26	-109.0	16.0	-321.0	534.0	-78.7	-425.0	39.2	544.0	61.40	-10.6	89.4	5.5	58.2	265.6	6.1	171.9	31.1	.63
27	-1.3	7.7	2.5	-16.2	4.0	17.5	17.8	18.6	1.41	-5.1	94.9	292.1	4.3	40.0	76.4	201.2	12.9	.46
28	-7.6	8.4	12.6	-7.5	15.5	15.1	16.8	16.4	2.13	77.7	22.3	300.1	12.7	48.7	54.8	201.9	32.2	.44
29	-.6	-16.8	-51.6	-57.5	-12.3	58.1	21.8	68.8	1.76	28.1	71.9	65.2	14.5	181.8	60.0	328.0	25.7	.70
30	-52.7	321.0	-289.0	327.0	5.7	-275.0	37.3	520.0	42.20	3.3	96.7	338.8	47.9	236.7	10.7	137.5	40.1	.67
31	-16.3	36.7	-18.1	-74.1	9.8	90.4	18.0	93.5	7.45	.0	100.0	296.5	5.3	171.2	81.0	27.2	7.3	.42
32	-28.7	94.3	-32.2	-128.0	64.2	157.0	27.0	171.0	11.00	-11.0	89.0	300.9	11.4	110.1	78.4	210.4	2.1	.58
33	-4.1	11.4	22.4	-78.4	21.8	82.6	19.2	82.3	3.53	11.1	88.9	276.4	6.7	30.0	73.8	184.6	14.7	.57
34	-12.2	19.6	5.8	-51.8	82.8	64.0	21.3	97.5	8.80	11.6	88.4	281.0	26.4	75.9	61.3	185.7	10.6	.57
35	-172.0	482.0	-172.0	-1330.0	440.0	1500.0	35.8	1570.0	93.00	-.2	99.8	290.0	8.7	112.6	81.3	20.0	.4	.69
36	-12.6	58.9	6.2	-36.3	16.6	48.9	26.7	59.4	3.44	-18.9	81.1	308.8	3.9	44.8	57.0	216.3	32.7	.63
37	-18.5	41.4	97.0	51.2	-18.0	-32.7	35.8	84.6	7.42	-20.9	79.1	161.9	44.5	40.9	27.7	291.1	32.8	.41
38	3.3	-1.6	10.7	-13.5	15.7	10.2	22.6	22.3	8.85	-2.5	97.5	253.6	28.6	38.3	56.2	154.4	16.4	.20
39	-24.4	40.9	-32.7	-262.0	23.6	286.0	23.6	270.0	14.50	7.5	92.5	279.8	3.0	160.4	84.0	10.1	5.2	.43
40	20.6	-1.9	208.0	-535.0	218.0	515.0	21.9	582.0	19.40	7.7	92.3	265.6	12.0	28.6	68.7	171.8	17.4	.69
41	2.5	8.4	-13.0	-22.1	-9.5	19.5	14.4	25.4	1.34	16.2	83.8	103.1	8.0	205.9	57.8	8.2	31.0	.43
42	-20.7	51.2	80.3	59.6	104.0	-38.9	19.0	126.0	13.20	31.9	68.1	215.7	55.3	59.5	32.4	322.3	11.2	.45
43	-144.0	247.0	-150.0	-255.0	55.3	399.0	30.5	438.0	18.70	-6.7	93.3	310.1	9.0	183.2	75.2	42.0	11.7	.64
44	-117.0	195.0	-751.0	-376.0	-555.0	492.0	31.1	744.0	68.70	61.9	38.1	50.2	36.3	214.2	52.6	314.5	7.8	.41
45	-4.8	1.3	-48.8	-142.0	-41.9	147.0	26.6	148.0	2.21	12.3	87.7	87.6	8.4	205.6	72.4	355.3	15.3	.59
46	-16.3	31.3	-47.2	-86.0	-36.8	102.0	19.2	99.8	4.16	28.6	71.4	107.4	5.9	211.1	66.3	14.9	22.8	.48
47	NOT AVAILABLE						N.A.	N.A.	N.A.	N.A.	N.A.	N.A.	N.A.	N.A.	N.A.	N.A.	N.A.	.00
48	-6.6	13.8	-20.7	-77.5	-5.7	84.1	22.8	80.1	2.18	11.1	88.9	100.4	.6	193.2	77.0	10.3	13.0	.49
49	-18.9	31.7	-119.0	108.0	-77.9	-89.4	22.7	167.0	15.10	-8.2	91.8	15.8	54.8	242.5	25.8	141.1	22.2	.41
50	-19.9	-8.9	-75.3	69.8	-84.3	-49.9	21.8	119.0	4.91	-10.3	89.7	32.9	51.3	254.9	30.8	151.6	21.1	.72
51	-3.6	8.6	-11.4	-67.7	-3.6	71.2	21.0	68.9	2.94	6.2	93.8	97.4	.9	192.8	81.1	7.2	8.8	.60
52	-.1	-10.0	3.2	-12.5	16.3	12.5	18.0	20.7	1.41	-12.5	87.5	245.1	23.3	100.4	62.1	341.4	14.4	.60
53	124.0	-66.7	192.0	-387.0	977.0	263.0	31.6	983.0	58.80	-9.5	90.5	260.5	35.9	76.5	54.1	169.1	1.9	.69
54	-77.5	138.0	-61.3	-116.0	31.8	194.0	27.7	207.0	15.80	-12.0	88.0	311.8	8.4	177.9	78.0	43.0	8.5	.58
55	-35.7	4.6	-90.1	64.6	6.9	-28.9	23.4	65.4	8.85	-24.2	75.8	356.6	43.9	97.6	11.2	198.6	44.0	.58
56	10.1	12.6	-8.6	28.1	-.5	-38.2	19.2	34.8	3.09	-9.9	90.1	352.0	79.8	242.0	3.5	151.4	9.5	.55

=====

Explanation of symbols same as for Table 8.

TABLE 12. DOUBLE COUPLE MOMENT TENSOR SOLUTIONS FOR SEISMIC EVENTS AT SECTION G-21

#	Seismic moment tensor components						t0	M0	ERR	P-axis		T-axis		N-axis		fault type	QI
	M11	M12	M13	M22	M23	M33				OP	DP	OT	DT	OB	DB		
1	-2.2	3.9	-4	-7.0	.7	9.2	18.2	9.2	1.68	299.5	2.6	122.4	87.3	29.5	.1	reverse	.55
2	-32.1	-37.8	-313.0	-15.7	-69.9	47.8	27.3	325.0	22.50	18.0	40.5	187.2	49.0	283.4	5.4	reverse	.66
3	-8.9	-14.5	-35.3	4.9	-122.0	4.0	20.4	128.0	7.76	66.7	43.7	260.9	45.5	183.6	7.2	reverse	.36
4	-3.6	13.9	-73.0	-39.4	435.0	43.0	34.9	443.0	27.80	280.5	42.2	98.6	47.8	189.6	.9	reverse	.66
5	11.8	79.7	-122.0	-846.0	-54.4	834.0	35.8	855.0	21.60	95.1	1.5	194.7	81.3	4.8	8.6	reverse	.73
6	-16.2	65.1	-24.8	54.1	99.4	-37.9	25.4	131.0	7.91	310.4	44.7	70.6	26.9	180.0	33.2	normal	.37
7	36.8	-61.5	-88.3	-249.0	147.0	212.0	32.5	295.0	41.20	263.5	15.1	142.7	62.3	380.0	22.6	reverse	.63
8	22.5	105.0	18.4	302.0	337.0	-325.0	32.5	473.0	19.20	277.3	66.0	75.9	22.6	169.2	7.8	normal	.53
9	-33.9	183.0	-214.0	-530.0	218.0	564.0	37.3	653.0	28.60	290.8	13.0	152.4	72.9	23.4	11.0	reverse	.37
10	-2.5	5.4	-7.7	2.9	35.1	-.4	23.0	36.4	1.74	291.8	44.5	92.9	43.9	192.3	9.6	normal	.61
11	29.5	-4.7	-44.0	-45.3	54.8	15.7	24.3	80.9	5.95	282.6	33.2	152.5	44.6	32.2	27.1	reverse	.73
12	-2.5	-16.2	-38.4	115.0	75.9	-113.0	30.0	143.0	10.60	310.8	69.8	101.2	17.8	194.2	9.4	normal	.73
13	-3.6	4.7	-.9	-5.8	2.7	9.4	14.7	9.9	1.17	307.8	7.8	91.4	80.3	217.0	5.7	reverse	.44
14	-7.4	7.2	7.9	11.3	1.4	-3.9	18.4	14.6	2.32	166.5	34.3	67.3	13.2	319.4	52.5	strike slip	.49
15	46.0	-25.2	-194.0	-649.0	-270.0	603.0	25.3	710.0	11.90	84.9	12.3	214.2	71.0	351.7	14.2	reverse	.63
16	-21.3	11.5	-118.0	17.3	-60.6	4.0	28.7	135.0	6.41	17.7	43.3	216.6	45.1	116.8	9.6	reverse	.74
17	-5.5	13.6	-1.0	3.2	11.9	2.3	24.5	18.8	4.13	317.0	22.8	61.9	31.4	197.5	49.5	strike slip	.50
18	.1	6.3	-6.6	-37.7	.0	37.6	22.7	38.7	.95	279.3	.8	184.8	80.1	9.5	9.8	reverse	.69
19	-29.1	-45.5	-143.0	-1.7	2.1	30.8	30.6	153.0	10.70	16.2	36.6	162.7	48.3	273.0	17.1	reverse	.69
20	.1	8.1	5.0	-15.5	8.1	15.4	17.6	19.8	2.24	289.8	9.6	39.7	63.7	195.4	24.3	reverse	.48
21	1.5	-2.3	-55.0	-13.2	271.0	11.8	32.6	276.0	15.70	280.5	43.8	102.5	46.2	11.4	1.0	reverse	.71
22	2.7	10.9	7.1	-20.9	29.8	18.2	24.0	38.0	5.11	280.1	26.6	56.7	55.5	179.4	20.4	reverse	.28
23	-3.9	4.1	-11.2	8.2	30.6	-4.3	22.5	33.6	4.90	301.9	47.4	98.2	40.1	198.6	12.0	normal	.53
24	-4.8	2.7	-13.0	6.1	-8.7	-1.3	23.2	16.8	8.69	14.1	43.5	233.9	39.0	125.7	21.1	normal	.31
25	-32.1	451.0	-356.0	-1260.0	-157.0	1300.0	41.1	1410.0	43.40	107.9	.9	200.8	73.3	17.6	16.6	reverse	.68
26	-146.0	33.6	-248.0	533.0	-77.9	-387.0	39.2	544.0	63.60	4.9	58.2	265.0	6.1	171.3	31.1	normal	.67
27	-1.9	6.8	2.8	-15.6	4.0	17.4	17.8	18.6	1.39	291.6	4.3	39.5	76.4	200.6	12.9	reverse	.54
28	-2.0	9.2	3.0	-8.8	8.8	10.8	16.8	16.4	2.06	300.1	12.7	50.5	57.2	202.7	29.7	reverse	.51
29	6.2	-24.1	-37.0	-53.1	-15.9	46.9	21.8	68.8	2.36	65.2	14.5	181.4	59.7	327.9	26.0	reverse	.74
30	-48.7	310.0	-296.0	315.0	11.4	-267.0	37.3	520.0	41.80	338.8	47.9	236.2	11.1	136.7	40.0	normal	.71
31	-16.3	36.7	-18.0	-74.1	9.9	90.4	18.0	93.5	7.46	296.5	5.3	170.9	81.1	27.2	7.2	reverse	.50
32	-41.0	69.5	-28.0	-117.0	60.3	158.0	27.0	171.0	9.26	300.3	11.4	109.5	78.4	209.9	2.1	reverse	.65
33	5.5	12.3	20.9	-78.5	20.6	73.0	19.2	82.3	3.58	276.4	6.7	27.0	71.6	184.3	17.0	reverse	.64
34	-1.6	19.8	2.3	-54.2	77.9	55.8	21.3	97.5	8.45	281.0	26.4	76.3	61.3	185.8	10.4	reverse	.63
35	-174.0	481.0	-171.0	-1330.0	440.0	1500.0	35.8	1570.0	93.00	290.0	8.7	112.6	81.3	20.0	.4	reverse	.52
36	-14.0	37.6	16.6	-27.5	22.4	41.5	26.7	59.4	3.32	308.4	4.1	44.8	57.0	215.8	32.7	reverse	.68
37	-1.0	45.5	66.6	24.2	9.7	-23.3	35.8	84.6	16.00	161.9	44.5	40.9	27.7	291.1	32.8	normal	.22
38	2.8	-1.4	10.8	-13.1	15.4	10.2	22.6	22.3	8.84	253.2	28.8	38.3	56.2	154.1	16.2	reverse	.27
39	-5.3	44.4	-28.6	-261.0	23.3	266.0	23.6	270.0	14.80	279.8	3.0	160.0	84.0	10.1	5.2	reverse	.52
40	62.9	-8.8	191.0	-536.0	210.0	474.0	21.9	582.0	19.40	265.6	12.0	26.9	67.8	171.6	18.4	reverse	.74
41	11.8	10.2	-11.0	-21.9	-7.7	10.2	14.4	25.4	3.33	103.1	8.0	199.9	40.4	3.9	48.5	strike slip	.47
42	-3.4	20.1	77.4	52.3	83.7	-48.9	19.0	126.0	12.10	215.7	55.3	59.2	32.5	322.0	11.0	normal	.53
43	-144.0	211.0	-151.0	-254.0	45.8	398.0	30.5	438.0	18.10	309.5	8.9	183.2	75.2	41.4	11.8	reverse	.69
44	-9.5	-111.0	-524.0	-200.0	-474.0	209.0	31.1	744.0	62.50	50.2	36.3	214.0	52.6	314.4	7.8	reverse	.50
45	4.9	-2.2	-27.7	-142.0	-41.3	137.0	26.6	148.0	3.69	87.6	8.4	216.4	76.7	356.1	10.2	reverse	.65
46	3.0	35.3	-28.4	-85.6	-28.8	82.6	19.2	99.8	5.12	107.4	5.9	211.1	66.3	14.9	22.9	reverse	.55
47	N O T A V A I L A B L E						N.A.	N.A.	N.A.	N.A.	N.A.	N.A.	N.A.	N.A.	N.A.	?	.00
48	1.0	15.1	-16.5	-77.3	-4.8	76.3	22.8	80.1	2.87	100.4	.6	193.3	77.4	10.3	12.6	reverse	.56
49	-22.7	41.0	-106.0	103.0	-79.6	-79.8	22.7	167.0	15.00	15.8	54.8	242.5	25.8	141.1	22.2	normal	.50
50	-24.9	1.0	-61.5	67.6	-83.5	-42.7	21.8	119.0	4.91	34.4	51.9	254.9	30.8	152.3	20.1	normal	.76
51	.0	9.0	-8.6	-67.6	-3.1	67.6	21.0	68.9	2.92	97.4	.9	193.8	82.4	7.3	7.5	reverse	.66
52	-3.2	-7.7	1.7	-9.8	15.1	13.0	18.0	20.7	1.37	244.1	23.1	100.4	62.1	340.5	14.8	reverse	.66
53	-2.9	-38.4	193.0	-304.0	914.0	307.0	31.6	983.0	61.90	259.6	35.9	76.5	54.1	168.5	1.4	reverse	.73
54	-79.0	100.0	-61.3	-115.0	23.7	194.0	27.7	207.0	13.80	311.2	8.3	177.9	78.0	42.5	8.6	reverse	.64
55	-33.2	-6.3	-34.2	61.7	14.3	-28.5	23.4	65.4	10.50	356.7	43.5	97.6	11.2	198.8	44.3	strike slip	.61
56	6.6	14.5	-7.0	27.0	-1.0	-33.6	19.2	34.8	3.08	352.0	79.8	242.0	3.5	151.4	9.5	normal	.30

=====

Explanation of symbols same as for Table 9.

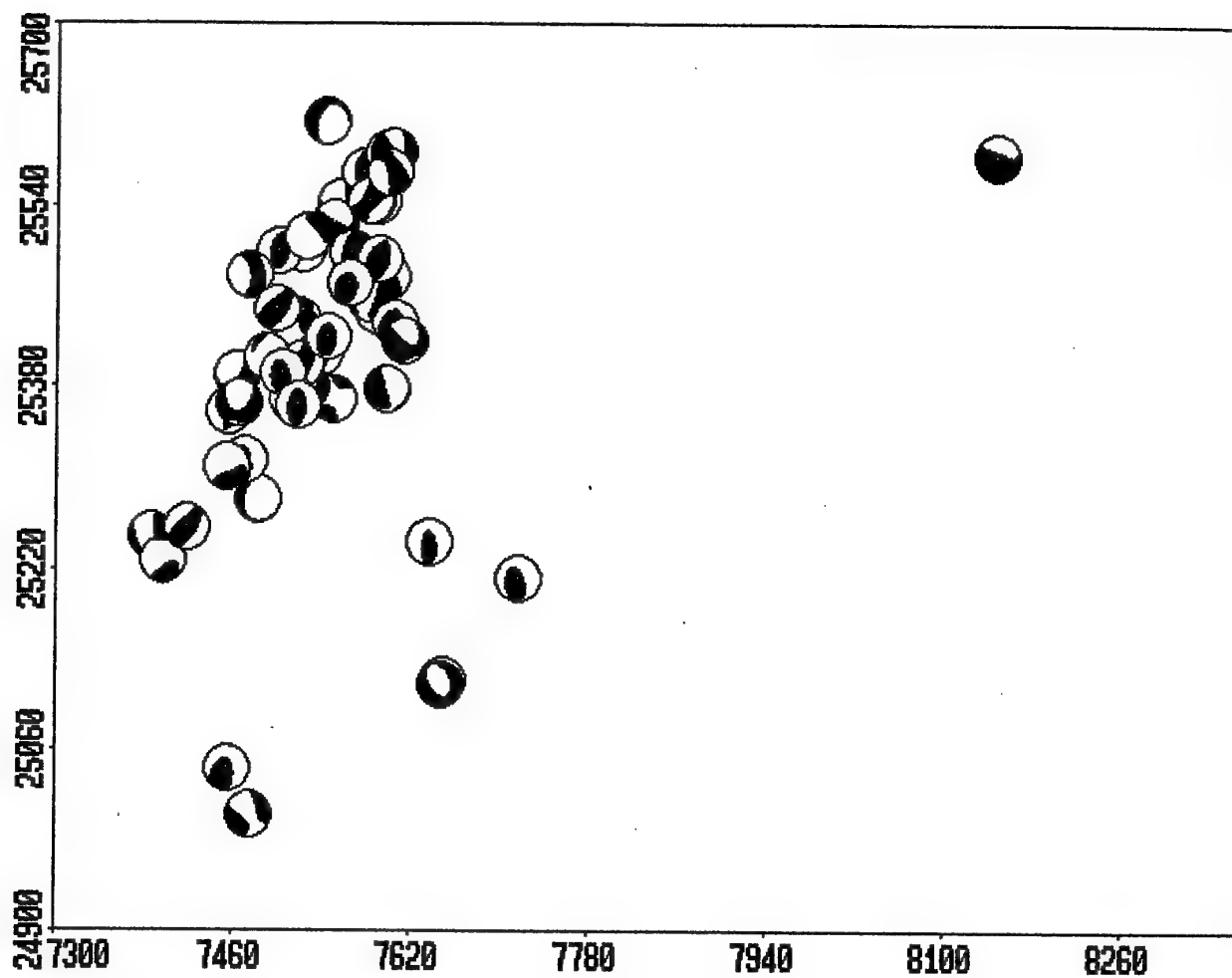


FIGURE 38. Horizontal distribution of full moment tensor solutions for seismic events at section G-21. Equal-area lower-hemisphere projection is used.

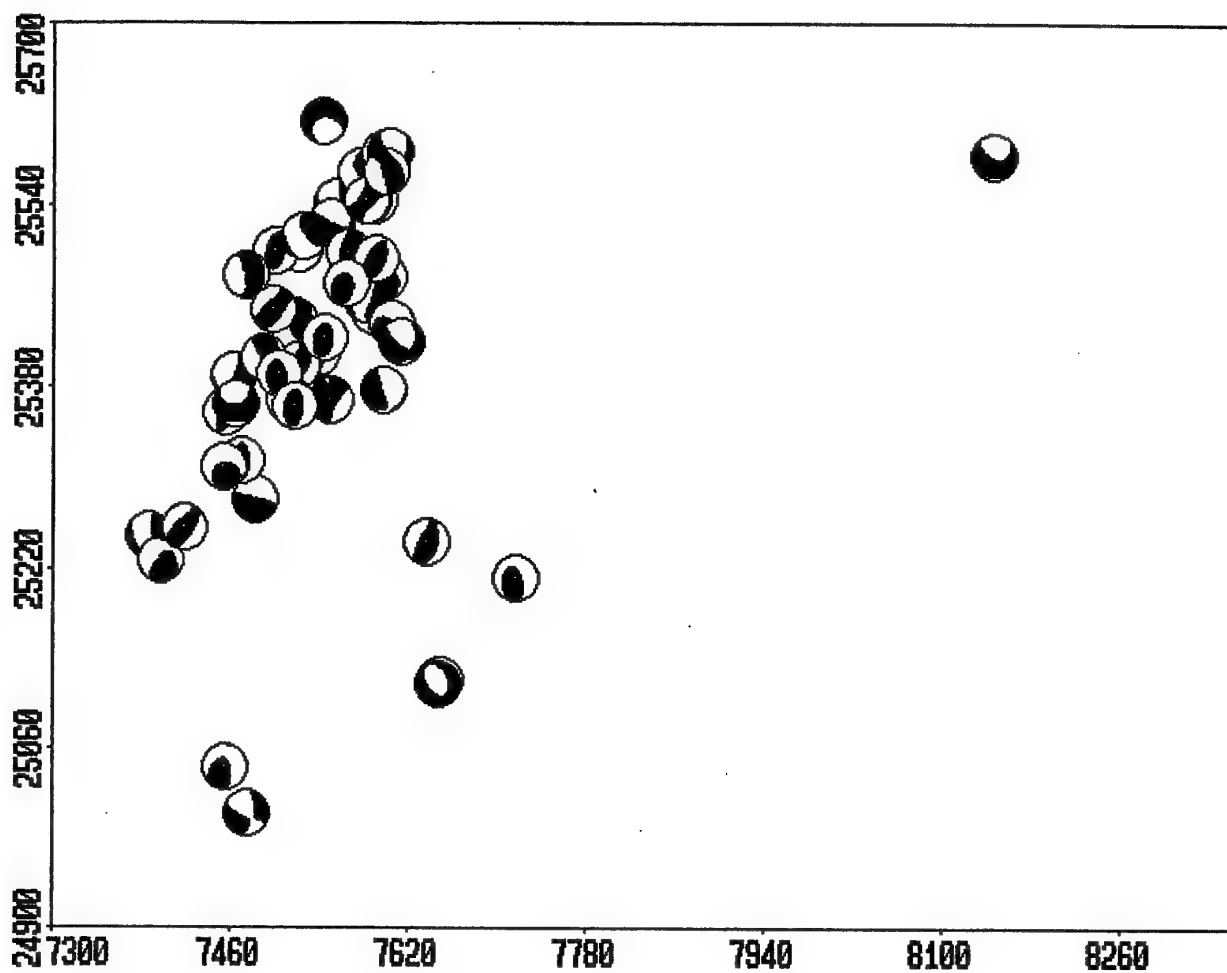


FIGURE 39. Horizontal distribution of deviatoric moment tensor solutions for seismic events at section G-21. Equal-area lower-hemisphere projection is used.

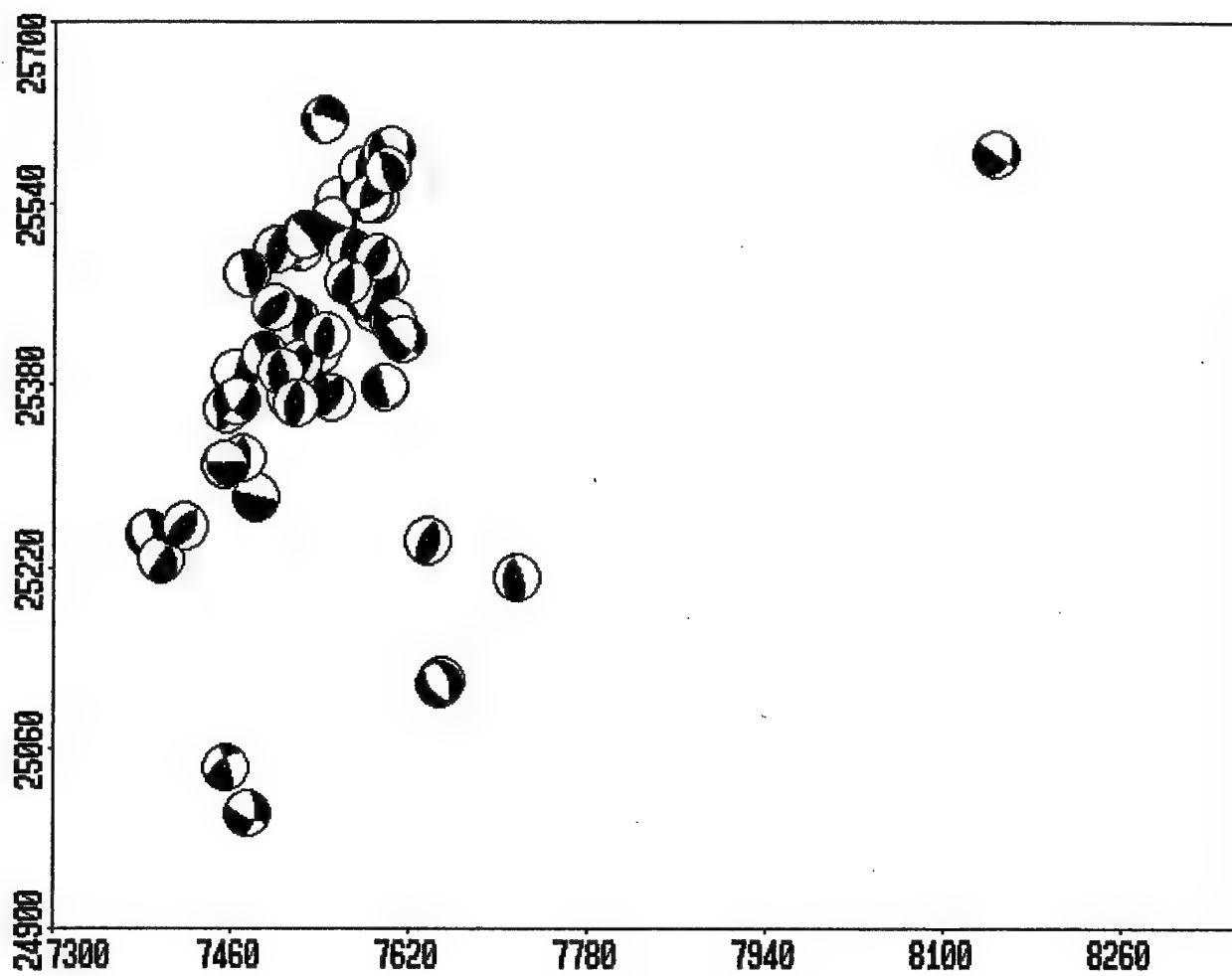


FIGURE 40. Horizontal distribution of double couple moment tensor solutions for seismic events at section G-21. Equal-area lower-hemisphere projection is used.

## 7. CONCLUSIONS

The objective of this research has been to investigate possible time variations of source parameters and source mechanism of seismic events forming sequences at a Polish copper mine. To accomplish this objective we selected Polkowice copper mine, situated in the Lubin copper mining district in south-western Poland. Its underground digital seismic network is composed of 22 stations with vertical-component sensors and 3 stations with three-component sensors. Two mining sections G-32 and G-21, characterized by the highest level of seismicity in the mine, were considered. Altogether 34 seismic events from section G-32, which occurred between May 1994 and May 1995, and 56 events from section G-21, which occurred between October 1994 and May 1995, were selected for our study.

In contrast to South African gold mines, seismic sequences are seldom observed in Polish copper mines. The search for regular seismic sequences at Polkowice mine, in a sense used in earthquake seismology, was not successful. The selected seismic events, on the other hand, form close clusters in a sense that they occurred in small well defined areas and within a defined time period. They can be considered therefore as a series of closely related events associated with mining works in the two sections. The two series are characterized by a rather low values of fractal dimension,  $D=2.0$  for the events at section G-32 and  $D=2.2$  for the events at section G-21, in comparison with those from natural seismicity. The decreasing of fractal dimension indicates that fracture events became more strongly correlated with advancing fracturing.

The selected seismic events from the both sections have moment magnitude ranging from 1.2 to 3.0 and seismic energy between  $1 \cdot 10^4$  and  $1 \cdot 10^8$  J. The corner frequency of P waves ranges from 2.2 to 13 Hz and the corner frequency of S waves ranges between 2.8 and 7.3 Hz. The corresponding source radius is in the range from about 75 to 370 m. The scaling relations imply that the self-similarity rule is probably valid there, but the range of observations is very narrow. The stress drop is not high and it ranges from 0.025 to 0.56 MPa and the apparent stress ranges from 0.002 to 0.063 MPa. The apparent stress is roughly ten times lower than the stress drop.

All computed source parameters of seismic events from section G-32 show similar distribution in time. There is one outstanding event with magnitude 2.7 preceded by an event of magnitude 2.3. Their source parameters are of the highest values, while those of the other events are randomly distributed in time. The only pattern observed in time distributions is the presence of small seismic events directly following the main event and forming a kind of quiescent interval before the occurrence of larger events at the end of the series. The time distribution of the source parameters of seismic events from section G-21 is even less regular than that from section G-32. There are two outstanding events with moment magnitude 3.0 and 2.7. These two events are most distinctly marked by their source radius rather than by their seismic moment or seismic energy.

The first *P*-wave motion amplitudes were inverted in the time domain to produce three types of seismic moment tensors: the full tensor, the deviatoric tensor, and the double couple tensor. The deviatoric and double couple solutions are to great extent similar, whereas the full solutions are for some events different from the other two, often showing large non-shearing components. These most probably result from unfavorable distribution of seismic stations on the focal sphere. The constrained deviatoric tensor solutions show also occasionally large non-shearing components, but in most cases their contribution to the focal mechanism is smaller than 20 percent of the solution.

A number of seismic events from the central part of section G-32 have similar focal mechanism with one nodal plane running in the E-W direction and the pressure quarter of the focal sphere situated to the south of this plane. Similarly, many seismic events from the most active area of section G-21 have similar focal mechanism which can be interpreted as a reverse fault with the N-S strike. How far the regular pattern observed in the space distribution of focal mechanisms is associated with mining works in the area is difficult to assess, since a detailed information on daily mining activity is not available.



## REFERENCES

- Aki, K. (1965). Maximum likelihood estimate of  $b$  in the formula  $\log N = a - bM$  and its confidence limits. *Bull. Earthq. Res. Inst. Tokyo Univ.* **43**, 237-239.
- Aki, K. (1981). A probabilistic synthesis of precursory phenomena. In *Earthquake Prediction - an International Review* (D. W. Simpson and P. G. Richards, eds.), Maurice Ewing Vol. 4, pp. 566-574. Am. Geophys. Union, Washington, D. C.
- Aki, K., and Richards, P. G. (1980). *Quantitative Seismology. Theory and Methods*. Freeman, San Francisco.
- Andrews, D. J. (1986). Objective determination of source parameters and similarity of earthquakes of different size. In *Earthquake Source Mechanics* (S. Das, J. Boatwright, and C. H. Scholz, eds.), Maurice Ewing Vol. 6, pp. 259-267. Am. Geophys. Union, Washington, D. C.
- Bak, P., and Tang, C. (1989). Earthquakes as a self-organized critical phenomenon. *J. Geophys. Res.* **94**, 15,635-15,637.
- Boatwright, J. (1984). Seismic estimates of stress release. *J. Geophys. Res.* **89**, 6961-6968.
- Boatwright, J., and Fletcher, J. B. (1984). The partition of radiated energy between  $P$  and  $S$  waves. *Bull. Seism. Soc. Am.* **74**, 361-376.
- Boatwright, J., and Quin, H. (1986). The seismic radiation from a 3-D dynamic model of a complex rupture process. In *Earthquake Source Mechanics* (S. Das, J. Boatwright, and J. H. Scholz, eds.), Maurice Ewing Vol. 6, pp. 97-109. Am. Geophys. Union, Washington, D. C.
- Boore, D. M., and Boatwright, J. (1984). Average body-wave radiation coefficients. *Bull. Seism. Soc. Am.* **74**, 1615-1621.

- Brune, J. N. (1970). Tectonic stress and the spectra of seismic shear waves from earthquakes. *J. Geophys. Res.* **75**, 4997-5009.
- Brune, J. N. (1971). Correction. *J. Geophys. Res.* **76**, 5002.
- Bullen, K. E., and Bolt, B. A. (1985). *An Introduction to the Theory of Seismology*. Cambridge University Press, Cambridge (U. K.).
- Burdick, L. J. (1978).  $t^*$  for S waves with a continental ray path. *Bull. Seism. Soc. Am.* **68**, 1013-1030.
- De Natale, G., Iannaccone, G., Martini, M., and Zollo, A. (1987). Seismic sources and attenuation properties at the Campi Flegrei volcanic area. *Pure Appl. Geophys.* **125**, 883-917.
- Del Pezzo, E., De Natale, G., Martini, M., and Zollo, A. (1987). Source parameters of microearthquakes at Phlegraean Fields (Southern Italy) volcanic area. *Phys. Earth Planet. Interiors* **47**, 25-42.
- Di Bona, M., and Rovelli, A. (1988). Effects of the bandwidth limitation on stress drops estimated from integrals of the ground motion. *Bull. Seism. Soc. Am.* **78**, 1818-1825.
- Evison, F. (1977). Fluctuations of seismicity before major earthquakes. *Nature* **266**, 710-712.
- Fehler, M., and Phillips, W. S. (1991). Simultaneous inversion for  $Q$  and source parameters of microearthquakes accompanying hydraulic fracturing in granitic rock. *Bull. Seism. Soc. Am.* **81**, 553-575.
- Feignier, B., and Young, R. P. (1992). Moment tensor inversion of induced microseismic events: Evidence of non-shear failures in the  $-4 < M < -2$  moment magnitude range. *Geophys. Res. Lett.* **19**, 1503-1506.
- Fitch, T. J., McGowan, D. W., and Shields, M. W. (1980). Estimation of seismic moment tensor from teleseismic body wave data with application to intraplate and mantle earthquakes. *J. Geophys. Res.* **85**, 3817-3828.

- Fujii, Y., and Sato, K. (1990). Difference in seismic moment tensors between microseismic events associated with a gas outburst and those induced by longwall mining activity. In *Rockbursts and Seismicity in Mines* (C. Fairhurst, ed.), pp. 71-75. Balkema, Rotterdam.
- Giardini, D. (1984). Systematic analysis of deep seismicity: 200 centroid-moment tensor solutions for earthquakes between 1977 and 1980. *Geophys. J. Roy. Astr. Soc.* **77**, 883-914.
- Gibowicz, S. J. (1984). The mechanism of large mining tremors in Poland. In *Rockbursts and Seismicity in Mines* (N.C. Gay and E. H. Wainwright, eds.), Symp. Ser. No. 6, pp. 17-28. S. Afr. Inst. Min. Met., Johannesburg.
- Gibowicz, S. J. (1990). Keynote lecture: The mechanism of seismic events induced by mining - A review. In *Rockbursts and Seismicity in Mines* (C. Fairhurst, ed.), pp. 3-27. Balkema, Rotterdam.
- Gibowicz, S. J. (1993). Keynote address: Seismic moment tensor and the mechanism of seismic events in mines. In *Rockbursts and Seismicity in Mines* (R. P. Young, ed.), pp. 149-155. Balkema, Rotterdam.
- Gibowicz, S. J. (1995). Scaling relations for seismic events induced by mining. *Pure Appl. Geophys.* **144**, 191-209.
- Gibowicz, S. J., and Wiejacz, P. (1994). A search for the source non-shearing components of seismic events induced in Polish coal mines. *Acta Geophys. Pol.* **42**, 81-110.
- Gibowicz, S. J., Bober, A., Cichowicz, A., Droste, Z., Dychtowicz, Z., Hordejuk, J., Kazimierczyk, M., and Kijko, A. (1979). Source study of the Lubin, Poland, tremor of 24 March 1977. *Acta Geophys. Pol.* **27**, 3-38.
- Gibowicz, S. J., Niewiadomski, J., Wiejacz, P., and Domanski, B. (1989). Source study of the Lubin, Poland, mine tremor of 20 June 1987. *Acta Geophys. Pol.* **37**, 111-132.
- Gibowicz, S. J., Harjes, H.-P., and Schäfer, M. (1990). Source parameters of seismic events at Heinrich Robert mine, Ruhr basin, Federal Republic of

- Germany: Evidence for nondouble-couple events. *Bull. Seism. Soc. Am.* **80**, 88-109.
- Gibowicz, S. J., Young, R. P., Talebi, S., and Rawlence, D. J. (1991). Source parameters of seismic events at the Underground Research Laboratory in Manitoba, Canada: Scaling relations for the events with moment magnitude smaller than -2. *Bull. Seism. Soc. Am.* **81**, 1157-1182.
- Gilbert, F. (1970). Excitation of the normal modes of the earth by earthquake sources. *Geophys. J. Roy. Astr. Soc.* **22**, 223-226.
- Grassberger, P. (1983). Generalized dimensions of strange attractors. *Phys. Lett. A* **97**, 227-230.
- Guo, Z., and Ogata, Y. (1995). Correlation between characteristic parameters of aftershock distributions in time, space and magnitude. *Geophys. Res. Lett.* **22**, 993-996.
- Hanks, T. C., and Kanamori, H. (1979). A moment magnitude scale. *J. Geophys. Res.* **84**, 2348-2350.
- Haskell, N. A. (1964). Total energy and spectral density of elastic wave radiation from propagating faults. *Bull. Seism. Soc. Am.* **54**, 1811-1841.
- Hirabayashi, T., Ito, K., and Yoshii, T. (1992). Multifractal analysis of earthquakes. *Pure Appl. Geophys.* **138**, 591-610.
- Hirata, T. (1987). Omori's power law aftershock sequences of microfracturing in rock fracturing experiments. *J. Geophys. Res.* **92**, 6215-6221.
- Hirata, T., Satoh, T., and Ito, K. (1987). Fractal structure of spatial distribution of microfracturing in rock. *Geophys. J. Roy. Astr. Soc.* **67**, 697-717.
- Ito, K. (1992). Towards a new view of earthquake phenomena. *Pure Appl. Geophys.* **138**, 531-548.
- Ito, K., and Matsuzaki, M. (1990). Earthquakes as self-organized critical

phenomena. *J. Geophys. Res.* **95**, 6853-6860.

Jones, L. M., and Molnar, P. (1979). Some characteristics of foreshocks and their possible relationship to earthquake prediction and premonitory slip on faults. *J. Geophys. Res.* **84**, 3596-3608.

Kagan, Y. Y., and Knopoff, L. (1980). Spatial distribution of earthquakes: The two-point correlation function. *Geophys. J. Roy. Astr. Soc.* **62**, 303-320.

Kanamori, H., and Anderson, D. L. (1975). Theoretical basis for some empirical relations in seismology. *Bull. Seism. Soc. Am.* **65**, 1073-1096.

Kanamori, H., and Given, J. W. (1981). Use of long-period surface waves for rapid determination of earthquake source parameters. *Phys. Earth Planet. Interiors* **27**, 8-31.

Kennett, B. L. N. (1988). Radiation from a moment-tensor source. In *Seismological Algorithms* (D. J. Doornbos, ed.), pp. 427-441. Academic Press, London.

Knopoff, L., and Gilbert, F. (1959). Radiation from a strike-slip fault. *Bull. Seism. Soc. Am.* **49**, 163-178.

Langston, C. A. (1981). Source transmission of seismic waveforms: The Koyna, India earthquakes of September 13, 1967. *Bull. Seism. Soc. Am.* **71**, 1-24.

Lawson, C. L., and Hanson, R. J. (1974). *Solving Least Square Problems*. Prentice-Hall, Englewood Cliffs, N. J.

McGarr, A. (1992a). An implosive component in the seismic moment tensor of a mining-induced tremor. *Geophys. Res. Lett.* **19**, 1579-1582.

McGarr, A. (1992b). Moment tensors of ten Witwatersrand mine tremors. *Pure Appl. Geophys.* **139**, 781-800.

McGarr, A., and Green, R. W. E. (1978). Microtremor sequences and tilting in a deep mine. *Bull. Seism. Soc. Am.* **68**, 1679-1697.

- Madariaga, R. (1976). Dynamics of an expanding circular fault. *Bull. Seism. Soc. Am.* **66**, 639-666.
- Mandelbrot, B. B. (1982). *The Fractal Geometry of Nature*. Freeman, San Francisco.
- Mendecki, A. J. (1993). Keynote address: Real time quantitative seismology in mines. In *Rockbursts and Seismicity in Mines* (R. P. Young, ed.), pp. 287-295. Balkema, Rotterdam.
- Mendoza, C., and Hartzell, S. H. (1988). Aftershock patterns and main shock faulting. *Bull. Seism. Soc. Am.* **78**, 1438-1449.
- Mogi, K. (1963). Some discussions on aftershocks, foreshocks and earthquake swarms - the fracture of a semi-infinite body caused by inner stress origin and its relation to the earthquake phenomena (3). *Bull. Earthq. Res. Inst. Tokyo Univ.* **41**, 615-658.
- Montalbetti, J. R., and Kanasevich, E. R. (1970). Enhancement of teleseismic body phases with a polarization filter. *Geophys. J. Roy. Astr. Soc.* **21**, 119-129.
- O'Connell, D. R. H., and Johnson, L. R. (1988). Second-order moment tensors of microearthquakes at The Geysers geothermal field, California. *Bull. Seism. Soc. Am.* **78**, 1674-1692.
- Ogata, Y. (1983). Estimation of the parameters in the modified Omori formula for aftershock frequencies by maximum likelihood procedure. *J. Phys. Earth* **31**, 115-124.
- Oncescu, M. C. (1986). Relative seismic moment tensor determination for Vrancea intermediate depth earthquakes. *Pure Appl. Geophys.* **124**, 931-940.
- Pagaczewski, J. (1972). Catalogue of earthquakes in Poland in 1000-1970 years. *Publ. Inst. Geophys. Pol. Ac. Sci.* **51**, 3-36.
- Park, J., Vernon, F. L., and Lindberg, C. R. (1987). Frequency dependent

polarization analysis of high-frequency seismograms. *J Geophys. Res.* **92**, 664-674.

Patton, H., and Aki, K. (1979). Bias in the estimate of seismic moment tensor by the linear inversion method. *Geophys. J. Roy. Astr. Soc.* **59**, 479-495.

Plesinger, A., Hellweg, M., and Seidl, D. (1986). Interactive high-resolution polarization analysis of broadband seismograms. *J. Geophys.* **59**, 129-139.

Press, W. H., Flannery, B. P., Teukolsky, S. A., and Vetterling, W. T. (1990). *Numerical Recipes: The Art of Scientific Computing*. Cambridge University Press, New York.

Revalor, R., Josien, J. P., Besson, J. L., and Magron, A. (1990). Seismic and seismoacoustic experiments applied to the prediction of rockbursts in French coal mines. In *Rockbursts and Seismicity in Mines* (C. Fairhurst, ed.), pp. 301-306. Balkema, Rotterdam.

Rovelli, A., Cocco, M., Console, R., Alessandrini, B., and Mazza, S. (1991). Ground motion waveforms and source spectral scaling from close-distance accelerograms in a compressional regime area (Friuli, northeastern Italy). *Bull. Seism. Soc. Am.* **81**, 57-80.

Sadovskiy, M. A., Golubeva, T. V., Pisarenko, V. F., and Shnirman, M. G. (1984). Characteristic dimensions of rock and hierarchical properties of seismicity. *Izv. Acad. Sci. USSR Phys. Solid Earth* **20**, 87-96.

Salski, W. (1977). Tectonic development of the copper bearing area of the Fore-Sudetic Monocline. *Ann. Soc. Geol. Pologne* **47**, 27-48.

Sato, K., and Fujii, Y. (1989). Source mechanism of a large scale gas outburst at Sunagawa coal mine in Japan. *Pure Appl. Geophys.* **129**, 325-343.

Scherbaum, F. (1990). Combined inversion for the three-dimensional *Q* structure and source parameters using microearthquake spectra. *J. Geophys. Res.* **95**, 423-438.

- Scholz, C. (1972). Crustal movements in tectonic areas. *Tectonophysics* **14**, 201-217.
- Scholz, C. H. (1990). *The Mechanics of Earthquakes and Faulting*. Cambridge University Press, Cambridge (U. K.).
- Silver, P. G., and Jordan, T. H. (1982). Optimal estimation of scalar seismic moment. *Geophys. J. Roy. Astr. Soc.* **70**, 755-787.
- Sipkin, S. A. (1982). Estimation of earthquake source parameters by the inversion of waveform data: Synthetic waveforms. *Phys. Earth Planet. Interiors* **30**, 242-259.
- Snoke, J. A. (1987). Stable determination of (Brune) stress drops. *Bull. Seism. Soc. Am.* **77**, 530-538.
- Stump, B. W., and Johnson, L. R. (1977). The determination of source properties by the linear inversion of seismograms. *Bull. Seism. Soc. Am.* **67**, 1489-1502.
- Sykes, L. R. (1970). Earthquake swarms and sea-floor spreading. *J. Geophys. Res.* **75**, 6598-6611.
- Takayashu, H. (1990). *Fractals in the Physical Sciences*. Manchester University Press, Manchester.
- Utsu, T. (1961). Statistical study on the occurrence of aftershocks. *Geophys. Mag.* **30**, 521-605.
- Utsu, T. (1965). A method for determining the value of  $b$  in the formula  $\log n = a - bM$  showing the magnitude-frequency relation for earthquakes. *Bull. Hokkaido Univ.* **13**, 99-103 (in Japanese with English abstract).
- Utsu, T. (1971). Aftershocks and earthquake statistics, III. *J. Fac. Sci., Hokkaido Univ., Ser. VII* **3**, 379-441.
- Vidale, J. E. (1986). Complex polarization analysis of particle motion. *Bull. Seism. Soc. Am.* **76**, 1393-1405.



- Walter, W. R., and Brune, J. N. (1993). Spectra of seismic radiation from a tensile crack. *J. Geophys. Res.* **98**, 4449-4459.
- Wiejacz, P. (1992). Calculation of seismic moment tensor for mine tremors from the Legnica-Głogów copper basin. *Acta Geophys. Pol.* **40**, 103-122.
- Wiejacz, P. (1995). Moment tensors for seismic events from Upper Silesian coal mines, Poland. In *Mechanics of Jointed and Faulted Rock* (H.-P. Rossmanith, ed.), pp. 667-672. Balkema, Rotterdam.
- Wyss, M., and Brune, J. N. (1968). Seismic moment, stress and source dimensions for earthquakes in the California-Nevada region. *J. Geophys. Res.* **73**, 4681-4694.